University of Alberta

Template-Based Fabrication of Inorganic, Organic, and Liquid Crystalline Polymer Microstructured Thin Films

by

Anastasia Leila Elias 

A thesis submitted to the Faculty of Graduate Studies and Research
in partial fulfillment of the requirements for the degree of

Doctor of Philosophy

Department of Electrical and Computer Engineering

Edmonton, Alberta
Spring 2007

Your file Votre référence
ISBN: 978-0-494-29671-4
Our file Notre référence
ISBN: 978-0-494-29671-4

Abstract

Porous thin films deposited by glancing angle deposition (GLAD) are under study by many groups around the world due to their favorable characteristics, which include high porosity, structural tunability, and unique optical and mechanical properties. In this thesis, template-based fabrication processes are developed in which films deposited at glancing angle act as the master, enabling a variety of materials to be shaped on the micro- and nanoscale. The properties of these micro- and nanostructured films are investigated, particularly with an interest in using these materials in micro-actuator devices.

A single-templating process is used to fabricate metal and polymer thin films with engineered helical pores. Finite element modeling is used to show that the moduli of these materials can be tuned by varying the rise angle of the helices. A double-templating process is presented which can be used to fabricate polymer helices.

The thermal, mechanical, and optical properties of liquid crystalline polymers (LCP) are investigated. It is found that materials which contract in one direction by 22% when heated to 200 °C can be made by photo-polymerization of appropriate monomer mixtures. The thermomechanical properties of these materials are found to depend strongly on the alignment of the liquid crystalline moieties within the film and the applied boundary constraints. These results are confirmed by finite element modeling.

With an interest in shaping liquid crystalline polymers in single and double-templating processes, a nuclear magnetic resonance (NMR) study is conducted to determine the alignment of liquid crystals in a helical GLAD template. It is found that the liquid crystals follow the rise angle of the helices.

Single-templating, double-templating, photopatterning, and micro-transfer printing techniques are used to shape liquid crystalline polymers on the micro and nanoscale. Actuation of the structures formed using each of these techniques is presented. It is found that single-phase photopatterning can be used to pattern planar structures which expand by up to 9% when heated to 200 °C. A single-templating process can be used to make selectively-reinforced liquid crystalline polymer and isotropic polymer layers, which undergo significant changes in surface topography when heated.

Acknowledgment:

While I am the 'first author' of this thesis, there is a long list of people who made valuable contributions to this work. I would like to take this opportunity to thank as many of them as possible.

First and foremost I would like to thank my supervisor, Dr. Michael Brett. At the end of my first year of University Dr. Brett convinced me to enter to Engineering Physics program, which set the course for the last 7 years of my education. 3 years later I joined his lab as a graduate student. Dr. Brett has been an approachable and supportive supervisor, who has always encouraged me to pursue whatever lines of scientific study have caught my interest along the way. I am privileged to have been able to carry out my grad studies in the GLAD group.

During the course of thesis work I have been fortunate to have had the opportunity to undertake collaborative projects with a number of different research groups. I would like to extend my sincere thanks to Dr. Dick Broer and Dr. Kees Bastiaansen, who welcomed me into their lab at the Technische Universiteit Eindhoven, and treated me like one of their own students.

I would also like to acknowledge Dr. Gregory Crawford at Brown University, without whom Chapter 5 would not exist. I am grateful for your guidance and hospitality. Thanks also to Matt Sousa, Jim Eakin, and Scott Woltman with whom I worked on the NMR project.

Thesis work in microfabrication would not have been possible without the excellent tools provided by the University of Alberta Micromachining and Nanofabrication Facility. Thanks to Ken, Keith, Stephanie, Dionne, Melissa, Bob, Mirwais, Kristian, Les, and everyone else who has kept this impressive, open access facility running over the years. The user community at the Nanofab is second to none, and I have benefited greatly from the exchange of ideas and problem solving that takes place therein.

As are most graduates of the GLAD group, I am indebted to George Braybrook for his incredible SEM work, which is displayed throughout this thesis. Tuesday and Thursday afternoons at the SEM with George were always an enjoyable part of my week. Thank you for patiently searching through many hundreds to thousands of samples with me.

I would like to thank Karin Hayward, the woman-behind-the-scenes who keeps the GLAD group running smoothly. I would also like to acknowledge Ben Bathgate, who was always happy to help me build something in the lab, especially if I threatened to do it myself.

There were many people who helped me with experiments at the Technische Universiteit Eindhoven, and Philips Research in the Netherlands. These include SEM-experts Pauline Schmidt and Marc van Maris; Chris Hendriks, who provided assistance with nanoindentation; Titie Mol, who instructed me in the use of the thermal mechanical analyzer; and Jules Kierkels, who trained me to use the dynamic mechanical analyzer.

There are a multitude of graduate students at the University of Alberta and the Technische Universiteit Eindhoven to whom I owe thanks for assistance along the way. These include James Gospodyn, who I can always count on to do me a favor; Casper van Oosten whom I email regularly in the Netherlands to carry out 'one last experiment' on my behalf; Joost Valeton, a Dutch officemate who assisted me with DSC measurements, kept me company at the lab on weekends, and, most importantly, made sure that there was regular supply of coffee in our office; Shufen Tsoi, contact-angle measurer extraordinaire; Matthew Hawkeye, who performed an "emergency" deposition for me when I was in the Netherlands and missing a sample; and Dr. Jeremy Sit, who provided technical assistance particularly in times of crisis. I would also like to acknowledge the two summer students who assisted with my project: Sumudu Fernando, programming wizard, and Bryan Szeto, who once suffered heat-stroke after spending all day in the nanofab processing samples for me on a day when the temperature was kept very high to keep the humidity low.

Undergrad and grad school would not have been the same without the company of Andy van Popta and Peter Hrudey, with whom I spent way too many hours in the South Lab doing homework. It has been a pleasure to work with you.

I would like to thank my mother Darlene and my brother Zack, particularly for tolerating me during my undergraduate years when I assigned a maximum volume at which they were allowed to watch television while I was studying. Thanks for being my support system.

Lastly I would like to acknowledge my husband and best collaborator Dr. Ken Harris, who is always happy to discuss science over dinner or spend a long weekend in the lab, and who willingly proof-read this thesis more than once.

Table of Contents

1 Micro- and Nanostructuring of Inorganic and Organic Materials 1

1.1 Introduction 1

1.2 Intention 2

1.3 Scope 3

1.4 References 5

2 Background: Glancing Angle Deposition 7

2.1 Introduction 7

2.2 Physical Vapor Deposition 7

2.3 Structure of Films Deposited by Evaporation 8

2.4 Oblique Angle Deposition 11

2.5 Glancing Angle Deposition 13

2.5.1 *Deposition Angle* 13

2.5.2 *Substrate Rotation* 16

2.5.3 *Film Growth and Morphology* 18

2.5.4 *Crystallinity* 19

2.5.5 *Materials* 20

2.6 Applications of Porous Thin Films Deposited by GLAD 22

2.7 References 25

3 Template Based Fabrication: Single-Templating 29

3.1 Macroporous Thin Films 29

3.2 Templating From GLAD Thin Films 31

3.3 Fabrication of Non-Polar Polymer Perforated Thin Films 34

3.4 Fabrication of Metallic Perforated Thin Films - Nickel 37

3.4.1 *Master Template Fabrication* 40

3.4.2 *Matrix Filling* 41

3.4.3 *Matrix Etch-Back* 43

3.4.4 *Template Removal* 43

3.5 Fabrication of Metallic Perforated Thin Films – Gold 44
3.6 Mechanical Characterization of Nickel Perforated Thin Films 45
3.6.1 *Finite Element Modeling*.....46
3.6.2 *Nanoindentation*.....54
3.7 Conclusion 59
3.8 References.....59

4 Template-Based Fabrication: Double-Templating 63
4.1 Polymer Helices.....63
4.2 Polymers 65
4.3 UV Initiators 67
4.4 Fabrication 69
4.5 Liquid Crystalline Polymer Helices.....78
4.6 References.....79

5 A Deuterium Nuclear Magnetic Resonance Study of the Alignment of Nematic Liquid Crystals in a GLAD Thin Film.....81
5.1 Liquid Crystals.....81
5.2 Liquid Crystal Alignment 83
5.3 Nuclear Magnetic Resonance 87
5.4 Deuterium Nuclear Magnetic Resonance (2H-NMR) 91
5.5 Determination of LC alignment in a GLAD film 97
5.6 Modeling: Predicting Alignment 99
5.7 Results and Conclusions 104
5.8 References.....106

6 Properties of Liquid Crystalline Polymers (LCP) 109
6.1 Introduction to Liquid Crystalline Polymers 109
6.2 Thermomechanical Properties of Macroscopic Samples of LCP 115
6.2.1 *Materials*.....115

6.2.2 *Sample Preparation* 115
6.2.3 *Thermomechanical Characterization* 118
6.3 Optical Properties of Uniaxially-Aligned LCP Thin Films 121
6.3.1 *Theory* 121
6.3.2 *Measurements* 123
6.4 Mechanical properties of samples confined to a surface 127
6.4.1 *Experimental Method* 129
6.4.2 *White-light Interferometry* 130
6.4.3 *Experimental Results* 133
6.4.4 *Modeling* 136
6.5 Conclusion 142
6.6 References 143

7 Micro-Patterning LCP Using Templating-Based Processes 148
7.1 Introduction 148
7.2 GLAD Templating: Liquid Crystalline Polymer Helices 149
7.2.1 *Fabrication* 149
7.2.2 *Actuation* 153
7.3 Fabrication of LCP-PTFs from templates deposited by GLAD 155
7.3.1 *Fabrication* 155
7.3.2 *Actuation* 159
7.3.3 *Theoretical Calculations* 161
7.4 Bilayer composite films selectively-reinforced with nanorebar 170
7.4.1 *Fabrication* 171
7.4.2 *Actuation* 176
7.4.2.1 *Selectively-Reinforced Homeotropic Films* 176
7.4.2.2 *Selectively-Reinforced Cholesteric Films* 179
7.4.2.3 *Selectively-Reinforced Isotropic PolymerFilms* 180
7.4.3 *Summary* 182
7.5 Conclusion 182
7.6 References 183

8 Micro-Patterning of LCP: Photopatterning & Micro-Transfer Printing...185

8.1 Introduction....185

8.2 Photopatterning....185

8.2.1 *Fabrication*....187

8.2.2 *Actuation*....191

8.2.2.1 *Actuation of Multi-Phase Photopatterned Samples*....191

8.2.2.2 *Actuation of Single-Phase Photopatterned Samples*....193

8.3 Micro-Transfer Printing....196

8.3.1 *Fabrication*....196

8.3.2 *Actuation*....200

8.4 Conclusion....201

8.5 References....202

9 Conclusion....203

9.1 Summary of Results....203

9.2 Outlook....206

9.3 References....209

Appendix 1: MATLAB Code for NMR Modeling....210

List of Tables

3.1 Parameters employed in finite element model for helically-perforated GLAD films 51

4.1 Summary of lamps 68

6.1 Alignment-dependent thermal actuation 134

6.2 Average thermal expansion coefficients 139

6.3 Average thermal expansion coefficients of cholesteric and planar films ... 141

7.1 Geometric parameters used to determine the modulus of nanorebar 166

7.2 Top-etched perforated thin film material parameters 167

List of Figures

2.1 Thin film nucleation and growth 10

2.2 Deposition angle (α) and film growth angle (β) 12

2.3 Glancing angle deposition 14

2.4 Tait's rule 15

2.5 The in-plane substrate angle phi 16-

2.6 Assorted GLAD films 17

2.7 Aluminum film deposited by glancing angle deposition 20

3.1 Perforated thin film fabrication process 33

3.2 SiO_2 GLAD film spin-coated with polystyrene/xylene mixture 35

3.3 Polystyrene perforated thin films 37

3.4 An electroplating set-up 38

3.5 Fabrication of a nickel perforated thin film 40

3.6 Gold perforated thin film 45

3.7 Finite element analysis 47

3.8 Normal and shear stress 49

3.9 Parameters of inverted helix 51

3.10 Elastic modulus as a function of rise angle and cross-sectional radius 52

3.11 Elastic modulus as a function of coil-spacing and cross-sectional radius .54

3.12 Nanoindentation 55

3.13 Berkovich Tip 56

3.14 Nickel PTFs for nanoindentation 58

4.1 Ethylene and polyethylene 65

4.2 Methyl methacrylate monomer and polymer 66

4.3 Irgacure 184 67

4.4 Fabrication of polymer helices using a double-templating process 69

4.5 Multifunctional acrylates 71

4.6 Elastic modulus of acrylate polymers as a function of frequency 72

4.7 FTIR 76
4.8 Polymer Helices 77

5.1 Liquid crystalline molecules 82
5.2 Thermotropic liquid crystals 82
5.3 Common liquid crystal alignments 84
5.4 Transmission electron microscopy 85
5.5 Cholesteric liquid crystals 86
5.6 The Zeeman effect 88
5.7 Vector representation of a deuterium nuclei in a magnetic field 90
5.8 5CB-αd_2 spectra 93
5.9 The powder pattern 94
5.10 Splitting frequency 95
5.11 GLAD sample 97
5.12 Alpha-deuterated 4'-pentyl-4-cyanobiphenyl (5CB-αd_2) 98
5.13 Hypothetical alignments 100
5.14 Frequency domain spectra based on hypothetical alignments 103
5.15 NMR results for a helical GLAD film filled with 5CB-αd 104

6.1 Liquid crystalline monomers 110
6.2 Preparation of liquid single crystal elastomers 111
6.3 Actuation of a liquid crystalline elastomer 112
6.4 Fabrication of uniaxially aligned LCP thin films 117
6.5 Thermal actuation of uniaxially-aligned LCP film 118
6.6 Parallel and perpendicular thermomechanical behavior 119
6.7 Optical properties of liquid crystals 121
6.8 Vector representation of light incident on the liquid crystalline film 122
6.9 Transmittance of light through a birefringent sample 124
6.10 Birefringence as a function of temperature 126
6.11 LC configurations 128
6.12 A simplified interferometer 131

6.13 Thermal actuation of surface-anchored samples....133
6.14 Actuation of free-standing and substrate-anchored films....135
6.15 Sample geometry and boundary conditions....137
6.16 Finite element modelling of homeotropic films....140
6.17 Modeled deformation of a cholesteric film....142

7.1 Poly(M1:M2, 88:12) polymer helices....149
7.2 LC alignment in liquid crystalline polymer helices....150
7.3 Fabrication of electrically-aligned liquid crystalline polymer helices....152
7.4 Contact angle of water on ITO....153
7.5 Actuation of liquid crystalline polymer helices....154
7.6 Liquid crystalline polymer perforated thin film....156
7.7 Lithographically-patterned perforated thin film....158
7.8 Actuation of a liquid crystalline polymer perforated thin film....159
7.9 Etch-back of perforated thin films....160
7.10 Top view of a cross-sectional slice of a composite film....163
7.11 Fractional densities as a function of film position (h)....165
7.12 Local modulus of a perfectly-etched and imperfectly-etched PTF....167
7.13 Etch-removal of the master template from the bottom....170
7.14 Schematic diagram of the bilayer structure....170
7.15 A selectively-reinforced bilayer composite film....171
7.16 Fabrication of selectively-reinforced bilayer composite films....173
7.17 SEM images of selectively-reinforced bilayer composite films....175
7.18 Bird's eye view of a homeotropic, selectively-reinforced sample....177
7.19 Surface profile of homeotropic, selectively-reinforced sample....177
7.20 Actuation of a homeotropic, selectively-reinforced sample....178
7.21 Actuation of a cholesteric, selectively-reinforced sample....179
7.22 TEGDA monomer....180
7.23 A selectively-reinforced TEGDA sample....181
7.24 Actuation of a selectively-reinforced TEGDA sample....181

8.1 Single and multi-phase photopatterning 188
8.2 Multi-phase patterned samples 189
8.3 Single-substrate multi-phase photopatterned structures 190
8.4 Surface profile of a multi-phase sample 191
8.5 Multi-phase patterned sample 192
8.6 Actuation of a single-phase patterned structure 193
8.7 Actuation comparison of patterned and unpatterned samples 195
8.8 Surface profile of single-phase patterned sample 196
8.9 Micro-transfer printing 197
8.10 Printed structures 198
8.11 Molecule M3 198
8.12 Actuation of a sample made by micro-transfer printing 200

List of Symbols

Symbols from the Greek Alphabet

α – deposition angle formed between the source and substrate

$\underline{\alpha}$ – matrix containing the anisotropic linear thermal expansion coefficients

$\alpha_{\perp}$ – thermal expansion coefficient perpendicular to the molecular alignment

$\alpha_{\perp}$ – thermal expansion coefficient parallel to the molecular alignment

β – column inclination angle

β – an experimentally determined constant characterizing the broadening of a GLAD structure

β_{α} – 'natural' column inclination angle for deposition at angle α

γ – magnetogyric ratio

γ_{ij} – shear strain in the ij plane

ε – strain

ε_i or ε_{ii} – strain in the i direction

$\underline{\varepsilon}$ – strain matrix

$\varepsilon(t)$ – difference between strain at time t and in the stress free state

ε_{full} – strain in a fully etched PTF

$\varepsilon_{partial}$ – strain in a partially etched PTF

θ_B – angle formed between a director and a magnetic field

θ_{LC} – angle formed between a liquid crystal and a director

θ_r – rise angle

$\theta_{\perp}$ – angle formed between helical arm and substrate normal

λ – wavelength

λ_m – Bragg wavelength

λ_{min} – minimum wavelength reflected by a cholesteric LC structure

λ_{max} – maximum wavelength reflected by a cholesteric LC structure

Λ – path length difference

μ – magnetic moment

μ_o – permittivity of free space

ν – Poisson's ratio

ν_c – Poisson's ratio of a coating

ν_L – Larmor frequency

$\delta\nu$ – splitting frequency

$\delta\nu_B$ – bulk splitting frequency

ξ_m – magnetic coherence length

ρ_{GLAD} – fractional density of a GLAD film with respect to the bulk density

ρ_p – fractional density of the polymer in a PTF

ρ_r – fractional density of the nanorebar in a PTF

ρ_v – fractional fraction of the voids in a PTF

σ – stress

σ_{ii} – stress in the i direction

$\underline{\sigma}$ – stress matrix

σ – standard deviation

τ – time constant

τ_{ij} – shear stress applied in the i plane in the j direction

ϕ – in-plane substrate rotation angle

ϕ_w – phase difference between two monochromatic waves

ϕ_o – central angle in the phi-sweep method

$\phi(x,y)$ – phase difference at position x,y

$\Delta\chi$ – anisotropy of the diamagnetic susceptibility

$\Delta\varphi$ – phase difference

ω – frequency

Symbols from the Latin Alphabet

a_v – area occupied by a void within the plane of a film

A – area

A – coefficient in the Cauchy equation

A_{En} – area of element n

A_{tip} – area of a nanoindenter tip

B – magnetic field

B_0 – stationary magnetic field

B_1 – oscillating magnetic field

$B_{parallel}$ – orientation in which magnetic field is applied parallel to the helices

$B_{perpendicular}$ – orientation in which magnetic field is applied perpendicular to the helices

c – fitting coefficient (Chapter3)

$\underline{\underline{C}}$ – stiffness tensor

Δd – measusred thermal expansion

d – cross-sectional diameter of a helix

d – indentation depth

d_f – final or maximum indentation depth

d_l – diffusion length

D – helix cross-sectional diameter

D – diffusion constant

du – incremental change in sample length

dy – differential thickness section over which du is measured

E_α – Zeeman energy level

E_β – Zeeman energy level

ΔE – displacement of an energy level in a magnetic field

E – Young's modulus

E_c – Young's modulus of a coating

E_p – Young's modulus of a polymer

E_r – Young's modulus of rebar

E_v – Young's modulus of a void

E_{eff} – Effective modulus of perforated thin film

E_{bulk} – Bulk modulus of a material

$E_\perp$ – Young's modulus in an LCP film measured perpendicular to the LCs

$E_{||}$ – Young's modulus in an LCP film measured parallel to the LCs

E_{loc} – the local modulus within an imperfectly etched PTF

$f(t)$ – time domain NMR signal

$F(\omega)$ – Fourier transform of f(t)

F – force

F_{rest} – restoring force

G – shear modulus

h – height within the thickness of a GLAD film

$h(x,y)$ – height distribution across a surface

h_f – film thickness

$h_{200^\circ C}$ – film thickness measured at 200°C

$h_{25^\circ C}$ – film thickness measured at 25°C

H – hardness

I – nuclear spin quantum number

I – intensity

I_i – intensity of an input beam

I_{ei} – intensity of an input beam in the extraordinary direction

I_{oi} – intensity of an input beam in the ordinary direction

I_{ef} – intensity of an output beam in the extraordinary direction

I_{of} – intensity of an output beam in the ordinary direction

I_1 – average intensity of an interference pattern

I_2 – interference modulated intensity

K – an elastic constant

k – Boltzmann's constant

L – dimension of a structure

L – difference between measured and modeled value of transmission

l – sample length

l_0 – initial sample length

Δl – change in sample length

m – a constant of proportionality

m – an odd integer

m_I – magnetic quantum number

M – net magnetization

N – number of turns

N_q – number of times a signal is sampled for the numerical computation of a FT

N_α - Number of magnetic moments aligned parallel to an external field

N_β – Number of magnetic moments aligned anti-parallel to an external field

N_v – number of voids within area A

N_r – number of rebar structures within area A

n – number of measurements

n – an integer

n_I – number of permitted spin alignments in a magnetic field

$\boldsymbol{n}$ – director vector

n_ϕ – substrate rotation step indexer

n_{ave} – average refractive index of a GLAD-LC composite

Δn – birefringence

Δn_{ave} – average refractive index of a liquid crystalline layer

n_e – extraordinary refractive index

n_{GLAD} – refractive index of a GLAD film

n_o – ordinary refractive index

n_∞ – index of refraction at infinity

P – applied pressure

P – pitch

R – helical radius

$\bar{r}$ – positional vector

r_c – cross-sectional radius of a helical structure

r_h – helical radius

S – order parameter

$\underline{\underline{S}}$ – compliance tensor

S_B – bulk order parameter

S_c – coil spacing

S_u – slope of the unloading curve in nanoindentation

t – time

t_p – magnetization pulse duration

T – temperature

T_o – interval over which a signal is sampled for the numerical computation of a FT

T – duration of a sample for the numerical computation of a FT

T – transmitted intensity

T_o – input intensity

T_{mod} – modeled transmission

T_{meas} – measured transmission

T_g – glass transition temperature

T_{sub} – temperature at the substrate

T_m – melting temperature

ΔT – change in temperature

u_1 – displacement of node 1

u_2 – displacement of node 2

ΔV – change in volume

w – width of a GLAD column

$x°$ – angle increment

z – arbitrary signal

$z_{filtered}$ – arbitrary signal, filtered

Abbreviations

^{2}H-NMR – deuterium nuclear magnetic resonance

5CB-αd_2 – alpha-deuterated 4'-pentyl-4-cyanobiphenyl

Alq_3 – tris(8-hydroxyquinoline) aluminum

BOE – buffered oxide etch

CCD – charge coupled device

CPG – controlled porous glass

DMA – dynamic mechanical analysis

fft – fast Fourier transform, a MATLAB function

FID – free induction decay

FT – Fourier Transform

FTIR – Fourier transform infrared spectroscopy

GLAD – glancing angle deposition

IPA - isopropanol

ITO – indium tin oxide

LC – liquid crystal

LCP – liquid crystalline polymer

LIGA – lithographie, galvanoformung, abformung

M1 – monoacrylate monomer, as shown in Figure 6.1

M2 – diacrylate monomer, as shown in Figure 6.2

M3 – hydrogen-bridged monomer, as shown in Figure 6.

MEMS – microelectromechanical system

MMA – methyl methacrylate

NMR – nuclear magnetic resonance

PDLCs – polymer dispersed liquid crystals

PDMS – polydimethylsiloxane

PLD – pulsed laser deposition

PMA – poly(methylacrylate)

PMMA – poly(methyl methacrylate)

PGMEA – propylene glycol methyl ether acetate

PVC- polyvinylchloride

PVD – physical vapor deposition

PTF – perforated thin film

RF – radio frequency

RIE – reactive ion etching

RM – reactive mesogen

SEM – scanning electron microscopy

TMA – thermogravimetric analysis

TMA – thermal mechanical analysis

TEGDA – triethylene glycol diacrylate

UV – ultraviolet

1 Micro- and Nanostructuring of Inorganic and Organic Materials

1.1 Introduction

Microsystems are becoming increasingly prevalent in a variety of fields. Display technologies, chemical and biological analysis systems, and sensors are examples of systems that are becoming faster, cheaper, more sensitive, and more versatile as their dimensions are scaled downward [1]. For example, microfluidics researchers are developing 'lab-on-a-chip' systems that can be used to perform medical diagnostic tests on minute quantities of fluid, allowing results to be obtained in a fraction of the time (at a fraction of the cost) required to process larger samples [2]. In the field of sensors, accelerometers with dimensions measuring a few cm^2 have been used in automobile airbag systems since 1993 [1]. In liquid crystal display technologies, the pixels (with dimensions of 20 μm to 100 μm) found in flat panel displays (such as in laptop computers) are direct descendants of the 7-bar numerical displays with minimum dimensions in the mm-range found in digital watches and calculators [3, 4]. These are only a few examples of the large number of devices that are now manufactured using microfabrication.

New manufacturing techniques are still required to shape materials on the micro- and nanoscale. The most mature technologies are those developed by the integrated circuit industry. The downscaling in component size achieved in microelectronics over the past 40 years is primarily due to advances in fabrication techniques (rather than by the integration of new materials) [5, 6]. During this time, major effort has gone into developing and refining methods of patterning planar circuits composed of inorganic materials such as silicon, silicon dioxide, and gold. Photolithography, thin film deposition, chemical mechanical polishing, and wet and dry etching are a few of the enabling technologies developed for use in the fabrication of microelectronics. These tools can be used in a cycle of deposition, patterning, and etching to build up multi-layered structures. However, the structures made using this cycle are predominantly planar in nature, which is not necessarily the ideal geometry for devices used in

applications outside of microelectronics. In addition, silicon itself is not necessarily the ideal material for use in all micro-scaled applications. One example of an area that could benefit from the incorporation of new materials is micro-actuator devices: as these devices become smaller, more flexible materials are required to achieve comparable deformations. The maximum strain that silicon is able to undergo without fracture is on the order of 1% [7]. Therefore, less brittle materials such as polymers and elastomers, which can undergo strains of up to as much as 500% are of interest for this application [8, 9]. New techniques must be added to the microfabrication toolbox to enable the patterning of a wider variety of materials (such as polymers) in less planar forms.

When constructing miniaturized systems, it is important to consider that as the dimensions of a material are reduced, its properties can change significantly. For example, thin films can have significantly higher elastic moduli than their bulk counterparts, as the size parameter (film thickness) approaches the characteristic length (grain size) that determines the material property [10]. Likewise, the optical and electronic properties of semiconductor clusters (quantum dots) have been shown to vary considerably as the scale of the material ranges from a few atoms to a bulk material [11]. The forces acting on a material or structure can also change in significance as its dimensions (L) are reduced, for example surface tension (which scales with L^1) can become overwhelmingly large, while gravitational forces (which scale with L^3) become less significant [12]. Therefore, when considering new fabrication technologies and materials for integration in micro-scaled devices, it is crucial to understand how the materials properties and behavior differ at macro and microscopic scales.

1.2 Intention

The purpose of the work described in this thesis is to investigate novel techniques for shaping a variety of materials on the micro/nano-scale, and to determine how the properties of the materials change as the dimensions of the material are reduced. Emphasis is placed on template-based fabrication processes in which porous thin films deposited by glancing angle deposition acts as the master. A wide range of inorganic and organic materials are investigated, with an emphasis on liquid crystalline polymers. The

patternability, processability, and material properties of liquid crystalline polymers are examined with an interest in incorporating these materials into micro-actuator devices.

1.3 Scope

In the first part of this thesis, fabrication techniques based on single- and double-templating of thin films deposited using glancing angle deposition (GLAD) are developed to assemble a toolbox of materials that can be shaped on the micro- and nanoscale. In Chapter 2, glancing angle deposition is itself described. This technique is used to make the master films used in the single- and double-templating processes described in Chapters 3 and 4. In Chapter 3, single-templating is investigated. It is shown that this method can be used to make thin films with tailored pore structure from a variety of difficult-to-evaporate materials, including nickel, gold, isotropic polymers, and liquid crystalline polymers. In Chapter 4, a double-templating process that can be used to fabricate polymer helices is presented. Before the work described in this thesis the fabrication of multiple polymer helices with submicron dimensions over large areas had not been demonstrated in the literature.

One focus of this thesis is to examine the mechanical properties of templated structures with an eye on using these materials in actuator devices. It has been shown previously that direct GLAD films have interesting mechanical properties. Mechanically, helical GLAD films have been shown to behave as microscopic springs, undergoing a much larger strain in response to an applied stress than a solid film of the same material [13]. Therefore, in the second part of Chapter 3, the mechanical properties of single-templated GLAD films are both probed experimentally and modeled using finite element analysis. This work is undertaken with an emphasis on tunability by examining how a change in the architecture of the GLAD template film will affect the mechanical properties of the sample.

One obstacle to using GLAD films directly in microelectromechanical systems is the limited actuatability of the materials from which films have been fabricated to date. Therefore, stimulus-responsive liquid crystalline polymers are extensively investigated, with a focus on structuring these materials on the micro- and nanoscale. Liquid

crystalline polymers have been described in the literature as a type of 'artificial muscle' owing to their ability to convert thermal, chemical or electromagnetic energy into large amplitude mechanical deformations. It has been shown previously that GLAD-liquid crystal composites have interesting optical properties, as the highly porous GLAD films impart ordering to the liquid crystalline molecules, which themselves have anisotropic optical properties. Here we investigate the use of GLAD films to align liquid crystalline monomers which then react to form polymers with anisotropic mechanical properties. The first step in this work is to determine the alignment that results when liquid crystals are infiltrated into a GLAD template film. While the optical properties of GLAD-liquid crystal systems have been extensively investigated, the alignment of liquid crystalline molecules in a GLAD film has never been determined [14, 15]. In Chapter 5, nuclear magnetic resonance spectroscopy (NMR) is used to discern the alignment of deuterated liquid crystals in a helical GLAD film. Knowledge of this alignment is critical both for constructing and understanding the behavior of liquid crystalline polymer actuator devices templated from GLAD films, and also for optimizing GLAD-liquid crystal optical devices such as switchable photonic crystals.

In Chapter 6, the optical, mechanical, and thermo-mechanical properties of thermally-actuated liquid crystalline polymers with varying composition are investigated in order to optimize these materials for use in actuator devices. It is found that the properties of liquid crystalline polymer films depend strongly on whether they are free-standing or substrate-anchored. This effect is modeled using finite element analysis. The suitability of using this material in micro-scaled devices is discussed.

In Chapter 7, three template-based fabrication processes which can be used to make microstructured liquid crystalline polymer films are then investigated. These include single-templating, double-templating, and a modified single templating process. This modified single-templating process can be used to make composite structures comprised of a perforated thin film selectively reinforced with GLAD 'nanorebar', mounted on a thick layer of polymer. The actuation of each of these three types of structures is studied,

and theoretical calculations are performed to account for the difference in behavior exhibited by the films manufactured using the two single-templating processes.

Finally, in Chapter 8, three alternative techniques for fabricating microstructured liquid crystalline polymer thin films are investigated. The first process is a 'photopatterning' process in which liquid crystalline monomers are polymerized through a mask to produce patterned areas of material with different liquid crystal alignment. The second process also makes use of photopatterning, this time to produce well-defined lines of aligned liquid crystalline polymer mounted on a bare substrate which expand and contract when heated and cooled. The third alternative technique is based on a simple printing process, and has many advantages. Actuation of structures fabricated using each of these processes is presented.

1.4 References

1. Amato, I., *Future chips - Micromachines - Fomenting a revolution, in miniature.* Science, 1998. **282**(5388): p. 402-405.
2. Verpoorte, E. and De Rooij, N.F., *Microfluidics meets MEMS.* Proceedings of the Ieee, 2003. **91**(6): p. 930-953.
3. Varghese, S., Narayanankutty, S., Bastiaansen, C.W.M., Crawford, G.P. and Broer, D.J., *Patterned alignment of liquid crystals by micro-rubbing.* Advanced Materials, 2004. **16**(18): p. 1600-1605.
4. Kobayashi, S., Hori, H. and Tanaka, Y., *Active Matrix Liquid Crystal Displays*, in *Handbook of Liquid Crystal Research*, P.J. Collings and J.S. Patel, Editors. 1997, Oxford Press: New York.
5. Campbell, S.A., *The Science and Engineering of Microelectronic Fabrication.* 2nd ed. 2001, New York: Oxford University Press.
6. Kingon, A.I., Maria, J.P. and Streiffer, S.K., *Alternative dielectrics to silicon dioxide for memory and logic devices.* Nature, 2000. **406**(6799): p. 1032-1038.
7. Khang, D.Y., Jiang, H.Q., Huang, Y. and Rogers, J.A., *A stretchable form of single-crystal silicon for high-performance electronics on rubber substrates.* Science, 2006. **311**(5758): p. 208-212.
8. Odian, G.G., *Principles of Polymerization.* 3rd ed. 1991: Wiley-Interscience.
9. Quake, S.R. and Scherer, A., *From micro- to nanofabrication with soft materials.* Science, 2000. **290**(5496): p. 1536-1540.
10. Arzt, E., *Overview no. 130 - Size effects in materials due to microstructural and dimensional constraints: A comparative review.* Acta Materialia, 1998. **46**(16): p. 5611-5626.
11. Alivisatos, A.P., *Semiconductor clusters, nanocrystals, and quantum dots.* Science, 1996. **271**(5251): p. 933-937.

12. Spearing, S.M., *Materials issues in microelectromechanical systems (MEMS).* Acta Materialia, 2000. **48**(1): p. 179-196.
13. Seto, M.W., Dick, B. and Brett, M.J., *Microsprings and microcantilevers: studies of mechanical response.* Journal of Micromechanics and Microengineering, 2001. **11**(5): p. 582-588.
14. Sit, J.C., Broer, D.J. and Brett, M.J., *Liquid crystal alignment and switching in porous chiral thin films.* Advanced Materials, 2000. **12**(5): p. 371-373.
15. Robbie, K., Broer, D.J. and Brett, M.J., *Chiral nematic order in liquid crystals imposed by an engineered inorganic nanostructure.* Nature, 1999. **399**(6738): p. 764-766.

2 Background: Glancing Angle Deposition

2.1 Introduction

Throughout the work described in this thesis, porous thin films with tunable pore architecture are fabricated using a templating process in which inorganic films comprised of independent columnar structures with tunable morphologies act as the master. The purpose of this chapter is to present an introduction to the process used to produce the master: glancing angle deposition (GLAD).

GLAD is a type of physical vapor deposition (PVD) in which precise control over substrate position, substrate angle, and deposition rate are employed to deposit films with controlled density, column angle, and column geometry. Standard PVD processes such as evaporation, sputtering, and pulsed laser deposition can be used to generate the flux in the GLAD process, although evaporation is typically the simplest to employ for reasons that will be described. To explain how and why porous films with isolated structures can be fabricated using glancing angle deposition, this chapter begins with a brief overview of physical vapor deposition in Section 2.2, accompanied by a discussion on the relationship between deposition conditions and film structure in Section 2.3. A review of oblique angle deposition is then presented in Section 2.4. Glancing angle deposition is itself described in Section 2.5. The growth and structure of films deposited by GLAD are discussed, and materials which are, and are not compatible with this process are identified. In Section 2.6 some of the applications and limitations of these films are presented to provide motivation and context for the work described in the remainder of this thesis.

2.2 Physical Vapor Deposition

Physical vapor deposition (PVD) is a common microfabrication process used to make thin films. The term PVD encompasses techniques such as evaporation and sputtering, which are workhorses of the microfabrication industry. These processes were first demonstrated and commercially implemented in the mid-to-late 1800s [1]. In PVD processes, the solid source material (which is usually elemental or a simple compound)

undergoes a change in phase to a gas. This vapor recondenses at the substrate, forming a solid thin film. Unlike chemical vapor deposition, in which gaseous reactants form a solid product at the substrate, no chemical reactions take place in most PVD processes.

The main characteristic that differentiates the various types of PVD processes is the method in which the source material is induced to enter the vapor phase. Different techniques include evaporation, in which the source material is heated into the vapor phase; sputtering, in which the target material is bombarded with high energy ions from a plasma, causing one or more atoms to be ejected; and pulsed laser deposition, in which material is ejected when the target is illuminated with a high energy laser pulse. The discussion below will focus on evaporation, since this process is most relevant to glancing angle deposition for reasons which will be identified in Section 2.5.1.

In evaporation, the source material is induced to enter the vapor phase by heating, using either a resistive heater or a beam of high-energy electrons. This process is directional: evaporated or sublimated flux is emitted from the source with $cos^n\theta$ dependence, where n is determined by the geometry of the melt and has a value equal to or greater than 1 [1]. The highest concentration of atoms is therefore located in the direction normal to plane of the source. This process is performed under vacuum, where a typical base pressure would be less than 10^{-6} Torr to prevent contaminants from the air (such as oxygen) from reacting with the material being deposited. The pressure in the chamber during evaporation is also kept low (less than 10^{-4} Torr) to prevent collisions between atoms, which would reduce the directionality of the flux. When evaporated flux reaches the substrate it recondenses, forming a solid thin film. The growth kinetics of evaporated thin films will be described in detail in Section 2.3.

2.3 Structure of Films Deposited by Evaporation

A principle determinant of the mechanical, optical, electronic, and chemical properties of a thin film is the structure of the film itself [2]. Some of the characteristics that fall under the general designation of structure include film morphology, which describes the overall geometry or shape of the film; grain size, which is a measure of the distance over which

long-range crystalline order propagates; and crystallinity, which is a description of the type of ordering present (or lack thereof). The structure of evaporated thin films can vary greatly depending on deposition conditions such as temperature, base pressure, deposition pressure, deposition rate, throw distance (distance between the source and substrate), material, and source size and geometry. There are many papers available on this subject in the literature [3-8].

In order to understand why the properties of a film vary as a function of deposition parameters, it is necessary to understand the mechanism by which films grow. When a film is deposited, the first atoms that reach the substrate are randomly dispersed. Unlike atoms in the bulk of the film, these atoms are only loosely adsorbed to the surface, and are therefore highly mobile. While many such atoms undergo desorption back to the vapor phase, a critical number of atoms may form an island of solid material in a process known as nucleation [1]. These islands increase in size as they incorporate new adatoms from the vapor phase or mobile atoms from the surface of the substrate. As the islands grow in size they may eventually coalesce, forming a continuous film interspersed with voids. Since the islands are not topologically flat, geometric shadowing can take place, blocking parts of the substrate from the line-of-sight impingement of the flux from the source [1]. When new atoms arrive at the substrate, they are loosely bonded to the surface and can diffuse a small distance before becoming bonded into the film at energetically favorable positions. If adatoms do not possess sufficient energy to diffuse into the voids, then these voids may be preserved and incorporated into the film. This process is illustrated schematically in Figure 2.1:

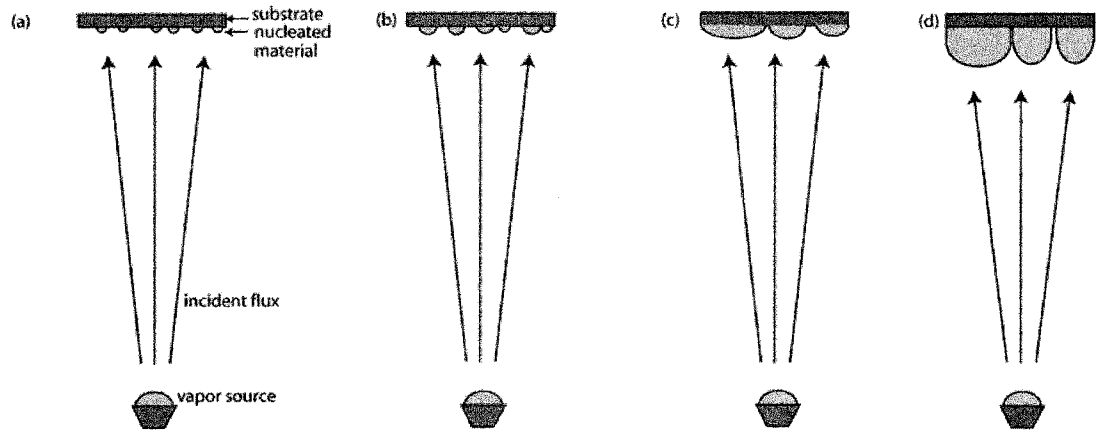

Figure 2.1: Thin film nucleation and growth. When a film is deposited by evaporation, material initially nucleates in discrete locations on the substrate (a). As the deposition continues, these nucleation sites increase in size (b) and eventually coalesce (c), forming a relatively solid film which increases in thickness in the direction perpendicular to the substrate. In the case shown here, some of the voids are preserved (d).

Beyond nucleation, the three main processes influencing structure in evaporated thin films are: shadowing, as evaporation is a highly directional process in which the flux travels from the source to substrate in a line-of-sight trajectory; adatom diffusion, which occurs when new atoms arriving at the substrate move a limited distance before becoming a part of the solid film; and bulk diffusion, which takes place when atoms within the solid film undergo a rearrangement [1]. In some cases desorption, which occurs when atoms loosely bonded to the surface return to the gas phase, can also play a role [8]. Adatom diffusion, bulk diffusion, and desorption are temperature dependent processes which are more likely to occur at higher temperatures. At sufficiently high temperatures, adatom and bulk diffusion can reduce the effect of shadowing [9].

Due to the temperature dependence of bulk and adatom diffusion effects, the morphology and crystallinity of evaporated thin films depend strongly on the temperature of the substrate relative to the melting temperature of the deposited material. A number of structure-zone models have been developed over the years to describe and predict the structure of evaporated thin films based on the deposition parameters. One such system is the Movchan-Demchisin model, which was developed based on empirical observation of the properties of evaporated metal films [6]. This scheme can be used to predict the

structure of a film based on the ratio of the temperature at the substrate (T_{sub}) to the melting temperature of the material (T_m). The Movchan-Demchisin model includes three zones. Zone 1 covers the lowest T_{sub}/T_m values ($T_{sub}/T_m < 0.3$), and within this zone the film growth is dominated by shadowing, as surface and bulk diffusion are extremely limited. Resultantly, films deposited under Zone 1 conditions are comprised of columnar structures interspersed with voids [10]. The structures themselves are either nanocrystalline or amorphous, comprised of clusters with diameters of 1 nm – 3 nm [10]. In the intermediate T_{sub}/T_m range (Zone 2, $0.3 < T_{sub}/T_m < 0.5$) surface diffusion can take place, which allows the voids between adjacent nucleation sites to be filled. When adjacent islands meet they coalesce, forming columnar grains (of crystalline material) with well-defined grain boundaries (i.e., interfaces between regions of different crystallographic orientation). The grains themselves are columnar in nature, with grain boundaries generally oriented perpendicular to the substrate (although the orientation can vary with deposition angle). The surfaces of films deposited in Zone 2 are considerably smoother than for films deposited in Zone 1, and may exhibit faceting. In the highest T_{sub}/T_m range (Zone 3, $0.5 < T_{sub}/T_m > 1$), bulk diffusion can take place in addition to surface diffusion, resulting in the formation of large, equiaxed grains with well-defined crystallinity. While in the deposition of solid thin films it may be desirable to work within Zone 3 to achieve large grain sizes and dense films, in Section 2.5 it will be shown that it is the qualities of Zone 1 which are emphasized in glancing angle deposition.

2.4 Oblique Angle Deposition

It has long been known that the structure of evaporated films can be influenced by changing the angle formed between the substrate normal and the vapor source during deposition (α) [11]. In 1966 Nieuwenhuizen and Haanstra evaporated a series of aluminum films at angles α ranging from 30° to 80° and used electron microscopy to measure the resulting angle of the crystal columns (β, measured from the substrate normal, as shown in Figure 2.2). They found that the following equation could be used to relate the column angle to the angle of deposition: $\tan(\alpha) = 2\tan(\beta)$ [11]. This equation is called the tangent rule.

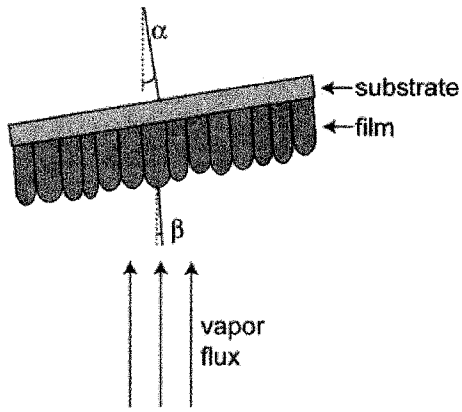

Figure 2.2 Deposition angle (α) and film growth angle (β). The angle between the substrate and the flux (α) differs from the angle formed between the columnar film grains and the substrate normal (β).

That anisotropic optical and magnetic properties could be achieved through oblique angle deposition has been known since at least the 1950s [12-15]. In 1959 D.O. Smith evaporated permalloy (Fe-Ni) on tilted substrates (42° to 51°) and found that the deposited films were magnetically anisotropic [14]. The optical properties of obliquely evaporated aluminum thin films were examined in 1953 by L. Holland, who postulated that the angular dependence of transmission through a film deposited at 85° was caused by anisotropic grain growth preferentially oriented in the direction of deposition [16]. In 1959 N.O. Young and J. Kowal extended the concept of optical anisotropy to make circularly birefringent films by rotating the substrate continuously during deposition [15]. These films were deposited at oblique angles between α = 30° and α = 60°. Higher deposition angles have also been examined. In 1989 Motohiro and Taga deposited various metal oxides at angles ranging from α = 0° and α = 80° to examine the relationship between angle and birefringence (Δn), with the goal of making waveplates [3]. Substrate motion was also introduced during this study: for deposition at oblique angles, it was found that the direction of maximum optical anisotropy (i.e., the direction along which Δn was the largest) was oriented parallel to the direction of column growth (β). By rotating the substrate 180° (in the plane of the film, while maintaining a constant α) mid-way through the deposition a bilayer structure was created, such that the direction of maximum retardation could be oriented along an axis perpendicular to the plane of the substrate. Motohiro and Taga also observed the relationship between film density and

deposition angle (α) and attributed the form birefringence observed at high deposition angles to the porosity of the film.

A significant decrease in density as a function of deposition angle was also predicted theoretically by R.N. Tait *et al.* in 1993 [2]. That oblique deposition at very high angles ($\alpha > 70^{\circ}$) and precisely controlled substrate rotation could be combined to realize thin films comprised of engineered microstructures with tailored porosity was demonstrated in 1995 by Robbie, Brett *et al.*, to form the glancing angle deposition technique [17]. This process will be discussed in the next section. Refinements of this technique to achieve more control over features such as spacing between adjacent structures and the cross-sectional shape of the structures themselves are ongoing [18, 19].

2.5 Glancing Angle Deposition

Glancing angle deposition (GLAD) is achieved by combining the standard evaporation process with a large, oblique angle of incidence and precise control over both substrate angle and in-plane substrate orientation [20-22]. This results in the growth of porous thin films with engineered porosity, column angle, and column architecture. In Section 2.5.1, the effect of holding the substrate at a high angle of incidence will be discussed. In Section 2.5.2, the use of substrate motion to engineer film density, column angle, and column architecture will be described. In Section 2.5.3, the manner in which the film morphology evolves during a standard deposition at glancing angle will be examined. In Section 2.5.4, a short discussion on crystallinity will be given. Finally, in section 2.5.5, the materials which are, and are not compatible with this technique will be summarized.

2.5.1 Deposition Angle

In glancing angle deposition, flux is typically generated using resistive heating or electron beam evaporation, as in standard evaporation processes. However, rather than placing the substrate perpendicular to the stream of flux (as shown in Figure 2.1), it is held at a large oblique angle, such that the substrate normal forms an angle (α) of greater than 70° with respect to the source normal. This simple modification emphasizes the

shadowing effects which are already seen in Zone 1 of the Movchan-Demchishin model for evaporated thin films. Due to the combination of enhanced shadowing and limited adatom diffusion, the deposited film consists of columnar structures with large spacing between adjacent columns. An example of a columnar thin film deposited at glancing angle is shown in Figure 2.3.

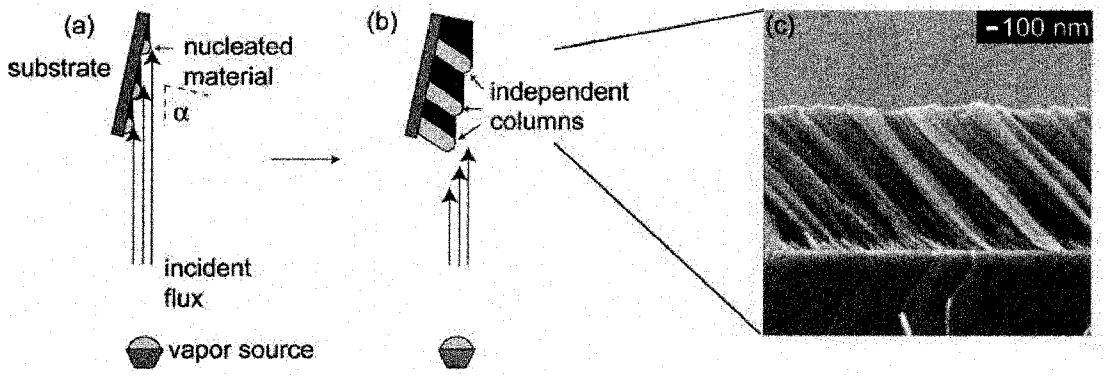

Figure 2.3: Glancing angle deposition. In glancing angle deposition the substrate is held at a high angle (α>70°) with respect to the vapor source (a). This results in the growth of a porous film comprised of independent microstructures or columns (b), as shown in this scanning electron micrograph (c). The film shown in (c) was deposited at 85°.

Both column angle (β) and porosity are strongly dependent on the angle formed between the substrate normal and the source (α) [17, 23, 24]. In the absence of substrate rotation the column angle (β=β_α) can be predicted from the deposition angle (α). At high angles of deposition (α > 60°), the column angle can no longer be well predicted by the tangent rule given in Section 2.4. Rather, Tait's rule was developed from geometric arguments, and verified using MgF_2 thin films deposited between 0° and 80° in 10° steps [2]. This rule is stated and plotted in Figure 2.4:

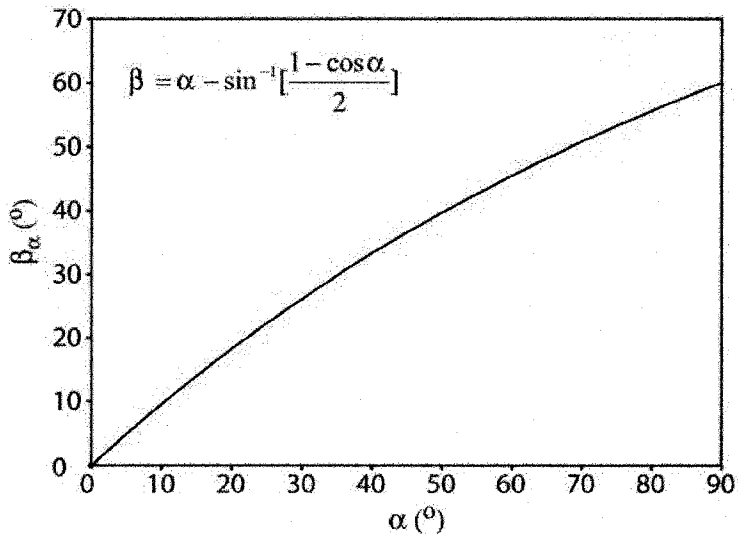

Figure 2.4: Tait's rule. Tait's rule can be used to predict the angle (β_α) formed between the column and the substrate normal for a given angle of deposition (α) and a stationary substrate.

While Figure 2.4 shows that the column angle (β_α) increases with the deposition angle, film porosity decreases [25]. This is due to the fact that at higher deposition angles increased shadowing effects lead to larger spacing between adjacent columns. The density of a film deposited by glancing angle deposition may be as low as 10% to 30% of the density of the bulk film, depending on the material employed [20].

Clearly, shadowing plays a critical role in glancing angle deposition. It is for this reason that evaporation is the preferred method of generating flux. As described in Section 2.3, evaporation is a very directional process: the flux emitted travels to the substrate without undergoing any collisions in a line-of-sight path. In sputtering, which is another common PVD process, flux is generated by accelerating the ions of a high energy plasma (generated using a process gas) into the target material. These ions undergo collisions that cause one or more target ions to be ejected. The vapor flux in the sputtering process can be considerably less collimated than in evaporation, since ejected atoms may undergo collisions with atoms in the process gas before they reach the substrate. These collisions will change the direction in which the flux travels, thereby reducing the effect of shadowing. Nonetheless, glancing angle deposition has been demonstrated using sputtering to generate the flux [26]. To do so, a low deposition rate and a long throw

distance were employed, and well-formed, independent structures characteristic of the GLAD process were achieved. Pulsed laser deposition has also been used in combination with the glancing angle technique to produce porous carbon films [27]. In this technique sample sizes must be kept very small to maintain uniformity [1]. Throughout this thesis evaporation is employed, due to the simplicity of the process.

2.5.2 Substrate Rotation

An additional feature of the glancing angle deposition process is that in-plane substrate motion can be incorporated to enable the production of complex columnar architectures, as well as to decouple the column angle (β) from the angle of deposition (α) [28]. When appropriate substrate motion is employed, β, the column angle, differs from the 'natural' column angle (β_α) predicted by Tait's rule.

A variety of tunable architectures can be achieved by incorporating in-plane substrate motion into the deposition process, since the direction of film growth generally tracks the direction of the source. To better describe this motion an angle ϕ is defined as the in-plane angle between an arbitrary point on the substrate and the vapor source, as illustrated in Figure 2.5:

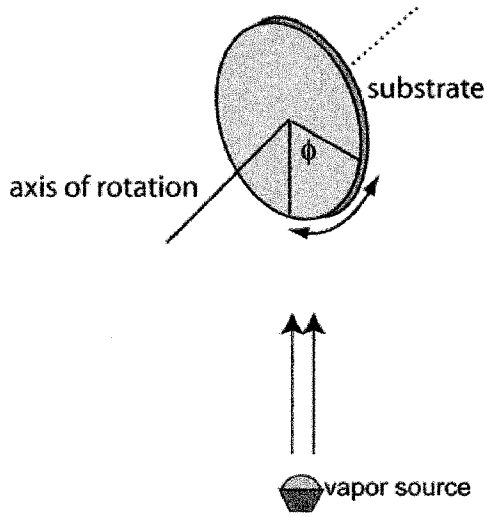

Figure 2.5: The in-plane substrate angle ϕ. ϕ can vary from 0 to 360° during the deposition, as the substrate rotates either clockwise or counter-clockwise.

For example, if the substrate is repeatedly and abruptly rotated 180° (i.e., ϕ is periodically increased by 180°) during the deposition, a zig-zag-like morphology results. Or, if ϕ is periodically increased by 90°, square-spiral structures are formed. Constant rotation of the substrate in one direction can be used to make helical structures, where the pitch and handedness are determined by the speed and direction of rotation respectively. This corresponds to a constant increase (or decrease) of ϕ throughout the deposition. In the limiting case where the substrate is rotated very quickly, the structures will again be column-like, since the helical pitch is smaller than the diameter of the columns themselves. In this case, the columns will be oriented in a direction perpendicular to the substrate. Examples of a few of these structures are shown in Figure 2.6.

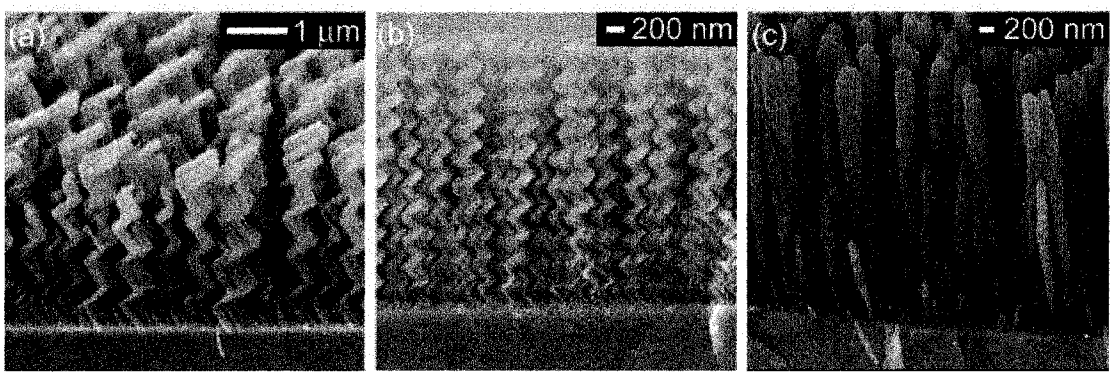

Figure 2.6: Assorted GLAD films. When the substrate is abruptly and repeated rotated through 180° during deposition, the resulting film has a zig-zag-like shape (a). A helical film can be deposited by continually rotating the film during deposition (b). When the speed of rotation results in a pitch that is smaller than the column width, the resulting architecture is that of a vertical post (c).

For the zig-zags and helices shown in Figure 2.6 (a) and (b), the column angle (which can also be called the rise angle) of the structures ($\beta = \beta_\alpha$) is dictated by the angle at which the film is deposited (α). For the vertical posts shown in Figure 2.6 (c), the relationship between the deposition angle (α) and the column angle (β) has been effectively decoupled. The posts are no longer oriented at the angle β_α, but rather at the angle $\beta \sim 0°$. Other advanced control algorithms can also be used to tailor the rise angle of the structures without affecting the film porosity [28]. For example, the spin-pause technique can be used to make posts which are oriented at an angle between 0° and the angle β_α, the 'natural' column angle for a given deposition angle. In the spin-pause technique the

substrate is rapidly rotated during the deposition, but periodically paused at a chosen value of ϕ. A longer pause tilts the column more towards β_α, while a shorter pause tilts the column more towards 0°. The spin-pause technique can also be used to change the rise angle of a helical structure (the angle formed between the helical arm and the plane of the substrate). In the normal deposition of a helical film, the substrate is rotated slowly through 360° during the deposition of a single helical pitch, in n_ϕ steps of x^o. In the-spin pause technique the substrate is rotated rapidly through 360° + $(x^o)n_\phi$ times. In this way the rise angle of the helix is tilted more towards the substrate normal, blending together the vertical post and helical morphologies.

Note that the precisely controlled architectures described above are only achievable using crystal oscillator thickness monitors to observe the deposition rate, and adjusting the angle ϕ accordingly. This system of feedback allows the morphology of the deposited film to be engineered [20].

2.5.3 Film Growth and Morphology

In this section, the manner in which films deposited by glancing angle deposition evolve during growth is discussed. When a film is deposited using this technique, nucleation occurs at random sites on the substrate (as in standard evaporation processes). Smooth substrates such as glass or silicon are preferred to achieve uniformly, but randomly nucleated, films, since undesired nucleation can occur preferentially at raised defects due to shadowing effects. As the film growth progresses from the initial nucleating sites, shadowing and limited adatom diffusion prevents the voids between nucleation sites from being filled.

Competition effects are a major driving force in the deposition of a film at glancing angle. In the first few hundred nanometers of growth, pillars which are slightly taller than their neighbors can shadow the structures around them, causing nearby pillars to become extinct. This effect is clearly visible in Figure 2.6 (c), in which many short pillars can be seen. To maintain a steady-state density characteristic of the deposition angle, as some columns become extinct, other columns must enlarge accordingly [19].

This effect is known as broadening. As the pillars broaden, the distance between adjacent pillars also becomes larger than during the initial stages of growth, which makes it more difficult for structures to effectively shadow others. Thus extinction occurs less frequently than during the initial stages of growth [29].

While in the SEM images shown in Figure 2.6 the helices, zig-zags, and vertical posts appear quite solid, transmission electron microscopy studies have shown that these structures are actually comprised of nanofibers with diameters of 1 nm to 5 nm [29, 30]. These studies have also revealed that the diameter of the fibers remains quite constant throughout growth. This suggests that the number of fibers in a pillar must increase during deposition, in a process known as bifurcation. As the deposition progresses, multiple new fibers can develop off of an existing fiber, likely due to self-shadowing. The presence of these fibers greatly increases the surface area of films deposited using this technique.

A number of techniques have been investigated to reduce bifurcation and broadening in films deposited by glancing angle deposition. One technique which has been developed to reduce broadening is called the "Phi Sweep method", in which the in-plane substrate angle ϕ is swept periodically back and forth around a central angle ϕ_o [18]. For example, when growing a slanted post the in-plane angle ϕ can be varied every 15 nm from ϕ_o+ 27.5° to ϕ_o - 27.5°. This reduces the competition effects seen in regular films deposited by glancing angle deposition, by alleviating (in one direction) some of the shadowing that takes place due to the directionality of the flux. This process is critical for improving the uniformity of films to be used in applications such as photonic crystals, which require exact periodicity, and which will be discussed in further depth in Section 2.6. However, for the work described in this thesis, helical films are deposited simply by rotating the substrate at a constant rotation rate with respect to the rate of deposition.

2.5.4 Crystallinity

As for most evaporated materials, the crystallinity of a film deposited at glancing angle depends strongly on the temperature of the substrate with respect to the melting

temperature of the material being deposited. As mentioned previously, low substrate temperatures are required when depositing a film by glancing angle deposition in order to preserve shadowing effects, and limit surface and bulk diffusion. In contrast, in thin film growth, well-defined crystallinity results when films are deposited at high temperatures where surface and bulk diffusion can occur [29]. For this reason, most films deposited by glancing angle deposition are either amorphous or nanocrystalline in nature. It has been demonstrated that amorphous TiO_2 samples which are annealed after deposition can undergo a transformation to a polycrystalline state with a minimal change in film morphology [30].

2.5.5 Materials

Fabrication of porous, microstructured thin films using glancing angle deposition has been demonstrated with a variety of inorganic materials, including Ge, C, SiO_2, Si, TiO_2, Ti, MgF_2, C, and Al_2O_3 [31]. However, not all inorganic materials can be nicely structured using this technique. An example of an inorganic material which is not compatible with this technique is Al. An aluminum film deposited at 85° while the substrate was rotated a single time is shown in Figure 2.7:

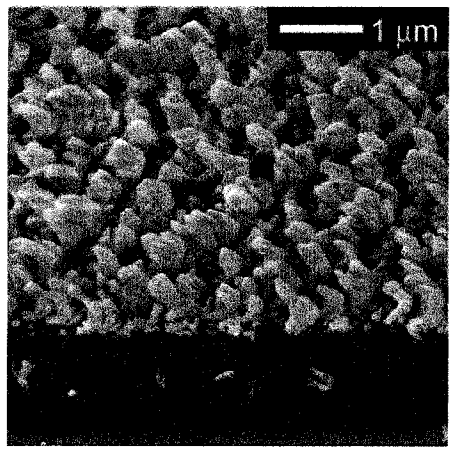

Figure 2.7: Aluminum film deposited by glancing angle deposition. When Al is deposited by glancing angle deposition the resulting structures are large, poorly defined, and show evidence of faceting.

The faceting visible in Figure 2.7 suggests that the atoms are organizing in a crystalline (or polycrystalline) lattice. Surface and/or bulk diffusion have lessened the effects of

shadowing, with detrimental results. One reason that a material such as Al is able to crystallize during deposition while materials such as Si and Ti are not may be due to the melting temperature of the materials: Si and Ti melt at relatively high temperatures (1410 °C and 1700 °C, respectively), while Al melts at a much lower temperature (659 °C) [32]. The ratio of T_m/T_{sub} for this material is therefore expected to be much higher.

It is also possible to engineer porous films with controlled microstructures using certain organic materials. Recently, the formation of thin films comprised of organic, chiral structures was demonstrated by evaporating tris(8-hydroxyquinoline) aluminum (Alq_3) at glancing angle [33]. Alq_3 is a luminescent, small molecule that has been extensively explored for use in organic light emitting diodes [34, 35]. The porous, chiral, microstructures formed by glancing angle deposition are also luminescent, emitting light that is partially circularly polarized. It is anticipated that it will also be possible to deposit other small molecule organic materials by glancing angle deposition. However, it is not possible to deposit high-molecular weight polymers directly by physical vapor deposition, since these materials do not exist in a vapor phase [36]. When a high-molecular weight polymer chain is heated, the material will decompose before it evaporates, although the chain fragments created may themselves be vaporous and these chains can undergo repolymerization at the substrate [37]. The deposited film will typically have shorter chain lengths, lower molecular weights, and different elemental composition than the source material. So, if polymer GLAD-like structures are desired they must be fabricated using other methods, such as the double-templating technique which will be described in Chapter 4. Note that the double-templating technique which will be described was developed and published before Alq_3 was evaporated at glancing angle.

Most of the films used in the work described in this thesis are deposited from SiO_2, which was chosen because this material is well known and easy to deposit at glancing angles, and also has favorable etch chemistry. A deposition angle of 85° was typically employed to create highly porous films. At this deposition angle, the film porosity is expected to be between 0.25 and 0.30 of the bulk density [25].

2.6 *Applications of Porous Thin Films Deposited by Glancing Angle Deposition*

Due to a number of advantageous characteristics, GLAD thin films are currently being explored for applications in a variety of fields by a number of research groups around the world [10, 38-42]. The list of applications described in this section is by no means exhaustive, and items on this list were chosen for their relevance to the work presented throughout this thesis.

The high porosity of GLAD films suggests that they may be useful for sensing gases such as water vapor, environmental pollutants, toxic chemicals, and process gases. For example, GLAD films employed in capacitive-based humidity sensors have been shown to exhibit high sensitivity to changes in humidity and also to exhibit fast response times owing to the accessibility of the pores (in contrast to a material such as porous alumina, where the pores are long with narrow openings through which gases must diffuse) [43, 44]. Existing work on humidity sensors has focused on easy-to-deposit materials such as Al_2O_3 and SiO_x. However, there are other materials that cannot be deposited directly (such as polyimide, a common material in humidity sensors [45]), that may also be of interest for study. Furthermore, fabricating sensors which are sensitive to other gases will require an altogether different set of chemistries. Therefore, replication techniques that could introduce the porosity and structure achieved using the GLAD process in materials that cannot be deposited directly could be of interest for sensing applications.

The highly-tunable architecture of GLAD films and the size-scale of the structures has led to a plethora of research into applications in the field of optics [3, 15, 46-49]. Helical GLAD films can be fabricated with the correct dimensions to interact with light and behave as Bragg reflectors for circularly polarized light [49]. These films selectively transmit and reflect light of opposite and like handedness, respectively. The wavelength at which this activity is centered is determined by the pitch of the helices, and can therefore be manipulated by varying the speed at which the substrate is rotated during deposition. This effect can be enhanced by the addition of liquid crystals, which creates a system that is also switchable [46]. There is some interest in optimizing these systems to

make reflective displays consisting of stacked left- and right-handed helices. However, the alignment of the liquid crystalline molecules within the GLAD films has never been discerned. The alignment of liquid crystalline molecules in any system is determined by a number of factors including elastic forces in the bulk of the material, the anchoring of the molecules along the surface of the cavity, and the cavity size and shape [50]. Due to the large surface-to-volume ratio of GLAD films, it is difficult to predict the interaction of liquid crystals within these complex pores theoretically. While a number of arrangements have been postulated based on the optical results, the alignment of liquid crystals in GLAD films remains unknown [51]. This information is critical for optimizing GLAD-LC optical devices. Furthermore, impregnating certain GLAD films with liquid crystals could also lead to the creation of switchable photonic crystals. Knowing the alignment of the liquid crystals within these structures will be vital for device fabrication and characterization.

Photonic crystals are nanostructured materials which exhibit an 'optical bandgap', forbidding the propagation of light/electromagnetic radiation at certain wavelengths, just as materials with electronic bandgaps forbid the existence of electrons at certain energy levels. The precise control over architecture achievable with the GLAD technique has also enabled the fabrication of the first three-dimensional photonic crystals in the form of square spirals [52, 53]. The concept of the square spiral photonic crystal was theoretically conceived by John and Toader at the University of Toronto [54]. This structure was designed by connecting together the 1^{st}, 3^{rd}, or 5^{th} nearest neighbors in a diamond lattice. Precise control is required to fabricate these structures with strict periodicity in the direction perpendicular to the plane of the substrate. In the plane of the substrate itself, lithographic seeds are used to define the location of the spirals. Exact periodicity is required to achieve a large bandgap, which is defined as the range of frequencies for which light cannot propagate. The width of a bandgap full width half maximum can be expressed as a percentage of the center frequency of the gap. A 10.9%, 3-dimensional bandgap at a center frequency of 1.65 μm was measured for photonic crystals deposited using GLAD [52]. Theoretical models have predicted that a photonic bandgap of 15% should be achievable for silicon square spirals, whereas an inverse

structure consisting of air square spirals in a silicon matrix should result in a bandgap of up to 24% [54].

Inverted helical structures have also been shown to have enhanced optical properties. Photoresist films perforated with helical pores have been shown to rotate linearly polarized light up to three times as strongly as the SiO_2 template films from which they were made [55]. One reason for this enhanced optical effect is that the index contrast between the photoresist film/air pore combination is higher than for the SiO_2 GLAD/air combination, which leads to higher optical activity [56]. Water absorbed on the surface of the SiO_2 film could degrade the index contrast of this film/pore combination even further. An additional advantage of the photoresist films perforated with helical pores is that they are far more mechanically stable than GLAD films, which are easily damaged when handled, since the structures can easily break off of the substrate when a shear stress is applied (such as by inadvertedly smudging the film with a finger during handling). The solid matrix of the perforated photoresist film is less delicate: unlike films deposited directly by glancing angle deposition these films can be touched directly without exhibiting signs of damage.

Outside of the field of optics, structures deposited by glancing angle deposition have also been investigated for use as resonant devices. Microhelices and microcantilevers have been fabricated, and their mechanical properties have been characterized using nanoindentation [57]. It was found that SiO_x microsprings exhibit behavior that is similar to that of macroscopic springs, undergoing considerably larger deformations in response to an applied force as compared with bulk SiO_x. The stiffness of the helical film was found to be 10^3 times less than the stiffness of a solid film of the same material. While the high level of control attainable over structure achievable using GLAD and the small dimensions suggest that this technique could be used to make micro- and nano-actuators, actuation of these devices has always remained a challenge. Singh *et al.* at Rensselaer Polytechnic Institute recently demonstrated electromechanical actuation of a 4-turn silicon helix coated fabricated using GLAD, coated with a thin layer of cobalt [58]. The helix was compressed by applying a DC current from an AFM tip, which was also used

to measure the displacement of the spring. However, the resulting strain was quite small: the helix, which was over 4 μm tall, contracted by only ~7 nm (0.2%). Clearly more responsive materials (exhibiting higher flexibility) would be advantageous for making actuator devices. Note that the successful deposition of the small-molecule organic material Alq_3 should not preclude an interest in fabricating polymer GLAD-like structures for micro-actuator devices. Polymers possess a number of advantages over small molecule organic materials, including increased solvent resistivity and reduced degradation at high temperatures. While Alq_3 dissolves in solvents such as chloroform [59], chemically crosslinked polymers have excellent resistance to dissolution in all solvents. The optical properties of Alq_3 structures have been found to degrade irreversibly on heating to 100 °C due to the volatility and limited bonding of the constituent molecules, whereas crosslinked polymers can be heated to at least 300 °C without breaking down (as measured by thermal gravimetric analysis). These characteristics make polymers better suited than Alq_3 for a variety of micro-actuator applications, some of which will be investigated later on in this thesis.

2.7 References

1. Ohring, M., *Materials Science of Thin Films*. 2nd ed. 2002, San Diego: Academic Press.
2. Tait, R.N., Smy, T. and Brett, M.J., *Modeling and characterization of columnar growth in evaporated films*. Thin Solid Films, 1993. **226**(2): p. 196-201.
3. Motohiro, T. and Taga, Y., *Thin-Film Retardation Plate by Oblique Deposition*. Applied Optics, 1989. **28**(13): p. 2466-2482.
4. Messier, R., Giri, A.P. and Roy, R.A., *Revised Structure Zone Model for Thin-Film Physical Structure*. Journal of Vacuum Science & Technology a-Vacuum Surfaces and Films, 1984. **2**(2): p. 500-503.
5. Hamberg, I., Hjortsberg, A. and Granqvist, C.G., *High-Quality Transparent Heat Reflectors of Reactively Evaporated Indium Tin Oxide*. Applied Physics Letters, 1982. **40**(5): p. 362-364.
6. Movchan, B.A. and Demchishin A.V., *Study of Structure and Properties of Thick Vacuum Condensates of Nickel, Titanium, Tungsten, Aluminium Oxide and Zirconium Dioxide*. Physics of Metals and Metallography-Ussr, 1969. **28**(4): p. 83-&.
7. Dirks, A.G. and Leamy, H.J., *Columnar Microstructure in Vapor-Deposited Thin-Films*. Thin Solid Films, 1977. **47**(3): p. 219-233.
8. Thornton, J.A., *High-Rate Thick-Film Growth*. Annual Review of Materials Science, 1977. **7**: p. 239-260.

9. Hentzell, H.T.G., Grovenor, C.R.M. and Smith, D.A., *Grain-Structure Variation with Temperature for Evaporated Metal-Films.* Journal of Vacuum Science & Technology a-Vacuum Surfaces and Films, 1984. **2**(2): p. 218-219.
10. Messier, R., Venugopal, V.C. and Sunal, P.D., *Origin and evolution of sculptured thin films.* Journal of Vacuum Science & Technology A, 2000. **18**(4): p. 1538-1545.
11. Nieuwenhuizen, J.M. and Haanstra, H.B., *Microfractography of Thin Films.* Philips Technical Review, 1966. **27**(3-4): p. 87-&.
12. Evans, J.W., *Solc Birefringent Filter.* Journal of the Optical Society of America, 1958. **48**(3): p. 142-145.
13. Smith, D.O., Cohen, M.S. and Weiss, G.P., *Oblique-Incidence Anisotropy in Evaporated Permalloy Films.* Journal of Applied Physics, 1960. **31**(10): p. 1755-1762.
14. Smith, D.O., *Anisotropy in Permalloy Films.* Journal of Applied Physics, 1959. **30**(4): p. S264-S265.
15. Young, N.O. and Kowal, J., *Optically Active Fluorite Films.* Nature, 1959. **183**(4654): p. 104-105.
16. Holland, L., *The Effect of Vapor Incidence on the Structure of Evaporated Aluminum Films.* Journal of the Optical Society of America, 1953. **43**(5): p. 376-380.
17. Robbie, K., Friedrich, L.J., Dew, S.K., Smy, T. and Brett, M.J., *Fabrication of thin-films with highly porous microstructures.* Journal of Vacuum Science and Technology A, 1995. **13**(3): p. 1032-1035.
18. Jensen, M.O. and Brett, M.J., *Porosity engineering in glancing angle deposition thin films.* Applied Physics A: Materials Science & Processing, 2005. **80**: p. 763-768.
19. Dick, B., Brett, M.J. and Smy, T., *Controlled growth of periodic pillars by glancing angle deposition.* Journal of Vacuum Science and Technology B, 2003. **21**(1): p. 23-28.
20. Robbie, K. and Brett, M.J., *Sculptured thin films and glancing angle deposition: Growth mechanics and applications.* Journal of Vacuum Science and Technology A, 1997. **15**(3): p. 1460-1465.
21. Robbie, K. and Brett, M.J., *Method of depositing shadow sculpted thin films*, in *US Patent.* 1999, The Governors of the University of Alberta and Alberta Microelectronic Corporation: United States.
22. Robbie, K., Brett, M.J. and Lakhtakia, A., *Chiral sculptured thin films.* Nature, 1996. **384**(6610): p. 616-616.
23. Tait, R.N., Smy, T. and Brett, M.J., *Modeling and Characterization of Columnar Growth in Evaporated-Films.* Thin Solid Films, 1993. **226**(2): p. 196-201.
24. Gospodyn, J., Brett, M.J. and Sit, J.C. *Characterization by variable angle spectroscopic ellipsometry of dielectric columnar thin films produced by glancing angle deposition.* in *Engineered Porosity for Microphotonics and Plasmonics.* Mater. Res. Soc. Proc. 797: W5.19.1-6.
25. Gospodyn, J. and Sit, J.C., *Characterization of dielectric columnar thin films by variable angle Mueller matrix and spectroscopic ellipsometry.* Optical Materials, 2006. **29**: p. 318-325.

26. Sit, J.C., Vick, D., Robbie, K. and Brett, M.J., *Thin film microstructure control using glancing angle deposition by sputtering.* Journal of Materials Research, 1999. **14**(4): p. 1197-1199.
27. Vick, D., Tsui, Y.Y., Brett, M.J. and Fedosejevs, R., *Production of porous carbon thin films by pulsed laser deposition.* Thin Solid Films, 1999. **350**(1-2): p. 49-52.
28. Robbie, K., Sit, J.C. and Brett, M.J., *Advanced techniques for glancing angle deposition.* Journal of Vacuum Science and Technology B, 1998. **16**(3): p. 1115-1122.
29. Malac, M. and Egerton, R.F., *Observations of the microscopic growth mechanism of pillars and helices formed by glancing-angle thin-film deposition.* Journal of Vacuum Science & Technology A, 2001. **19**(1): p. 158-166.
30. Colgan, M.J., Djurfors, B., Ivey, D.G. and Brett, M.J., *Effects of annealing titanium dioxide structured films.* Thin Solid Films, 2004. **466**(1-2): p. 92-96.
31. Robbie, K. and Brett, M.J., *Glancing angle deposition of thin films*, in *US Patent.* 2001, The Governors of the University of Alberta and Alberta Microelectronic Corporation: United States.
32. Maissel, L.I. and Glang, R., *Handbook of thin film technology.* 1970, New York: McGraw-Hill.
33. Hrudey, P.C.P., Westra, K.L. and Brett, M.J., *Highly ordered organic Alq3 chiral luminescent thin films fabricated by glancing-angle deposition.* Advanced Materials, 2006. **18**(2): p. 224-+.
34. Tang, C.W. and Vanslyke, S.A., *Organic Electroluminescent Diodes.* Applied Physics Letters, 1987. **51**(12): p. 913-915.
35. Ohmori, Y., Fujii, A., Uchida, M., Morishima, C. and Yoshino, K., *Fabrication and Characteristics of 8-Hydroxyquinoline Aluminum Aromatic Diamine Organic Multiple-Quantum-Well and Its Use for Electroluminescent Diode.* Applied Physics Letters, 1993. **62**(25): p. 3250-3252.
36. Biederman, H., *Organic films prepared by polymer sputtering.* Journal of Vacuum Science & Technology a-Vacuum Surfaces and Films, 2000. **18**(4): p. 1642-1648.
37. Biederman, H., Stelmashuk, V., Kholodkov, I., Choukourov, A. and Slavinska, D., *RF sputtering of hydrocarbon polymers and their derivatives.* Surface & Coatings Technology, 2003. **174**: p. 27-32.
38. Lintymer, J., Gavoille, J., Martin, N. and Takadoum, J., *Glancing angle deposition to modify microstructure and properties of sputter deposited chromium thin films.* Surface & Coatings Technology, 2003. **174**: p. 316-323.
39. Buzea, C., Kaminska, K., Beydaghyan, G., Brown, T., Elliott, C., Dean, C. and Robbie, K., *Thickness and density evaluation for nanostructured thin films by glancing angle deposition.* Journal of Vacuum Science & Technology B, 2005. **23**(6): p. 2545-2552.
40. Kesapragada, S.V. and Gall, D., *Two-component nanopillar arrays grown by Glancing Angle Deposition.* Thin Solid Films, 2006. **494**(1-2): p. 234-239.
41. Hodgkinson, I. and Wu, Q.H., *Inorganic chiral optical materials.* Advanced Materials, 2001. **13**(12-13): p. 889-+.
42. Lakhtakia, A. and Messier, R.F., *Sculptured Thin Films: Nanoengineered Morphology and Optics with CD.* 2005, Bellingham, Washington, USA: Spie Press.

43. Harris, K.D., Huizinga, A. and Brett, M.J., *High-speed porous thin film humidity sensors.* Electrochemical and Solid State Letters, 2002. **5**(11): p. H27-H29.
44. Steele, J.J., van Popta, A.C., Hawkeye, M.M., Sit, J.C. and Brett, M.J., *Nanostructured gradient index optical filter for high-speed humidity sensing.* Sensors and Actutors B, 2006: p. In Press.
45. Kang, U.S. and Wise, K.D., *A high-speed capacitive humidity sensor with on-chip thermal reset.* Ieee Transactions on Electron Devices, 2000. **47**(4): p. 702-710.
46. Sit, J.C., Broer, D.J. and Brett, M.J., *Liquid crystal alignment and switching in porous chiral thin films.* Advanced Materials, 2000. **12**(5): p. 371-373.
47. Hrudey, P.C.P., Taschuk, M., Tsui, Y.Y., Fedosejevs, R. and Brett, M.J., *Optical Properties of Porous Nanostructured Luminescent Y2O3:Eu Thin Films.* Journal of Vacuum Science & Technology A, 2005. **23**(4): p. 856-861.
48. Kennedy, S.R. and Brett, M.J., *Porous broadband antireflection coating by glancing angle deposition.* Applied Optics, 2003. **42**(22): p. 4573-4579.
49. van Popta, A.C., Sit, J.C. and Brett, M.J., *Optical properties of porous helical thin films.* Applied Optics, 2004. **43**(18): p. 3632-3639.
50. Crawford, G.P., Vilfan, M., Doane, J.W. and Vilfan, I., *Escaped-Radial Nematic Configuration in Submicrometer-Size Cylindrical Cavities - Deuterium Nmr-Study.* Physical Review A, 1991. **43**(2): p. 835-842.
51. Robbie, K., Broer, D.J. and Brett, M.J., *Chiral nematic order in liquid crystals imposed by an engineered inorganic nanostructure.* Nature, 1999. **399**(6738): p. 764-766.
52. Kennedy, S.R., Brett, M.J., Miquez, H., Toader, O. and John, S., *Optical properties of a three-dimensional silicon square spiral photonic crystal.* Photonics and Nanostructures, 2003. **1**: p. 37-42.
53. Kennedy, S.R., Brett, M.J., Toader, O. and John, S., *Fabrication of tetragonal square spiral photonic crystals.* Nano Letters, 2002. **2**(1): p. 59-62.
54. Toader, O. and John, S., *Proposed square spiral microfabrication architecture for large three-dimensional photonic band gap crystals.* Science, 2001. **292**(5519): p. 1133-1135.
55. Harris, K.D., Sit, J.C. and Brett, M.J., *Fabrication and optical characterization of template-constructed thin films with chiral nanostructure.* IEEE Transactions on Nanotechnology, 2002. **1**(3): p. 122-128.
56. Hodgkinson, I., Wu, Q.H., Knight, B., Lakhtakia, A. and Robbie, K., *Vacuum deposition of chiral sculptured thin films with high optical activity.* Applied Optics, 2000. **39**(4): p. 642-649.
57. Seto, M.W., Dick, B. and Brett, M.J., *Microsprings and microcantilevers: studies of mechanical response.* Journal of Micromechanics and Microengineering, 2001. **11**(5): p. 582-588.
58. Singh, J.P., Liu, D.L., Ye, D.X., Picu, R.C., Lu, T.M. and Wang, G.C., *Metal-coated Si springs: Nanoelectromechanical actuators.* Applied Physics Letters, 2004. **84**(18): p. 3657-3659.
59. Colle, M. and Brutting, W., *Thermal, structural and photophysical properties of the organic semiconductor Alq3.* physica Status Solidi A, 2006. **201**(6): p. 1095-1115.

3 Template-Based Fabrication: Single-Templating

In this chapter, single-templating processes that can be used to structure metals and non-polar polymers with GLAD-like helical pores are explored. These processes have been published in the IEEE/ASME Journal of Microelectromechanical Systems [1]. In addition, finite element modeling is used to predict the mechanical properties of these materials. Some parts of this work have been published in the Journal of Materials Research [2].

3.1 Macroporous Thin Films

Inorganic and organic macroporous materials (materials with pore sizes of 50 nm and larger) can be made using many different methods, which can be subdivided into direct and indirect methods. Both of these types of methods will be described in this section, starting with direct methods. In direct methods, pores are introduced into solid materials. For example, electrochemical and photoelectochemical etching can be used to make pores in a number of semiconductors and metals, including Si, Al_2O_3, GaAs and InP [3-5]. In this process (also called anodization), an electric field is applied to the material during chemical etching (which sometimes occurs under illumination, depending on the doping of the wafer). This leads to the formation of long, straight pores oriented perpendicular to the surface of the substrate. Pore size diameter can vary from less than 50 nm to around 500 nm, depending on factors such as doping, voltage, illumination intensity, and electrolyte concentration [4, 6]. For semiconducting materials, pore growth occurs as the material is dissolved. The dissolution process normally involves a charge-carrier transfer, which is more likely to occur at the bottom of a pore than along a sidewall or at the surface of the material [5]. In the case of alumina, pores form at the oxide-metal interface as the aluminum is oxidized, which causes a volume expansion of the material. Existing pits are reinforced as the oxidized material is pushed upwards away from the interface [6]. For both cases (semiconductors and metals), pores can be formed in ordered domains by 'pre-seeding' their locations using nanoindentation, and careful selection of seed location can also influence pore shape [7]. These electrochemical etching processes can be used to make beautiful, high aspect ratio pores

with engineered features. The primary drawback to this technique is that there is limited variation in the pore shape in the direction perpendicular to the plane of the substrate.

A number of direct-write processes can also be used to pattern complex porous structures into organic materials. In holographic patterning, the interference pattern of multiple beams is captured in a photoresist material [8]. Complex, periodic structures can be achieved using this method. A technique with even more precision is two-photon interference, in which arbitrary patterns can be written directly into a resist. One example of a porous structure with features on the order of microns that has been fabricated using this technique is a photonic bandgap structure called 'the woodpile' [9], which consists of layers of regularly spaced lines or beams, with beams in adjacent layers oriented at 90° with respect to each other. Woodpile structures has been fabricated with pitches of 650 nm to 1.5 μm. While in the past direct-write techniques were limited to organic materials, a new class of inorganic photoresists is emerging. SiCN woodpiles have been written directly using one such resist [10]. The main drawback of two-photon interference is the time (and therefore cost) required to pattern large areas.

In indirect macroporous material production methods, pores are molded from another structure. One extremely popular indirect technique for introducing spherical pores into organic and inorganic materials is templating from close-packed colloidal arrays of polystyrene, silica, or latex spheres [11]. Close-packed arrays of spheres are formed on a substrate by evaporating the solvent from a suspension of beads. These template are then replicated into semiconductors, metals, polymers, or ceramics using deposition processes including chemical vapor deposition, electroplating, solution processing and sol-gel technology. In these techniques, the matrix material fills the spaces between the beads in the close-packed arrays. The beads can then be removed, leaving a network of close-packed spherical pores [11-16]. Typical pore sizes range from 100 nm to 1 μm, depending on the dimensions of the spheres from which the porous material is cast [11]. Interest in this area is fueled by the potential for using these materials as photonic crystals [13].

Photonic crystals have been mentioned as an application of interest many times throughout this section; however, the interest in macroporous materials is not limited to this single application. The large surface-area to volume ratios of these materials also make them of interest for use in applications such as catalysis [15], sensors [17], and electrodes [18].

3.2 Templating From GLAD Thin Films

This section describes a technique for fabricating thin films perforated with helical macropores. While GLAD films themselves constitute porous materials, the replica films described in this chapter are of interest for a number of reasons. As described in Chapter 2, some materials cannot be deposited directly using the GLAD technique. These materials include some metals that form faceted crystal structures under available deposition conditions, metals with highly mobile adatoms, and high molecular weight polymers that are not compatible with vacuum deposition processes. Therefore, this technique is useful for increasing the materials available in the GLAD 'toolbox'. There is also a particular interest in templating GLAD square spirals for photonic crystal applications: while silicon square spirals deposited directly using the GLAD technique have been predicted to exhibit a maximum photonic bandgap of 15% (of the gap center frequency), the inverted structure comprised of air square spirals in a silicon matrix has been predicted to exhibit a maximum bandgap of 24% [19]. As mentioned in Chapter 2, templated films also show improved optical behavior with respect to direct GLAD films, exhibiting a higher selectivity in the transmission of left and right circularly polarized light [20]. One possible explanation for this behavior is that templated films have higher uniformity, as the smaller columns which have become extinct in the early stages of growth (due to competition effects described in Section 2.5.3) are not reproduced into the inverted structure. Whereas in direct films these columns may interfere with the light incident upon them and cause scattering, in templated films this 'forest' of material is masked. Another factor that can lead to increased optical activity is index contrast: it has been shown that for materials that exhibit chiral form birefringence, increasing the index contrast between the material and the voids surrounding it leads to increased Bragg

reflection and optical rotation [21, 22]. For the direct GLAD film that was characterized in the aforementioned study, the index contrast between the SiO_2 film and air matrix was 1.47-1.0 = 0.47, whereas for the photoresist templated film the contrast was 1.61-1.00=0.61 [20]. Furthermore, the index contrast of either system can be reduced by the adsorption of atmospheric water into the pores; this adsorption is less likely to take place in photoresist pores (as photoresist is hydrophobic) than in the voids of an oxide film (which are generally hydrophilic). There are also mechanical advantages to the perforated film structure. GLAD films are comprised of high aspect ratio structures anchored to a substrate. These columns fail easily when a shear stress is applied, due to the large moment arm of the structures and small interface between the structures and the substrate. A solid network of material perforated with helical pores is expected to be considerably more robust than a direct GLAD film. Solid thin films with helical macropores are also of interest as a means of exploring how the fundamental properties change as a material is patterned on the nanoscale. This issue will be explored at the end of this chapter.

An advantage of templating from master films deposited by glancing angle deposition is that a high degree of control over the pore size and shape can be achieved by varying the characteristics of the master film. As discussed in Chapter 2, advanced control algorithms for substrate motion can be combined with feedback from a thickness monitor to make a variety of shapes and structures including slanted posts, helices, square spirals, and zig-zags. While in this work we focus on helical master films, the techniques described are entirely compatible with other GLAD structures. In addition, the GLAD process itself can be used to deposit films over relatively large areas: in a typical deposition in our research lab a 4 in. wafer acts as the substrate, and the resulting film is quite uniform over this area. Recently colleague J. Gospodyn used ellipsometry to measure the thickness of a helical Al_2O_3 GLAD film at 9 different points in a grid distributed across a 4 in. silicon wafer, and found that the thickness of the 2081 nm thin film varied by 58 nm from the thickest to thinnest measured points (3%). Therefore, master templates covering large areas can be easily and reliably fabricated.

It has been previously shown by K.D. Harris *et al.* that films deposited by glancing angle deposition could be used as 'positive' masters from which 'negative' replicas could be templated [23]. In this process helical and chevron GLAD films were replicated into a layer of photoresist (HPR 504, Fuji Films), which is an organic material that can be easily infiltrated into a GLAD film by spin-coating. Photoresist is comprised of 3 parts: a solvent, a resin, and a dissolution inhibitor. The dissolution inhibitor is a small molecule, and the resin is comprised of single-chain polymer strands of repeating units. The resin and inhibitor are dissolved in the solvent, and can therefore be spin-coated to form thin films. In this process, most of the solvent evaporates during spin-coating and remaining solvent is baked out of the sample. When the dissolution inhibitor is illuminated in ultraviolet (UV) light in the presence of water vapor, this molecule undergoes a photoreaction that causes it to become soluble in basic solutions. Both exposed and unexposed resists are soluble in most organic solvents.

When HPR 504 is spin coated into a GLAD film, it fills the film and forms a small excess layer on top. This excess layer can be removed by exposing the resist to UV light and dipping the sample in developer (Microposit 354 Developer, Rohm and Haas Electronic Materials). The GLAD master film itself can then be removed in an appropriate wet etchant. The process for making these perforated thin films (PTFs) is illustrated in Figure 3.1:

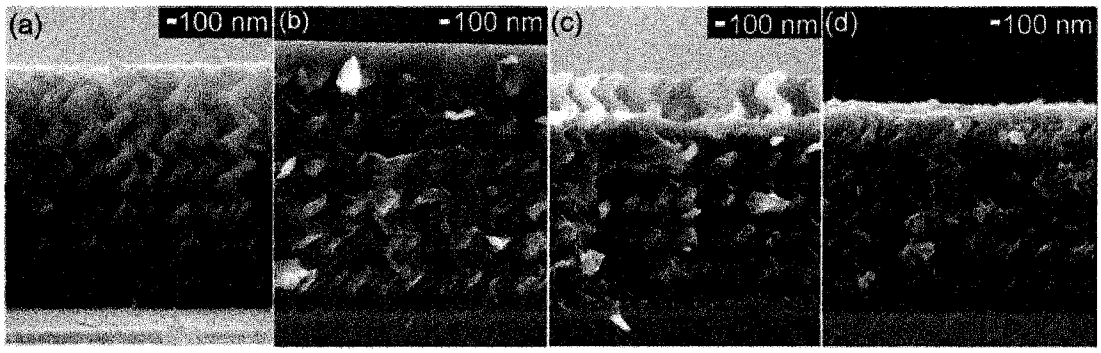

Figure 3.1: Perforated thin film fabrication process. A master GLAD film with the desired features is deposited from SiO_2 (a). The master film is filled by spin-coating (b). The matrix material typically extends beyond the top of the GLAD film. Therefore, the top layer of this material must be removed by wet or dry etching to allow access to the GLAD master film (c). In the last step the GLAD film is removed using an isotropic wet etchant, leaving a thin film perforated with helical macropores (d).

Photoresist is a convenient matrix material for a number of reasons. The viscosity of photoresist (HPR 504) is well-suited for filling GLAD films. Materials that are considerably more viscous tend to form a thick capping layer on top of the GLAD master that must be removed with a precisely controlled etch step (the parameters of which can be difficult to determine accurately), whereas materials that are considerably less viscous coat only the surface of the GLAD structures rather than filling them. Etch chemistry selectivity is another positive characteristic of this material: once exposed, photoresist is readily soluble in an appropriate developer (in this case Microposit 354 Developer). This developer does not visibly change the SiO_2 GLAD film. When the GLAD film itself is removed using buffered oxide etch, the photoresist appears to remains unchanged.

In the following sections, new techniques for fabricating perforated thin films from other materials are described. Section 3.3 focuses on a non-polar polymer which cannot be effectively spin-coated due to the incompatibility between hydrophilic GLAD surfaces and the non-polar polymer. Sections 3.4 and 3.5 detail the fabrication of metal perforated thin films using an electroplating process. The technique documented therein is the first process in the literature describing the fabrication of a metal thin film with helical pores having submicron dimensions. In Section 3.6, the mechanical characterization of metal perforated thin films is described, using both finite element modeling and nanoindentation. This investigation looks at how the properties of nickel thin films change as a result of being structured on the micro- and nanoscale.

3.3 Fabrication of Non-Polar Polymer Perforated Thin Films

Unlike photoresist, non-polar polymers such as polystyrene cannot be easily infiltrated into GLAD films using spin-coating, due to the polarity of the materials involved. Polystyrene is a fairly non-polar polymer, and therefore dissolves best in non-polar solvents such as xylene or hexane. To try and construct polystyrene perforated thin films, pellets of polystyrene were dissolved in xylene and spin-coated into a GLAD film. Residual solvent was driven off by baking the sample to 110 °C. The sample was then cleaved and examined by SEM, as shown in Figure 3.2:

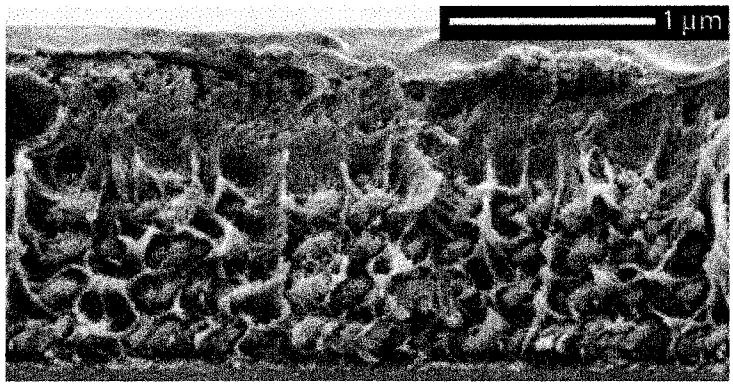

Figure 3.2: SiO_2 GLAD film spin-coated with polystyrene/xylene mixture. The GLAD film is quite poorly filled, as large voids are visible.

The resulting composite is 'stringy' in appearance, with visible pores, as shown in Figure 3.2. Other non-polar polymer/solvent combinations have been found to behave similarly. The GLAD layer was not well filled, and large pores are visible. The polystyrene itself is quite porous in appearance. These materials do not appear to be compatible.

Contact angle measurements have shown that GLAD films (particularly the SiO_2 GLAD films employed throughout this thesis) are quite hydrophilic (and therefore polar), as water droplets on an untreated GLAD film have a contact angle of essentially 0° [24]. Therefore it is understandable that non-polar solvents and polymers will be less compatible with GLAD films than polar ones.

As polystyrene could not be well filled into GLAD films using spin-coating, it was necessary to find an alternative method to fill the film: melt-processing. This technique was used with an alumina template. Alumina was chosen as the template rather than silicon to emulate a paper in the literature in which polystyrene was infiltrated into long narrow pores of porous alumina by melt-processing [25]. To infiltrate the Al_2O_3 template a small pellet of polystyrene (<20 mg in weight, molecular weight 100,000 g/mol, Alfa Aesar) was placed on top of the template and slowly heated to a maximum temperature of 230 °C (in a nitrogen environment). This maximum temperature was held for 3 to 6 hours to give ample time for the melted polystyrene to be drawn into the template by capillary action. The sample was then slowly cooled to room temperature over 8 to 12

hours. To verify that decomposition of the polystyrene does not occur during heating, thermogravimetric analysis (TMA) – in which the weight of a polystyrene granule is monitored with high precision as the sample is heated – was also conducted on the sample. If the polymer undergoes decomposition gaseous by-products are expected to form, which would lower the weight of the solid sample. However, for the material employed in this experiment, no change in weight was observed as the sample was heated to 300 °C, suggesting that the polymer does not decompose at the temperature at which the template GLAD film was filled (230 °C).

Reasonably good filling of the GLAD template can be achieved using melt-processing, although the thickness uniformity of the sample overall is less than ideal (as shown in Figure 3.3 (a)). When heated the pellet formed a large droplet on top of the sample, with a contact angle of 5°. Good, uniform filling was achieved in a ring approximately 100 μm wide surrounding this central drop. The well-filled and overfilled regions are shown in Figure 3.3(a). In the well-filled region, a perforated thin film could be formed by removing the Al_2O_3 by etching in a 45% solution of KOH for 30 minutes. Due to the relatively long etch-time involved, an SiO_2 etch-stop layer was incorporated into the template: before the master Al_2O_3 film was deposited a 400 nm layer of SiO_2 was evaporated onto the substrate. During the deposition of the SiO_2 layer the substrate was rotated rapidly (16 times) as the deposition angle was increased from 30° to 85°, such that this layer evolved from a solid film to the start of independent columnar structures. During the etch-removal of the alumina template this layer acted as a barrier, preventing the KOH from etching under the Al_2O_3 into the silicon substrate beneath. After the KOH etch step, a polystyrene perforated thin film remained, as shown in Figure 3.3 (a) and (b).

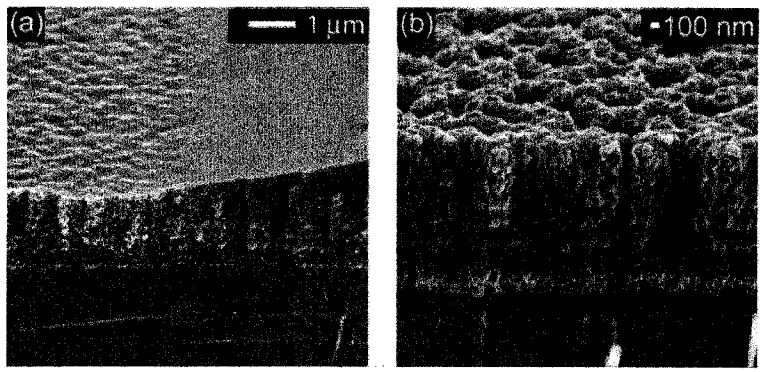

Figure 3.3: Polystyrene perforated thin films. When a pellet of polystyrene is melted, the material is drawn into the template, forming a ring of perfectly filled material around a central droplet of overfilled material (a). The Al_2O_3 in this ring can be removed by immersing the sample in KOH, leaving a polystyrene perforated thin film (b).

More uniform filling could potentially be achieved using shavings, smaller granules, or evenly dispersed powders of polystyrene. Nonetheless, films with well-defined helical pores are formed which could potentially be incorporated into sensor applications. It is expected that this technique could also be used to effectively manufacture perforated thin films from other non-polar polymers. This technique has not been demonstrated previously, and allows a whole new class of materials to be shaped with GLAD-based features.

3.4 Fabrication of Metallic Perforated Thin Films - Nickel

Metal perforated thin films can be fabricated using an electroplating process to infiltrate the GLAD film with the matrix material. Electroplating is a common deposition process that is used to apply metallic coatings to conductive surfaces. Applications of this process range from applying decorative finishes on jewelry to depositing wear-resistant finishes on car parts [26]. Electroplating is also an important tool in microfabrication, as this process is used to make copper interconnects in integrated circuits [27].

There are two types of reactions which are central to electroplating: oxidation reactions and reduction reactions. Both of these reactions can occur when a metal ($M_{(s)}$) is immersed into a solution which contains the salt of the metal ($MA_{(aq)}$). In a reduction

reaction, ions migrate from the solution to the metal, where they can combine with free electrons to form a solid. This process is summarized in Equation 3.1:

$$M^{x+}_{(aq)} + xe^- \rightarrow M_{(s)} \qquad [3.1]$$

In an oxidation reaction, the solid metal enters the solution, leaving behind electrons on the surface of the metal. This is summarized in Equation 3.2:

$$M_{(s)} \rightarrow M^{x+}_{(aq)} + xe^- \qquad [3.2]$$

Electrons are therefore produced at a surface which is undergoing an oxidation reaction and consumed at a surface which is undergoing a reduction reaction. In electroplating, the oxidation reaction occurs at the anode, and the reduction reaction (and therefore deposition) occurs at the cathode. The anode and cathode are electrically connected, usually across a voltage source which forces the electrons to travel from anode to cathode. A sketch of an electroplating set-up is shown in Figure 3.4:

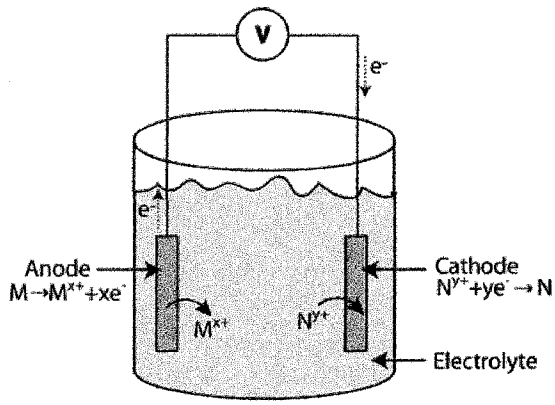

Figure 3.4: An electroplating set-up. The cathode and anode are partially immersed in the electrolyte, and connected externally by an electrical circuit. Electrons flow from the anode to cathode, where they undergo a reduction reaction.

The anode can be the same material as the metal being deposited or different, although if a different, non-inert material is employed, unwanted ions are introduced into the solution which may be plated preferentially onto the cathode. An inert platinum electrode may also be used, in which case it is the ions present in the solution (such as OH^-) that will be oxidized.

Despite this simple description, electroplating is a complicated process with a multitude of variables which must be carefully controlled, including: bath composition, salt concentration, pH, temperature, current density, cathode geometry, anode-to-cathode spacing, additives, and agitation [26]. Deposition rate (and therefore thickness), ductility, hardness, stress, uniformity, and brightness of the deposited material are a few of the characteristics that can change when the above mentioned parameters are varied.

When electrodepositing into a GLAD film, a metal layer beneath the porous film acts as an electrode. However, the GLAD film itself greatly complicates the electroplating process as it acts as an insulator, disrupting the ionic conductive path from the solution to the cathode itself and distorting the electric field between the two electrodes. Electroplating through non-conductive layers has been demonstrated a number of times previously in the literature. Electroplating through lithographic masks was first demonstrated in the 1960s, and can be used to reproduce the features of the masks with very high precision. This process is sometimes referred to as "metallic micromolding" "electroforming" or "LIGA (Lithographie, Galvanoformung, Abformung") [28, 29]. In this type of through-plating process, a substrate is first coated with a metal electrode, on top of which a mask layer is patterned using techniques such as optical lithography, e-beam lithography, or even x-ray lithography. Metal can then be plated into the features defined by the mask layer onto the metal electrode beneath. After plating, the photoresist can be stripped, leaving high aspect ratio structures (in LIGA the metal structure can subsequently act as a mold for further replication). Resolutions on the scale of a few nanometers can potentially be achieved.

Electroplating through porous alumina to form nickel nanowires for magnetic storage has also been demonstrated [30]. There are some challenges associated with plating through high aspect ratio structures, which include incomplete wetting of the features by the electrolyte (which can be solved using a wetting agent); depletion of the electrolyte at the cathode due to limited diffusion processes; and the reduction and build-up of hydrogen gas at the cathode also due to diffusion limited processes. Hydrogen gas can be a natural

by-product when plating non-noble metals [31], and, if allowed to accumulate, the resulting change in the pH of the solution can lead to the incorporation of pores in the final structure [32]. Plating conditions must therefore be carefully controlled.

In the remainder of this section a step-by-step description of the fabrication of a nickel perforated thin film will be given. The steps of this process are illustrated in Figure 3.5, and described in further detail below.

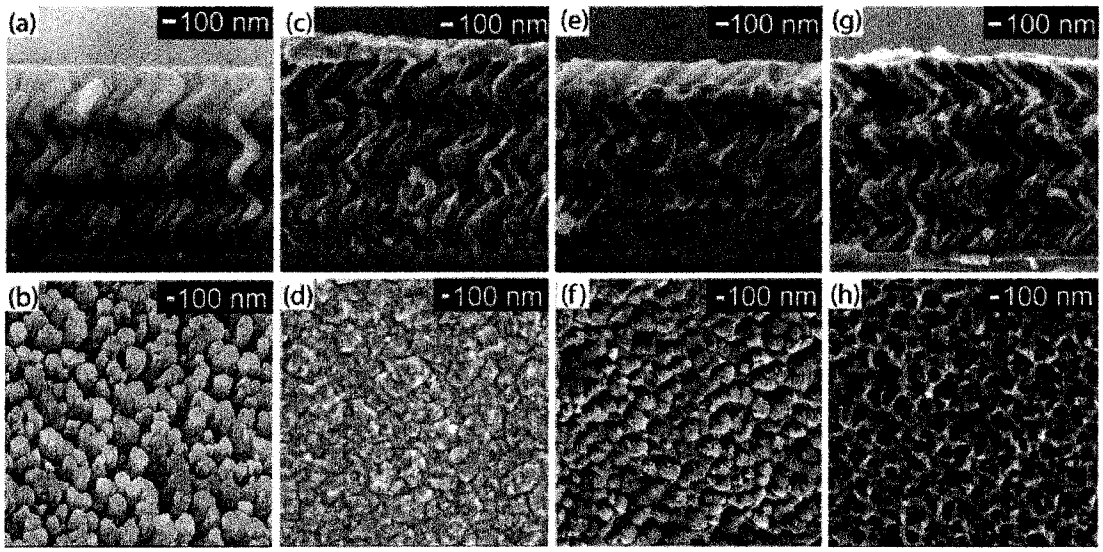

Figure 3.5: Fabrication of a nickel perforated thin film. The film is imaged from the side (top row) and top (bottom row). A master film is deposited by glancing angle deposition onto a substrate coated with a thin conducting layer, which acts as an electrode during the electrodeposition process (a,b). This film is filled with metal by electroplating, completely covering the template GLAD film (c,d). The top of the master film is uncovered by wet etching of the matrix film (e,f). The master film is removed in an anisotropic wet etchant (g,h).

3.4.1 Master Template Fabrication

In this process, a thin layer of metal is deposited onto the silicon substrate (usually by sputtering) before the master GLAD film is deposited. This layer acts as an electrode in subsequent processing steps. For the film shown in Figure 3.5, a 75 nm layer of chromium is visible beneath the master film in the side view images (a,c,e,g). In subsequent experiments it was found that much higher uniformity in film thickness could be achieved across a larger area of film when a NiCr electrode layer was employed,

resulting in a thickness uniformity of ±5% over a rectangular sample measuring 1 cm by 0.7 cm. The improved uniformity seen when a NiCr layer was used may be due to the fact that electroplated nickel exhibits better adhesion with nickel than chromium [33].

It is expected that any GLAD oxide film could be used as the master film, provided that the oxide can be selectively etched with respect to the matrix material. The film shown in Figure 3.5 (a) and (b) is a three-turn SiO_2 helical film with a 400 nm pitch deposited at 85°, although other architectures, thicknesses, and pitches are also easily achievable using this technique. SiO_2 was chosen as the template material because it can be easily and selectively etched.

3.4.2 Matrix Filling

In the fabrication of metal perforated thin films, the matrix material is filled into the GLAD template by electroplating. To deposit nickel, a commercially prepared nickel sulfamate electroplating solution was chosen as the electrolyte (SN10, Transene). This solution contains nickel sulfamate $\{Ni(SO_3NH_2)_2 \cdot 4H_2O\}$, boric acid $\{H_3BO_3\}$, and nickel chloride {NiCl}. Nickel sulfamate is often selected for plating in electroforming processes due to the low stress in the deposited film [32]. During deposition, a number of complex processes occur in the electrolyte, some of which involve adsorption on the surface of the anode and cathode. While the mechanisms of deposition and exact role of each additive are not precisely understood, a few of these processes are described below [31].

Two of the reactions which can occur at the cathode during electroplating are shown in Equation 3.3 and 3.4:

$$Ni^{2+}_{(aq)} + 2e^- \rightarrow Ni_{(s)} \qquad [3.3]$$

$$2H^+_{(aq)} + 2e^- \leftrightarrow H_{2(g)} \qquad [3.4]$$

As nickel is reduced, the thickness of the film increases. The reduction of hydrogen at the cathode leads to the production of hydrogen gas, which can influence the final

structure of the film. It can also change the pH of the solution, which could lead to the hydrolysis of hydroxyl ions, as shown in Equation 3.5 [31]:

$$4OH^- \rightarrow 2H_2O + O_{2(g)} + 4e^- \qquad [3.5]$$

For this reason boric acid is included as a buffer, as illustrated in Equation 3.6:

$$B(OH)_3 + H_2O \leftrightarrow B(OH)_4^- + H^+ \qquad [3.6]$$

Boric acid may also inhibit the production of hydrogen at the surface by surface adsorption [31]. Meanwhile NiCl is thought to be essential in ensuring proper dissolution of the anode by preventing the formation of nickel hydroxide at the surface [26] .

In the two-electrode process used to deposit nickel into the GLAD film shown in Figure 3.4, a layer of chromium sputter-coated onto the substrate before the deposition of the GLAD film acted as the cathode, and a piece of nickel foil acted as the anode. Plating took place in a home-built polyvinylchloride (PVC) tank in which the sample and the anode could be clamped at a constant separation of 2.7 cm. Plating through a thick porous oxide layer can be difficult as this layer can distort the electric field between the electrodes. When plating into pores the rate must be kept low to allow sufficient time for Ni^{2+} cations to diffuse from the solution to the cathode. In our experiments the current density was maintained at approximately 0.85 mA/cm^2. This current density is quite small: when plating from nickel sulfamate baths, current values of less than 10 mA/cm^2 are considered low [34]. Nonetheless this value was selected to allow sufficient time for diffusion of the electrolyte into the pores. During the electroplating process, the current tended to drift upwards. This likely occurred because as the GLAD film was filled, both the amount of oxide shielding the cathode from the anode and the distance that ions had to diffuse through the oxide to reach the cathode were reduced. To maintain a constant current, the voltage was typically decreased by 20% to 25% during electrodeposition.

The electrolyte solution was heated to between 35 °C and 50 °C, as per the manufacturer's directions. Temperature control was important for maintaining the desired concentration of boric acid in the solution, since at lower temperatures the

solubility of boric acid can decrease, leading to the formation of chains of polyborate ions as this acid precipitates out [34].

Using the electroplating process described above, good filling and acceptable thickness uniformity were achieved. The correct duration of the electroplating process required to completely fill the matrix material up to the top of the GLAD structures was determined by eye, by examining the appearance of the film at regular intervals. When the appearance of the film changed from dull to shiny the process was terminated, as a shiny appearance indicated that the nickel film had formed a solid layer on top of the GLAD structures (which normally scatter light).

3.4.3 Matrix Etch-back

As the plated material was typically deposited to a level above the tips of the GLAD film, it was necessary to remove some of this material before the master film could be etch-removed. For the sample shown in Figure 3.5, this was accomplished by immersing the sample in an isotropic wet etch consisting of a dilute solution of nitric acid (35% in deionized water). After the sample was quickly dipped in the etching solution, it was immediately rinsed in deionized water to stop the etching process. The results of this step can be seen in Figures 3.5 (e) and 3.5 (f).

The matrix etch-back step could also be avoided by terminating the plating process before a solid layer of nickel formed on top of the GLAD master, leaving the GLAD structures only partially filled. However, when the film was only partially filled, it was much more difficult to determine the correct duration of the plating step.

3.4.4 Template Removal

The final step of the single-templating process is to remove the master film. When a SiO_2 film is employed, the master film can be removed by immersing the sample in a 10:1 mixture of ammonium fluoride (NH_4F) and hydrofluoric acid (HF, 49%), which is a standard glass etchant called buffered oxide etch (BOE, Arch Chemicals). This etchant selectively dissolves the SiO_2 without significantly affecting the nickel matrix, the electrode layer, or the silicon wafer itself. Equation 3.7 describes the reaction that takes

place as SiO_2 is etched [35]. The ammonium fluoride acts as a buffer, dissociating to produce additional HF, as shown in Equation 3.8.

$$SiO_{2(s)} + 6HF_{(l)} \rightarrow SiF_{6(g)} + 2H_2O_{(l)} + H_{2(g)} \quad [3.7]$$

$$NH_4F \Leftrightarrow NH_{3(g)} + HF_{(l)} \quad [3.8]$$

For the templating work described in this chapter, a sample was immersed in the etchant for 5 min. After etching, the film was thoroughly rinsed in deionized water, leaving the porous nickel film with helical pores shown in Figures 3.5 (g) and (h). The SEM images show that the helical structures have been well replicated into the nickel matrix.

3.5 Fabrication of Metallic Perforated Thin Films – Gold

Gold perforated thin films can also be made using an electrodeposition process. During our experiments electroplating was conducted using a 24 K mirror bright solution (Technic-Gold 25 RTU, Technic Inc). This solution was selected mainly for safety, as, unlike most gold plating solutions, it is cyanide-free. The gold in the solution is in the form of sodium gold sulfite ($Na_3Au(SO_3)_2$). In this process a 130 nm layer of NiCu (30% Ni by weight, 70% Cu by weight) sputtered onto a silicon wafer was selected to act as the electrode. Other electrode layers were also tested, but were discarded due to poor adhesion to the silicon wafer or GLAD film (Pt, Cu), or poor etch resistance in buffered oxide etch (Ti). Plating was performed in a PVC tank, at constant voltage and at a temperature of 50 °C, as per the suggestion of the electrolyte supplier. A silicon wafer sputtered with a layer of Pt was employed as the anode. A current density of 1.1 A/cm^2 was initially used, although again the current density drifted upwards during the process by around 50%. After electroplating, excess gold coating the top of the master film was removed by immersing the sample in a solution of KI/I_2 for 30 s, as per Equation 3.9 [36]:

$$I_{2(aq)} + 2Au_{(s)} \rightarrow AuI_{(aq)} \quad [3.9]$$

KI is included in the mixture to increase the solubility of the I_2 [37]. Due to the poor adhesion between the gold and the electrode layer, the gold film would typically separate from the substrate during this process. This film (effectively a membrane) could be

handled with tweezers. The master film was removed by immersing the membrane in BOE for 210 s and rinsing with water. The flexible nature of the resulting film presented a challenge for mounting the sample for SEM imaging. A master film and gold perforated thin film are shown in Figures 3.6 (a) and (b).

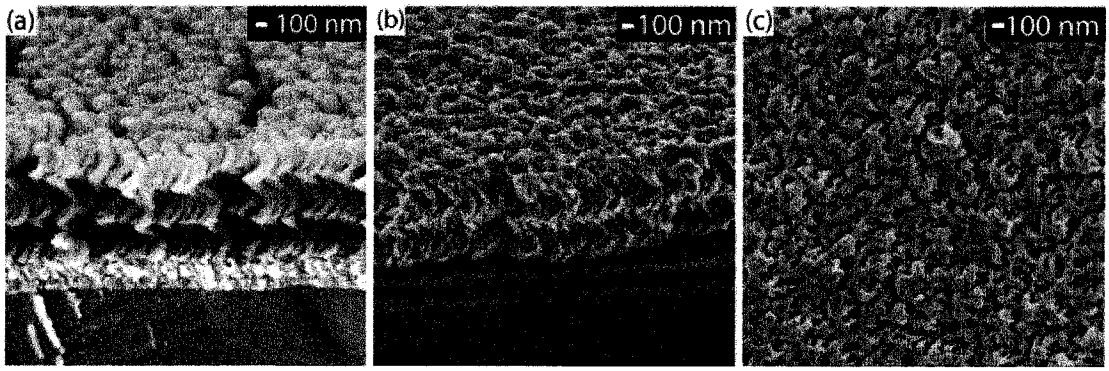

Figure 3.6: Gold perforated thin film. Master template (a), perforated thin film as seen from the side (b) and top (c). In the side view the gold film has barely lifted off of the silicon substrate. The thin NiCu electrode layer is also visible beneath the film.

3.6 Mechanical Characterization of Nickel Perforated Thin Films

When the dimensions of a material are reduced to the nanoscale, mechanical properties such as Young's Modulus [38, 39], bending strength [40], and hardness can change dramatically [41]. One reason that these properties can change is due to microstructural constraints, which become significant as the characteristic dimension of the material becomes comparable to the size of the grains from which it is comprised [42]. For example, thin films deposited by chemical vapor deposition can consist of columnar grains which are tall and narrow. If the width of these columns is smaller than a normal grain size, then the material can exhibit increased hardness with respect to a bulk material, since the grain boundaries prevent dislocations from moving through the material [41]. The purpose of this section is to examine how the properties of nickel thin films change as a result of structuring them with helical pores, and to determine whether the mechanical properties of these films can be tuned by varying the architecture of the master film [2].

It has been shown previously that helical SiO_x GLAD films behave like microscopic springs, undergoing much larger elastic deformations in response to an applied force than a bulk sample of the same material [43]. For solid films perforated with helical pores, a similar effect is expected, although to a lesser extent. While GLAD films are comprised of individual helices that could be compressed independently, perforated thin films are a continuous matrix of material that must be deformed as a single unit.

The mechanical behavior of a compressed spring can be determined analytically [44], however the problem of an inverted spring is considerably more complex. In this section the elastic modulus of perforated thin films is modeled using finite element modeling, and the results obtained are compared with values measured by nanoindentation.

3.6.1 Finite Element Modeling

Finite element analysis is a tool that can be used to solve a variety of engineering problems numerically, rather than analytically [45]. The problems are described in terms of differential equations accompanied by appropriate boundary conditions, where the equations stem from the physics of the problem itself. Examples of systems which may be solved using this method include electrical networks, mechanical systems, and systems involving heat transfer.

The purpose of the finite element model described here is to determine the displacement of an inverted spring structure (i.e., perforated thin film) when a uniform force is applied to the top face of the structure. This reflects the situation encountered when compressing forces are applied to a perforated thin film templated from GLAD helices. The geometry of this problem makes it very difficult (if not impossible) to compute a solution analytically. Instead this material is modeled as an elastic solid, which means that when a given stress (σ) is applied, the resulting strain (ε) can be computed using Hooke's law, as stated in Equation 3.10. The definitions of stress and strain are also stated explicitly in Equation 3.11 and Equation 3.12, respectively.

$$\sigma = E\varepsilon \qquad [3.10]$$

$$\sigma = \frac{F}{A} \qquad [3.11]$$

$$\varepsilon = \frac{du}{dy} \qquad [3.12]$$

Where E is the elastic modulus of the material (also called Young's modulus), F is the force applied to an area A, and du is the incremental change in length over a differential section dy of an object with total length y. Combining these equations, the force on an element in the system can then be described by Equation 3.13:

$$F = EA\frac{du}{dy} \qquad [3.13]$$

As an example, take the simple case of an arbitrary structure subjected to a force in one direction, as illustrated in Figure 3.7. To determine the displacement of the system (u_1, u_2), the structure is subdivided into a collection of nodes, as shown.

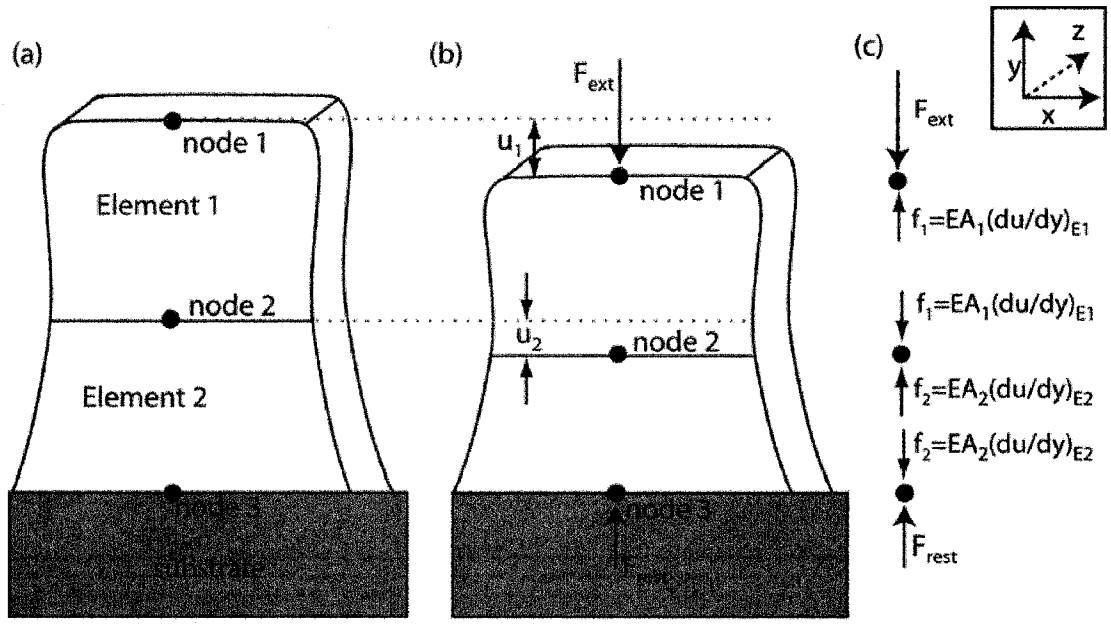

Figure 3.7: Finite element analysis. An arbitrary shape can be subdivided into elements with 3 nodes (a). When an external force F_{ext} is applied to node 1, the shape undergoes an elastic deformation (b). A free-body diagram for each element can be drawn (c), where static equilibrium dictates that the net force at each node must be 0. The coordinate system is shown in the top right hand corner of the figure.

A differential equation can then be written for each node. Since the system is static, the sum of the forces at each node must be zero. The differential equations describing node 1, node 2 and node 3 are given in Equation 3.14, 3.15, and 3.16 respectively:

$$EA_{E1}\left(\frac{du}{dy}\right)_{E1} - F_{ext} = 0 \qquad [3.14]$$

$$EA_{E1}\left(\frac{du}{dy}\right)_{E1} - EA_{E2}\left(\frac{du}{dy}\right)_{E2} = 0 \qquad [3.15]$$

$$F_{rest} - EA_{E2}\left(\frac{du}{dy}\right)_{E2} = 0 \qquad [3.16]$$

In this system A_{E1} and A_{E2} are the average cross-sectional areas of Element 1 and Element 2 (in a plane perpendicular to the force), and $(du/dy)_{E1}$ and $(du/dy)_{E2}$ are the strains in Element 1 and Element 2. There are three unknowns in the total system: $(du/dy)_{E1}$, $(du/dy)_{E2}$, and F_{rest}. In finite element analysis, there are a number of different techniques which can be used to find solutions to these equations. The example given here is quite simple and could be solved directly. For more elaborate problems with complex geometries there are a variety of matrix analysis techniques, simplification principles, and approximation methods which can be used to generate and solve systems of equations numerically and arrive at a solution which describes the displacement at each node and throughout the material [45, 46].

In the example given above, a force was applied in the negative y direction, and a system of equations was developed to determine the resulting displacement in a parallel direction. However, this only gives a small picture of the deformation that occurs as a result of the applied force. For most materials a compression in one direction (in this case in the negative y direction) is accompanied by an expansion in the two perpendicular directions. The lateral strains (ε_x, ε_z) that accompany an axial strain can be calculated, provided that the Poisson's ratio (ν) of the material is known. In the case of an isotropic materials, these parameters are related by Equation 3.17 [47]:

$$\nu = -\frac{\varepsilon_x}{\varepsilon_y} = -\frac{\varepsilon_z}{\varepsilon_y} \qquad [3.17]$$

In addition, there is another type of stress that must be considered: shear stress. Above, only normal stress was considered. Normal stress is a compressive or tensile stress that is applied perpendicular to the cross-section of the material, as shown in Figure 3.8:

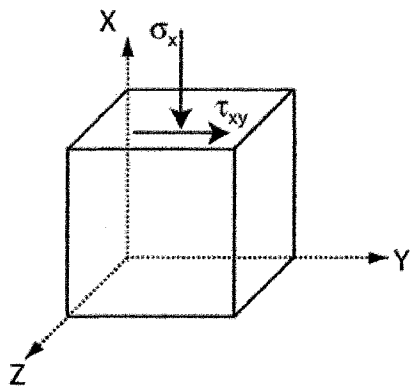

Figure 3.8: Normal and shear stress. A normal stress (σ_x) is applied perpendicular to the surface of the material, whereas a shear stress (τ_{xy}) is applied parallel to the surface.

As shown in Figure 3.8, shear stress is applied in a direction parallel to the face of the material. This stress causes the material to change in shape, but not in volume. In Figure 3.8 the shear stress τ_{xy} is written with two subscripts, one indicating the plane to which the stress is applied (X) , and the other indicating the direction (Y). A shear stress τ_{xy} will result in a shear strain γ_{xy}. These two values are related by a shear modulus G, just as normal stresses and strains are related by an elastic modulus E. The shear and elastic moduli are themselves related, as shown in Equation 3.18:

$$E = 2G(1+\nu) \qquad [3.18]$$

To fully characterize a material, a constitutive equation must be given which describes the relationship between all of the normal (σ_{xx}, σ_{yy}, *and* σ_{zz}) and shear (τ_{xy}, τ_{xz}, τ_{yx}, τ_{yz}, τ_{zx}, τ_{zy}) stresses, and normal (ε_{xx}, ε_{yy}, *and* ε_{zz}) and shear (γ_{xy}, γ_{xz}, γ_{yx}, γ_{yz}, γ_{zx}, γ_{zy}) strains. Each type of stress may be written as a function of the nine strains, just as each strain may be expressed as a function of the nine stresses. In the most general forms, the relationships between all of these components are given in Equations 3.19 and 3.20:

$$\underline{\varepsilon} = \underline{\underline{S}}\,\underline{\sigma} \qquad [3.19]$$

$$\underline{\sigma} = \underline{\underline{C}}\,\underline{\varepsilon} \qquad [3.20]$$

Where $\underline{\varepsilon}$ is the strain matrix, $\underline{\sigma}$ is the stress matrix, $\underline{\underline{S}}$ is the compliance tensor and $\underline{\underline{C}}$ is the stiffness tensor. The stiffness and compliance tensors each contain 81 elements. For isotropic, linear, elastic materials, Equation 3.19 can be written as shown in Equation 3.21:

$$\begin{Bmatrix} \varepsilon_x \\ \varepsilon_y \\ \varepsilon_z \\ \gamma_{xy} \\ \gamma_{xz} \\ \gamma_{yx} \\ \gamma_{yz} \\ \gamma_{zx} \\ \gamma_{zy} \end{Bmatrix} = \frac{1}{E} \begin{bmatrix} 1 & -\nu & -\nu & 0 & 0 & 0 & 0 & 0 & 0 \\ -\nu & 1 & -\nu & 0 & 0 & 0 & 0 & 0 & 0 \\ -\nu & -\nu & 1 & 0 & 0 & 0 & 0 & 0 & 0 \\ 0 & 0 & 0 & 2(1+\nu) & 0 & 0 & 0 & 0 & 0 \\ 0 & 0 & 0 & 0 & 2(1+\nu) & 0 & 0 & 0 & 0 \\ 0 & 0 & 0 & 0 & 0 & 2(1+\nu) & 0 & 0 & 0 \\ 0 & 0 & 0 & 0 & 0 & 0 & 2(1+\nu) & 0 & 0 \\ 0 & 0 & 0 & 0 & 0 & 0 & 0 & 2(1+\nu) & 0 \\ 0 & 0 & 0 & 0 & 0 & 0 & 0 & 0 & 2(1+\nu) \end{bmatrix} \begin{Bmatrix} \sigma_x \\ \sigma_y \\ \sigma_z \\ \tau_{xy} \\ \tau_{xz} \\ \tau_{yx} \\ \tau_{yz} \\ \tau_{zx} \\ \tau_{zy} \end{Bmatrix} \qquad [3.21]$$

When an external load (F/A) is present, the equation which governs the system can be expressed as shown in Equation 3.22:

$$\underline{\underline{C}}\,\underline{\varepsilon} - \underline{F/A} = 0 \qquad [3.22]$$

In the work described here, the commercial finite element software ANSYS was employed. The geometric parameters, material properties (elastic modulus and Poisson's ratio), and boundary conditions were defined. Geometrically, the film was represented as a single unit, consisting of an array of 9 spring-like voids defined in a solid block of material. The rise angle, helical radius, cross-sectional radius, number of turns, and thickness of the helical structures could all be manipulated within the model to investigate the relevance of each parameter. Most of these parameters are illustrated in Figure 3.9, and the values used in the simulations are summarized in Table 3.1.

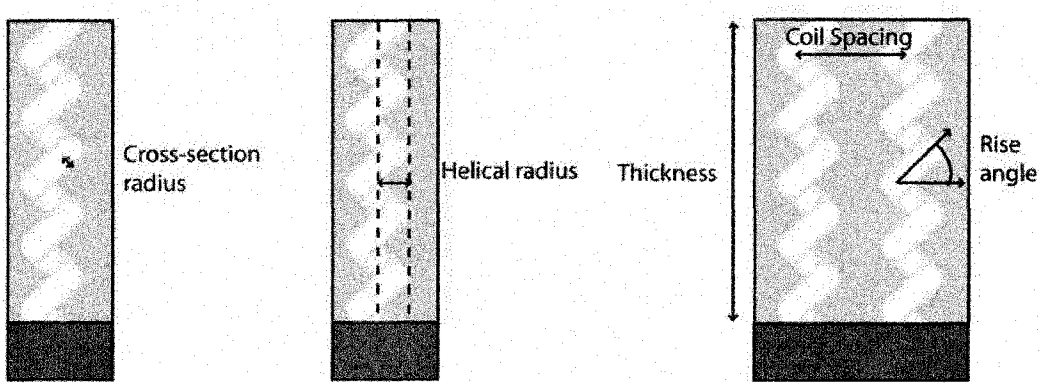

Figure 3.9 Parameters of inverted helix. Cross-sectional radius, helical radius, thickness, rise angle, and coil spacing are all parameters that can be manipulated within the finite element model.

Parameter	Symbol	Value
Cross-sectional radius	r_c	35 nm, 50 nm
Helical radius	r_h	75 nm
Thickness	t_f	550 nm
Rise angle	θ_r	20° to 70°
Number of turns	N	Dependent on rise angle
Coil spacing	S_c	260 nm

Table 3.1 Parameters employed in finite element model for helically-perforated GLAD films.

Note that in this case the rise angle (θ_r) is not equal to the column angle (β) defined in Chapter 2, as β is measured from the substrate normal, whereas θ_r is measured from the plane of the substrate.

The number of turns was not explicitly defined in the model, but rather was dependent on the rise angle and overall thickness. The number of turns can be determined using equation 3.23:

$$N = \frac{t_f}{\pi 2 r_h \tan \theta_r} \qquad [3.23]$$

The solid was defined as an elastic solid, with a bulk modulus of 210 GPa, and a Poisson's ratio of 0.31, which are standard values for nickel [48]. Ideally a very large number of helices would be modeled at a time to mimic the behavior of an actual sample. In actuality, it is difficult to include more than a few helices due to the large number of nodes required to model this complex structure. An array of 9 inverted helices was chosen as the structure in the model, to approximate the proper geometry without making the model overly complex. The model was meshed using as many as 170,000 nodes, arranged in 10-node tetrahedral elements. Increasing the number of nodes was found to have little outcome on the behavior of the model.

The modulus was determined by applying a uniform pressure to the top face of the structure (mimicking the load applied by the indenter tip), and determining the resulting displacement of this face. The modulus could then be calculated using Equation 3.24:

$$E = \frac{\sigma}{\varepsilon} = \frac{F/A}{\Delta l/l} \qquad [3.24]$$

In the first model, the influence of both the rise angle and the cross-sectional radius were investigated. To do so, the rise angle was varied in 10° increments for cross-sectional radii of 35 nm and 50 nm. The results are shown in Figure 3.10, normalized to the bulk modulus of nickel:

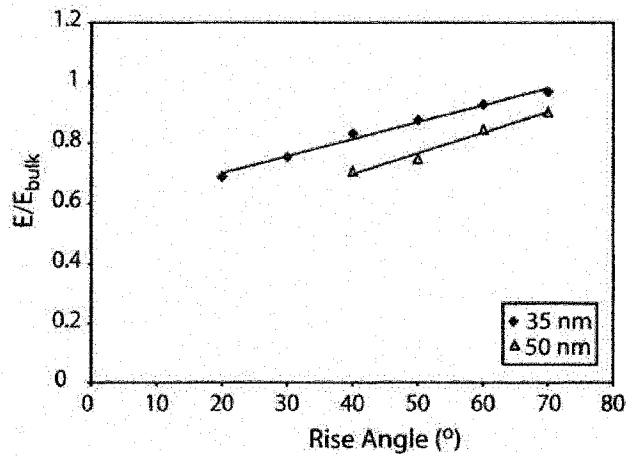

Figure 3.10 Elastic modulus as a function of rise angle and cross-sectional radius. These results were generated using ANSYS finite element modeling.

In actual GLAD films, the rise angle (θ_r) can be varied by changing the angle of deposition (α), as the rise angle generally decreases with increasing deposition angle. Practically speaking, the minimum rise angle that can be achieved is around 30°, depending on the material evaporated [49]. The maximum rise angle achievable can reach 90° if the spin-pause technique is employed [50]. In this technique the substrate is rotated in incremental amounts during growth, as in the fabrication of standard helical films, however at each step the substrate is rapidly rotated through an additional 360° to tilt the helical arms upward towards the substrate normal.

Unlike the rise angle, the cross-sectional radius is not easily controlled, as the diameter of the helical arms of the film tend to increase during a typical deposition in order to maintain a constant density as some columns terminate due to competition. The values employed here are representative of typical values seen in GLAD films.

The results of the model show that by varying the rise angle from 40° to 90°, the modulus of the film can be tuned from between 0.65 of the bulk modulus to close to the bulk modulus itself. Since the rise angle is easily varied, this allows the possibility of engineering the mechanical properties of a given material. The results shown in Figure 3.10 indicate that the rise angle is much more important in determining the modulus than the cross-sectional radius. Note that for comparison the modulus of the film with the 35 nm helical pores was estimated using effective medium theory, by multiplying the fill fraction of the matrix by the bulk modulus of nickel. In this case the modulus was predicted to vary only from 0.84 to 0.94 of the bulk material as the rise angle was varied from 20° to 90°. This indicates that the change in modulus as a function of rise angle predicted by finite element analysis results from the spring-like nature of the pores, and not solely from the change in density of the material that results from changing the rise angle.

The effect of varying the coil spacing was also investigated for a rise angle of 50°, a cross-sectional radius of 35 nm, and a helical radius of 75 nm. The results are shown in Figure 3.11:

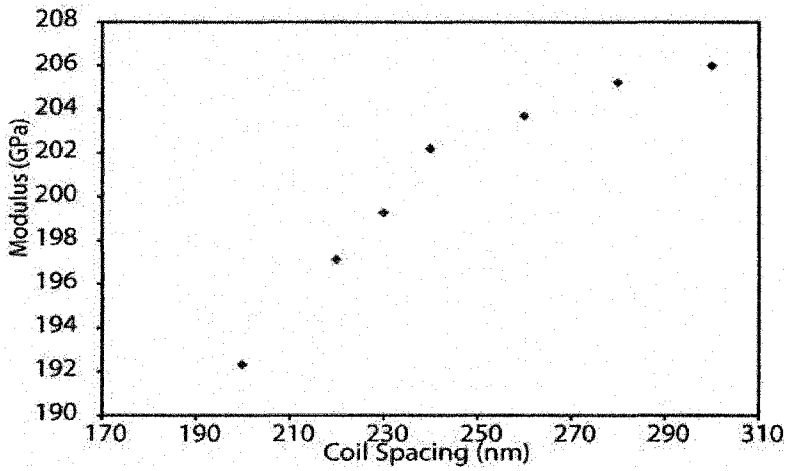

Figure 3.11 Elastic modulus as a function of coil-spacing and cross-sectional radius. These results were produced using finite element modeling. As the coil spacing increases, the modulus approaches the bulk modulus (210 GPa).

The results of the finite element modeling show that as the coil spacing is increased from 200 nm to 300 nm the elastic modulus varies by less than 10%. While it is possible to strictly control the spacing of the coils of a GLAD film using lithographically patterned substrates (where the location of column growth is dictated by the seeds) the results shown in Figure 3.11 indicate that there is very little advantage to be gained by this extra work, as the effect on the modulus is minimal. This also implies that the random spacing seen in GLAD films deposited onto bare substrates is not significantly detrimental to achieving uniform mechanical properties.

3.6.2 Nanoindentation

Nanoindentation is a surface characterization technique developed in 1992 for measuring the elastic modulus (E) and hardness (H) of a material, although in this study we are concerned only with the elastic modulus as it is expected to undergo the largest change as a result of nanostructuring of the material. The elastic modulus of a material was discussed and defined in Section 3.6.1. The hardness of a material is a measure of how much it resists plastic deformation [47].

Nanoindentation is particularly relevant for thin films, which can exhibit anisotropic mechanical properties, and are not easily removed from the substrate for characterization using conventional measurement techniques. In the nanoindentation technique a tip of known geometry (particularly area) is pushed into the film with known force. A piezoelectric feedback system monitors the displacement of the tip as a function of force, generating a curve of load vs. displacement which can be analyzed to determine the elastic modulus and hardness of the material. This concept is illustrated in Figure 3.12:

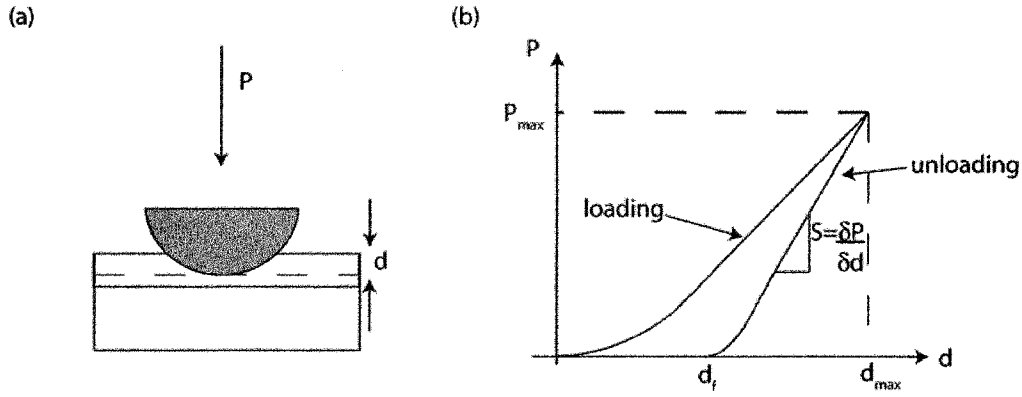

Figure 3.12 Nanoindentation. A tip of known geometry is pressed into a thin film with known force, and its displacement into the sample is monitored using feedback (a). The modulus and hardness of the sample can be calculated from the resulting pressure (P) vs. displacement (d) curve (b).

When the tip is pressed into the sample, the film undergoes a deformation which is partially plastic and partially elastic. For this reason the elastic modulus of the material is calculated from the unloading curve, which is assumed to be entirely elastic. The modulus can be deduced from the slope of the unloading curve (S_u) using Equation 3.25, provided that the area of the tip (A_{tip}) is known:

$$E = \frac{\sqrt{\pi}}{2}\frac{S_u}{\sqrt{A_{tip}}} \qquad [3.25]$$

Despite the simplicity of this formula, there are a number of challenges associated with this technique. The modulus determined from this formula actually reflects the combined modulus of the nanoindenter and the sample, and is therefore typically slightly lower than

actual. This error can be corrected for. Another of the difficulties associated with this technique is in accurately determining the area of interaction between the tip and the film, particularly as a function of contact depth. Sometimes during the nanoindentation process material is displaced from underneath of the indenter, forming a ring of material around the tip itself. This excess material can lead to a discrepancy between the expected and actual contact area, yielding a smaller than actual modulus. For extremely thin films (microns in thickness or less), the response measured by the indenter can also include a contribution from the substrate. Indentation of a sample is typically performed over a range of indentation depths to pinpoint the effect of the substrate, allowing affected data to be excluded. A general rule of thumb is that the indentation depth should be limited to less than one tenth of the film thickness to avoid 'feeling' the effect of the substrate. Nanoindentation is a powerful characterization tool provided that all of these challenges are understood.

To confirm the accuracy of the model, the elastic modulus of nickel perforated thin films were tested using nanoindentation (Hysitron Triboindenter, tested at the Hysitron Laboratory, Minneapolis). A Berkovich indenter tip was selected for testing. This tip is somewhat like a pyramid, and is formed by the meeting of three faces at a point. Each face has an angle of 142.3° at the point, causing the overall profile of the tip to be quite flat. A drawing of such a tip is shown in Figure 3.13:

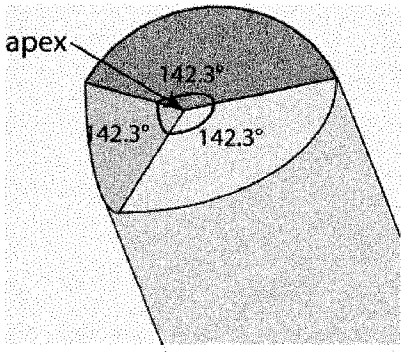

Figure 3.13 Berkovich Tip.

The Berkovich tip is a classic tip in nanoindentation, and is used for high modulus thin films with thicknesses greater than around 200nm [51]. The low radius of curvature of

the tip itself makes it relatively easy to accurately determine the area of contact between the tip and the substrate at a given indentation depth.

Nanoindentation was performed on two samples: a perforated thin film described below and a solid sample of nickel 1400 nm in thickness that was deposited from the same electroplating solution. Nanoindentation was performed at a variety of depths to verify that the values measured were not representative of the combined modulus of the film of the substrate. Ultimately, by comparing the modulus measured at different depths, an indentation depth of 25 nm was deemed to be acceptable to avoid measuring an effect from the substrate itself. For each sample the film was loaded to a depth of 25 nm, held for 2 s, and unloaded. The stiffness was then determined by fitting the power law to the curve (for values between 15% and 85% of the maximum pressure). The power law is described in Equation 3.26:

$$P = c(d - d_f)^m \qquad [3.26]$$

In this equation P is the applied pressure (for which the area function of the tip must be known), d is the contact depth, d_f is the final contact depth (as shown in Figure 3.12) and c and m are fitting coefficients. The slope of this equation (S_u) can then be calculated at an indentation depth (d), and, knowing the corresponding contact area (A), the modulus can be calculated using Equation 3.25.

The perforated thin film used for testing was prepared using the technique outlined in Section 3.4, with a few modifications. Rather than electrodepositing nickel past the top of the GLAD film, etching back this layer, and then removing the GLAD structures, the film was only partially filled by electroplating, which enabled the GLAD structures to be removed directly without etching back the nickel. In addition a NiCr layer deposited onto the substrate was used as the electrode rather than just Cr, allowing significantly better uniformity to be achieved.

SEM images of the nickel perforated thin film are shown in Figure 3.14:

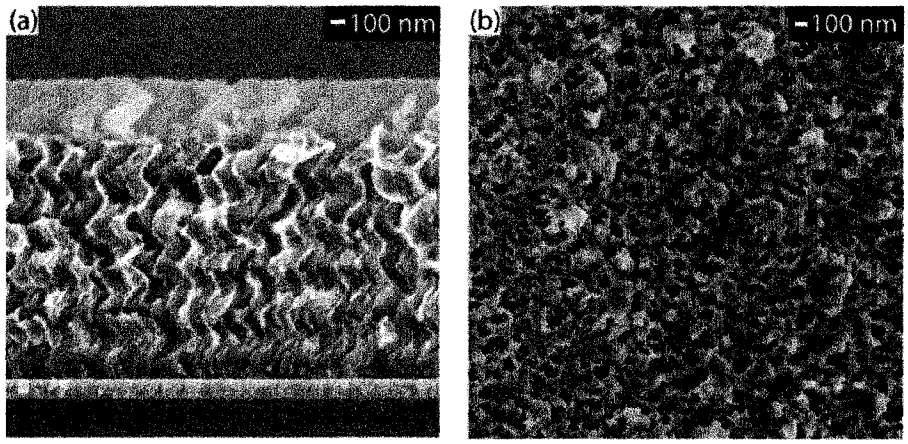

Figure 3.14 Nickel PTFs for nanoindentation. During fabrication, the film is plated only part of the way through (a), allowing the GLAD template to be easily removed. The final porous Ni film is shown from the top (b).

From a visual inspection of the images in Figure 3.14, the parameters of the film can be estimated. The average thickness was determined to be 700 nm, the column spacing was determined to be 220 nm, the helical radius was estimated to be 55 nm, the cross-section radius was estimated to be 50 nm, and the rise angle was measured to be 43°. For these values the model predicted the elastic modulus of the material to be 170 ± 10 GPa (based on a bulk modulus of 210 GPa). The actual modulus of the sample was determined using nanoindentation, and was found to be 154 GPa, which is in good agreement with the model (differing by only 10%).

The modulus of the solid thin film (1400 nm thick) was also measured using nanoindentation and was found to be slightly lower than the modulus of bulk Ni. This reduction may result from size-confinement effects placed on the material by the thickness of the film, or possibly from the way in which the film was prepared (electrodeposition).

Overall it was found that finite element modeling could be used to predict the behavior of macroporous thin films, and that the elastic modulus of these films could be manipulated by changing the architecture of the pores themselves.

3.7 Conclusion

In this chapter a technique for fabricating porous thin films with highly controllable pore architectures has been presented. Two templating methods have been developed: one based on melt-processing, and the second based on electroplating. Finite element modeling was used to investigate the mechanical properties of thin films with helical pores, and it was found that the modulus of a material could be tuned between $0.65E_{bulk}$ and $\sim 0.90E_{bulk}$ by varying the rise angle of the helix from 40° to 70°. The validity of the model was verified by testing a nickel film with helical pores with a rise angle of 43°. The ability to manufacture perforated thin films from a variety of materials expands the number of materials available in the GLAD 'toolbox', and it is anticipated that these films could be useful in a variety of applications in which GLAD is already being explored, such as optics and sensors. One further application for these types of films will be explored in Chapter 4, which is as an intermediate template for the fabrication of polymer helices.

3.8 References

1. Elias, A.L., Harris, K.D. and Brett, M.J., *Fabrication of helically perforated gold, nickel, and polystyrene thin films.* Journal of Microelectromechanical Systems, 2004. **13**(5): p. 808-813.
2. Fernando, S.P., Elias, A.L. and Brett, M.J., *Mechanical properties of helically perforated thin films.* Journal of Materials Research, 2006. **21**(5): p. 1101-1105.
3. Foll, H., Langa, S., Carstensen, J., Christophersen, M. and Tiginyanu, I.M., *Pores in III-V semiconductors.* Advanced Materials, 2003. **15**(3): p. 183-198.
4. Wehrspohn, R.B. and Schilling, J., *Electrochemically prepared pore arrays for photonic-crystal applications.* Mrs Bulletin, 2001. **26**(8): p. 623-626.
5. Chazalviel, J.N., Wehrspohn, R.B. and Ozanam, F., *Electrochemical preparation of porous semiconductors: from phenomenology to understanding.* Materials Science and Engineering B-Solid State Materials for Advanced Technology, 2000. **69**: p. 1-10.
6. Li, A.P., Muller, F., Birner, A., Nielsch, K. and Gosele, U., *Hexagonal pore arrays with a 50-420 nm interpore distance formed by self-organization in anodic alumina.* Journal of Applied Physics, 1998. **84**(11): p. 6023-6026.
7. Masuda, H., Asoh, H., Watanabe, M., Nishio, K., Nakao, M. and Tamamura, T., *Square and triangular nanohole array architectures in anodic alumina.* Advanced Materials, 2001. **13**(3): p. 189-192.

8. Campbell, M., Sharp, D.N., Harrison, M.T., Denning, R.G. and Turberfield, A.J., *Fabrication of photonic crystals for the visible spectrum by holographic lithography.* Nature, 2000. **404**(6773): p. 53-56.
9. Deubel, M., Von Freymann, G., Wegener, M., Pereira, S., Busch, K. and Soukoulis, C.M., *Direct laser writing of three-dimensional photonic-crystal templates for telecommunications.* Nature Materials, 2004. **3**(7): p. 444-447.
10. Pham, T.A., Kim, D.P., Lim, T.W., Park, S.H., Yang, D.Y. and Lee, K.S., *Three-Dimensional SiCN Ceramic Microstructures via Nano-Stereolithography of Inorganic Polymer Photoresists.* Advanced Functional Materials, 2006. **16**(9): p. 1235-1241.
11. Yang, D., Qi, L.M. and Ma, J.M., *Hierarchically ordered networks comprising crystalline ZrO2 tubes through sol-gel mineralization of eggshell membranes.* Journal of Materials Chemistry, 2003. **13**(5): p. 1119-1123.
12. Holland, B.T., Blanford, C.F. and Stein, A., *Synthesis of macroporous minerals with highly ordered three-dimensional arrays of spheroidal voids.* Science, 1998. **281**(5376): p. 538-540.
13. Arsenault, A.C., Clark, T.J., Von Freymann, G., Cademartiri, L., Sapienza, R., Bertolotti, J., Vekris, E., Wong, S., Kitaev, V., Manners, I., Wang, R.Z., John, S., Wiersma, D., and Ozin, G.A., *From colour fingerprinting to the control of photoluminescence in elastic photonic crystals.* Nature Materials, 2006. **5**(3): p. 179-184.
14. Wang, Z.Y., Ergang, N.S., Al-Daous, M.A. and Stein, A., *Synthesis and characterization of three-dimensionally ordered macroporous carbon/titania nanoparticle composites.* Chemistry of Materials, 2005. **17**(26): p. 6805-6813.
15. Blanco, A., Chomski, E., Grabtchak, S., Ibisate, M., John, S., Leonard, S.W., Lopez, C., Meseguer, F., Miguez, H., Mondia, J.P., Ozin, G.A., Toader, O., and van Driel, H.M., *Large-scale synthesis of a silicon photonic crystal with a complete three-dimensional bandgap near 1.5 micrometres.* Nature, 2000. **405**(6785): p. 437-440.
16. Fu, M., Zhou, J., Xiao, Q.F., Li, B., Zong, R.L., Chen, W. and Zhang, J., *ZnO nanosheets with ordered pore periodicity via colloidal crystal template assisted electrochemical deposition.* Advanced Materials, 2006. **18**(8): p. 1001-1004.
17. Harris, K.D., McBride, J.R., Nietering, K.E. and Brett, M.J., *Fabrication of porous platinum thin films for hydrocarbon sensor applications.* Sensors and Materials, 2001. **13**(4): p. 225-234.
18. Kiema, G.K. and Brett, M.J., *Effect of thermal annealing on structural properties and electrochemical performance of carbon films with porous microstructure.* Journal of the Electrochemical Society, 2004. **151**(5): p. E194-E198.
19. Toader, O. and John, S., *Proposed square spiral microfabrication architecture for large three-dimensional photonic band gap crystals.* Science, 2001. **292**(5519): p. 1133-1135.
20. Harris, K.D., Sit, J.C. and Brett, M.J., *Fabrication and optical characterization of template-constructed thin films with chiral nanostructure.* IEEE Transactions on Nanotechnology, 2002. **1**(3): p. 122-128.
21. van Popta, A.C., Sit, J.C. and Brett, M.J., *Optical properties of porous helical thin films.* Applied Optics, 2004. **43**(18): p. 3632-3639.

22. Hodgkinson, I., Wu, Q.H., Knight, B., Lakhtakia, A. and Robbie, K., *Vacuum deposition of chiral sculptured thin films with high optical activity.* Applied Optics, 2000. **39**(4): p. 642-649.
23. Harris, K.D., Westra, K.L. and Brett, M.J., *Fabrication of perforated thin films with helical and chevron pore shapes.* Electrochemical and Solid State Letters, 2001. **4**(6): p. C39-C42.
24. Tsoi, S., Fok, E., Sit, J.C. and Veinot, J.G.C., *Superhydrophobic, high surface area, 3-D SiO2 nanostructures through siloxane-based surface functionalization.* Langmuir, 2004. **20**(24): p. 10771-10774.
25. Steinhart, M., Wendorff, J.H., Greiner, A., Wehrspohn, R.B., Nielsch, K., Schilling, J., Choi, J. and Gosele, U., *Polymer nanotubes by wetting of ordered porous templates.* Science, 2002. **296**(5575): p. 1997-1997.
26. Schlesinger, M. and Paunovic, M., *Modern Electroplating*. 2002, Toronto: Wiley Interscience.
27. Reid, J., *Copper electrodeposition: Principles and recent progress.* Japanese Journal of Applied Physics Part 1-Regular Papers Short Notes & Review Papers, 2001. **40**(4B): p. 2650-2657.
28. Romankiw, L.T., *A path: From electroplating through lithographic masks in electronics to LIGA in MEMS.* Electrochimica Acta, 1997. **42**(20-22): p. 2985-3005.
29. O'Sullivan, E.J., Cooper, E.I., Romankiw, L.T., Kwietniak, K.T., Trouilloud, P.L., Horkans, J., Jahnes, C.V., Babich, I.V., Krongelb, S., Hegde, S.G., Tornello, J.A., LaBianca, N.C., Cotte, J.M., and Chainer, T.J., *Integrated, variable-reluctance magnetic minimotor.* Ibm Journal of Research and Development, 1998. **42**(5): p. 681-694.
30. Nielsch, K., Wehrspohn, R.B., Barthel, J., Kirschner, J., Fischer, S.F., Kronmuller, H., Schweinbock, T., Weiss, D. and Gosele, U., *High density hexagonal nickel nanowire array.* Journal of Magnetism and Magnetic Materials, 2002. **249**(1-2): p. 234-240.
31. Deligianni, H. and Romankiw, L.T., *Insitu Surface pH Measurement During Electrolysis Using a Rotating pH Electrode.* IBM Journal of Research and Development, 1993. **37**(2): p. 85-95.
32. Gad-el-Hak, M., *The MEMS handbook.* The Mechanical engineering handbook series. 2002, Boca Raton, FL: CRC Press.
33. Frazier, A.B. and Allen, M.G., *Metallic microstructures fabricated using photosensitive polyimide electroplating.* Journal al Microelectromechanical Systems, 1993. **2**(2): p. 87-94.
34. Kelly, J.J., Goods, S.H., Talin, A.A. and Hachman, J.T., *Electrodeposition of Ni from low-temperature sulfamate electrolytes I. Electrochemistry and film stress.* Journal of the Electrochemical Society, 2006. **153**(5): p. C318-C324.
35. Campbell, S.A., *The Science and Engineering of Microelectronic Fabrication.* 2nd ed. 2001, New York: Oxford University Press.
36. Williams, K.R., Gupta, K. and Wasilik, M., *Etch rates for micromachining processing - Part II.* Journal of Microelectromechanical Systems, 2003. **12**(6): p. 761-778.
37. *Personal Communication* Westra, K., 2006

38. Lukic, B., Seo, J.W., Bacsa, R.R., Delpeux, S., Beguin, F., Bister, G., Fonseca, A., Nagy, J.B., Kis, A., Jeney, S., Kulik, A.J., and Forro, L., *Catalytically grown carbon nanotubes of small diameter have a high Young's modulus.* Nano Letters, 2005. **5**(10): p. 2074-2077.
39. Seto, M.W., Dick, B. and Brett, M.J., *Microsprings and microcantilevers: studies of mechanical response.* Journal of Micromechanics and Microengineering, 2001. **11**(5): p. 582-588.
40. Sundararajan, S. and Bhushan, B., *Development of AFM-based techniques to measure mechanical properties of nanoscale structures.* Sensors and Actuators a-Physical, 2002. **101**(3): p. 338-351.
41. Arzt, E., *Overview no. 130 - Size effects in materials due to microstructural and dimensional constraints: A comparative review.* Acta Materialia, 1998. **46**(16): p. 5611-5626.
42. Shan, Z.W., Stach, E.A., Wiezorek, J.M.K., Knapp, J.A., Follstaedt, D.M. and Mao, S.X., *Grain boundary-mediated plasticity in nanocrystalline nickel.* Science, 2004. **305**(5684): p. 654-657.
43. Seto, M.W., Robbie, K., Vick, D., Brett, M.J. and Kuhn, L., *Mechanical response of thin films with helical microstructures.* Journal of Vacuum Science & Technology B, 1999. **17**(5): p. 2172-2177.
44. Young, W.C., Budynas, R.G., Roark, R.J. and Knovel (Firm), *Roark's formulas for stress and strain.* 7th ed. 2002, New York: McGraw-Hill, pp 398.
45. Moaveni, S., *Finite Element Analysis: Theory and Application with ANSYS.* 2nd ed. 2003, Upper Saddle River, NJ: Pearson Education Inc.
46. Buchanan, G.R., *Schaum's Outline of Theory and Problems of Finite Element Analysis.* 1995, New York: McGraw-Hill.
47. Callister, W.D.J., *Materials Science and Engineering, An Introduction.* 5th ed. 2000, New York: John Wiley & Sons.
48. Callister, W.D.J., *Materials Science and Engineering, An Introduction.* 3rd ed. 1994, New York: John Wiley & Sons.
49. Tait, R.N., Smy, T. and Brett, M.J., *Modeling and characterization of columnar growth in evaporated films.* Thin Solid Films, 1993. **226**(2): p. 196-201.
50. Robbie, K., Sit, J.C. and Brett, M.J., *Advanced techniques for glancing angle deposition.* Journal of Vacuum Science and Technology B, 1998. **16**(3): p. 1115-1122.
51. Tsui, T.Y., Ross, C.A. and Pharr, G.M., *A method for making substrate-independent hardness measurements of soft metallic films on hard substrates by nanoindentation.* Journal of Materials Research, 2003. **18**(6): p. 1383-1391.

4 Template-Based Fabrication: Double-Templating

In this chapter, a double-templating method which can be used to fabricate polymer helices is presented. The results of this study were published in the Journal of Micromechanics and Microengineering [1].

4.1 Polymer Helices

As discussed in Section 2.5, some materials cannot be deposited directly as porous thin films using glancing angle deposition. This group of materials includes high molecular weight polymers, which consist of long strands of repeating units, and crosslinked polymer networks. These materials cannot be evaporated, as they do not exist in a vapor phase [2]. Energy supplied to polymers tends to cause chain scission rather than a change of phase. Nonetheless, GLAD-like helices could be useful in a variety of applications. One suggested use of polymer GLAD-like helices is in mechanical devices such as actuators, valves, resonant filters, and transducers, since polymers are generally much less stiff than the inorganic materials from which films can be deposited directly using glancing angle deposition [3]. In addition, the mechanical properties of polymers can be easily tuned by blending materials with different characteristics. Another possible application of GLAD-like polymer helices is as sensor devices. The advantages of the high-surface area of GLAD films for sensor devices have already been mentioned in section 2.6. An additional useful characteristic of polymers is chemical tunability: polymers can be designed with different functional groups that enables them to specifically adsorb different target vapors [4]. As polymers posses highly tunable chemical properties, the ability to engineer high-surface area GLAD-like polymer structures could be very useful towards making sensors designed to interact with specific molecules or vapors. High-surface area polymers are also of interest in a variety of bio-applications, due to biocompatibility and functionalizability [5]. In these systems, increased surface area could result in enhanced sensitivity.

There are a few techniques described in the literature which can be used to manufacture polymer helices with submicron dimensions. For example, two-photon lithography has been used to make a single oscillating helical microspring and ball [6]. In this direct

write process, the focal spot of a UV laser is moved through a photosensitive sample, selectively polymerizing the illuminated area [7]. Individual structures are written one at a time, which can be time consuming. Multiple beam interference holography has also been used to make GLAD-like helical structures, by interfering 6 beams in a photosensitive material. This work was first published in September 2005, after the publication of the work described in this chapter in January of the same year [8]. While theoretically it might be possible to ramp up interference holography to large areas, the work presently described in the literature is greatly limited in terms of uniformity even over a few microns of the substrate. In addition, the helical structures are visibly connected to each other by excess material, limiting their freedom of motion. Fabrication of parylene-c polymer helices was demonstrated in August 2005 using a chemical vapor deposition process [9]. In this technique, the reactive components in a pyrolysis process were sprayed out of a nozzle onto a substrate held at an oblique angle of 80°. These helices had limited uniformity in the direction perpendicular to the substrate, evolving from a very fibrous structure to a more solid one.

In this chapter, a double-templating process for fabricating polymer helices is described using 5 different polymers. This was the first technique presented in the literature for large-area fabrication of multiple helices with submicron dimensions. In this process single-templated photoresist perforated thin films (described in Chapter 3) are used as intermediate templates for the production of polymer helices, which are made from different types of acrylates. These acrylates have elastic moduli which are two orders of magnitude lower than any of materials which had been deposited directly using the GLAD technique at the time that this work was undertaken. Since the time that this work was completed, it was also shown that Alq_3, a small molecule organic material, could be deposited directly by glancing angle deposition. This material has a bulk modulus of approximately 8 GPa, as measured using nanoindentation. However, Alq_3 dissolves in some organic solvents (such as chloroform) and the morphology of nanostructured Alq_3 thin films degrades irreversibly upon heating. Therefore polymer-GLAD structures would still be preferable to Alq_3 in a variety of mechanical applications.

4.2 Polymers

In this section an introduction to polymers will be given, with a focus on polyacrylates, as this is the type of material used to make the helices described in section 4.3. A polymer is a large molecule comprised of covalently bonded repeating units. Some polymers are naturally occurring, such as rubber and starch, while others are synthesized in the lab. The composition of a polymer is determined by the monomers (repeating units) from which it is produced. A polymer with an extremely simple structure is polyethylene. The monomer for this polymer contains only 6 atoms: 4 hydrogens and 2 carbons. The monomer and polymer are shown in Figure 4.1:

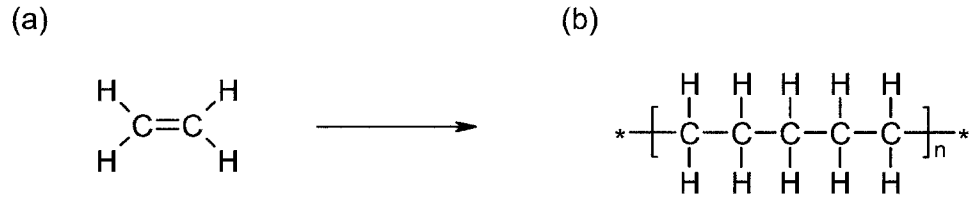

Figure 4.1: Ethylene and polyethylene. The monomer (a) and polymer (b) molecules are shown.

Polyethylene is a vinyl polymer, which strictly speaking means that the monomer contains the vinyl group CH_2=CH-. Many other polymers have this basic structure, where the H atoms are replaced by other molecules or groups. For example if all of the hydrogen atoms are replaced by fluorine atoms the end result is polytetrafluoroethylene (otherwise known as Teflon). In practice, most polymers made from monomers with carbon-carbon double bonds which are converted to single bonds in the polymerization process are referred to as vinyl polymers [10].

The polymer helices described in this chapter are made from different types of acrylates. Acrylate monomers are a type of vinyl monomers containing the group CH_2=CHCOOR. Methacrylates contain the group CH_2=C(CH_3)COOR (where R can be another molecule or group). A famous type of acrylate is methyl methacrylate (MMA), which is shown in Figure 4.2:

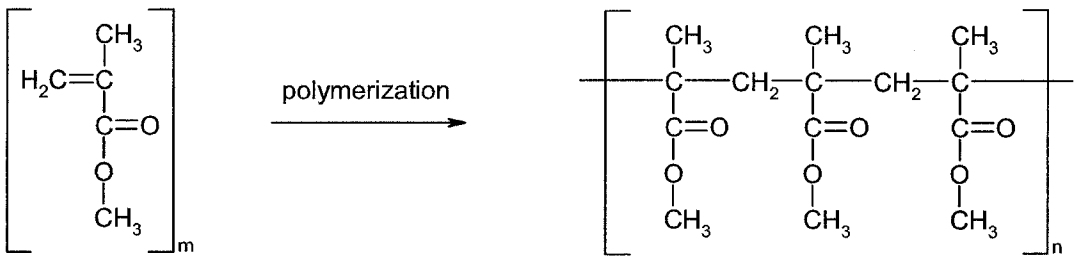

Figure 4.2: Methyl methacrylate monomer and polymer. The monomer unit contains a carbon-carbon double bond, which is broken during polymerization.

Poly(methyl methacrylate) (PMMA) is an amorphous polymer which is glassy at room temperature, having a modulus of approximately 1 to 3 GPa. This high modulus is partly due to the limited mobility of the chains due to the presence of the methyl group (CH_3) at the top of the molecule, as shown in Figure 4.2. If this methyl group is not present (as in poly(methylacrylate) {PMA}) the chains can move much more easily, and the resulting material is soft and rubbery rather than hard and glassy at room temperature.

The mechanical properties of a polymer are also dependent on how heavily the polymer is crosslinked. PMMA is a linear polymer, and adjacent strands are not covalently bonded together (i.e., they are not chemically crosslinked). Monomers with multiple reactive groups can be polymerized to form heavily crosslinked networks. In other circumstances monoacrylates (which have one carbon-carbon double bond) can be combined with diacrylates (which have two carbon-carbon double bonds) to form crosslinked polymers, where the exact material properties is dependent on the ratio of mono:diacrylate monomers. This topic will be discussed in further detail in Chapter 6.

A common method of polymerizing vinyl monomers is by free-radical polymerization [11]. In this method, free-radicals are created from an initiator (in our case a photo-initiator, which will be discussed in more depth in Section 4.3). The free radicals from the initiator 'attack' the carbon-carbon double bond, bonding with one of the carbon atoms via the second electron in the double bond. This leaves the other carbon atom electron deficient, which causes it to 'attack' another double bond. This reaction

propagates until two chains meet up and all atoms are satisfied (chain termination), or until vitrification (transition to a glassy state) occurs and the chains possess insufficient mobility for the reaction to continue [12]. In the latter case, free-radicals are trapped in the system. Vitrification can be overcome by heating to increase the mobility of the chains, thereby increasing the extent of polymerization [13].

4.3 UV Initiators

As mentioned above, photoinitiators can be used to begin polymerization reactions. These molecules decompose when illuminated with ultraviolet (UV) light, creating highly reactive radicals which can then attack monomers. One such initiator, 1-hydroxy-cyclohexyl-phenyl-ketone (Irgacure 184, CIBA [14]), is shown in Figure 4.3:

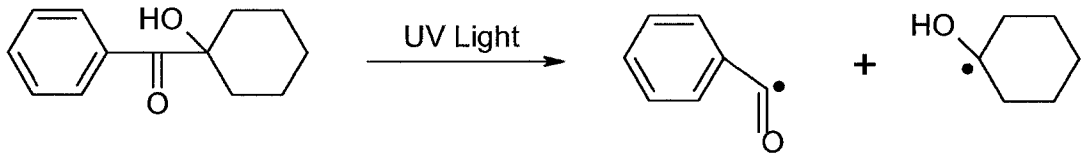

Figure 4.3: 184 Initiator. When this photoinitiator is irradiated with light at an appropriate wavelength, it decomposes, producing free radicals.

This molecule is used throughout this thesis, and absorbs strongly at wavelengths below 380 nm. To polymerize a sample, Irgacure 184 is mixed with monomers at a small concentration (1% to 2%). To promote mixing, monomers and initiator are dissolved in a solvent (such as dichloromethane) which is subsequently removed by evaporation. The mixture can then be polymerized in UV light.

Various light sources have been employed throughout this work to initiate polymerization reactions. These include a homebuilt UV lamp in shutter casing with Philips PL-S 10 bulb (9 W), a Philips solarium with 4 Philips Cleo 150 W bulbs, a mask aligner with mercury lamp, and an Oriel Instruments Arc Lamp with Ushio UXM502MD bulb. The intensities of these lamps are summarized in Table 4.1:

Lamp	Intensity
Hg lamp in mask aligner	20m W/cm^2 at 360 nm
Philips solarium	4m W/cm^2 over 360 nm – 370 nm, 2 cm from lamp
Home-built UV lamp	4m W/cm^2 over 360 nm – 370 nm, 8.5 cm from lamp
Oriel Instruments Arc Lamp with Ushio UXM502MD Hg(Xe) bulb [15]	175 mW/cm^2 at the housing, falls off rapidly 100m W/cm^2 at 2 cm

Table 4.1 Summary of lamps

Different lamps were used in different experiments, for a variety of reasons. Most of the samples described in this chapter were made using the home-built UV lamp, with the sample placed at a distance of approximately 8.5 cm from the bulb; or the Philips solarium, with the sample placed at a distance of approximately 2 cm from the bulb. The solarium was used mainly when an oxygen-free environment was not required, such as for curing the optical adhesive used to fabricate cells and for polymerizing samples in a cell configuration. The home-built lamp was used in combination with an enclosed chamber which could be flushed with nitrogen to polymerize open samples such as those on single substrates in an oxygen-free environment, for reasons which will be discussed in the next paragraph. Exposure times of 1 minute typically sufficed using these lamps, although frequently exposures of 5 minutes have been employed. The HgXe arc lamp was used when a more collimated light source was desired, as this lamp had a small light source that could be easily configured to be a large distance from the sample. This lamp could also be used with a 20 cm collimating tube.

An additional characteristic of free-radical initiators is that they must be used in an oxygen-free environment to prevent reactions with air. In the presence of air, radicals from both the initiator and the growing chains can scavenge oxygen, effectively quenching these radicals [16]. It is therefore necessary to limit the amount of oxygen present during polymerization. This can be achieved in three ways. The first way is to polymerize the monomer mixture in a cell (i.e., between two glass plates which are in good contact with the monomer). The oxygen present in the cell is quickly consumed, and additional oxygen is unable to permeate into the monomer mixture at a significant

rate. The second way is to polymerize the sample in a box into which a light flow of nitrogen is introduced. Both of these approaches are used in the work described in this thesis. Alternatively, the sample could be polymerized under vacuum.

4.4 Fabrication

Polymer helices can be fabricated using the double-templating process illustrated in Figure 4.4.

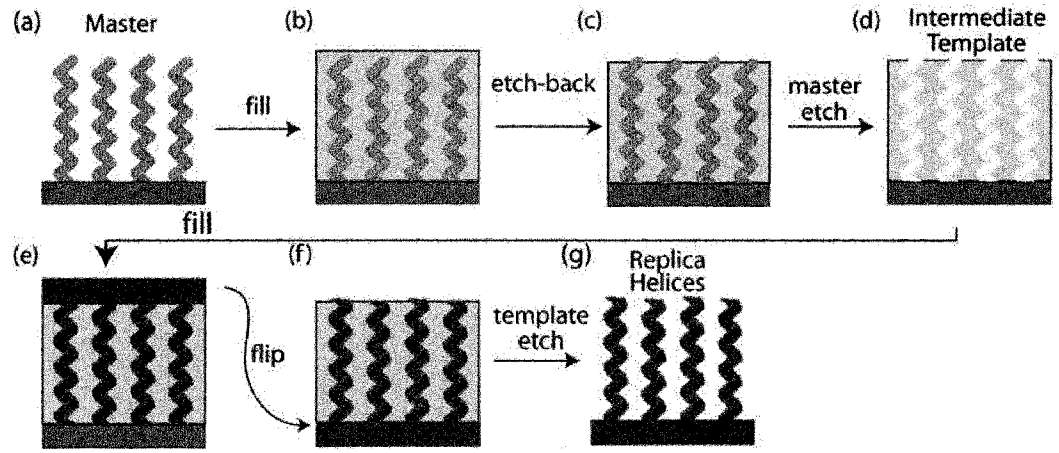

Figure 4.4: Fabrication of polymer helices using a double-templating process. A SiO_2 master film is deposited using glancing angle deposition (a). The master film is filled with photoresist by spin-coating (b). The top layer of photoresist is removed to allow a wet-etchant to access the master film (c). The master film is removed in a wet-etchant, leaving the porous, intermediate template (d). A mixture of monomer and initiator can then be filled into the intermediate template, and polymerized (e). Typically the monomer mixture over-fills the pores, and collects in a layer on top of the intermediate template. The polymer/photoresist layer can be removed from the substrate by immersing the sample in liquid nitrogen. The sample is flipped over, and the excess polymer becomes the substrate (f). Finally, the intermediate template is removed by washing the sample in a solvent such as ethanol, leaving polymer helices mounted on a polymer substrate (g).

In this process, a master film is deposited using glancing angle deposition, as described in Chapter 2 of this thesis. Excellent control over pitch, handedness, film thickness, and number of turns can be achieved using this process. For the work described in this chapter this master is usually deposited from SiO_2, which is easy to evaporate using the GLAD process and which can be selectively etched in buffered oxide etch. From this

master a photoresist intermediate template is produced, using the procedure described in Chapter 3. Photoresist was chosen as the material for most intermediate templates for a number of reasons. The first reason is that photoresist perforated thin films can easily be fabricated with high uniformity over large areas (entire 4 in. wafers can be successfully processed at a time). The second reason is that photoresist can be easily dissolved at the end of the process, to release the final polymer helices (as was shown in Figure 4.4 (g)). One limitation of using photoresist as the intermediate template is that it is miscible with most organic solvents, including acetone, isopropanol (IPA), ethanol, tetrahydrofuran, hexane, heptane, butyl acetate, and toluene. Therefore the monomer mixtures from which the helices themselves are polymerized cannot contain any solvents to modify their viscosity. In addition, some small molecule monomers can themselves diffuse into the photoresist, destroying the template. These monomers must therefore be avoided.

To avoid dissolving the photoresist template, monomers with relatively high molecular weights were employed. In specific the following 4 monomers were successfully incorporated into the fabrication process: (1) pentaerythritol triacrylate (Aldrich 24,679-4), (2) pentaerythritol tetraacrylate (Aldrich 40,826-3), (3) dipentaerythritol pentaacrylate (Polysciences Inc. 16311), and (4) dipentaerythritol pentaacrylate/hexaacrylate mixture (Aldrich 40,728-3). These large molecules cannot easily diffuse into a thin film of photoresist, and therefore do not dissolve the template. These molecules are shown in Figure 4.5 on the next page.

(a)

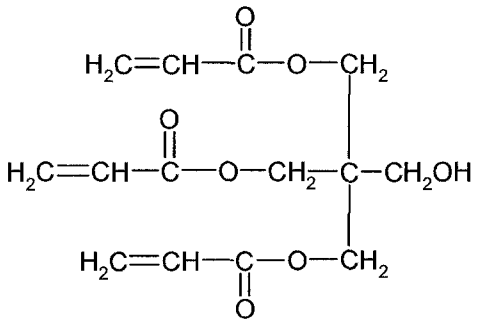

(b)

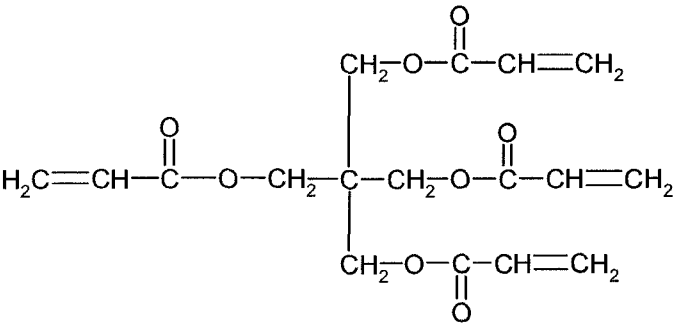

(c)

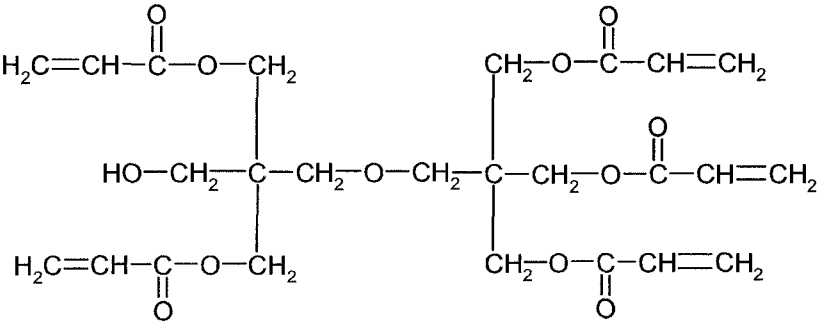

(d)

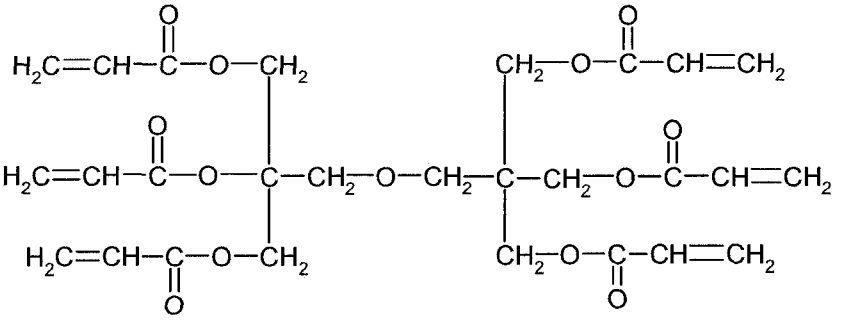

Figure 4.5: Multifunctional acrylates. Pentaerythritol triacrylate (a) has three reactive sites, pentaerythritol tetracrylate (b) has four, dipentaerythritol pentacrylate (c) has five, and dipentaerythritol hexacrylate (d) has six.

The elastic moduli of the 4 polyacrylates were measured in tension using dynamic mechanical analysis (DMA, Q800, TA Instruments). To do so, thin films of each polymer were prepared by polymerizing the monomer mixtures in glass cells, with a cell gap of approximately 100 μm (using the Philips solarium lamp). In these cells the thickness of the gap was regulated using 2 layers of tape as a spacer. After polymerization the cells were annealed to 100 °C, opened, and the films were removed. The films were then clamped into the DMA instrument using a thin film clamp, and the elastic modulus of each film was measured as a function of frequency.

Recall from Chapter 3 that the elastic modulus is the ratio between the applied stress (σ) and the strain (ε) in a material. This value can be determined from the applied force (F) and resulting amplitude of motion (Δl), provided that the cross-sectional area of the sample (A) and the length of the sample (l) are known. These relationships are given in Equation 4.1:

$$E = \frac{\sigma}{\varepsilon} = \frac{F/A}{l/\Delta l} \qquad [4.1]$$

The results of the DMTA measurements on the 4 acrylates are shown in Figure 4.6:

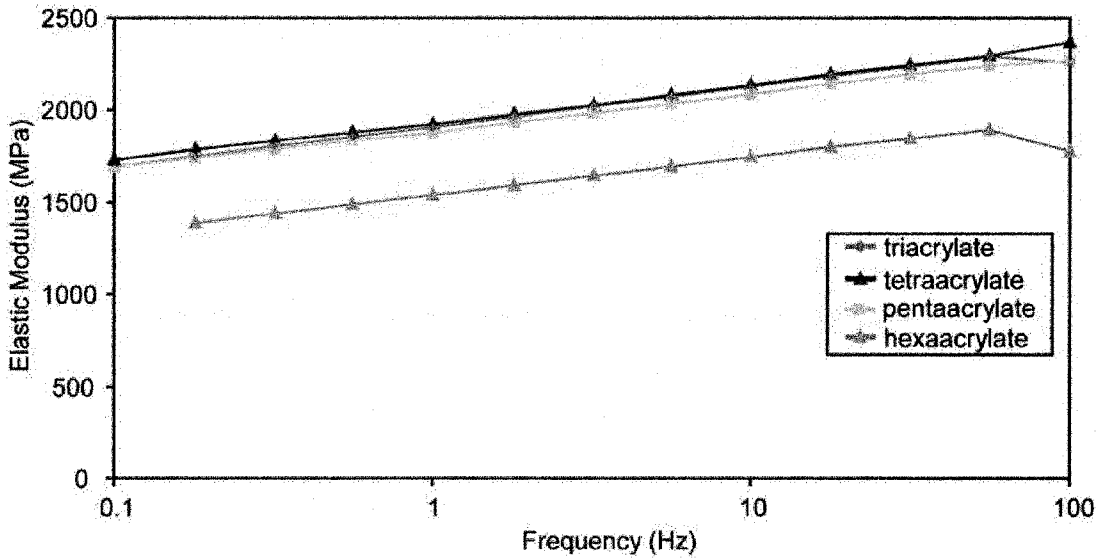

Figure 4.6: Elastic modulus of acrylate polymers as a function of frequency.

As can be seen from Figure 4.6, the behavior of these materials is frequency dependent, as for most polymers. This is due to the fact that polymers are viscoelastic, which means that these materials behave partly as elastic solids and partly as viscous fluid [17]. Viscous behavior is exemplified when an applied stress results in a time-dependent deformation. As the name suggests, viscous deformations are characterized by a 'flow' of the molecules within the material. The changes in shape of the material that occur within the viscous regime are non-recoverable. When a stress is applied to a polymer, its response can be partly viscous and partly elastic. One factor that determines how the material will behave is the rate at which the stress is applied. When the stress occurs rapidly, the molecules in the material do not have time to re-arrange and flow. The response is therefore elastic, which is instantaneous. When the stress is applied more gradually the material has more time to undergo a viscous response. This is why the elastic modulus increases with frequency. In dynamic mechanical analysis, a periodic force is applied to the material. When the material is stretched, the elastic modulus can be considered a measure of how much of the energy expended in pulling on the material can be recovered as the material returns to its original shape. At lower frequencies, more of the stress is expended on the viscous response, and less of a reversible, elastic deformation occurs. This results in a lower apparent elastic modulus. At higher frequencies, more of the energy is stored in the elastic deformation. The material therefore exhibits a higher elastic modulus.

The viscoelastic properties of a material are also strongly temperature dependent: at relatively low temperatures a polymer will exhibit very elastic behavior; at relatively high temperatures a polymer will exhibit very viscous behavior; and at intermediate temperatures a polymer can respond to a stress with a combination of viscous and elastic behavior. The temperature at which a material undergoes a transition from a glassy to rubbery state is called the glass transition temperature (T_g). The data presented in Figure 4.6 was collected at room temperature, which is generally within the glassy state of these materials [18]. Therefore, overall it is expected that their behavior is much more elastic than viscous.

Figure 4.6 indicates that the elastic moduli of these highly crosslinked, glassy polymers are all quite similar, although the modulus of the hexacrylate was unexpectedly and consistently around 400 MPa lower than the other polymers. Recall that the hexacrylate is actually a blend of dipentaerythritol penta- and hexaacrylate. It was very unexpected that this sample should have a lower modulus than the others, if anything the modulus is expected to be higher due to additional crosslinking. The measured value may be due to be a systematic error in the measurement itself, possibly resulting from the use of an incorrect sample geometry. These results are consistent with nanoindentation results found in the literature: the modulus of a 3000 nm thick pentacrylate thin film was found to be 4.86 ± 0.32 GPa [19]. Overall the moduli of these materials are approximately an order of magnitude lower than the materials from which GLAD could previously be deposited directly.

To make polymer helices, a photoresist perforated thin film made using single-templating was employed as a template itself. First the monomer was combined with a UV initiator such as Irgacure 184 (which was shown in Figure 4.3), forming a highly viscous liquid, which could be introduced into the template using vacuum filling. This mixture was then placed in a glass bell jar along with a piece of the intermediate template, and the chamber was evacuated to approximately 1200 Pa. The intermediate template was dipped into the monomer mixture, and allowed to sit until most of the trapped air was released (i.e., allowed to sit until bubbles of air stopped forming in the mixture). The chamber was then slowly vented to atmospheric pressure over 2-3 minutes, during which time the mixture was forced into the pores. Note that an excess layer of monomer mixture also remained on top of the intermediate template. The sample could then be transferred to a box into which a light flow of nitrogen was introduced. The monomer mixture was polymerized in this nitrogen flow by irradiation with UV light (365 nm) for 5 minutes. During polymerization the samples were sometimes heated to 100 °C in order to overcome vitrification effects and promote conversion of the monomers [20].

Fourier transform infrared spectroscopy (FTIR) could be used to qualitatively determine the extent to which a sample was polymerized (i.e., the extent to which the C=C double

bonds were converted to single bonds as the monomers were incorporated into a polymer chain or network). FTIR is a common technique for identifying organic materials, which was first introduced in the 1940s. In this technique, a sample is irradiated with infrared light, which causes vibrational and rotational excitation of the bonds of chemical groups within the molecules, as well as interactions between molecules [21]. The wavelength at which the incident radiation is absorbed is indicative of the specific types of bonds present. In this characterization technique, the transmission of a beam of infrared radiation through a sample is measured in order to determine the wavelength of radiation that has been absorbed. Rather than measuring at each wavelength or frequency, a beam containing many frequencies is employed, and the spectrum is generated from the Fourier transform of the transmitted signal.

To evaluate the fabrication technique used in this chapter and characterize the conversion of the samples, the absorbance spectra of a polymerized and an un-polymerized sample are compared. These spectra provide information about the chemical structure of the material. The spectra for a thin, spin-coated film of dipentaerythritol pentacrylate (without initiator) and for a sample polymerized for 5 minutes and heat treated to 55° C are shown in Figure 4.7. These spectra were collected using a BioRad FTS 6000 spectrometer. The samples analyzed were spin-coated from dilute solutions onto ZnSe windows, which are transparent in the IR.

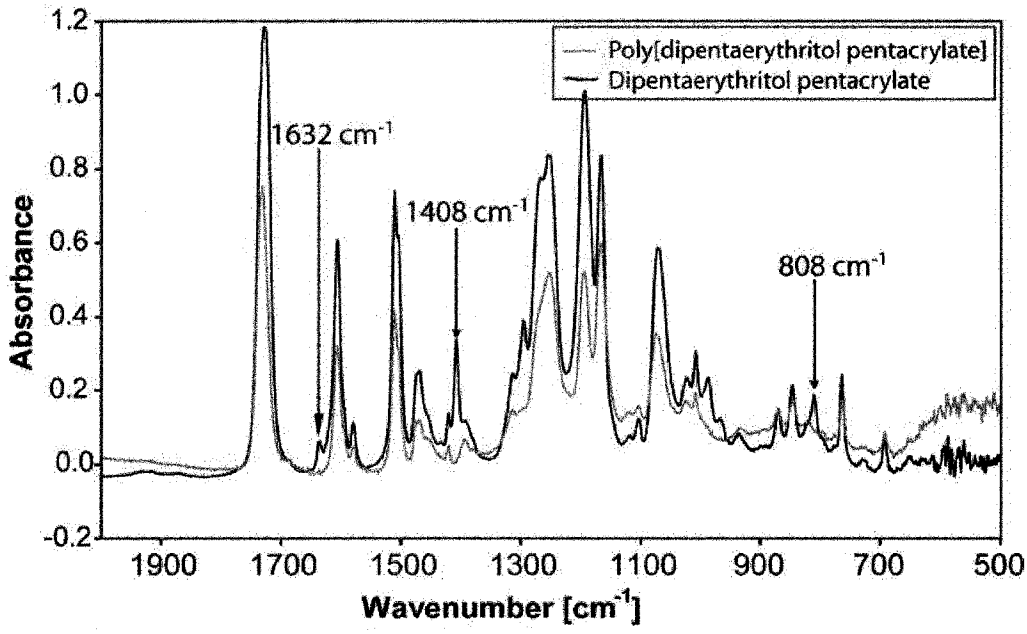

Figure 4.7: FTIR. This graph shows the FTIR spectra of dipentaerythritol pentacrylate monomer (dark line) and poly[dipentaerythritol pentacrylate] (light line). The CH_2=CH absorbance peak at 1408 cm^{-1} present in the monomer is not found in the polymerized sample.

The degree of polymerization can be gauged by observing the vinyl absorption bands in the infrared spectrum of the material before and after polymerization. These bands are located at 1632 cm^{-1} [22], 1408 cm^{-1} [23], and 808 cm^{-1} [19, 24], and are present in the monomer mixture, but not in the polymerized film. Therefore we can conclude that most of the monomer molecules have undergone polymerization.

After polymerization, the polymer helices could be released from the intermediate template using one of two techniques. The first method was simply to soak the sample in acetone for a few hours in order to dissolve the intermediate template. This process was quite slow as most of the photoresist was shielded from the acetone by the thick layer of excess polymer on the top of the sample. As the intermediate template dissolved, the polymer helices also detached from the silicon substrate, leaving a free-standing film of polymer helices anchored on a layer of polymer. The second technique is to release the composite layer from the silicon substrate by immersing the sample in liquid nitrogen, which induces a large in-plane stress between the substrate and thin films owing to the difference in thermal expansion coefficients. The photoresist can then be quickly etched

in an organic solvent or photoresist developer, again leaving polymer helices on a polymer substrate. SEM images of polymer helices are shown in Figure 4.8:

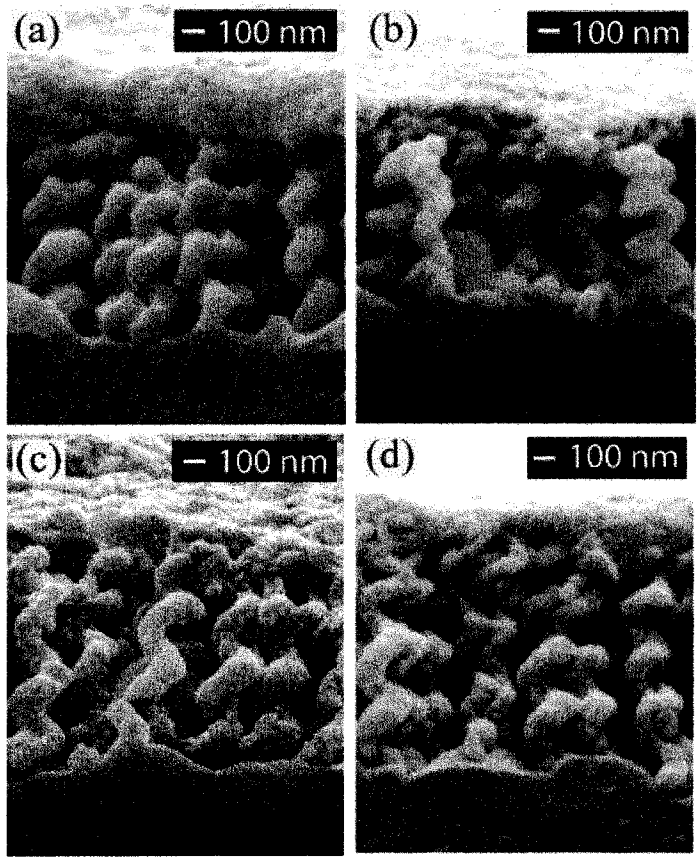

Figure 4.8: Polymer helices. Poly[pentaerythritol triacrylate] helices (a), poly[pentaerythritol tetracrylate] helices (b), poly[dipentaerythritol pentacrylate] helices (c), and poly[dipentaerythritol hexacrylate] helices (d).

Although the samples imaged in Figure 4.8 have been flipped over (as explained in Figures 4.4 (e) and (f)) a small layer of solid film is visible on the top of the helices. This is a continuous layer which could only have been generated if some of the monomer mixture was able to seep between the intermediate template and the substrate during polymerization. This layer provides additional mechanical stability to the helices.

4.5 Liquid Crystalline Polymer Helices

Inorganic helical films deposited by glancing angle deposition have been investigated for use as mechanical devices [25]. It has been suggested that polymer helices would be advantageous owing to the comparatively low modulus, and therefore high deformability, of these materials. In this chapter a fabrication technique which can be used to make polymer GLAD-like structures was presented. However, the question of how to actuate these structures has not been answered. One idea is to use this fabrication technique to make *liquid crystalline* polymer helices, since liquid crystalline polymers are known to undergo mechanical deformations in response to an applied stimulus.

Liquid crystalline polymers will be explained in greater depth in Chapter 6, but are mentioned here to give some idea of the motivation for the work described in Chapter 5. Liquid crystalline polymers are a class of polymers made from monomers that are highly anisotropic in shape. These monomers can form mesophases between a liquid and a crystalline solid. Although the molecules are fluid in these mesophases, a key feature of liquid crystallinity is that the molecules exhibit some kind of order beyond that found in an isotropic liquid. This order is most commonly orientational, which means that the molecules point on average in a common direction. In some cases liquid crystals may also exhibit limited positional order; for example, in the smectic phase molecules are arranged in layers. The order of liquid crystalline monomers can be preserved by polymerization. If a liquid crystalline polymer can then be made to undergo a transition to a state with lower ordering (using a stimulus such as heat, UV, or exposure to water vapor), then this action can be accompanied by a significant change in shape and volume. For this reason liquid crystalline polymers are potentially of interest for use in actuator devices. Investigating the patterning, properties, and actuation of these materials will be a major focus for the remainder of this thesis. In Chapter 5, the alignment of liquid crystals in a GLAD film is examined, to provide an idea of how the liquid crystalline molecules in a single or double-templated film will be oriented. In Chapter 6, the properties of macroscopic samples are examined, and compared to the properties of liquid crystalline polymer thin films anchored to a substrate. In Chapter 7, liquid crystalline polymers will be shaped using the templating techniques which have already

been described, as well as a modified version of single-templating. The responsivity of these structures will be examined. Finally, in Chapter 8, some alternative methods for patterning liquid crystalline polymers will be explored. Each of these chapters will provide important information towards making microscaled liquid crystalline polymer actuator devices.

4.6 References

1. Elias, A.L., Harris, K.D., Bastiaansen, C.W.M., Broer, D.J. and Brett, M.J., *Large-area microfabrication of three-dimensional, helical polymer structures.* Journal of Micromechanics and Microengineering, 2005. **15**(1): p. 49-54.
2. Biederman, H., *Organic films prepared by polymer sputtering.* Journal of Vacuum Science & Technology a-Vacuum Surfaces and Films, 2000. **18**(4): p. 1642-1648.
3. Seto, M., *Mechanical Response of Microspring Thin Films*, in *Department of Electrical and Computer Engineering.* 2004, University of Alberta: Edmonton.
4. Grate, J.W., Patrash, S.J. and Abraham, M.H., *Method for Estimating Polymer-Coated Acoustic-Wave Vapor Sensor Responses.* Analytical Chemistry, 1995. **67**(13): p. 2162-2169.
5. Jensen, J.B., Hoiby, P.E., Emiliyanov, G., Bang, O., Pedersen, L.H. and Bjarklev, A., *Selective detection of antibodies in microstructured polymer optical fibers.* Optics Express, 2005. **13**(15): p. 5883-5889.
6. Kawata, S., Sun, H.B., Tanaka, T. and Takada, K., *Finer features for functional microdevices - Micromachines can be created with higher resolution using two-photon absorption.* Nature, 2001. **412**(6848): p. 697-698.
7. Coenjarts, C.A. and Ober, C.K., *Two-photon three-dimensional microfabrication of poly(dimethylsiloxane) elastomers.* Chemistry of Materials, 2004. **16**(26): p. 5556-5558.
8. Pang, Y.K., Lee, J.C.W., Lee, H.F., Tam, W.Y., Chan, C.T. and Sheng, P., *Chiral microstructures (spirals) fabrication by holographic lithography.* Optics Express, 2005. **13**(19): p. 7615-7620.
9. Pursel, S., Horn, M.W., Demirel, M.C. and Lakhtakia, A., *Growth of sculptured polymer submicronwire assemblies by vapor deposition.* Polymer, 2005. **46**(23): p. 9544-9548.
10. Stevens, M.P., *Polymer Chemistry: An Introduction.* 3rd ed. 1999, New York: Oxford University Press.
11. Bortnick, N.M., *Polyacrylics*, in *Encyclopedia of materials : science and technology*, K.H.J. Buschow and e. al., Editors. 2001, Elsevier: Amsterdam.
12. Anseth, K.S., Bowman, C.N. and Peppas, N.A., *Polymerization Kinetics and Volume Relaxation Behavior of Photopolymerized Multifunctional Monomers Producing Highly Cross-Linked Networks.* Journal of Polymer Science Part a-Polymer Chemistry, 1994. **32**(1): p. 139-147.

13. Stansbury, J.W., Trujillo-Lemon, M., Lu, H., Ding, X.Z., Lin, Y. and Ge, J.H., *Conversion-dependent shrinkage stress and strain in dental resins and composites.* Dental Materials, 2005. **21**(1): p. 56-67.
14. CIBA_Specialty_Chemicals, *Ciba IRGACURE 184 Photoinitiator Product Info Sheet*, Basle, 1999,
15. Harris, K.D., Cuypers, R., Scheibe, P., van Oosten, C.L., Bastiaansen, C.W.M., Lub, J. and Broer, D.J., *Large amplitude light-induced motion in high elastic modulus polymer actuators.* Journal of Materials Chemistry, 2005. **15**(47): p. 5043-5048.
16. Studer, K., Decker, C., Beck, E. and Schwalm, R., *Overcoming oxygen inhibition in UV-curing of acrylate coatings by carbon dioxide inerting, Part I.* Progress in Organic Coatings, 2003. **48**(1): p. 92-100.
17. Callister, W.D.J., *Materials Science and Engineering, An Introduction.* 3rd ed. 1994, New York: John Wiley & Sons.
18. Anseth, K.S., Bowman, C.N. and Peppas, N.A., *Dynamic-Mechanical Studies of the Glass-Transition Temperature of Photopolymerized Multifunctional Acrylates.* Polymer Bulletin, 1993. **31**(2): p. 229-233.
19. Geng, K.B., Yang, F.Q., Druffel, T. and Grulke, E.A., *Nanoindentation behavior of ultrathin polymeric films.* Polymer, 2005. **46**(25): p. 11768-11772.
20. McCabe, J.F. and Wassell, R.W., *Thermal-Expansion of Composites.* Journal of Materials Science-Materials in Medicine, 1995. **6**(11): p. 624-629.
21. Harwood, L.M. and Claridge, T.D.W., *Introduction to organic spectroscopy.* 1997, Oxford, England ; New York: Oxford University Press.
22. Broer, D.J., *Liquid Crystalline Networks Formed by Photoinitiated Chain Cross-linking*, in *Liquid Crystals in Complex Geometries:Formed Polymer and Porous Networks*, G.P. Crawford, Editor. 1996, CRC Press: London, Brisol PA.
23. Kim, D.S. and Seo, W.H., *Ultraviolet-curing behavior and mechanical properties of a polyester acrylate resin.* Journal of Applied Polymer Science, 2004. **92**(6): p. 3921-3928.
24. Lide, D.R., *CRC handbook of chemistry and physics : a ready-reference book of chemical and physical data.* 77th ed. 1996, Boca Raton, Fla.: CRC Press.
25. Seto, M.W., Dick, B. and Brett, M.J., *Microsprings and microcantilevers: studies of mechanical response.* Journal of Micromechanics and Microengineering, 2001. **11**(5): p. 582-588.

5 A Deuterium Nuclear Magnetic Resonance Study of the Alignment of Nematic Liquid Crystals in a GLAD Thin Film

In this chapter, nuclear magnetic resonance (NMR) is used to discern the alignment of liquid crystalline molecules in a helical GLAD template. The results of this chapter have been published in the Journal of Applied Physics [1].

5.1 Liquid Crystals

Liquid crystallinity is a property that was first observed in 1888 by the Austrian Friedrich Reintzer when a sample that he was heating exhibited two distinct transition points, the first from a solid to a cloudy liquid, and subsequently (at a higher temperature) to a clear liquid [2]. Today liquid crystals are ubiquitous, as they are found in a variety of display devices from calculators to digital watches to the liquid crystal displays (LCDs) in laptop computers and televisions.

Liquid crystalline materials exhibit one or more mesophases between a crystalline solid and an isotropic liquid. In these phases, the molecules are able to flow (unlike in a solid), and yet exhibit more ordering than in an isotropic liquid. Due to the anisotropic shape of liquid crystalline molecules, they are able to exhibit orientational ordering (in which molecules point in a common average direction), and can in some instances also exhibit different degrees of positional ordering (such as in the smectic phase, in which the liquid crystals are arranged in layers). The two main types of liquid crystalline mesogens are calamitic (having a rod-like shape) and discotic (having a disc-like shape). Examples of each of these types of liquid crystals (LCs) are shown in Figure 5.1:

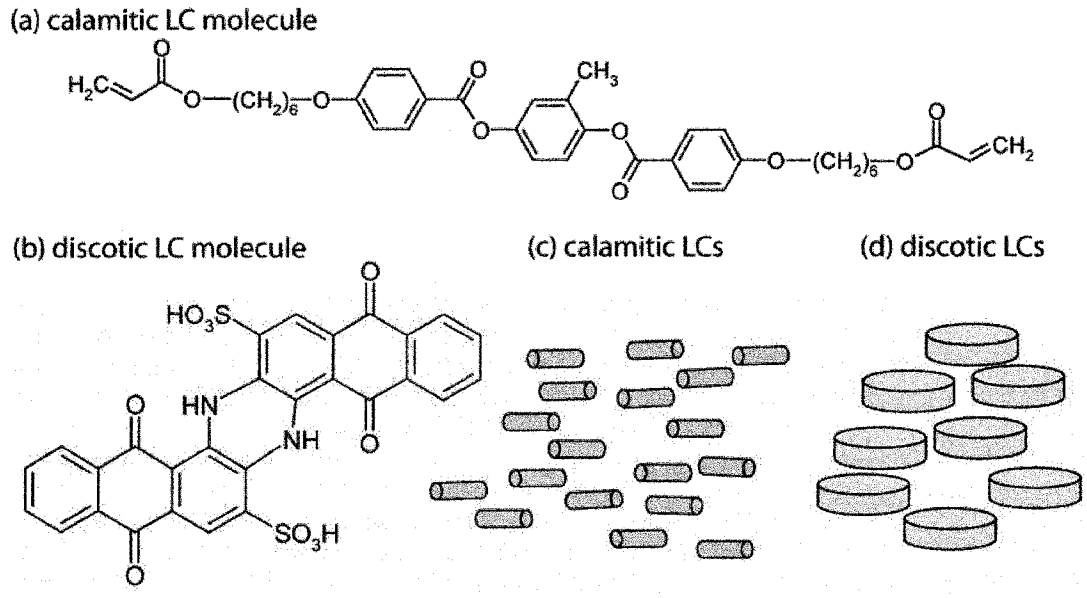

Figure 5.1: Liquid crystalline molecules. Two of the most common types of liquid crystalline molecules are calamitic (rod-like) and discotic (disk-like). Molecular drawings representative of calamitic and discotic LCs are shown in (a) and (b). In the liquid crystalline mesophase shown here these LCs exhibit orientational (but not positional) order, as shown in (c) and (d).

Liquid crystals (LCs) can also be classified by the mechanism responsible for their ordering. This thesis focuses on thermotropic liquid crystals, which form a liquid crystalline phase when they are heated from a solid towards a liquid. A simple phase diagram for an arbitrary thermotropic calamitic liquid crystal is shown in Figure 5.2.

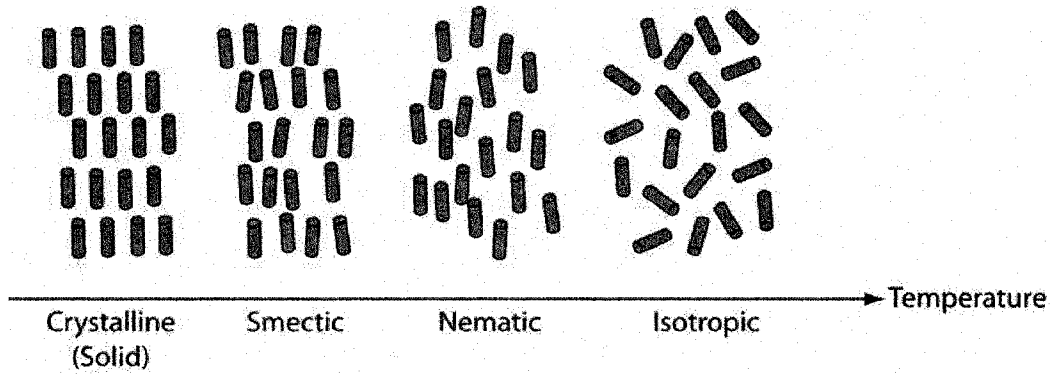

Figure 5.2: Thermotropic liquid crystals. These LCs exhibit various mesophases as a function of temperature. In the crystalline phase, the molecules are held firmly in a lattice. In the smectic phase, molecules have some fluidity, and are arranged loosely in layers, oriented one average in one direction. In the nematic phase, the LCs exhibit orientational (but not positional order). Finally, in the isotropic (or liquid) phase, the molecules are randomly arranged.

At low temperatures, the molecules form a crystalline solid. As the material is heated it can undergo a transition to the smectic phase, in which the LCs possess translational motion, orientational order (with the LCs pointing along a director), and some two dimensional positional ordering, as they are arranged in planes in one direction. At higher temperatures, the material can exist in the nematic phase, in which the LCs are randomly arranged in terms of position, but nonetheless possess some orientational order. Finally, at even higher temperatures, the molecules take on completely random orientations and positions, which is described as the isotropic phase. The diagram shown in Figure 5.2 is for an arbitrary liquid crystal: some liquid crystals undergo fewer mesophases (for example, the smectic phase may not be exhibited) or more mesophases (for example, exhibiting additional smectic phases with varying degrees of ordering within the layers).

There are also some liquid crystalline phases which appear as a function of concentration in a solvent. These are the lyotropic LCs which represent a class of LCs entirely different from the thermotropic LCs described above. However, in this thesis we are interested only in thermotropic, calamitic liquid crystals in the nematic phase.

5.2 Liquid Crystal Alignment

For liquid crystals in the nematic phase, the director configuration in a confined geometry results from a balance between the bulk elastic energy of the liquid crystals and surface anchoring effects [3]. There are a variety of surface treatments and layers that can be used to dictate the alignment of the liquid crystalline molecules with which they are in contact. These include rubbed polymer layers [4], self-assembled monolayers [5, 6], silane surfactant layers [7], and thin (<1000 Å) layers of obliquely evaporated SiO_x [8, 9]. Contact with any of these can induce order that will propagate over macroscopic dimensions. Different treatments can be used to align liquid crystals parallel to the surface of the substrate (planar alignment), perpendicular to the surface of the substrate (homeotropic alignment), or at an intermediate angle. Examples of these surface-driven alignment configurations are shown in Figure 5.3:

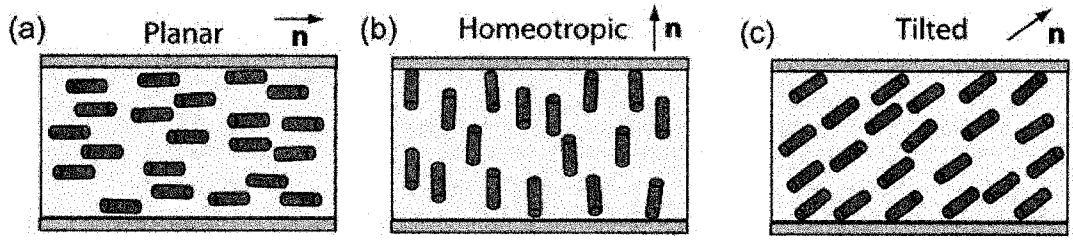

Figure 5.3: Common liquid crystal alignments. In these schematic diagrams, the LCs are shown in cells which consist of a top and bottom alignment layer, such as rubbed polyimide on glass. Planar alignment is defined as the case where the LCs lay parallel to the alignment surface (a). Homeotropic alignment occurs when the long axes of the LCs are oriented perpendicular to the surface (b). LCs can also be aligned at angles between these two extremes, which is called a pre-tilt angle (c).

Also shown for each case is the nematic director (***n***), which defines the direction of average orientation of the molecules. In all of these cases the LCs are said to be uniaxially-aligned, as the long axis of each molecule points along a single director. Note that ordering in these systems is never perfect, due to the molecular motions of the liquid crystals. Rather the individual liquid crystalline molecules form an angle θ_{LC} with the director, where the angle θ_{LC} is small for a well ordered system. There is a parameter that describes how well the LCs in a sample are aligned with the director: the order parameter (S). The order parameter is temperature dependent, and tends to decrease with increasing temperature. The mathematical definition of the order parameter is shown in Equation 5.1, and is averaged over all molecules. This value can range from perfect order (S=1) to complete randomness (S=0).

$$S = \frac{1}{2}\left\langle 3\cos^2\theta_{LC} - 1 \right\rangle \qquad [5.1]$$

When liquid crystals are confined to porous materials with large surface area to volume ratios, complex and varied director profiles can result. The interaction of liquid crystals with a variety of confining materials has been studied. Some of these systems include Anopore and Nucleopore membranes, comprised of isolated high aspect ratio pores [10]; controlled porous glass (CPG), made up of interconnected cylindrical pores [11]; and polymer dispersed liquid crystals (PDLCs), consisting of isolated spherical cavities in a polymer matrix [12, 13]. The director profiles that result in these systems are influenced

by a number of factors including cavity size, pore shape, and surface chemistry and properties [14, 15]. Cavity size is especially important for systems with at least one dimension on the order of a few hundred nanometers or less.

Films deposited by glancing angle deposition also have a large surface area to volume ratio, which results in complex director profiles when these films are infiltrated with liquid crystals. While helical GLAD films appear quite solid in the SEM images shown in Chapter 2 of this thesis, transmission electron microscopy studies have revealed that the surface of the helices is actually fibrous [16]. The fibers of which the helices are comprised can be seen in Figure 5.4:

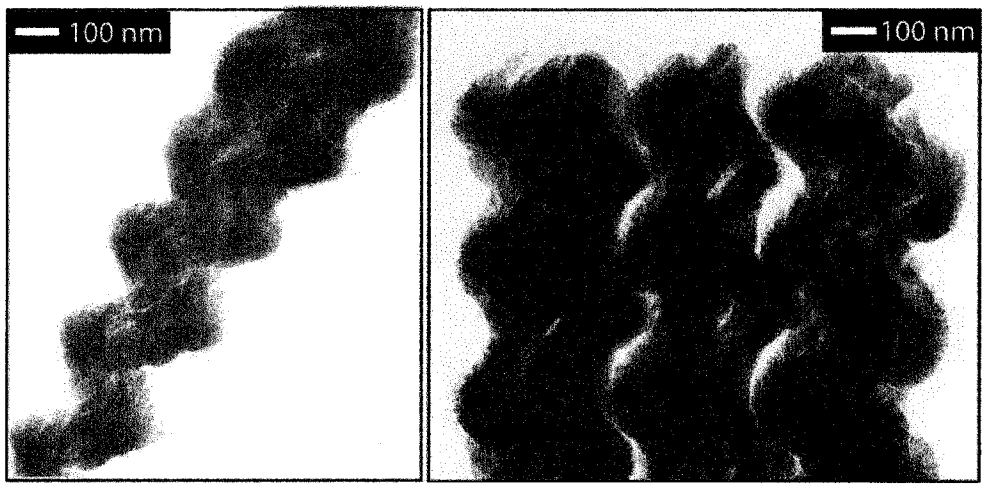

Figure 5.4: Transmission electron microscopy. These images allow the fine, hairy detail of the helical SiO_2 GLAD structures to be seen.

Porosimetry measurements described in the literature have shown that for manganese films deposited at $\alpha > 80°$ the surface area of the film is an order of magnitude greater than for a flat film. A value of 9 cm^2/cm^2 was measured for a film approximately 500 nm thick, although this value scales with thickness so thicker films will have even higher surface areas [17].

The alignment of liquid crystals in a GLAD templates has been studied in the past. In 1999 it was found that chiral GLAD films could impart chiral ordering to a system of liquid crystals [18]. This study suggested that the role of a GLAD film was similar to

that of a chiral dopant, which can be added to a system of LCs to induce cholesteric behavior. In the cholesteric phase LCs are aligned in planes: in each plane the LCs are uniaxially aligned, but the direction of alignment rotates between planes in a helical manner. This concept is illustrated in Figure 5.5:

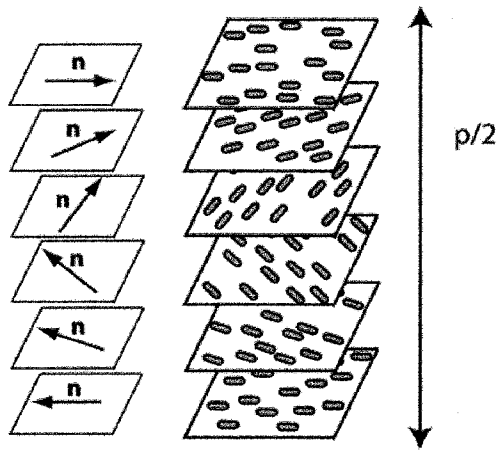

Figure 5.5: Cholesteric liquid crystals. The order in this phase can be thought of in terms of planes: in each plane the liquid crystals are uniaxially aligned, but the director (***n***) rotates between adjacent planes. The distance required to make one full rotation is defined as the pitch (p).

The distance required for the director to make one full rotation is defined as the pitch (p). Cholesteric films exhibit circular dichroism, selectively transmitting and reflecting circularly polarized light of opposite and like handedness, respectively, to the LCs. This effect is wavelength dependent: selective reflection is only seen for light which falls within the range from $\lambda_{min}=pn_o$ to $\lambda_{max}=pn_e$ where n_e and n_o are the extraordinary and ordinary refractive indices of the liquid crystals (which are birefringent). This is called Bragg reflection. Cholesteric liquid crystal films can exhibit very strong reflection bands, reflecting up to almost 100% of the circularly polarized light of one-handedness incident upon them (in the region of wavelengths defined above) [19].

In the GLAD-LC optical characterization study mentioned above, cells were constructed by taping together two 15-turn MgF_2 GLAD films with a 350 nm pitch in a cell configuration [18]. Liquid crystals were then infiltrated into the cell by capillary filling. When the transmission of left- and right-handed circularly polarized light through the cell was measured, it was found that the transmission of left-handed light was approximately

25% lower than for right-handed light. This shows that the left-handed circularly polarized light was selectively reflected, and that some chiral alignment must have been achieved. Using the same formulae as for cholesteric LCs combined with effective medium theory, the position of the reflection peak can be predicted, as given in Equation 5.2:

$$\lambda_{peak} = n_{ave} \times p = \left[\rho_{GLAD} n_{GLAD} + (1 - \rho_{GLAD}) \left(\frac{n_e + n_o}{2} \right) \right] \times p \qquad [5.2]$$

Where n_{GLAD} is the index of refraction of the bulk GLAD film material (1.38), and ρ_{GLAD} is the fractional density of the film with respect to the bulk density. Using this equation, the location of the peak was consistently lower than expected unless an unreasonably high density (60% of the bulk density) was assumed for the GLAD film. This suggests that the LCs are not simply aligned in the plane of the substrate with a chiral twist (as for cholesteric LCs), but that a more complex alignment results.

It has also been shown that hybrid GLAD-LC systems are switchable: the selective transmission of one handedness of circularly polarized light can be 'turned off' by applying an electric field across the cell [20]. In this case, the liquid crystals aligned in a direction normal to the substrate, and the circular dichroism was eliminated.

Despite the interesting optical properties of GLAD-LC systems, the alignment of the liquid crystalline molecules in a GLAD template has not previously been determined. A need to know persists – both for improving GLAD optical devices and for predicting and optimizing the behavior of liquid crystalline polymer actuators fabricated using template-based fabrication techniques in which a film deposited by GLAD acts as the master. This chapter describes the determination of the alignment of liquid crystals in a GLAD film using deuterium nuclear magnetic resonance (^{2}H-NMR).

5.3 Nuclear Magnetic Resonance

Nuclear magnetic resonance (NMR) is a spectroscopy technique which was first demonstrated in 1946 [21]. This technique can be used to collect information about the

environment surrounding a nucleus which possesses spin, and therefore a magnetic moment (μ) [22]. When a nucleus with non-zero spin is placed in a strong magnetic field, only certain orientations of the molecule with respect to the field are permitted, due to the quantization of energy associated with each state. The number of permitted alignments (n_I) can be calculated from Equation 5.3, in which I is the nuclear spin quantum number.

$$n_I = (2I + 1) \qquad [5.3]$$

For example, for a ^{1}H nucleus, which possesses a spin of ½, only 2 orientations are permitted: parallel and anti-parallel to the magnetic field (which has magnitude B). These orientations are defined by a magnetic quantum number (m_I). The magnetic quantum number ranges from $-I$ to $+I$ in integer steps, so for the proton nucleus $m_I = \pm$ ½, and there is a quantized energy level associated with each magnetic quantum number. These energy levels are displaced from the zero energy configuration by the amount described in Equation 5.4 [22]:

$$\Delta E = m_I \mu B \qquad [5.4]$$

This displacement of energy levels (E_α and E_β) in the presence of a magnetic field is called the Zeeman effect, and is illustrated in Figure 5.6:

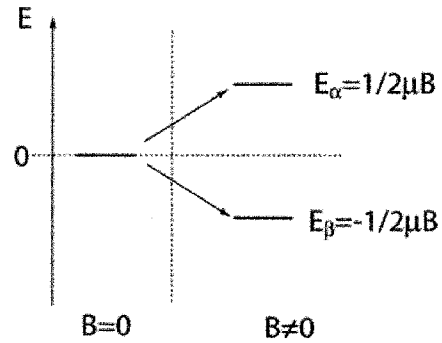

Figure 5.6: The Zeeman effect. In the presence of a magnetic field, a nucleus with spin I=1/2 has two quantized energy levels, corresponding to parallel and antiparallel alignment of the magnetic moment vector and the external magnetic field.

Due to the small magnetic moment of the nucleus, the difference between the E_α and E_β is small. Therefore, in a magnetic field there will be only slightly more magnetic moments aligned parallel to the field than anti-parallel to the field. The population of each state is governed by the Boltzmann distribution, and the ratio between the two populations (N_α and N_β) is given by Equation 5.5:

$$\frac{N_\alpha}{N_\beta} = e^{(E_\alpha - E_\beta)/kT} \qquad [5.5]$$

In this equation, k is Boltzmann's constant and T is the temperature. For proton NMR, the difference in population between the two states is usually on the order 1 in 10^4 [23]. Because there are slightly more magnetic moments aligned with the field than against it, the sample has a net magnetization (M) in the direction of the field. Transitions from the lower to higher energy state can be induced by supplying the nuclei with energy from an oscillating magnetic field. When the magnetic moment of a nucleus is aligned in a static magnetic field (B_0), it can be perturbed by applying an oscillating magnetic field (B_1) in a perpendicular direction. When B_1 is removed, the nuclei will precess back towards the lower energy state at their Larmor frequency (ν_L). The Larmor frequency is proportional to the strength of the applied field as well as the magnetogyric ratio (γ) of the nucleus, which is a fundamental quantity and has units of rad/(T·s). The Larmor frequency can be calculated using Equation 5.6 [23]:

$$\nu_L = \frac{\gamma B_0}{2\pi} Hz \qquad [5.6]$$

In a typical NMR set-up, the magnetic field B_0 is supplied by a large superconducting magnet, which has a magnitude of a few Tesla. It would be impossible to supply an equally large field B_1 to tip the magnetization away from the direction of the stationary field B_0. Nonetheless, the field B_1 can be small and still perturb the magnetic moment provided that the frequency of the field is close to the Larmor resonance, allowing nuclear magnetic resonance to be achieved [24]. The field B_1 is supplied by a coil, which is also used to detect the signal. Typically the sample is inserted into the small coil, which is placed within a heat-insulated probe. The probe itself is then inserted into the center of the superconducting magnet which provides the external field B_0 [24].

Rather than applying an oscillating field B_1 with a range of frequencies one by one and measuring the response, most NMR set-ups apply a single pulse containing a range of frequencies. For an atom with a spin of $I=1$ (such as the deuterium nuclei used in this study) the duration of the pulse can be chosen such that the net magnetization undergoes a $\pi/2$ rotation away from the direction of the external magnetic field, as shown in Figure 5.7 [21].

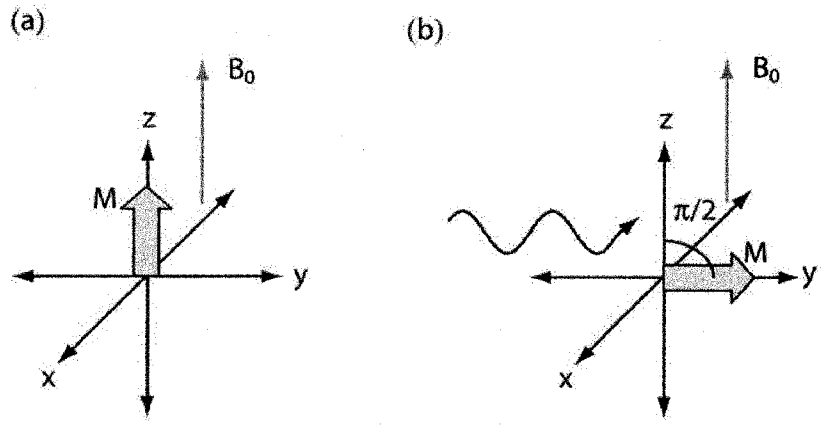

Figure 5.7: Vector representation of a deuterium nuclei in a magnetic field. When the magnetic field B_0 is applied in the positive z direction, the net magnetization (M) is also along this direction (a). An oscillating magnetic field (B_1) can be applied in a direction perpendicular to z, which causes a perturbation of the net magnetization (b).

The duration of the pulse (t_p) required to rotate the magnetization through the angle $\pi/2$ can be calculated using Equation 5.7 [21]:

$$t_p = \frac{\pi/2}{B_1 \gamma} \qquad [5.7]$$

After the pulse is applied, the free induction decay signal (FID) of the sample is measured using the same coil. This signal is generated as the magnetic moments relax towards the lower energy state (along the direction of the field B_0). Recall that as relaxation occurs, the magnetic moment of the nuclei precesses around the axis of the field B_0 at the Larmor frequency. The Fourier transform of the FID can be used to generate a spectrum of

intensity vs. frequency, and the spectrum is comprised of the sum of contributions from individual nuclei.

From the description given above, one might expect the overall spectrum of a sample containing either proton or deuterium nuclei to consist of a single peak at the Larmor frequency of the nucleus. Recall that the Larmor frequency of a nucleus is dependent on two things: the magnetogyric ratio (γ) and the magnetic field strength (B_0). However, the local environment of each nucleus modifies the magnetic field that it 'sees', causing small shifts in the associated Larmor frequency and energy levels. This results in distinctive spectra that can be used, for example, to identify the structure of unknown molecules.

5.4 Deuterium Nuclear Magnetic Resonance (^{2}H-NMR)

An effective technique for determining liquid crystal alignment in confined cavities is deuterium magnetic resonance (^{2}H-NMR) [10, 11, 13, 14, 25, 26]. In this technique, the host material is filled with liquid crystals deuterated at a single specific site on the molecule. Due to the anisotropic shape of these molecules, the resulting NMR spectra can exhibit splitting that is dependent on the orientational order of the nematic liquid crystals. ^{2}H-NMR has been used to determine the alignment of liquid crystals in a variety of the confined geometries mentioned in Section 5.2, including Anopore and Nucleopore membranes [25], controlled porous glass (CPG) [11], and polymer dispersed liquid crystals (PDLCs) [13, 26]. In addition to providing information about the director profile in the nematic phase, ^{2}H-NMR has also been used to observe unexpected phase behavior. For example, for deuterated liquid crystals in Nucleopore cavities, it has been shown that surface-induced ordering can persist well into the isotropic phase of the bulk material [25].

In ^{2}H-NMR, deuterated LCs are used to collect information on the alignment of molecules with respect to an external magnetic field. Deuterium (^{2}H) is a naturally occurring isotope which makes up 0.02% of all hydrogen nuclei [22]. The nucleus of a deuterium atom contains 1 neutron and 1 proton, whereas ^{1}H contains only a proton.

Deuterium has a spin of 1, which means that there are three permitted energy levels when the molecule is placed in a magnetic field. For the 7.05 T magnet used in the experiments described here, the resonant frequency of ^{2}H is 46 MHz. To collect information about liquid crystal alignment using NMR, a specific hydrogen atom in the liquid crystal is replaced with a deuteron, allowing information on orientation to be extracted from the NMR absorption spectra, since the frequency at which the deuterons absorb is dependent on their angular orientation with respect to the field. This allows much more precise spectra to be generated than just by probing liquid crystals with proton NMR (^{1}H-NMR), as there are many proton nuclei in each liquid crystal, each of which is in a slightly distinct magnetic environment, and each of which would generate an independent signal.

As mentioned above, ^{2}H has a Larmor frequency of 6.5360 MHz/T. However, like in proton NMR spectroscopy, the peaks in the spectra are modified by the environment surrounding the deuterons. In this case, due to the uniaxiality of the molecules, symmetric line splittings appear in the spectra [27].

There are two factors which determine the position of the two peaks which appear in the spectra of uniaxially aligned liquid crystals in the nematic phase: the overall order of the system (S) and the angle (θ_B) formed between the director and the magnetic field (B_0). The relationship between these two factors and the separation between the peaks ($\delta\nu$) is given by Equation 5.8 [26]:

$$\delta\nu = \frac{\delta\nu_B}{S_B} S\left(\frac{3}{2}\cos^2\theta_B - \frac{1}{2}\right) \qquad [5.8]$$

In this equation, $\delta\nu_B$ is the splitting when the bulk liquid crystals are perfectly aligned with the external magnetic field, and S_B is the order parameter in the bulk phase. A few example spectra are shown in Figure 5.8:

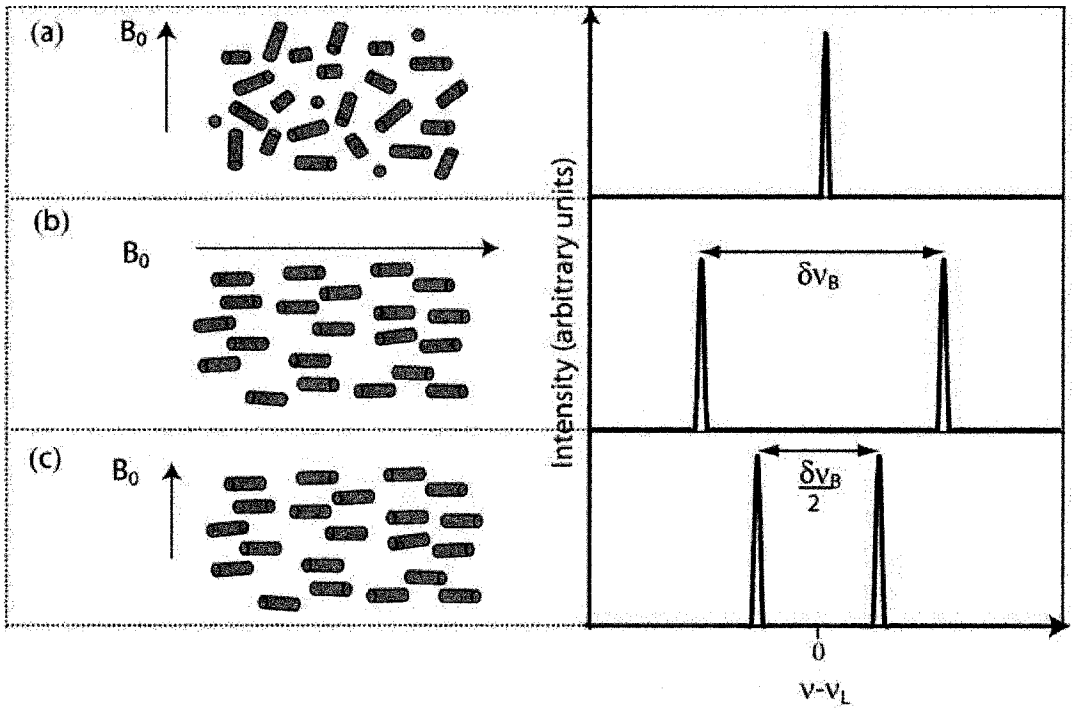

Figure 5.8: 5CB-αd_2 spectra. Spectra are shown for three different configurations. If the liquid crystals are in the isotropic phase, motional averaging causes the spectrum to have only a single peak at ν-ν_L = *0* (a). If the LCs are in the nematic phase and uniaxially aligned in the direction of the field B_0, then symmetric peaks are seen at the frequencies $\pm\nu_B$ (b). If the nematic LCs with uniaxial alignment are aligned in a direction perpendicular to the field B_0, then the peaks are seen at the frequencies $\pm\nu_B/2$.

When liquid crystals in the nematic phase are confined in porous materials, complex director structures can result. Both the order parameter and the angle between the director and external field take on angular dependencies. For a liquid crystal at position ($\bar{r}$), the frequency of the splitting ($\delta\nu(\bar{r})$) is related to the angle between the local director and the magnetic field ($\theta_B(\bar{r})$) by Equation 5.9:

$$\delta\nu(\bar{r}) = \delta\nu_B \frac{S(\bar{r})}{S_B}\left[\frac{3}{2}\cos^2\theta_B(\bar{r}) - \frac{1}{2}\right] \qquad [5.9]$$

In this equation, $\delta\nu_B$ is the splitting frequency of the bulk material, and $S(\bar{r})/S_B$ is the relative order parameter of the system being measured as compared with the order

parameter of the bulk material for which $\delta\nu_B$ is given. Throughout this work this ratio is taken to be 1.

Each deuterated liquid crystal in the system makes an individual contribution to the spectrum, which is comprised of a superposition of the individual spectra. For example, if the molecules are aligned in a plane parallel to the magnetic field with a random and uniform distribution of all angles a 'powder pattern' spectrum results, consisting of two large peaks at $\pm\delta\nu_B/2$, with smaller shoulders at $\pm\delta\nu_B/4$, and a roll-off in between, as shown in Figure 5.9 (a):

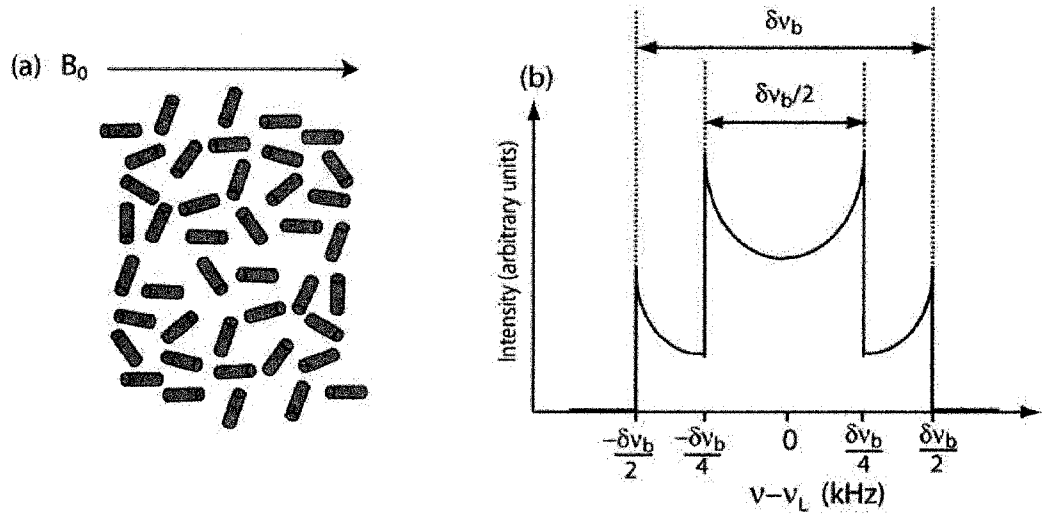

Figure 5.9: The powder pattern. If the liquid crystals (in the nematic phase) are aligned in a plane parallel to the magnetic field with a random and uniform distribution of angles ($\theta_B(\vec{r})$) between each molecule and the magnetic field B_0, then the resulting spectrum is comprised of a superposition of peaks from every angle (b).

The unusual shape of this spectrum results from the fact that the relationship between splitting frequency and the angle between the director and magnetic field is not linear. The solution to Equation 5.9 for all angles from 0° to 90° is shown in Figure 5.10:

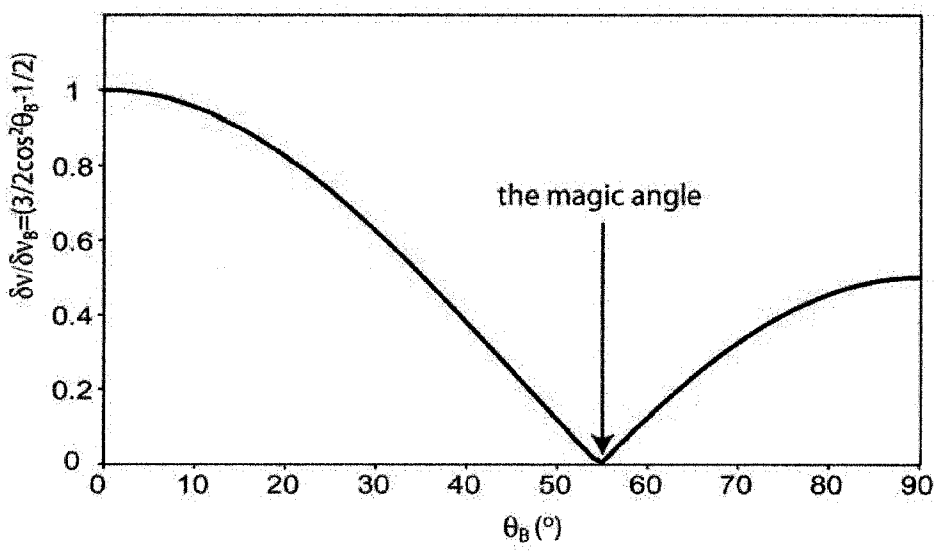

Figure 5.10: Splitting frequency. The splitting frequency ($\delta\nu$) corresponding to each angle θ_B is shown, normalized to the splitting frequency of the bulk ($\delta\nu_B$). The solution to this function is not linear, so some frequencies are more heavily weighted than others. The magic angle (54.5°) – which results in a splitting frequency of 0 kHz – is indicated.

The fact that the slope changes significantly as a function of angle and that some splitting frequencies correspond to more than one angle contribute greatly to the distinctive, non-uniform shape of the powder pattern shown in Figure 5.9.

To be able to use NMR to study the alignment of liquid crystals in a GLAD film, a few conditions must be met. These conditions concern the diffusion length of the molecules during the time scale of the measurements, and the ability of the external magnetic field B_0 to influence the alignment of the LCs. Because of the integrative nature of the NMR technique, the collected spectrum depends strongly on the time scale of the measurement. If the molecules are allowed sufficient time to diffuse during a measurement, molecular averaging leads to a single peak at $\nu - \nu_L = 0$ with a small (~100 Hz) full-width half maximum, as for the isotropic phase. However, if the time scale of the measurement is sufficiently short, then the system can be approximated as 'static'. Whether or not the system is static within the time scale of the measurement can be determined by

calculating the average distance that a molecule can diffuse, and comparing it with the characteristic dimension of the cavity in which it is confined. The length of diffusion (d_l) for the system can be calculated from equation 5.10 [10]:

$$d_l \sim \sqrt{D/\delta\nu} \qquad [5.10]$$

Where D is the diffusion constant (~10^{-11} m^2s^{-1}), and in the nematic phase $\delta\nu \sim \delta\nu_B$, which is approximately 55 kHz in this study. The diffusion length in the nematic phase is therefore ~13 nm, which is much smaller than the average spacing between posts in a GLAD film. The spectrum can be considered relatively static.

The extent to which the alignment of the liquid crystals is affected by the external magnetic field is gauged by the magnetic coherence length (ξ_M). When a magnetic field is applied to a bulk sample of deuterated liquid crystals, most of the liquid crystals will align with the field. However, within a certain distance from the solid surfaces bounding the liquid crystals the alignment will be unaffected. Magnetic coherence length is a measure of the thickness of this unaffected layer. It can be computed from Equation 5.11 [10]:

$$\xi_M = \left(\frac{\mu_o K}{\Delta\chi}\right)^{1/2} \frac{1}{B} \qquad [5.11]$$

Where K is an elastic constant that is dependent on liquid crystal interactions (~10 pN), $\Delta\chi$ is the anisotropy of the diamagnetic susceptibility (10^{-7}), μ_o is the permittivity of free space, and B is the magnetic field strength (in this case 7.05 T). Overall the coherence length is estimated to be around 1.6 μm. Since this length is much bigger than the spacing between helices the alignment of the liquid crystals should be dictated by the surface of the GLAD film without being affected by the external magnetic field, which makes it possible to determine the alignment of the liquid crystals in the GLAD film using this technique.

5.5 *Determination of LC alignment in a GLAD film: Materials and Methods*

The main purpose of the work described in this chapter is to determine the alignment of liquid crystals in a helical GLAD film. To determine the alignment of LCs in a GLAD fim, multiple 10-turn SiO_2 GLAD films were deposited at an angle of 85° on 4 in. silicon substrates for use in this study. SEM images of one such film are shown in Figure 5.11:

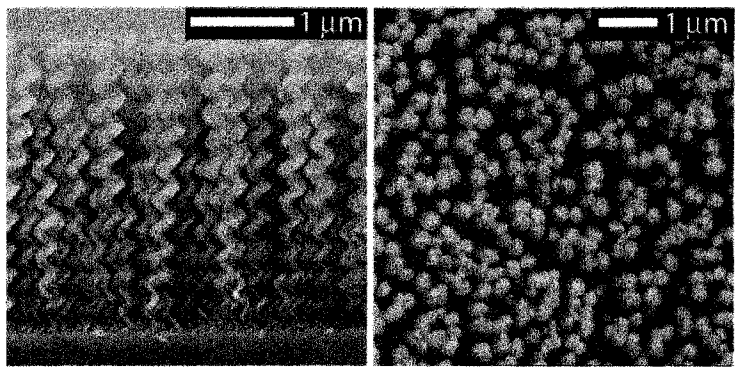

Figure 5.11 GLAD sample. The GLAD film used in this study is comprised of 10-turn helical structures, shown from the side (a) and top (b).

As can be seen in this figure, the diameter of the helical structures is typically on the order of 50 nm to 150 nm, and the space between these randomly dispersed helices can vary from less than 50 nm to more than 300 nm. The average rise angle of the helices was determined from Figure 5.11, by measuring the angle formed between the helical arm and the plane of the substrate at 15 different points. The average rise angle (θ_r) was found to be 41°, with a standard deviation of 3°. This means that the average angle between the helical arms and the substrate normal (θ_n) was 49°. One reason for the range of angles measured is the broadening of the structures: as the film increases in thickness, competition effects cause the diameter of each helix to increase.

The liquid crystal chosen for investigation was alpha-deuterated 4'-pentyl-4-cyanobiphenyl (5CB-αd_2). In this molecule, the deuteron replaces the first hydrogen next to the core (in the alpha position). This molecule is shown in Figure 5.12:

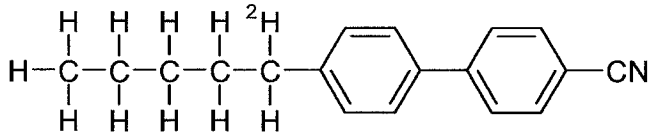

Figure 5.12: Alpha-deuterated 4'-pentyl-4-cyanobiphenyl (5CB-αd_2).

The non-deuterated version of 5CB-αd_2, which is called 5CB or K15, is a commonly used liquid crystal that is thermodynamically similar to 5CB-αd_2. This molecule is nematic from 23 °C to 35 °C. For this study the temperature of the sample was controlled at 27 °C.

Liquid crystals were infiltrated into GLAD templates by solution processing. 5CB-αd_2 was diluted with a solvent (such as tetrahydrofuran or propylene glycol monomethyl ether acetate [PGMEA]) to achieve the desired viscosity, and spin-coated into the GLAD film. Visual inspection of the samples was employed to determine optimal filling conditions such as spin-speed and liquid crystal concentration in the diluted mixture: if the film appeared smooth and highly reflecting after filling, then it was deemed to be over-filled, and if the film appeared to scatter light then it was judged to be under-filled. Comparison of a variety samples allowed conditions on the boundary between these two states (under-filled and over-filled) to be selected. After filling, the silicon substrates were cleaved into narrow strips approximately 10 mm in width and 25 mm in length. These strips could then be stacked in an NMR sample tube, using thin pieces of Teflon placed at either end of the tube as spacers to prevent damage to the surface of one strip from the bottom of another. The results shown in this chapter were obtained from a tube containing 9 strips. 9 strips of substrate measuring 10 mm by 25 mm coated with films 3.2 μm thick contain an extremely small volume of 5CB-αd_2: less than 10 μL. For this reason, the signal collected for each NMR measurement was extremely faint. Extensive averaging could be used to obtain reasonable signal-to-noise ratios, as noise scales as $1/\sqrt{n}$, where n is the number of measurements collected. Measurements were performed using a 7.05 T superconducting magnet and a solid-state spectrometer (AVANCE™ 300/Ultrashield™, 300 MHz, 89 mm, Bruker BioSpin GmbH). Measurements (in the form of free induction decay signals) were collected, averaged over 30×10^6 signals, and

transformed into spectra in the frequency domain. These spectra could then be compared with spectra generated based on hypothetical alignment distributions in order to determine the actual alignments of the liquid crystals. The generation of the hypothetical spectra will be discussed in the following section.

Note that measurements were collected for two different orientations of the sample with respect to the external magnetic film: with the substrate normal parallel and perpendicular to the field B_0.

5.6 Modeling: Predicting Alignment

Equation 5.8 and the Fourier transform were employed to generate a number of spectra based on hypothetical director configurations for liquid crystals in a helical GLAD film. The starting point for generating the hypothetical director configurations (and therefore angular distribution of LCs) was to determine whether the liquid crystals were more likely to align planar (parallel) or homeotropic (perpendicular) to the surface of the GLAD films themselves. To accomplish this, SiO_2 was evaporated onto glass substrates under conditions similar to the films used in the study, except that the substrates were held at normal incidence with respect to the source. Cells were then constructed from these substrates and filled with non-deuterated 5CB. When these samples were examined between crossed polarizers, the resulting alignment was found to be multi-domain planar, indicating that the LCs were aligned parallel to the surface of the glass in random domains on the substrate. It was then concluded that the alignment at the surface of the GLAD films would also be planar, and that the angle formed between each liquid crystal and the plane of the substrate would be dictated by the rise angle of the helix. This assumes that the fibers visible in the TEM image shown in Figure 5.4 are, on average, aligned parallel to the rise angle.

Assuming planar alignment at the surface of the helices, three different configurations were hypothesized: case 1, case 2, and case 3. Case 1 assumed a uniform alignment, with the liquid crystalline molecules lying parallel to the helical arms and following the twist of the helices at a constant rise angle. In the plane of the substrate this would result in a

net circular distribution, only with the LCs tilted out of the plane of the substrate at an angle of θ_r = 41°. Case 2 is similar to case 1, only allowing for a small Gaussian distribution in tilt angles (σ = 3°). Case 3 is much different from the first 2, and is based on the escaped radial pattern sometimes witnessed in cylindrical pores (such as porous alumina). In this case the LCs are aligned parallel to the helical structures at their surface, but evolve as a function of radius to be completely perpendicular to the plane of the substrate at the center of each 'pore'. The tilt angle with respect to the substrate normal therefore progresses from 49° to 0°. Note that the number of molecules aligned at each angle over this range is proportional to the radius at which they are located, and therefore there will be a much larger contribution to the spectrum from molecules at lower angles (closer to 0°) than higher ones (closer to 49°). These 3 hypothetical alignments are illustrated in Figure 5.13:

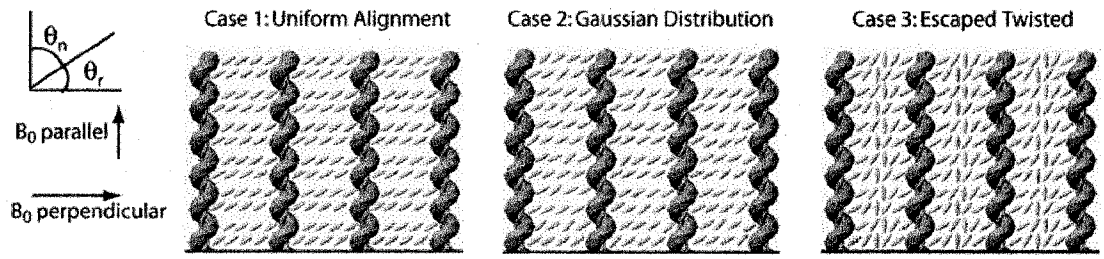

Figure 5.13 Hypothetical alignments. Three different theoretical alignments are presented for LCs in a GLAD film, generated based on planar alignment at the surface of the helical structures. The orientation of the external magnetic field with respect to the samples is also shown. Two orientations are considered: parallel and perpendicular to the helical structures/substrate normal. The definitions of θ_r (the rise angle) and θ_n (the angle formed with respect to the substrate normal) are also shown.

For each assumed alignment, the corresponding spectrum (in the frequency domain) and free induction decay (FID) signal (in the time domain) can easily be computed using MATLAB. For example, take case 1, in which the liquid crystalline molecules are assumed to form a uniform angle of θ_r = 41° with respect to the substrate (ie: the molecules follow the rise angle of the helices). The liquid crystals follow the twist of the helix, with a rotating director. For the case when the stationary field is applied parallel to the helices it is easy to determine the angle between each liquid crystal and the field, as every liquid crystal forms the same angle with the field ($\theta_B = \theta_n$ = 49°). If the stationary field B_0 is applied perpendicular to the helical posts, the distribution of angles is slightly

more complicated. If the LCs are projected into the plane of the substrate, then the angle formed between the *projection of* each LC and the field B_0 ranges from 0° to 90° with an equal distribution. But, the LCs are in fact tilted out of the plane. The minimum angle between any liquid crystal and the field is θ_n = 41°. Therefore $\theta_B(\bar{r})$ in fact ranges uniformly from 41° to 90°. The signal is therefore expected to resemble a modified powder pattern. The FID can be calculated using an exponential Fourier series. To express the signal in this way, the contribution from each deuterium nucleus must be determined. Each angle (from 41° to 90°) will contribute to the spectrum at a certain splitting frequency $\delta\nu$, as was shown in Equation 5.9.

The FID of the signal can be calculated by adding together the exponential component corresponding to each frequency, $\delta\nu_n$, as shown in Equation 5.12.

$$f(t) = \left[\exp(2j\pi\delta\nu_1 t) + \exp(2j\pi\delta\nu_2 t) + \exp(2j\pi\delta\nu_3 t) + \ldots\right]e^{-t/\tau} \qquad [5.12]$$

The decaying exponential is included to represent the decay of the transverse magnetization with time [24]. The time constant (τ) is chosen to correspond to the relaxation time of the deuteron, which in this case is $(2500)^{-1}$ s.

To generate the spectrum of this signal in the frequency domain, the Fourier transform of the signal must be taken. The Fourier transform $F(\omega)$ and the time domain representation of the signal $f(t)$ are related using Equations 5.13 and 5.14 [28]:

$$F(\omega) = \int_{-\infty}^{\infty} f(t)e^{-j\omega t}dt \qquad [5.13]$$

$$f(t) = \frac{1}{2\pi}\int_{-\infty}^{\infty} F(\omega)e^{j\omega t}dt \qquad [5.14]$$

Therefore, the Fourier transform (Equation 5.1.3) can be used to determine the spectrum of the signal in the frequency domain. But, rather than solving this problem analytically, the fast Fourier transform function in MATLAB can be used to solve this problem numerically. In this numerical computation method the signal is sampled N_q times over

an interval T_o, where the duration of each sample is T. The duration of each sample is selected to be $4x10^{-6}$ s in accordance with the Nyquist theory which tells us that the sampling frequency must be 2 times the bandwidth of the desired spectrum. In this case we are interested in examining the signal over a range of -62.5 kHz to 62.5 kHz (125 kHz), so twice this bandwidth is 250 kHz, the inverse of which is $4x10^{-6}$ s. In order to have good frequency resolution, the number of samples is chosen to be 512 (512 can also be expressed as a power of 2, which is advantageous when using the fast Fourier transform). Therefore in the time domain the signal is calculated at intervals of $4x10^{-6}$ s, at 512 different points from t = 0 to t = 0.002044.

The fast Fourier transform of the signal is then taken using the 'fft' function in MATLAB. This algorithm transforms a discrete representation of the signal in the time domain into a discrete representation of the signal in the frequency domain [28]. This complicated algorithm exploits symmetry to solve the problem in fewer steps than the discrete Fourier transform. Once the solution is generated, it can be plotted as a function of frequency using the 'fftshift' function in MATLAB. The results of these simulations are shown in Figure 5.14, and the code used to generate the spectra for each case can be found in Appendix 1.

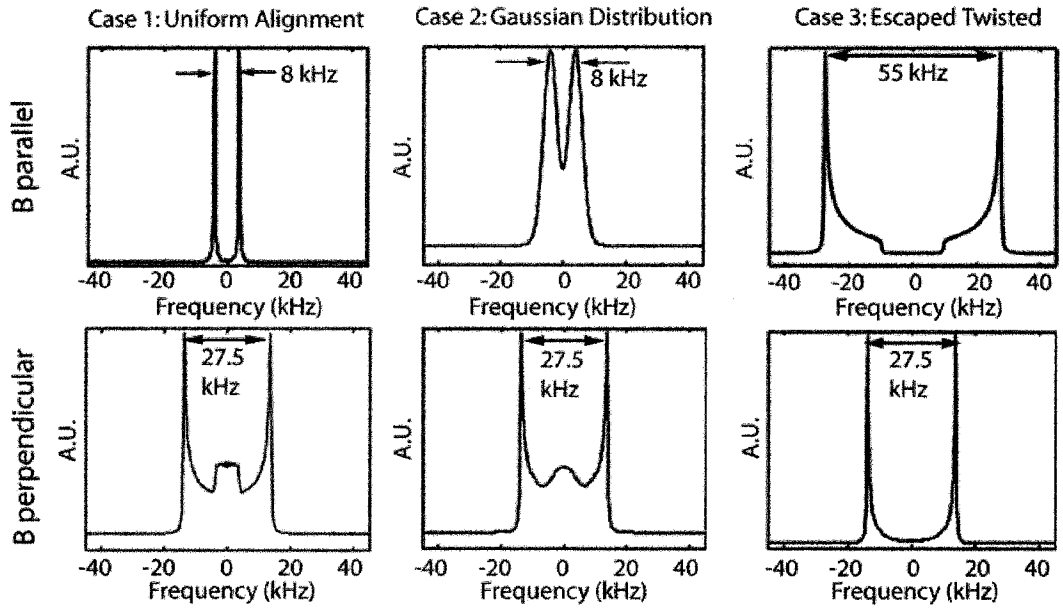

Figure 5.14: Frequency domain spectra based on hypothetical alignments. The spectra are shown for the hypothetical alignments of liquid crystals in a GLAD film (case 1, case 2, and case 3) which were described above. For each case, the alignment of the external magnetic field parallel and perpendicular to the helical structures (and substrate normal) is considered.

The information provided by the spectra simulated for parallel alignment of the helices with respect to the magnetic field is in itself quite telling. For case 1 we see a single splitting frequency of 8 kHz. The spectrum generated for case 2 (with the same orientation with respect to the magnetic field) is, as expected, similar to case 1 but with some broadening of the peaks (i.e.: the product of convolving the spectrum from case 1 with a Gaussian profile). For case 3 the spectrum is quite different, with a large contribution at the bulk splitting (55 kHz) and some lesser contributions in between, dropping to zero for frequencies at the center of the spectrum (corresponding to alignment at angles of greater than 49°. Note in particular that there is no contribution at $\delta\nu = 0$, which corresponds to the magic angle of 54.5°. These three spectra are in themselves quite distinct and should suffice to identify the unknown alignment of LCs in a helical GLAD film.

5.7 *Results and Conclusions*

The spectra collected for samples are shown in Figure 5.15 in red dashed lines.

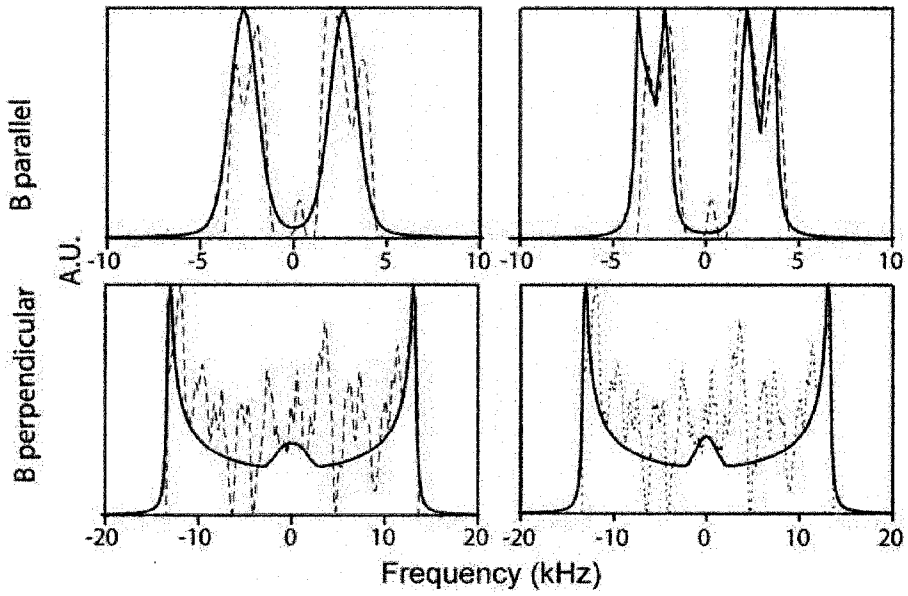

Figure 5.15: NMR results for a helical GLAD film filled with 5CB-αd_2. The results are shown in red dashed lines for parallel and perpendicular orientations between the helical axes and the external magnetic field. The measured spectrum for the case of parallel orientation between the helical posts and the stationary field B_0 is shown in (a) and (b), overlaid with different theoretical spectra. The measured spectrum for the case when the helical posts are oriented perpendicular to the stationary magnetic field is shown in (c) and (d), again overlaid with theoretical spectra.

Case 3, the escaped twisted director profile, can be immediately discarded based on these results. The spectrum for the $B_{parallel}$ orientation is comprised of broad peaks with an average splitting of 4 kHz, which corresponds to a angle of 50.8°. This supports the theory that the LCs are aligned with the twists of the helices at an average angle of 50.8° with respect to the substrate normal (which is in good agreement with the measured value of $\theta_n = 49^o \pm 3^o$). The slight discrepancy between angles might result from the fact that the fibers from which the helices are comprised are not aligned exactly parallel to the rise angle itself. In Figures 5.15 (a) and (c) the results are overlaid with the theoretical spectra for an angle θ_n = 50.8° with a Gaussian distribution of 3°, showing reasonably good agreement. In Figures 5.15 (b) and (d) the spectra are overlaid with the spectra that would result from having contributions from 2 specific angles: 49.6° ±1°and 51.7°± 1°.

While this fit is in reasonable agreement with the spectra, the physical reason for contributions from two very distinct angles is unclear. One possible explanation could be a slight misalignment of the samples in the NMR sample tube, causing the helices to tilt.

During this discussion, the spectrum for perpendicular orientation between the GLAD helices and the external magnetic field has not been mentioned. This signal is extremely noisy, due to the small effective area 'seen' by the signal collector. Therefore the alignment of the liquid crystals was deduced almost solely from the spectrum generated by parallel alignment of the helical posts and the stationary magnetic field, although the data collected when the helices were oriented perpendicular to the stationary field does provide a check for the results. The outer splitting frequency of 55 kHz is clearly visible, although the inner details of the spectrum are difficult to discern. Nonetheless, these results are consistent with the parallel case.

The results found here are also consistent with optical results discussed in Section 5.2. If the liquid crystals are tilted out of the plane of the substrate, the overall effect is to reduce the optical anisotropy of the system. When the liquid crystals are perfectly aligned in the plane of the substrate (as for cholesteric LCs) the anisotropy of the system is given by the equation $\Delta n = n_e - n_o$. However, for the GLAD-LC composite system, the NMR study has shown that the LCs are tilted out of the plane of the substrate. This reduces the effective anisotropy in the plane of the substrate which leads to circular dichroism. If, for example, the liquid crystals are tilted out of the plane at an angle of 45°, then the extraordinary index within the plane is reduced to midway between n_e and n_o. Therefore the peak wavelength of the system, as predicted by Equation 5.2, will be reduced. To achieve large circular dichroism, a large optical anisotropy is desired. Reducing the anisotropy reduces the ability of the system to selectively reflect one handedness of light. This is why there is only a 25% difference in the transmission of left and right circularly polarized light for the E7-MgF_2 system described in the literature, as compared with differences of almost exactly 50% for well aligned cholesteric filters.

In conclusion, we have shown that ^{2}H-NMR is an effective tool for determining the alignment of deuterated liquid crystals in a GLAD film. We have shown that LCs tend to align with the rise of the helices, with a small Gaussian distribution. ^{2}H-NMR could be a useful method for determining and optimizing the alignment of liquid crystals in a range of GLAD structures, including square spirals, towards the fabrication of switchable photonic crystals. While the director profile could vary with the type of liquid crystal employed, these results are still relevant for some types of non-deuterated liquid crystals. The non-deuterated version of 5CB-αd_2 is a common LC that comprises one component of E7, a common LC supplied by Merck which is quite popular due to the fact that it is nematic at room temperature. Therefore the results of the study are sufficiently general to be applicable in future work.

5.8 References

1. Elias, A.L., Brett, M.J., Sousa, M.E., Woltman, S.J., Crawford, G.P., Bastiaansen, C.W.M. and Broer, D.J., *Template induced chiral ordering in nematic liquid crystalline materials: A deuterium nuclear magnetic resonance study.* Journal of Applied Physics, 2006. **99**(11).
2. Hecht, E., *Optics.* 2002, Reading, Mass.: Addison-Wesley Pub. Co.
3. Miyano, K., *Wall-Induced Pretransitional Birefringence: A New Tool to Study Boundary Aligning Forces in Liquid Crystals.* Physical Review Letters, 1979. **43**(1): p. 51-54.
4. Ishihara, S., Wakemoto, H., Nakazima, K. and Matsuo, Y., *The Effect of Rubbed Polymer-Films on the Liquid-Crystal Alignment.* Liquid Crystals, 1989. **4**(6): p. 669-675.
5. Gupta, V.K. and Abbott, N.L., *Design of surfaces for patterned alignment of liquid crystals on planar and curved substrates.* Science, 1997. **276**(5318): p. 1533-1536.
6. Wilderbeek, H.T.A., Teunissen, J.P., Bastiaansen, C.W.M. and Broer, D.J., *Patterned alignment of liquid crystals on selectively thiol-functionalized photo-orientation layers.* Advanced Materials, 2003. **15**(12): p. 985-988.
7. Chen, W., Martinezmiranda, L.J., Hsiung, H. and Shen, Y.R., *Orientational Wetting Behavior of a Liquid-Crystal Homologous Series.* Physical Review Letters, 1989. **62**(16): p. 1860-1863.
8. Janning, J.L., *Thin film surface orientation for liquid crystals.* Applied Physics Letters, 1972. **21**(4): p. 173-174.
9. Motohiro, T. and Taga, Y., *Sputter-Deposited Siox Films for Liquid-Crystal Alignment.* Thin Solid Films, 1990. **185**(1): p. 137-144.
10. Crawford, G.P., Vilfan, M., Doane, J.W. and Vilfan, I., *Escaped-Radial Nematic Configuration in Submicrometer-Size Cylindrical Cavities - Deuterium Nmr-Study.* Physical Review A, 1991. **43**(2): p. 835-842.

11. Kralj, S., Zidansek, A., Lahajnar, G., Zumer, S. and Blinc, R., *Phase behavior of liquid crystals confined to controlled porous glass studied by deuteron NMR.* Physical Review E, 1998. **57**(3): p. 3021-3032.
12. Amimori, I., Eakin, J.N., Qi, J., Skacej, G., Zumer, S. and Crawford, G.P., *Surface-induced orientational order in stretched nanoscale-sized polymer dispersed liquid-crystal droplets.* Physical Review E, 2005. **71**(3): p. -.
13. Golemme, A., Zumer, S., Allender, D.W. and Doane, J.W., *Continuous Nematic-Isotropic Transition in Submicron-Size Liquid-Crystal Droplets.* Physical Review Letters, 1988. **61**(26): p. 2937-2940.
14. Ondris-Crawford, R.J., Crawford, G.P., Doane, J.W., Zumer, S., Vilfan, M. and Vilfan, I., *Surface Molecular Anchoring in Microconfined Liquid-Crystals near the Nematic Smectic-a Transition.* Physical Review E, 1993. **48**(3): p. 1998-2005.
15. Kralj, S., Zidansek, A., Lahajnar, G., Musevic, I., Zumer, S., Blinc, R. and Pintar, M.M., *Nematic ordering in porous glasses: A deuterium NMR study.* Physical Review E, 1996. **53**(4): p. 3629-3638.
16. Malac, M. and Egerton, R.F., *Observations of the microscopic growth mechanism of pillars and helices formed by glancing-angle thin-film deposition.* Journal of Vacuum Science & Technology A, 2001. **19**(1): p. 158-166.
17. Broughton, J.N. and Brett, M.J., *Electrochemical capacitance in manganese thin films with chevron microstructure.* Electrochemical and Solid State Letters, 2002. **5**(12): p. A279-A282.
18. Robbie, K., Broer, D.J. and Brett, M.J., *Chiral nematic order in liquid crystals imposed by an engineered inorganic nanostructure.* Nature, 1999. **399**(6738): p. 764-766.
19. Broer, D.J., Lub, J. and Mol, G.N., *Wide-Band Reflective Polarizers from Cholesteric Polymer Networks with a Pitch Gradient.* Nature, 1995. **378**(6556): p. 467-469.
20. Sit, J.C., Broer, D.J. and Brett, M.J., *Liquid crystal alignment and switching in porous chiral thin films.* Advanced Materials, 2000. **12**(5): p. 371-373.
21. Williams, D.H. and Fleming, I., *Spectroscopic methods in organic chemistry.* 4th ed. 1989, London ; New York: McGraw-Hill.
22. Campbell, D., Pethrick, R.A. and White, J.R., *Polymer characterization : physical techniques.* 2nd ed. 2000, Cheltenham, Glos., U.K.: S. Thornes.
23. Harwood, L.M. and Claridge, T.D.W., *Introduction to organic spectroscopy.* 1997, Oxford, England ; New York: Oxford University Press.
24. Keeler, J., *Understanding NMR Spectroscopy*, University of Cambridge, Department of Chemistry: Cambridge, 2002,
25. Crawford, G.P., Stannarius, R. and Doane, J.W., *Surface-Induced Orientational Order in the Isotropic-Phase of a Liquid-Crystal Material.* Physical Review A, 1991. **44**(4): p. 2558-2569.
26. Amimori, I., Eakin, J.N., Qi, J., Skacej, G., Zumer, S. and Crawford, G.P., *Surface-induced orientational order in stretched nanoscale-sized polymer dispersed liquid-crystal droplets.* Physical Review E, 2005. **71**(3): p. 031702-1 - 031702-11.
27. de Gennes, P.G. and Prost, J., *The Physics of Liquid Crystals.* Second ed. 1995, Oxford: Clarendon Press.

28. Lathi, B.P., *Signal Processing and Linear Systems*. 1998, Carmichael, California: Berkeley Cambridge Press.

6 Properties of Liquid Crystalline Polymers

In this chapter, the properties of free-standing and surface-anchored liquid crystalline polymer films are characterized, both experimentally and using finite element analysis. Some of the results presented here have been published in the Journal of Materials Chemistry [1].

6.1 Introduction to Liquid Crystalline Polymers

While silicon is the traditional and dominant material used in microfabrication, polymers are increasingly being investigated for use in microscaled devices such as lab-on-a-chip systems and optical components [2-4]. There are a number of characteristics that favor polymers for use over silicon, including: cost, processability, and tunability [5, 6]. In addition, polymers are of particular interest for micro-actuator devices owing to the large strains that they are able to undergo. As dimensions scale downwards, strain is especially important to achieve large ranges of motions for devices with small dimensions. A few examples of systems which incorporate micro-devices that could potentially benefit from the use of polymers include microfluidic valves and pumps [2, 7, 8], microgrippers [9], controllable surfaces for aerodynamic applications [10], and tunable microlenses [11].

Many different types of responsive polymers have been, and continue to be investigated for use in microdevices. These include conjugated polypyrrole, which undergoes a change in volume in response to an applied voltage (when immersed in a conducting solution) [12]; hydrogels, which can experience significant changes in volume as their ability to absorb water increases or decreases as a stimulus is applied [7, 8, 13]; and paraffin, which expands when heated and contracts when cooled [14]. This chapter focuses on liquid crystalline polymers, which are made from liquid crystalline monomers. Like the liquid crystals described in Chapter 5, liquid crystalline monomers are anisotropic in shape, exhibit mesophases between liquids and crystalline solids, and can be aligned using surface alignment techniques. Like the monomers described in Chapter 4, liquid crystalline monomers contain groups that can be reacted to form a polymer. Monomers that have 2 or more reactive end-groups are sometimes called crosslinkers,

because they can connect together linear chains of polymer to form a chemically linked network. Examples of liquid crystalline monomers with 1 and 2 reactive end-groups are shown in Figure 6.1:

(a) Monoacrylate liquid crystalline monomer

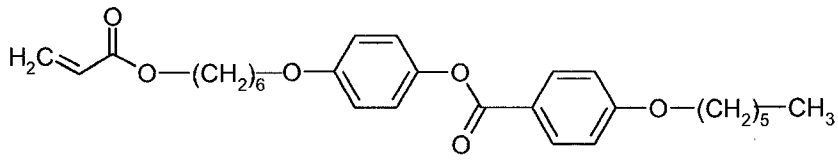

(b) Diacrylate liquid crystalline monomer (crosslinker)

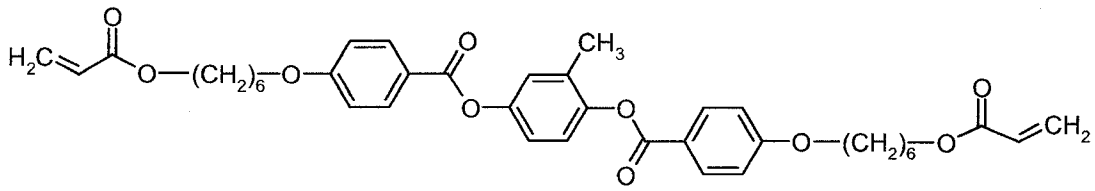

Figure 6.1: Liquid crystalline monomers. Calamitic (rod-like) liquid crystalline monomers are shown, which have with 1 (a) and 2 (b) C=C bonds that can react to form polymers. Monomers with 2 or more polymerizable groups are called crosslinkers, since they can join together 2 or more linear chains of molecules.

Liquid crystalline polymers are often described as a type of 'artificial muscle' as they are able to convert different types of energy (chemical, thermal, electromagnetic) into mechanical work [15-23]. One of the unique properties of liquid crystalline polymers is that, unlike the isotropic polymer materials mentioned in Chapter 4, the direction of deformation can be manipulated by controlling the alignment of the liquid crystalline units of which they are comprised. For example, macroscopic films which roll up when irradiated with UV light have been made using careful alignment of the liquid crystalline monomers [24].

A large section of the literature on liquid crystalline polymers is devoted to liquid crystalline elastomers (sometimes referred to as liquid single crystal elastomers) [16, 18, 25, 26]. Elastomers are a type of polymer which can undergo large, elastic deformations without fracturing [27]. The liquid crystalline elastomers consist of long, highly flexible liquid crystalline molecules connected by highly flexible crosslinking groups. Liquid

crystalline elastomers are usually prepared in a two-step process from a number of components. These components include a flexible, linear polymer backbone (such as poly(methylsiloxane) [18] or poly(methylhydrosiloxane) [25]), liquid crystalline molecules with one reactive end-group, and liquid crystalline and non-liquid crystalline crosslinker molecules which have two or more reactive end-groups. This concept is illustrated schematically in Figure 6.2 [18].

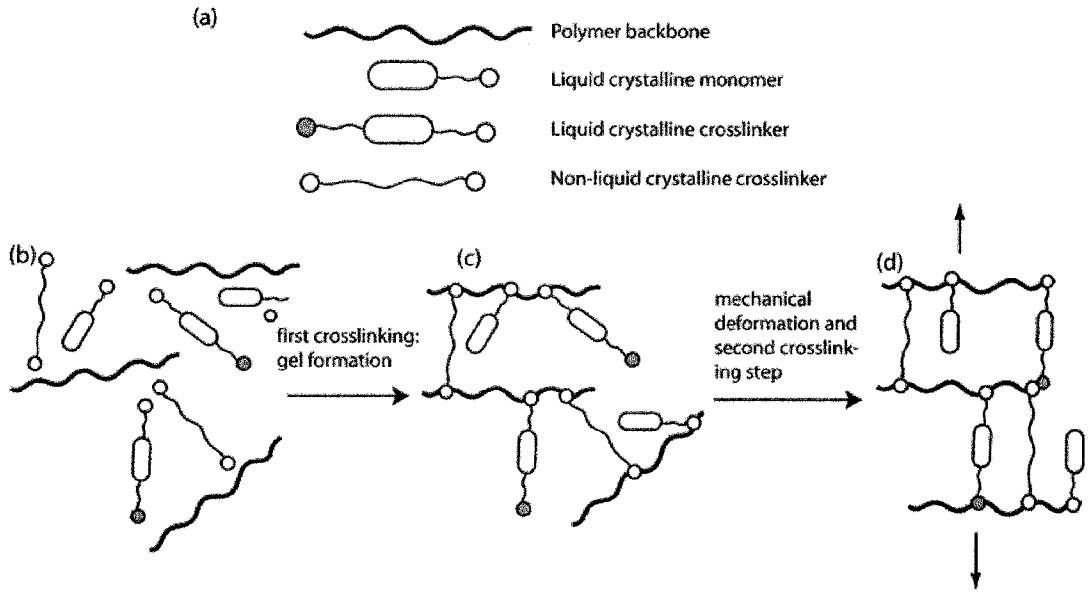

Figure 6.2: Preparation of liquid single crystal elastomers. The components of the elastomer are shown schematically in (a). The white and grey circles on the ends of the liquid crystalline monomer, liquid crystalline crosslinker, and non-liquid crystalline crosslinker denote different types of end-groups. Elastomers are formed from these components in a two-step process. In the first step one of the types of end-groups reacts with the flexible backbone, leading to the formation of a weakly crosslinked gel (c). The liquid crystals in the gel can then be aligned by mechanically deforming the sample, which causes the network to become highly ordered. This order can be preserved by completing the second crosslinking reaction (grey end-groups) (d).

In the first step a gel is formed, which consists of liquid crystals and non-liquid crystalline crosslinkers anchored to the linear polymer backbone. After this crosslinking step the sample is mechanically loaded, causing the liquid crystalline moieties to align with a high degree of order. After loading, this order is preserved by a second crosslinking step, in which the liquid crystalline crosslinkers are locked into place in the network. Note that these LC crosslinker molecules have a reactive end-group that is

chemically different from those reacted in the first crosslinking step to prevent fully crosslinking the sample during the first reaction [18, 28]. The liquid crystalline units within this sample are highly ordered, and if this order is reduced (for example by heating the elastomer towards the isotropic phase) then the sample can undergo large changes in shape. This concept is illustrated in Figure 6.3:

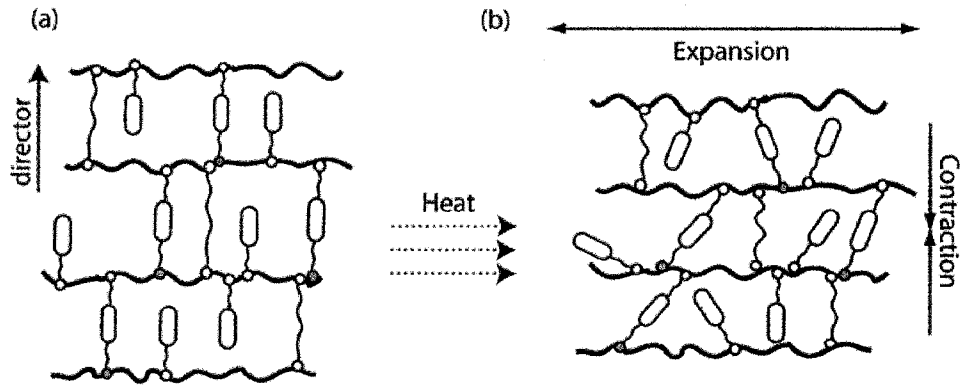

Figure 6.3: Actuation of a liquid crystalline elastomer. Upon heating, the order of the system is reduced, leading to a contraction along the director and expansion in all other directions.

As the order of the liquid crystalline units is reduced, the network itself undergoes a change in shape. Overall, the sample contracts in the direction parallel to the director, and expands in all other directions. This is due to a coupling between the flexible backbone and the liquid crystalline units themselves. Large deformations can be achieved in some types of these materials: liquid crystalline elastomer samples which contract to 25% of their initial length upon heating have been fabricated and characterized [20, 29].

Before liquid crystalline polymers (LCP) can be incorporated into micro-devices, further work must be done to develop techniques to shape these materials on the micro- and nanoscale, and the effect of reducing the dimensions of the material must be studied. The properties of macroscopic samples of liquid crystalline polymers are well documented in the literature; however there are only a few published studies describing micro-patterning of these materials. In 1995 Broer *et al.* showed that a relief structure with submicron features can be patterned into a liquid crystalline polymer by polymerizing the monomer in a mold [30]. In 2003 Wang *et al.* investigated the possibility of patterning LCP using

conventional lithographic techniques for MEMS devices [31]. In this work, LCP was treated as structural rather than active material, and efforts were taken to diminish rather than exploit the anisotropic properties of the polymer. In 2005 van der Zande *et al.* created thin films tiled with 100 μm by 100 μm squares of isotropic and nematic regions [32]. These films were made by selectively polymerizing liquid crystalline monomers (mixed with photoinitiator) in a 2-step exposure. First the sample was heated into the nematic phase and polymerized through a mask to preserve order in half of the squares. Then the sample was heated into the isotropic phase and subject to a flood exposure, to create a randomly ordered polymer in the remaining half of the squares. When viewed at the proper orientation through crossed polarizers, these films resemble checkerboards of black and white regions. These optical properties are desirable for transflective displays which use light from both the ambient environment and a backlight [32]. In 2005 Komp *et al.* prepared arrays of 0.5 mm diameter dots of liquid crystalline elastomer by selectively irradiating a photopolymerizable monomer mixture through a mask, and then washing away the unreacted material. However, the elastomer itself was unaligned. In 2006 Sousa *et al.* extended the work of van der Zande, using similar fabrication techniques to make heat-responsive actuator devices [33]. They found that, when heated, the aligned regions would expand approximately 1% more than isotropic regions due to the anisotropy in the thermal expansion coefficients of the liquid crystalline units comprising the polymer. This concept will be explained in further detail in Chapter 8, when photo-patterning will again be used to make micro-actuators. One other method for micro-patterning liquid crystalline polymers will be mentioned: In 2006 Keller *et al.* reported the fabrication of arrays of high aspect ratio pillars with radii as small as 2 μm comprised of aligned, liquid crystalline polymer [34]. These pillars were fabricated using soft lithography: a photo-polymerizable liquid crystalline monomer mixture was infiltrated into a polydimethylsiloxane (PDMS) mold, aligned in a magnetic field, and exposed to UV light. The sample could then be removed from the mold, leaving beautifully patterned pillars of LCP on a thin substrate of LCP. When the structures were removed from the substrate large (30%) contractions could be achieved on heating. These preliminary results were published in the Journal of the American Chemical Society in 2006.

In this chapter, as well as Chapters 7 and 8, the feasibility of using liquid crystalline polymers as active materials in micro-actuator devices is investigated by looking at the processibility, patternability, and thermo-mechanical behavior of liquid crystalline polymer [1]. An emphasis will be placed on substrate-anchored samples, since most microsystems are attached to a substrate of some sort. Note that while the liquid single crystal elastomers described above exhibit excellent responsivity, these materials are not considered here as they must be mechanically aligned by physically stretching the sample. This process is not readily compatible with microfabrication. Instead, liquid crystalline polymers which can be aligned using surface alignment techniques and polymerized using UV irradiation are studied. These materials can easily be prepared anchored on a substrate for convenient handling. The materials studied here are made from blends of monoacrylate and diacrylate liquid crystalline monomers.

This chapter will focus on investigating the properties of liquid crystalline polymers. In Section 6.2, the crosslinker (diacrylate) content will be optimized to achieve large deformations by examining the thermo-mechanical properties of free-standing macroscopic samples. In Section 6.3, a thermo-optical study will be presented to illustrate the connection between the optical and mechanical anisotropy of LCP and to verify the mechanism of deformation. In Section 6.4, the effect of confining LCP in two dimensions will then be examined by studying how the properties of this material change when one face of the film is securely attached to a glass substrate. Data collected using interferometry will be substantiated with finite element models.

In Chapter 7, three techniques for patterning LCP on the microscale will be discussed, and actuation of some of these structures will be presented. Each of these techniques is based on templating from thin films deposited by glancing angle deposition. In Chapter 8, three additional fabrication techniques will be presented, two of which are based on the photo-patterning work described above, and the last of which is called micro-transfer printing. Actuation of all of these structures will also be described.

6.2 *Thermo-mechanical Properties of Macroscopic Samples of Liquid Crystalline Polymer of Varying Crosslinker Concentration*

The mechanical properties of a crosslinked thin film can vary greatly with crosslinker concentration [35]. If the concentration of crosslinker is high, then the network will be tightly bonded together, resulting in a high modulus and low thermal expansion coefficient. If the concentration is decreased, then the modulus will decrease and the thermal expansion coefficient will increase; however, if the concentration of crosslinker becomes too low, then the deformation of individual liquid crystals will not be coupled to the network. The purpose of the work described in this section is to determine the optimal concentration of diacrylate liquid crystalline crosslinker in a monoacrylate liquid crystalline polymer thin film to achieve large deformations upon heating.

6.2.1 Materials

The liquid crystalline monomers selected for use throughout this work were shown in Figure 6.1, and will be referred to as M1 (for the monoacrylate) and M2 (for the diacrylate crosslinker). These molecules were selected for a few reasons, including: convenient processing temperatures, chemical compatibility, and availability. M1 does not dissolve photoresist, which is important for making helical films using the double replication process (as mentioned in section 4.5). This molecule was synthesized at Philips Research Laboratories by Johan Lub and co-workers. M2 was originally developed by Broer *et. al*, and is commercially available from Merck under the name RM82. Both of these monomers are types of acrylates, which means that they can be readily polymerized using free-radical initiators. To induce polymerization the monomers were mixed with 1% to 2% photoinitiator (by weight) and irradiated with UV light. The photoinitiator selected for most of these experiments was Irgacure 184 (CIBA), which was discussed in-depth in section 4.3.

6.2.2 Sample Preparation

One emphasis of this work has been to align the liquid crystalline monomers using techniques which are compatible with microfabrication processes. Here, samples are

prepared using surface alignment techniques which are already very commonly used for LC alignment in liquid crystal displays.

Samples were prepared for testing by polymerizing mixtures of M1, M2 and Irgacure 184 initiator in cells. These cells consisted of pieces of glass coated with thin layers alignment layers of polyimide (AL 3046, JSR). Polyimide is a standard alignment layer for the construction of optical liquid crystalline devices. This alignment layer was spin-coated from solution (spread at 500 rpm for 5 s, spun at 5000 rpm for 40 s), soft-baked (pre-baked on a hotplate for 10 minutes at 100 °C), hard-baked (heated for 90 minutes under rough vacuum at 180 °C), and rubbed unidirectionally with a velvet cloth (5 times) to dictate the direction of alignment. The resulting layer was very thin (<100 nm), and completely transparent. To construct the cells, 1 in. glass squares coated with rubbed polyimide were adhered together using Norland Optical Adhesive. To prepare samples for thermo-mechanical testing, the thickness of the gap between the cells was controlled by layering two pieces of tape and a glue/spacer mixture along the edge of the glass plates before constructing the cells. The glue/spacer mixture consisted of 18 μm glass fiber spacers mixed into the optical adhesive. The total gap of the cells was thus regulated to 60 μm to 80 μm. Note that thinner cell gaps are also achievable. For example, glue containing either 10 μm or 18 μm spacers can be used to achieve gaps of approximately 10 μm or 18 μm, or glue without spacers can be used to make cells with gaps of roughly 5 μm. Cells with different spacer layers will be used throughout this chapter to achieve films with varying thicknesses. For the samples produced for thermo-mechanical characterization, a large thickness was chosen to ensure that the thin film samples were thick enough to handle and measure. LC monomer mixtures were infiltrated into the cells by capillary action in the isotropic phase of the mixtures, typically at approximately 70 °C. The cells were then cooled to within the nematic phase of the mixture (55 °C to 58 °C), and polymerized in UV light for five minutes under a light flow of nitrogen. All of the samples described in this chapter were polymerized using either the Philips solarium or home-built UV lamp described in Section 4.3. After UV exposure, samples were heated to 100 °C to promote increased polymerization of the sample. After cooling, the cells could be opened and the samples could be removed from

both glass substrates using a razor blade. This fabrication process is summarized in Figure 6.4:

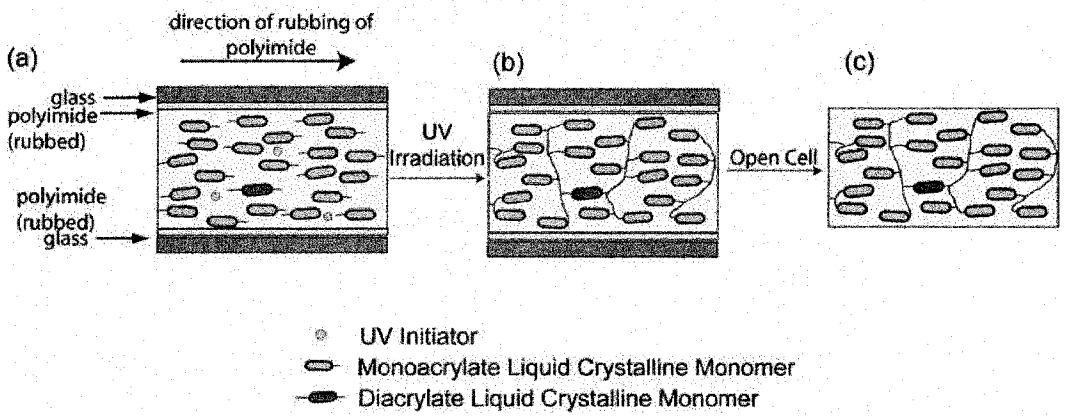

Figure 6.4: Fabrication of uniaxially-aligned LCP thin films. In this process a liquid crystalline monomer mixture is filled into a cell consisting of two glass plates coated with polyimide (a). The LC molecules align in the direction in which the polyimide was rubbed. The sample is polymerized in UV light (b). The film can then be removed from the glass plates (c).

As shown in Figure 6.4, the liquid crystalline molecules are aligned along a director dictated by the direction in which the polyimide was rubbed. These samples can be called 'uniaxially-aligned'. Samples with this alignment were selected for measurement to allow direct observation of the thermo-mechanical properties of the sample in the directions parallel and perpendicular to the long axes of the liquid crystals.

It has been demonstrated in the literature that the mechanical properties of UV-polymerized multifunctional polymers can change significantly upon annealing [36-38]. One explanation for this effect is that during polymerization, the material vitrifies before the polymerization reaction goes to completion. Throughout the first heating cycle, the viscosity of the material is reduced, and the polymerization reaction can continue. During the thermo-mechanical characterization described in the next section, it was found that the behavior of a sample on the first heating cycle was not reversible, although the behavior on subsequent heating cycles was. Therefore, before every characterization experiment (thermo-mechanical or otherwise), each sample was heated to 200 °C, which was usually the maximum temperature to which samples are heated during the actual

characterization. This ensured that the behavior of the samples in subsequent heating cycles was repeatable.

6.2.3 Thermo-mechanical Characterization

5 samples were prepared for characterization using the method outlined in section 6.2.2. The M2 crosslinker concentrations in these samples were: 5%, 10%, 12%, 15%, and 20% (by weight). Samples were characterized using a Pyris Thermal Mechanical Analyzer (Perkin Elmer). Each film was clamped at either end, and a small tensile force (50 mN) was employed to ensure that the films were fully extended. The sample and sample holder were then immersed in a small tube furnace, and the length of the sample was monitored as the temperature was cycled between 25 °C and 140 °C at a rate of 5 °C/min. The results are shown in Figure 6.5.

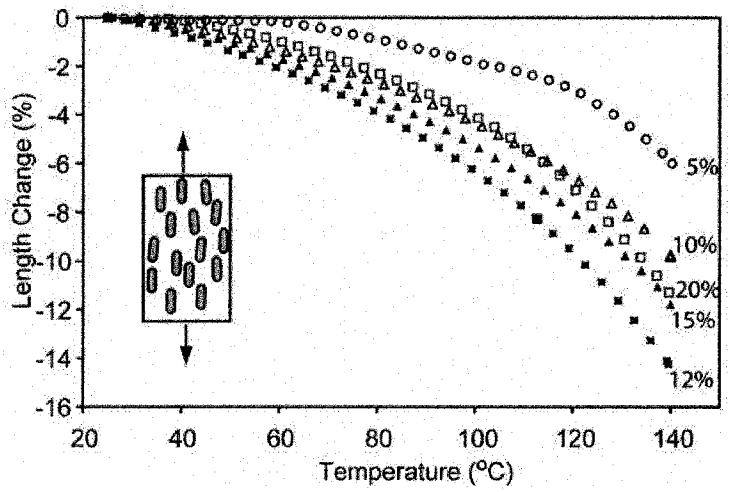

Figure 6.5: Thermal actuation of uniaxially-aligned LCP film. The contraction of liquid crystalline polymer films was measured using thermal mechanical analysis. 5 samples were measured, and in each case the length in the direction parallel to the director was monitored (as shown, inset). The length change is plotted relative to the initial length of the sample at room temperature. Each curve is labeled with the percent crosslinker (M2) in each sample (as a function of the total weight of liquid crystalline monomers in the sample). The largest contraction was seen for the sample containing 12% crosslinker.

The curves shown in Figure 6.5 were found to be reversible and repeatable in heating and cooling. Note that the length of each sample was monitored in the direction parallel to the director (the axis along which the molecules are aligned), so overall, a decrease in length was expected (and observed) upon heating. While it might be expected that the

sample with the lowest crosslinker content would be the most free to contract and therefore undergo the largest deformation, this is clearly not the case. We hypothesize that for the 5% and 10% systems, the motion of the liquid crystalline units is not sufficiently coupled to the network to cause a macroscopic deformation of the sample (this theory will be further explored in Section 6.3). The results show that the largest deformation was achieved for the sample containing 12% crosslinker. Based on these results a thermally responsive liquid crystalline polymer comprised of a ratio of 88:12 M1:M2 was used throughout the remainder of this study, and will be referred to as poly(M1:M2, 88:12). Since these samples also include 1% to 2% initiator, the actual percentages are typically around 86% M1, 12% M2, and 2% 184 initiator. Nonetheless the polymer will be referred to as poly(M1:M2, 88:12) to emphasise the relative concentration of these two components. Occasionally, the initiator Irgacure 369 (CIBA) was employed rather than Irgacure 184, but this change in initiator was not expected to significantly affect the properties of the samples.

For the poly(M1:M2, 88:12) sample, the change in length as a function of temperature was also measured for the direction perpendicular to the director. The results are shown in Figure 6.6:

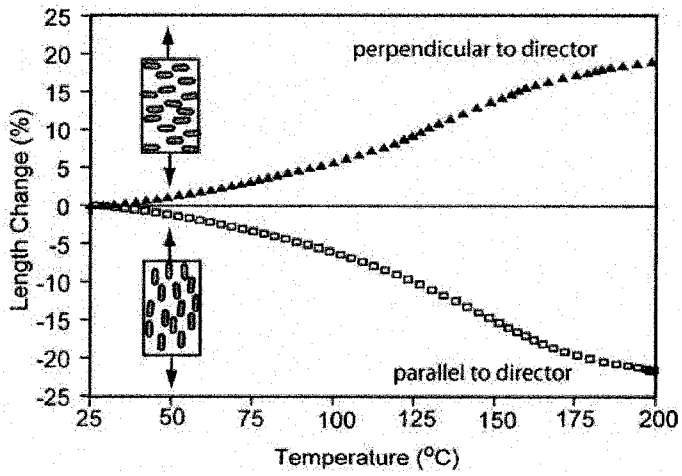

Figure 6.6: Parallel and perpendicular thermo-mechanical behavior. The expansion and contraction of a uniaxial thin film containing a ratio of 12:88 M2:M1 is shown, as measured in directions parallel and perpendicular to the director. The orientation of the LCs with respect to the direction of measurement is shown inset for both cases. Upon heating to 200 °C, the sample expands 19% in directions perpendicular to the director and contracts 22% along the director.

Overall, the film contracted along the director by 22%, and expanded in the direction perpendicular to the director by 19%. The total change in volume can be estimated from the equation $\frac{\Delta V}{V} \approx \frac{\Delta l_{parallel}}{l_{parallel}} + \frac{2\Delta l_{perpendicular}}{l_{perpendicular}}$, and works out to 16% [21]. Note that in the above equation the perpendicular direction is multiplied by two, because the film contracts in one dimension (along the director) and expands in the other two.

The elastic modulus of a uniaxial thin film containing 12% M2 and 88% M1 was measured in each direction using dynamic mechanical analysis, as described in Section 4.4. At 30 °C and a frequency of 1 Hz, the modulus was found to be 22 MPa perpendicular to the director and 125 MPa parallel to the director. The glass transition of the material was determined to be around 22 °C to 25 °C. The glass transition temperature (T_g) is the temperature below which the polymer is glassy and rigid, and above which the chains have some increased mobility. The modulus of these films is much higher than for the liquid single crystal elastomers described in the literature, which have very low moduli (for example: 500 Pa – 1 MPa at the nematic to isotropic transition temp [20]). Unfortunately, it was not possible to measure the mechanical properties of poly(M1:M2 88:12) at higher temperatures due to limitations of the instrument used to characterize the samples.

Note that while the glass transition temperature of the material is around room temperature, the samples discussed throughout this thesis are polymerized at elevated temperatures (typically 55 °C to 60 °C). This means that the polymerization reactions should not be significantly impeded by vitrification effects in which the network becomes stiff before all of the monomers are reacted, preventing further reactions from taking place. Recall that vitrification effects can also cause free volume to be trapped in the sample. Although vitrification effects should not be a problem for the samples described here due to their low glass transition temperatures, most of the samples described in this chapter (as well as Chapters 7 and 8) are heat treated (usually by heating to 200 °C) before characterization to ensure that the reaction has gone as far as possible, and also to relieve free-volume that may be trapped in the network.

6.3 *Optical Properties of Uniaxially-Aligned Liquid Crystalline Polymer Thin Films*

6.3.1 Theory

Examining the thermo-optical properties of a liquid crystalline polymer film can help to elucidate its thermo-mechanical behavior. The most common use for liquid crystals is in display devices, where these materials are exploited for their anisotropic optical properties. Liquid crystals are birefringent: they exhibit one index of refraction in the direction parallel to the long axis of the molecule (the extraordinary index n_e), and another index of refraction in all directions perpendicular to this axis (the ordinary index n_o). This concept is illustrated in Figure 6.7 (a):

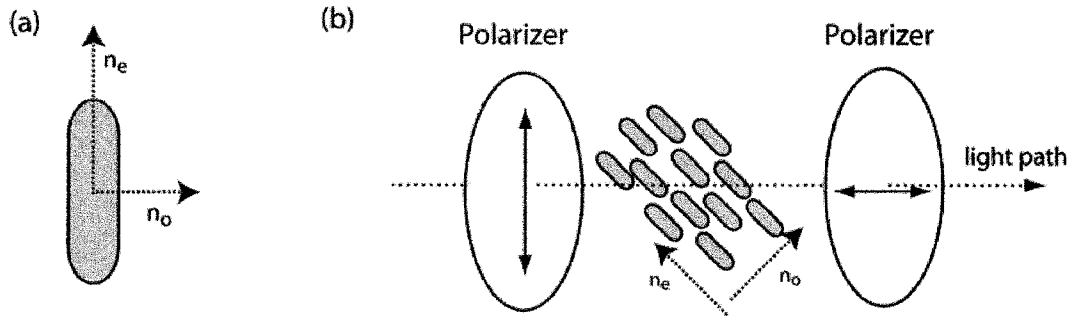

Figure 6.7. Optical properties of liquid crystals. Liquid crystals have one refractive index parallel to the long axis of the molecule (n_e), and another refractive index in all directions perpendicular to this axis (n_o) (a). If the LCs are well aligned within a film, then the film itself will also be birefringent, and can act as a waveplate, rotating the polarization of light which passes through crossed polarizers (b). The direction of the transmission axis of each polarizer is indicated by the direction of the arrows.

The birefringence of a liquid crystal can be observed by placing a uniaxially-aligned sample between crossed polarizers, as shown in Figure 6.7 (b). Normally, when a beam of light passes through a polarizer with a vertically oriented transmission axis and then encounters a polarizer with a horizontally oriented transmission axis (i.e., crossed polarizers) none of the light emerges, as both the horizontal and vertical components of the beams are absorbed. When a uniaxially-aligned liquid crystalline film is placed between the polarizers it acts as a waveplate, introducing a path length difference (Λ) between the extraordinary and ordinary components of the linearly polarized light

incident upon it. The path length difference is dependent on both the thickness (h_f) and refractive indices (n_e and n_o) of the film, as illustrated in Equation 6.1:

$$\Lambda = h_f(|n_e - n_o|) \qquad [6.1]$$

Transmission maxima in the light emerging from the second polarizer are observed when the orientation of the linearly polarized beam incident on the liquid crystalline film undergoes a 90° rotation (or a rotation of an odd multiple of 90°). In vector terms, this means that a phase difference of $m\pi$ (where m is an odd integer) must be introduced between the extraordinary and ordinary electric field vectors of the incident light, as demonstrated in Figure 6.8:

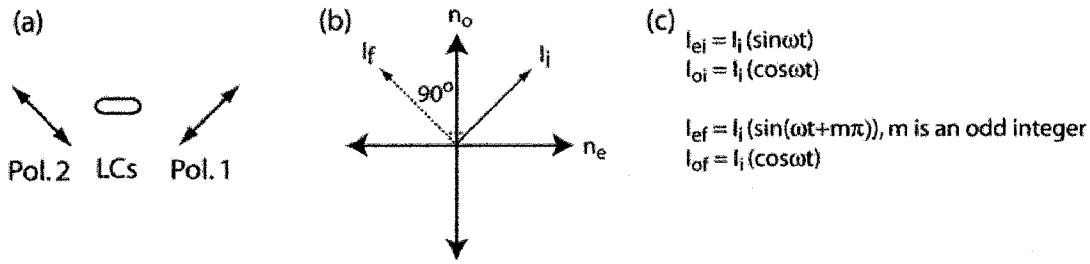

Figure 6.8: Vector representation of light incident on the liquid crystalline film. The orientation of the polarizers (Pol.1 and Pol.2) with respect to the film is shown in (a). In this frame of reference the angle of the initial beam (I_i) is taken to be at +45° (parallel to the fast axis of Pol. 1). To achieve maximum transmission, then the beam must be rotated by 90° (or some odd multiple of 90°) as it passes through the LC film so that it is parallel to Pol. 2, achieving a final angle of +135°. The mathematical representations of I_i and I_f broken down into components in the direction of n_o and n_e are shown in (c).

The relationship between path length difference (Λ) and phase difference ($\Delta\varphi$) is given by Equation 6.2 [39]:

$$\Lambda = \Delta\varphi(\lambda_o / 2\pi) = h_f|n_e - n_o| \qquad [6.2]$$

Therefore, knowing the film thickness (h_f), and by measuring the transmission of light through the film as a function of wavelength, it is possible to deduce the birefringence ($\Delta n = n_e - n_o$) of the film, although additional fitting algorithms must be employed to determine the value of the integer m [40, 41].

As mentioned, it is the unique optical properties of liquid crystals described here that make them ubiquitous for use in display devices (that is, combined with the additional property that liquid crystals can be switched between different orientations using an electric field). The birefringence described above is also exhibited by liquid crystalline polymers. An examination of the optical properties of a liquid crystalline film as a function of temperature should provide additional insight into the mechanism by which the film deforms. From the results of the thermo-mechanical study presented in Section 6.2, it is expected that as a uniaxially-aligned liquid crystalline polymer film is heated, the order of the system should decrease steadily as the film approaches the isotropic phase. When the isotropic phase is reached, the random alignment of the molecules throughout the sample will cause the overall average optical anisotropy of the system to approach 0. Therefore, as the sample is heated the birefringence of the system will necessarily decrease, as the molecules become less and less uniaxially-aligned.

6.3.2 Measurements

To verify the optical behavior of the samples as a function of temperature, the birefringence of a uniaxially-aligned samples of liquid crystalline polymers were measured as a function of temperature as the sample was heated from room temperature to 225 °C.

Samples was prepared as per the technique outlined in Section 6.2.2, only the gap of the cells in which the film was polymerized was controlled to approximately 18 μm by mixing glass fibers into the optical adhesive used to bond the glass plates together. After polymerizing the samples the cells were opened and the films were delaminated from the cells using a razor. The thickness of the films was confirmed using a micrometer.

Measurement of the birefringence itself was achieved using a Shimadzu 3102 spectrophotometer and integrating sphere, with a fitting procedure which will be described below. Data was collected by placing the sample at 45° between crossed

polarizers within the spectrophotometer and measuring the transmission through the sample as a function of wavelength. One such set of data is shown in Figure 6.9:

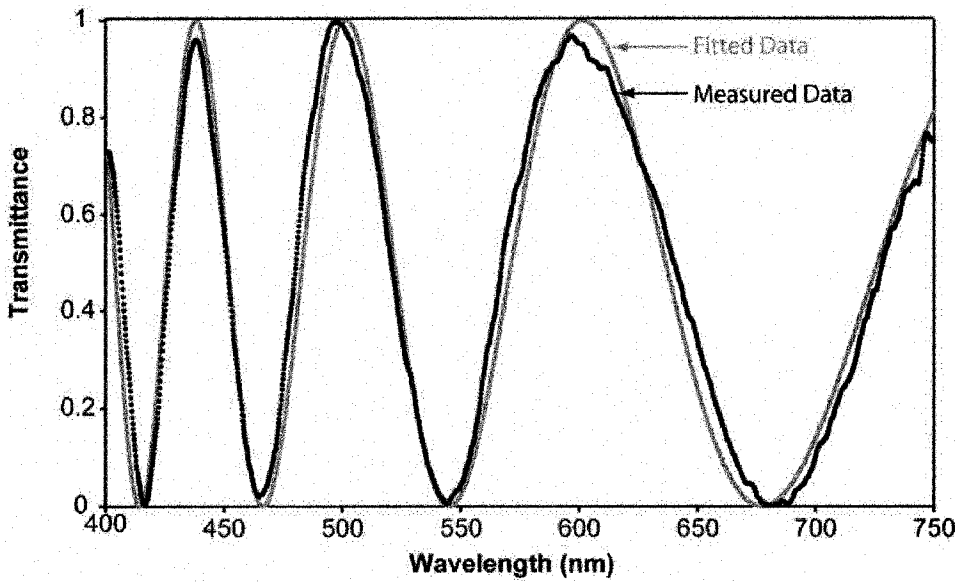

Figure 6.9: Transmittance of light through a birefringent sample. The data shown was collected with a sample containing 12% M2 oriented at 45° to crossed polarizers at 25 °C. The transmittance itself varies as a function of wavelength, with peaks occurring at wavelengths for which a phase difference of $m\pi$ (where m is an odd integer) is introduced between components of the incident beam which are parallel to the extraordinary and ordinary axes of the uniaxially-aligned liquid crystalline film. Likewise, minima occur at wavelengths for which a phase difference of nπ (where n is an even integer) is introduced between components of the incident beam which are parallel to the extraordinary and ordinary axes of the uniaxially-aligned liquid crystalline film. This figure illustrates measured data overlaid with fitted data. The measured data has been smoothed using a Gaussian averaging function described below.

Note that the measured data has been smoothed using a Gaussian averaging function that averages each data point with the 12 data points around it. The contribution of each data point towards the average is weighted using a Gaussian distribution, with a standard deviation of $\sigma = 2$, as illustrated in Equation 6.3:

$$z_{filtered}(m) = \sum_{n=-6}^{6} (z(m-n)) \frac{\exp(-n^2/2\sigma^2)}{\sigma\sqrt{2\pi}} \qquad [6.3]$$

In this equation $z_{filtered(m)}$ is the filtered value at the m^{th} data point. The transmission of light through a waveplate oriented at 45° to crossed polarizers can be fit using Equation 6.4 [40]:

$$T = \frac{1}{2} T_o \sin^2\left(\frac{\pi \Delta n h_f}{\lambda}\right) \qquad [6.4]$$

However, this equation cannot not be solved explicitly for Δn due to its periodic nature, as well as the fact that the square root must be taken to isolate the term Δn, which leads to multiple solutions. Therefore, a second equation must also be used to determine the correct value of Δn. The Cauchy Equation is a simple model which expresses the birefringence of a material as a function of wavelength. The Cauchy Equation is stated in Equation 6.5, where higher order terms have been ignored:

$$\Delta n \cong n_\infty + \frac{A}{\lambda^2} \qquad [6.5]$$

These problem can be solved iteratively using the Excel 'data solve' function provided that h_f, the sample thickness, is known. In this technique, values for A and n_∞ are estimated and Equation 6.5 is calculated for every wavelength. This value of (Δn) is then substituted into Equation 6.4 (also at every wavelength) to determine the modeled transmission ($T_{model(\lambda)}$). From here the least-squared method is used. The difference between the modeled and measured values of $T(\lambda)$ are computed and squared, as per Equation 6.6:

$$L(\lambda) = \left[T_{\mathrm{mod}}(\lambda) - T_{meas}(\lambda)\right]^2 \qquad [6.6]$$

The least-squared values of $L(\lambda)$ are then summed over all wavelengths, as shown in Equation 6.7:

$$L_2 = \sum_{\forall \lambda} L(\lambda) \qquad [6.7]$$

The values of A and n_∞ are then adjusted within the Excel function to minimize the value of L_2. The value of Δn at a specific wavelength can be calculated by substituting the

chosen values of A and n_∞ into Equation 6.5. This value of Δn can then be substituted into Equation 6.4 to generate the fitted data shown in Figure 6.9.

This algorithm was used to measure the birefringence of a free-standing sample of poly(M1:M2, 88:12) as the sample was heated from 25 °C to 225 °C, held, and cooled back to room temperature. The sample was heated and measured in 5 °C steps. For comparison, the birefringence of a film of 2.5% M2 and 97.5% M1 was also measured. The results of the study are illustrated in Figure 6.10. Note that the birefringence itself is wavelength dependent, and therefore the birefringence reported is for the wavelength λ=589nm.

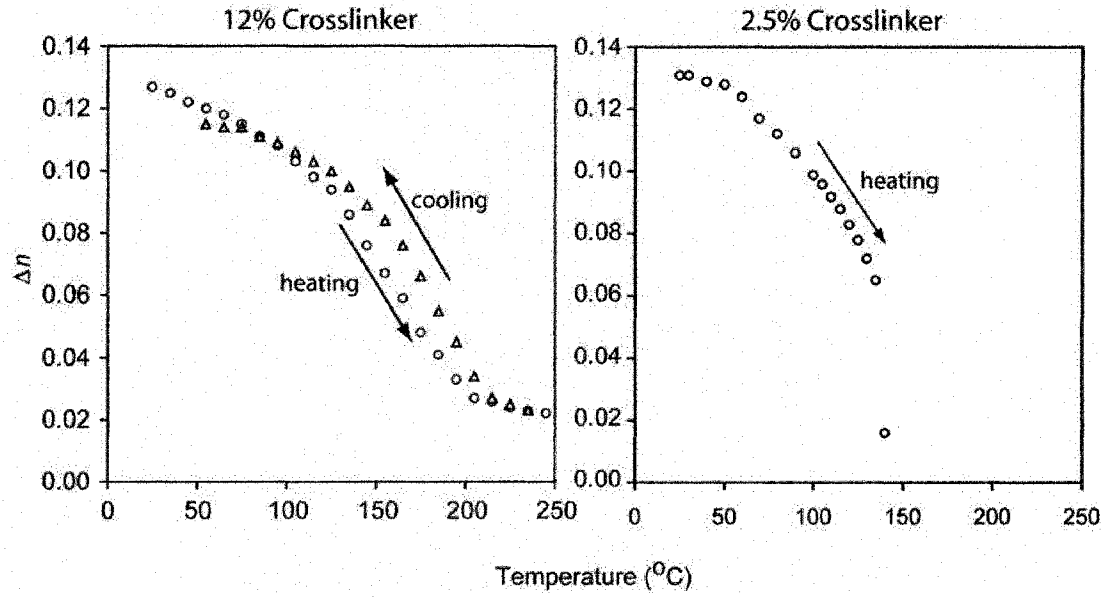

Figure 6.10: Birefringence as a function of temperature. The birefringence (at 589 nm) is shown as a function of temperature for free-standing films containing 12% and 2.5% crosslinker. The 12% film is measured in heating and cooling. Because this film was measured on its first heating cycle the measurements are not completely reversible. The 2.5% film is shown in heating only on the second heating cycle. The film containing only 2.5% crosslinker decreases in birefringence at a much lower temperature than the film containing 12% crosslinker.

At room temperature, both samples have a birefringence of around 0.12. The order parameter can be estimated from this value using the Haller method, and is approximately 0.6 [42-44]. Both samples experience a roll-off in birefringence as a function of temperature. For the 2.5% sample it became very difficult to discern any birefringence

above 140 °C, indicating that the film undergoes a nematic to isotropic transition around this temperature (recall that in the isotropic phase the liquid crystals have no net alignment and are randomly arranged). The film containing 12% crosslinker experienced a slower roll-off in birefringence, with the value approaching 0 above a temperature of 215 °C (although a small amount of birefringence does persist, due perhaps to the crosslinking molecules). Note that the 12% sample (poly(M1:M2, 88:12) was measured on its first heating cycle, which could explain why some hysteresis is visible. This hysteresis may also simply result from the difficulty in heating and cooling a free-standing thin film <20 μm thick, which may buckle or deform slightly due to its delicate nature. Nonetheless the film recovers most of its birefringence on cooling.

Recall from the results of the thermo-mechanical measurements in section 6.2, that films with very low crosslinker content exhibited reduced changes in dimension as a function of temperature than films containing 12% crosslinker. It was hypothesized that for films with lower crosslinker content the deformation of the LCs was insufficiently coupled to the network to cause a macroscopic deformation of the sample. This hypothesis is supported by the results illustrated in Figure 6.10, since it is clear from this data that the LCs themselves in the 2.5% film are undergoing a reduction in order with heating. This reduction in order is not, however, being transferred to the network overall.

6.4 Mechanical properties of samples confined to a surface – modeling and results

The focus of this section is to examine how the properties of liquid crystalline thin films change when their dimensions are scaled downwards. The purpose of this work is to evaluate the suitability of incorporating these materials into microdevices. The thin films investigated in Section 6.2 and 6.3 can already be considered 'micro', as they each have one dimension in the micron range (that is, film thickness). But, these samples are still very 'macro', as they are large enough to be manipulated easily by hand or with tweezers. An important consideration for samples which are microscaled in all three dimensions is how their properties will change as a result of being anchored to a substrate, since they would otherwise be very difficult to handle. When the free-standing films described

above are attached to a substrate, this substrate acts as a boundary, preventing the anchored face of the film from moving in the x, y, or z direction. The main focus of this section is to investigate how this confinement affects the thermo-mechanical behavior of the sample. This problem will be modeled using finite element modeling and explored experimentally using white light interferometry.

While up to now only samples with uniaxial alignment have been investigated, in this section liquid crystalline polymers with 4 different director profiles will be considered. These configurations are: (1) planar alignment, in which the LCs are uniaxially-aligned in the plane of the substrate (as before); (2) homeotropic alignment, in which the LCs are uniaxially-aligned along an axis perpendicular to the plane of the substrate; (3) isotropic, in which the alignment is entirely random; and (4) cholesteric, in which the director profile rotates along an axis perpendicular to the substrate (as discussed below). These 4 configurations are illustrated in Figure 6.11:

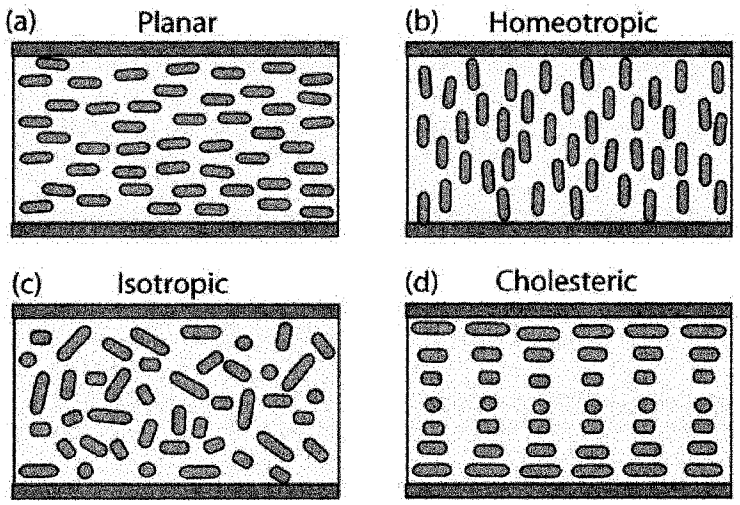

Figure 6.11: LC configurations. Schematic diagrams of liquid crystals exhibiting planar alignment (a), homeotropic alignment, isotropic (c) and cholesteric (also called chiral nematic) (d) are shown.

In addition to the nematic phase, the cholesteric phase (or chiral nematic phase, depicted in Figure 6.12(d)) is one of the common mesophases that can be exhibited by calamitic liquid crystals. In the cholesteric phase the director rotates about an axis perpendicular to the plane in which the long axes of the LCs themselves are aligned, forming a helical structure with pitch p. This alignment can be achieved by adding a chiral molecule or

chiral dopant to calamitic liquid crystals, where the concentration of the chiral dopant determines the pitch.

Liquid crystalline molecules in the cholesteric phase act as Bragg reflectors, selectively reflecting circularly polarized light whose wavelength (λ_m) matches the handedness and effective pitch of the chiral structures, as per Equation 6.8:

$$\lambda_m = p\Delta n_{ave} \qquad [6.8]$$

Where Δn_{ave} is the average index of refraction of the liquid crystalline layer [45]. This equation applies for light at normal incidence to the helical pitch; for light traveling off-axis a cosine term must be included in the denominator. The reflection bands of these films are often visible to the eye, and can fluctuate with temperature as thermal energy causes the liquid crystalline molecules to move further apart from each other, and to tilt out of the plane [46]. For mixtures of nematic liquid crystals and chiral dopants, this results in an increase in pitch with temperature. In fact mood rings, which are sold in many novelty stores, typically contain cholesteric liquid crystals whose pitch changes as a function of the body temperature of the wearer.

Chiral dopants can also be added to liquid crystalline monomer mixtures, allowing the preservation of the chiral ordering by polymerization. The dopant used in this work (BASF, LC 756) is itself an acrylate, and can be polymerized into the network. A molecular diagram of this molecule is not supplied here for proprietary reasons. Chiral dopant was added in a quantity of 5% of the total weight of the M1/M2 mixture.

6.4.1 Experimental Method

Liquid crystalline polymer samples of poly(M1:M2, 88:12) having each of the director configurations illustrated in Figure 6.11 were prepared using simple fabrication techniques. Films were prepared in a method similar to that described in 6.2.2, only smaller spacer layers (either glue containing glass fiber spacers, or glue alone) were used to achieve thinner samples with thicknesses ranging from 4 μm to 18 μm (thick layers were no longer required to handle the films). A planar sample was prepared using rubbed

polyimide alignment layers, as described in Section 6.2.2. A sample with homeotropic alignment was prepared using a similar method, only a surface treatment rather than an alignment layer was used to align the LCs. The glass plates from which the cells were made were treated with a UV ozone plasma for twenty minutes, which terminates the surface of the glass with OH groups that promote homeotropic alignment. The cells could then be constructed, filled, and polymerized as normal. Isotropic samples were made using cells with polyimide alignment layers, only after filling the cells were heated to 100 °C before being polymerized in UV light. Samples with a chiral director profile were prepared by polymerizing monomers in the cholesteric phase, which is induced by adding a chiral dopant to the mixture of liquid crystalline monomers.

In each case samples were polymerized in a cell and heat treated to 100 °C. After cooling the cells were opened with a razor blade, but this time the films were not delaminated, rather they were left anchored on one of the glass plates of the cell. The thickness of each sample was measured as a function of temperature using white-light interferometry.

6.4.2 White-light Interferometry

White-light interferometry is a powerful characterization tool that can be used to map the surface of a sample with a vertical resolution of a few nanometers [47]. This technique is widely used for topographical measurements due to a number of favorable attributes including: the non-destructive nature of the technique, the ability to measure optically rough surfaces, and the ability to resolve discontinuous height variations accurately [47, 48]. Using white light to measure distance is an older technique than might be expected, as Hooke first noted the relationship between white light interference fringes and distance in 1665.

In interferometry a single beam is split over two paths and recombined such that it interferes with itself. A very basic set-up is illustrated in Figure 6.12: light from a source is split into two waves by a beamsplitter. Half of the beam is directed to a reference mirror, where it is reflected back towards the detector (usually a charge coupled device (CCD) camera). The other half of the beam travels to the sample itself, and is reflected from the sample to the detector.

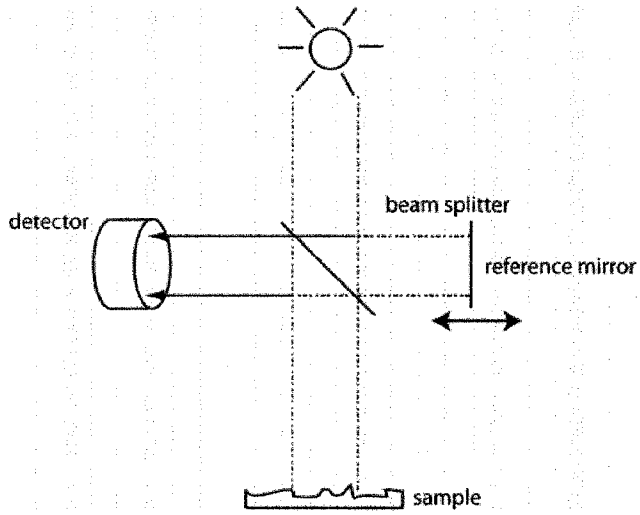

Figure 6.12: A simplified interferometer. Light from the source is split, and travels along two paths, one to a reference mirror and the other to the sample itself. Light is reflected and collected at the detector to form a spatially-dependent interference pattern.

The two beams interfere at the detector, producing a spatially dependent pattern which can be used to create a surface map of the sample. This interference pattern is only useful if the beams are relatively coherent, which is to say that they have a relatively constant phase difference between them for the length of the measurement. Otherwise the two beams can vary rapidly between perfectly in phase and perfectly out of phase, and when the measurement is averaged over a period of time no useful information will be extracted. If a laser is used as the source then the light is monochromatic, and typically has a very large coherence length (i.e., the phase and frequency of the beam does not change significantly over time or space). Good interference patterns can be generated regardless of the path length difference between the two arms of the interferometer. The intensity at a location *(x,y)* resulting from the interference of two beams is given by the interference equation, as shown in Equation 6.9 [49]:

$$I = I_1 + I_2 + 2(I_1 I_2)^{1/2} \cos(\phi_w(x,y)) \qquad [6.9]$$

In this equation I_1 is the intensity of beam 1, I_2 is the intensity of beam 2, and $\phi_w(x,y)$ is the phase difference between the beams at position (x,y). During measurement the reference mirror is moved in the direction parallel to the beam, and an algorithm is used to determine the phase difference ($\phi_w(x,y)$) at each point [47, 50, 51]. The height distribution across the surface can then be calculated using Equation 6.10 [50]:

$$h(x,y) = \frac{\lambda}{4\pi}\phi_w(x,y) \qquad [6.10]$$

This method is called phase-shifting interferometry [51]. The main problem with this fast and reliable technique is that there is a certain amount of ambiguity in the profile due to the 2π periodicity of the phase. Therefore the surface can only be mapped accurately provided that the change in height between adjacent points does not change by more than $\lambda/4$. Discontinuities in the surface and sharp sidewalls are therefore not mapped correctly.

Accurate resolution of more complex profiles with discontinuities can be made using white light interferometry. In this case the sample is illuminated by light from a white-light source, which necessarily has a very short coherence length. White light is composed of light of a broad range of frequencies, and therefore its phase can change rapidly over a few wavelengths. Therefore interference patterns can only be generated if the path length of each arm is very close to equal [50].

When a sample is measured, the reference mirror is moved in the direction of the beam. This changes the phase difference between the two arms. The interference pattern is often imaged using a computer, and during the measurement itself a pattern of light and dark fringes moves over the screen from one side to another. For surfaces with great topological variation, the fringes move from the lowest to highest surfaces (or vice-versa). The intensity as a function of mirror position is recorded at each pixel, from which a number of different algorithms may be used to generate a height map of the surface. This technique is free from ambiguity due to phase [48].

Characterization using white light interferometry was performed with the Fogale ZoomSurf 3-D optical profiling system. For these experiments a 5x lens was used to image the surface of the sample, allowing an area of 1200 μm x 1600 μm to be imaged at a time. The temperature of each sample was controlled using a home-built hot plate. To allow the thickness of each sample to be measured with respect to the baseline of the substrate, part of every film was removed with a razor to provide an area of reference. Averaging and multiple measurements were employed to ensure the precision of the results. Typically, thickness was determined by averaging the height of a large area of film (~1 mm^2) and subtracting from this the height of large areas (~1 mm^2) of substrate. These results were also verified by examining cross-sectional views generated by the Fogale software. Results generated by each of these methods were usually in good agreement with each other, although they sometimes differed by 10 nm to 80 nm (0.2% to 2% for a 5 μm thick film). In an additional quest for precision, each type of film was measured at least twice.

6.4.3 Experimental Results

The cross-sectional profile of one of the isotropic samples is shown in Figure 6.13:

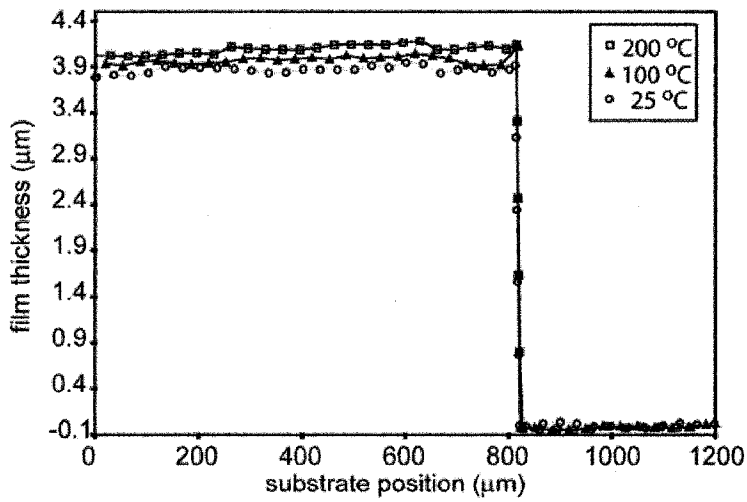

Figure 6.13: Thermal actuation of surface-anchored samples. The change in thickness of an isotropic sample anchored on the surface of a glass slide as a function of temperature is shown. This data was measured during cooling and the expansion and contraction of the film was found to be reversible. The baseline for the measurement is the surface of the glass slide, as seen at the lower step on the right hand side of the graph.

While for clarity Figure 6.13 shows the profile of an isotropic film at only three different temperatures, in most runs 6 to 12 data points were collected during heating and cooling. The results for the 4 different sample types are summarized in Table 6.1.

Director Profile	Measured Expansion at 200 °C (Δh)
Isotropic	5%
Homeotropic	2%
Planar	9%
Cholesteric	11%

Table 6.1: Alignment-dependent thermal actuation. The total thermal expansion of surface-anchored LCP samples with isotropic, homeotropic, planar and cholesteric alignment is summarized. The final thickness is measured at 200 °C, and values are expressed as a function of the film thickness at 25 °C.

These results are expressed as a percentage variation in the film thickness, as illustrated by Equation 6.1

$$\Delta h = \frac{h_{200\,^\circ C} - h_{25\,^\circ C}}{h_{25\,^\circ C}} 100\% \qquad [6.11]$$

In this equation $h_{25\,^\circ C}$ is the thickness at 25 °C, and $h_{200\,^\circ C}$ is the thickness as measured at 200 °C.

The out-of-plane expansion of each of the films measured is considerably less than the expansion of the free-standing films of identical composition characterized in Section 6.2. Note that like the films which were thermo-mechanically characterized in Section 6.2, both the homeotropic and planar films are comprised of liquid crystalline units which are uniaxially-aligned. The orientation of the director with respect to the direction of measurement is equivalent for the homeotropic anchored film and the free-standing film measured parallel to the director, and for the planar film and the free-standing film measured perpendicular to the director, as illustrated in Figure 6.14:

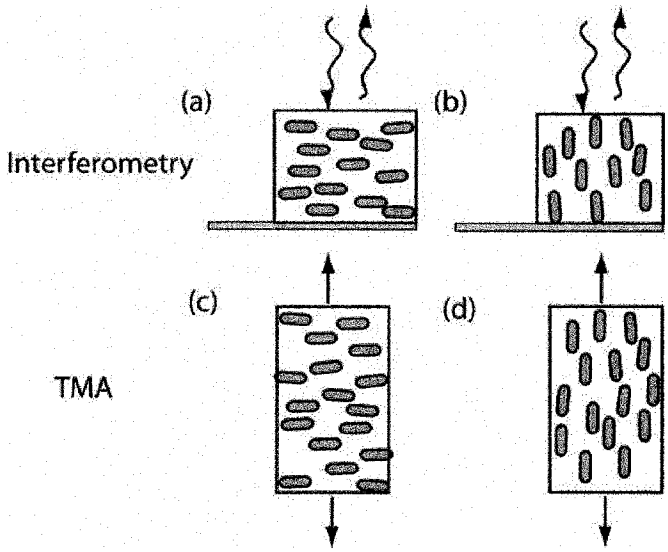

Figure 6.14: Actuation of free-standing and substrate-anchored films. If the free-standing films and anchored films were to behave identically, then it would be expected that the planar sample (a) would expand by 19%, as for the free-standing film measured perpendicular to the director (c), and that the homeotropic film (b) would shrink by 22% as was observed for the free-standing film measured parallel to the director (d).

If the free-standing and anchored films behaved identically then the planar film should have expanded by 19% and the homeotropic film should have contracted by 22%. However, each of these samples behaved much differently than their free-standing counterparts. The change in behavior was the most pronounced for the homeotropic sample: rather than contracting the anchored homeotropic film actually expanded by a small amount. This unexpected result is caused by the adhesion to the substrate: in order for the film to contract in thickness the liquid crystalline units must be free to expand in the plane of the substrate. This motion is impeded by the glass substrate, which prevents the expected deformation from occurring. A similar effect occurs for the planar film, only in this case the substrate prevents the sample from contracting in the plane of the substrate, which *diminishes* the overall expansion of the film. Nonetheless some expansion is possible. This behavior will be explored further using finite element modeling, as discussed in the next section.

6.4.4 Modeling

As in Chapter 3, finite element modeling was performed using ANSYS software. Recall that finite element analysis is a simulation tool in which the geometrical parameters, boundary conditions, and materials properties of an object are defined. The object is then subdivided into nodes. A load is applied, and a set of differential equations is defined at each node. These simultaneous equations are then solved numerically. In Chapter 3 the applied load was an external mechanical force applied to one face of the structure defined in the model. The force (F_{ext}) imparted a stress $\sigma = F/A$ to the object, where A was the area over which the stress was applied. Here the load is thermal: when the sample is heated, the material expands. The relevant equation describing the stress-strain relationship of the material is shown in Equation 6.12:

$$\underline{\sigma} = \underline{\underline{C}}\,\underline{\varepsilon} - \underline{\underline{\alpha}}\, l_0 \Delta T \qquad [6.12]$$

In Equation 6.12 $\underline{\underline{\alpha}}$ is a matrix containing the anisotropic, normal linear thermal expansion coefficients of the material, ΔT is the change in temperature, l_0 is the initial length of the sample, $\underline{\underline{C}}$ is the stiffness tensor, and $\underline{\varepsilon}$ is the strain matrix. In the absence of an external force all of the stress ($\underline{\sigma}$) within this system results from the interaction between the film and the substrate.

The starting point of this work was to develop models to mimic the thermo-mechanical behavior of the free-standing films described in Section 6.2. The anisotropic thermal expansion coefficients required to achieve modeled behavior which matched the behavior of the actual samples upon heating by 200 °C were determined. These coefficients were then used along with the correct boundary conditions to predict the behavior of anchored samples.

In the finite element models of both the anchored and free-standing films, the samples were geometrically defined as rectangular solids with x, y, and z dimensions of 100 μm, 1000 μm, and 10 μm respectively (corresponding to film width, length and height). In

each model every point in the film was free to move with three degrees of freedom, except for those points which were subject to fixed boundary conditions.

For free-standing films, boundary conditions were applied to both of the xz-planes to mimic the effect of the TMA sample clamp. These conditions prevented the points on either of the faces from deforming in the x and z directions. In addition, at one xz-plane the sample was also constrained in the y direction, as only one end of the sample was free to move in the TMA thin film clamp. These boundary conditions are illustrated in Figure 6.15(a).

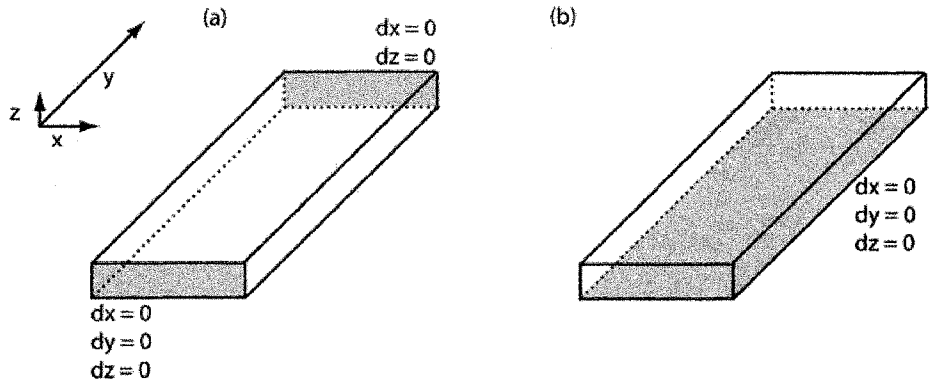

Figure 6.15: Sample geometry and boundary conditions. Constrained surfaces are shaded on the diagrams illustrating the sample geometry of free-standing (a) and surface-anchored (b) LCP thin films. Note that for the free-standing film, one end face is constrained in the x and z directions only.

The surface anchored films were governed by a different set of boundary conditions: the plane at $z = 0$ was forbidden from undergoing deformations in any of the three dimensions (as illustrated in Figure 6.15(b)). This boundary condition mimics the effect of the substrate to which the film is attached.

In each model three material properties were defined: Young's modulus (E), Poisson's ratio (ν), and the thermal expansion coefficient (α). Recall from Chapter 3 that Young's modulus is defined as the ratio between stress and strain. For this model, Young's modulus was defined as 10 MPa. While in reality this value was found both to depend on the alignment of the liquid crystals and to scale with temperature, varying this number

was found to have little effect on the model and thus the constant, isotropic value given here was deemed sufficient.

The definition of Poisson's ratio is stated in equation 6.13:

$$\nu = -\frac{\varepsilon_z}{\varepsilon_x} = -\frac{\varepsilon_y}{\varepsilon_x} \qquad [6.13]$$

Poisson's ratio is a measure of how much strain a material undergoes in a lateral direction (z, y, as written here) in response to a strain in the longitudinal direction (x) [52]. For a perfectly incompressible material, this value is 0.5. Here we define $\nu = 0.42$, which is a reasonable value for a polymer. Again this value was varied in a few of the models and was found to have little effect on the results.

The property that most strongly influenced the outcome of the model was the thermal expansion coefficient of the material. The thermal expansion coefficient (α) is a measure of the magnitude of the change in dimension (Δl) that the material undergoes in one direction as it is heated, as defined in Equation 6.14:

$$\alpha = \frac{\Delta l}{l_0}\frac{1}{\Delta T} \qquad [6.14]$$

Where l_0 is the initial length of the sample, and ΔT is the change in temperature. The thermo-mechanical behavior described in Section 6.2 is indicative that the thermal expansion coefficient of an aligned liquid crystalline polymer is anisotropic, varying strongly with the direction of orientation of the liquid crystals themselves. The TMA measurements of the uniaxially-aligned thin films were used to discern the thermal expansion coefficients $\alpha_\perp$ and $\alpha_{||}$ in the directions perpendicular and parallel to the long axis of the liquid crystals. Using the geometry and boundary conditions described above, the free-standing thin films were modeled. For each model, meshing was achieved using an automatic function that generated at least 6000 nodes, each of which was free to move with 3 degrees of freedom in response to the thermal load of 175 °C (that is, except for nodes subject to boundary conditions). To determine the correct values of α, the

perpendicular film was modeled, using a set of α values which had been estimated. The results were inspected, and the change in y position was plotted along the y-axis running down the center of the film. $\alpha_{\perp}$ was adjusted until a maximum change in position at one end of 220 μm (22%) was observed (recall that the other end of the film was constrained not to move in the y direction). The values of $\alpha_{\perp}$ and $\alpha_{||}$ were then used to model the parallel film, and $\alpha_{||}$ was adjusted until an expansion of 190 μm (19%) was observed. This process was repeated until the solutions converged. The final values of $\alpha_{\perp}$ and $\alpha_{||}$ are summarized in Table 6.2:

Variable	α (m/m)	α (ppm)
$\alpha_{\perp}$	0.00111	1110
$\alpha_{||}$	-0.00129	-1290

Table 6.2: Average thermal expansion coefficients. These coefficients were determined by modeling the behavior of free-standing films over the temperature range from 25 °C to 200 °C.

Whereas in reality the thermal expansion coefficient is temperature dependent, the values reported in Table 6.2 represent the average values over the temperature range from 25 °C to 200 °C. Knowing these values, the behavior of the 4 anchored thin films measured in Section 6.4.3 could be modeled. For example, for the homeotropic film $\alpha_x=\alpha_y=\alpha_{\perp}$, and $\alpha_z = \alpha_{||}$. Using these values of α, constraining the bottom face of the film in three dimensions, and applying a thermal load of 175 °C (corresponding to heating from 25 °C to 200 °C), the expected change in thickness of the homeotropic film was found to be +5%. This value was slightly higher than the measured value (2%) but does predict the trend that the film will expand rather than contract in thickness. A comparison of the modeled behavior of a free-standing and anchored homeotropic thin film is shown in Figure 6.16:

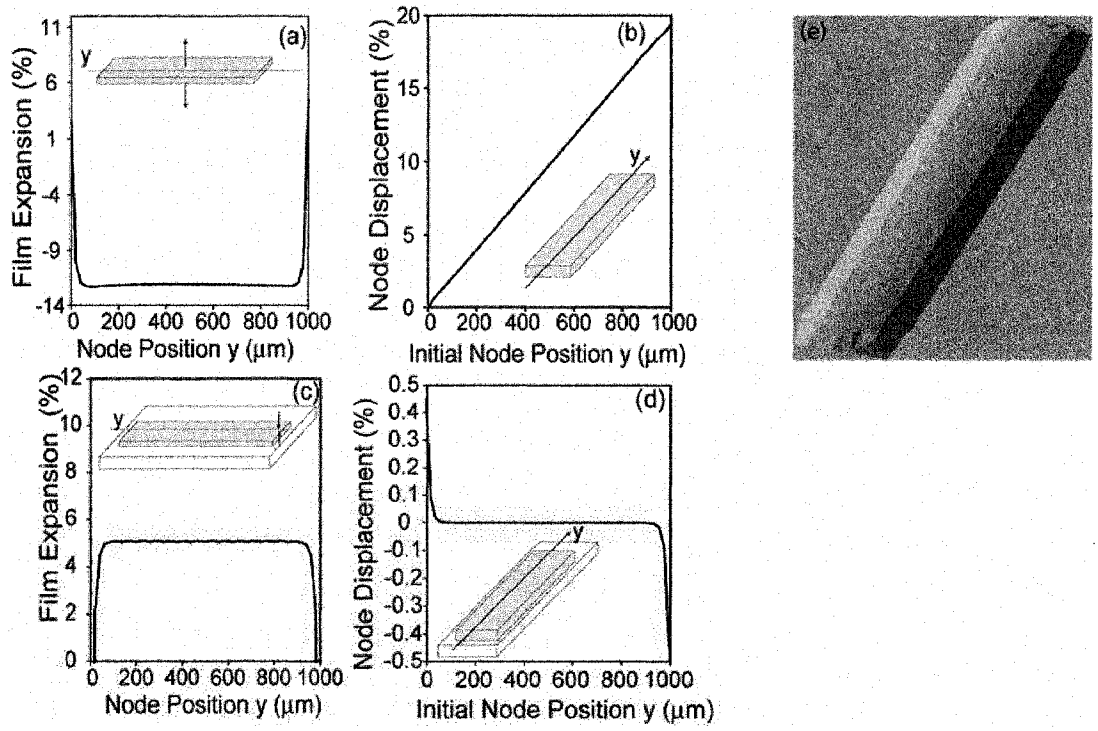

Figure 6.16: Finite element modeling of homeotropic films. The change in thickness and length of free-standing (a,b) and surface-anchored (c,d) homeotropic thin films that occurs upon heating to 200 °C was determined using finite element modeling. The free-standing film contracts by 13% in thickness at the center of the film (a), and expands by 19% in length (b). The anchored film behaves much differently, expanding by 5% in thickness (c) and undergoing almost no change in length (d). That a large amount of stress in generated as a result of confining one surface of the film is evident in (e), which is a plot of the deformed shape at 200 °C. Some stress is relieved as wrinkling at either end of the film.

Figure 6.16 (e) is a plot of the deformed surface-anchored shape at 200 °C. The sides of the film are clearly under strain, and some stress is relieved by wrinkling at either end of the length of the film (out-of-plane strain). These edge effects are difficult to predict precisely, and should not be considered exact. In thin film models found in the literature, samples are specified to be large enough that the edge effects can be discarded (such that the area of measurement is at least a few multiples of the film thickness away from the edge of the sample) [53]. This should not take away from the validity of the model towards the center of the film. Towards the center of the sample, all of the stress is manifested as tensile stress at the interface between the film and the substrate. This is not uncommon in thin films [54].

In the previous section, it was shown that a film with a chiral director profile was able to undergo a larger expansion than a film with planar alignment, despite the fact that in both cases the LCs are aligned in a plane parallel to the substrate. This can be explained by considering the anisotropic thermal expansion coefficients of each of these films (averaged over the temperature interval from 25 °C to 200 °C), which are summarized in Table 6.3:

Film	α_z (m/m)	α_y (m/m)	α_x (m/m)
Planar (director along y)	$\alpha_\perp = 0.00111$	$\alpha_\parallel = -0.00129$	$\alpha_\perp = 0.00111$
Cholesteric	$\alpha_\perp = 0.00111$	$(\alpha_\perp+\alpha_\parallel)/2 = -0.00009$	$(\alpha_\perp+\alpha_\parallel)/2 = -0.00009$

Table 6.3: Average thermal expansion coefficients of cholesteric and planar films.

For the cholesteric film, the thermal expansion coefficient within the plane of the substrate is quite low as compared with the planar film. The contraction and the expansion are shared equally between the x and y directions for the cholesteric film, whereas in order for the planar film to expand in thickness there must be a strong contraction of the film in the y direction and expansion in the z direction. This means that there will be considerably less stress generated at the substrate for the cholesteric film than for the planar film, and also that the substrate provides less of an inhibiting effect for the deformation of this sample. Therefore, the cholesteric sample is able to expand more than the planar film even though they both have identical expansion coefficients in the z direction. The cholesteric film was also modeled in ANSYS, and the results are shown in Figure 6.17:

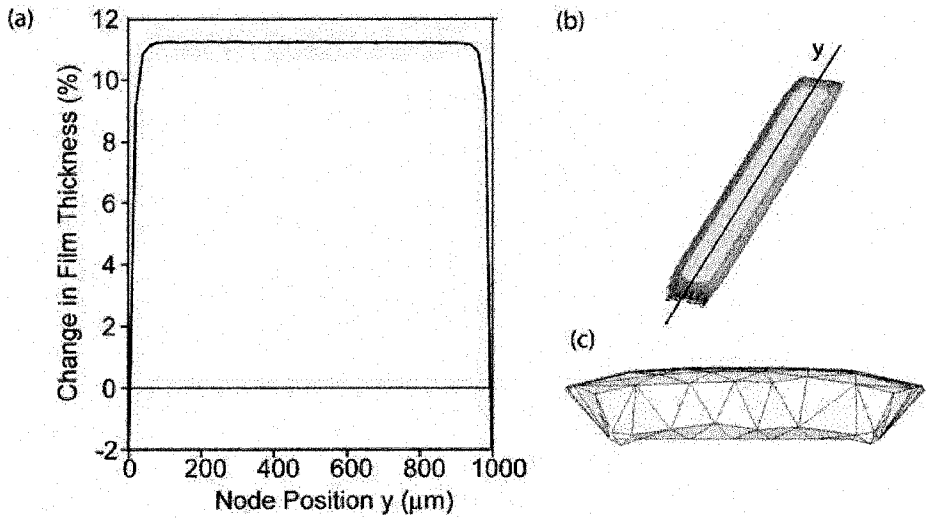

Figure 6.17: Modeled deformation of a cholesteric film. The change in film thickness along the center of the y-axis of the film (a) is quite uniform and attains a maximum value of 11%, which matches the experimental data well. The deformed shape is shown (b) along with a cross section of the film (*xz*-plane) at the center of the sample (c). A large expansion is achieved despite the confinement from the substrate.

The model predicts an expansion of 11% at the center of the film, which matches well with the measured results (11%). Since for the surface anchored films the largest deformations are achieved using cholesteric films, this will be the favored director profile for the microfabrication work described in Chapter 7: "Microfabrication of liquid crystalline polymers using template-based processing" and Chapter 8: "Microfabrication of liquid crystalline polymers: photopatterning and micro-transfer printing".

6.5 Conclusion

In this chapter, an investigation of the properties of liquid crystalline polymers has been described. Ordered liquid crystalline polymers undergo anisotropic changes in shape in response to a variety of stimuli including heat, light, and humidity. For simplicity, this chapter focused on the properties of thermally responsive materials. Thermo-mechanical measurements made using thermal mechanical analysis were used to determine the optimal concentration of crosslinker for a polymer made from a blend of mono- and diacrylate liquid crystalline monomers. It was found that free-standing, uniaxial thin films which contract in length by 22% when heated could be made by photopolymerizing a monomer mixture comprised of 12% diacrylate and 88% monoacrylate. 22% is

somewhat less than the contractions that can be achieved using liquid single crystal elastomers, however liquid single crystal elastomers are not well suited to this research as these materials can not easily be fabricated and patterned on the microscale with aligned liquid crystalline units. The samples fabricated in this chapter were aligned using surface alignment techniques which are more compatible with microfabrication. One reason for the reduced responsivity of these materials may be that their order parameter is not maximized: optical characterization of uniaxially-aligned films showed that they have a birefringence of around 0.12, which corresponds to an order parameter of roughly 0.6. Therefore, these systems begin with less order than liquid single crystal elastomers, which have an order parameter approaching 1. Nonetheless, 22% is a reasonably large strain. Optical characterization was also used to investigate the mechanism by which the sample deformed, and the change in shape of a uniaxially-aligned thin film was confirmed to be due to the loss in order that occurs upon heating.

In the last part of this chapter, the effect of anchoring a liquid crystalline polymer to a substrate was investigated, both experimentally and by finite element modeling. It was found that the substrate acted as a confinement layer, impeding the motion of liquid crystalline units along the boundary, and reducing the responsivity of the material. Despite this, films with a cholesteric director orientation were found to expand in thickness by 11% when heated, which is actually a relatively large strain for a MEMS material (in comparison, note that silicon can only attain strains of roughly 1% without fracturing [55, 56]). Therefore, the patterning of liquid crystalline polymers will be examined in the next chapter, with an eye on incorporating these materials into micro-actuator devices.

6.6 References

1. Elias, A.L., Harris, K.D., Bastiaansen, C.W.M., Broer, D.J. and Brett, M.J., *Photopatterned liquid crystalline polymers for microactuators.* Journal of Materials Chemistry, 2006. **16**(28): p. 2903-2912.
2. Koch, M., Evans, A.G.R. and Brunnschweiler, A., *The dynamic micropump driven with a screen printed PZT actuator.* Journal of Micromechanics and Microengineering, 1998. **8**(2): p. 119-122.

3. Syms, R.R.A., Yeatman, E.M., Bright, V.M. and Whitesides, G.M., *Surface tension-powered self-assembly of micro structures - The state-of-the-art.* Journal of Microelectromechanical Systems, 2003. **12**(4): p. 387-417.
4. Reid, J.R., Bright, V.M. and Butler, J.T., *Automated assembly of flip-up micromirrors.* Sensors and Actuators a-Physical, 1998. **66**(1-3): p. 292-298.
5. Quake, S.R. and Scherer, A., *From micro- to nanofabrication with soft materials.* Science, 2000. **290**(5496): p. 1536-1540.
6. Grate, J.W., Patrash, S.J. and Abraham, M.H., *Method for Estimating Polymer-Coated Acoustic-Wave Vapor Sensor Responses.* Analytical Chemistry, 1995. **67**(13): p. 2162-2169.
7. Agarwal, A.K., Sridharamurthy, S.S., Beebe, D.J. and Jiang, H.R., *Programmable autonomous micromixers and micropumps.* Journal of Microelectromechanical Systems, 2005. **14**(6): p. 1409-1421.
8. Harmon, M.E., Tang, M. and Frank, C.W., *A microfluidic actuator based on thermoresponsive hydrogels.* Polymer, 2003. **44**(16): p. 4547-4556.
9. Kohl, M., Krevet, B. and Just, E., *SMA microgripper system.* Sensors and Actuators a-Physical, 2002. **97-8**: p. 646-652.
10. Lyshevski, S.E., *Smart Flight Control Surfaces with Microelectromechanical Systems.* IEEE Transactions on Aerospace and Electronic Systems, 2002. **38**(2): p. 543-552.
11. Dong, L., Agarwal, A.K., Beebe, D.J. and Jiang, H.R., *Adaptive liquid microlenses activated by stimuli-responsive hydrogels.* Nature, 2006. **442**(7102): p. 551-554.
12. Smela, E., Inganas, O. and Lundstrom, I., *Controlled Folding of Micrometer-Size Structures.* Science, 1995. **268**(5218): p. 1735-1738.
13. Park, T.G. and Hoffman, A.S., *Synthesis and Characterization of Ph- and or Temperature-Sensitive Hydrogels.* Journal of Applied Polymer Science, 1992. **46**(4): p. 659-671.
14. Carlen, E.T. and Mastrangelo, C.H., *Surface micromachined paraffin-actuated microvalve.* Journal of Microelectromechanical Systems, 2002. **11**(5): p. 408-420.
15. Ikeda, T., Nakano, M., Yu, Y.L., Tsutsumi, O. and Kanazawa, A., *Anisotropic bending and unbending behavior of azobenzene liquid-crystalline gels by light exposure.* Advanced Materials, 2003. **15**(3): p. 201-205.
16. Finkelmann, H., Nishikawa, E., Pereira, G.G. and Warner, M., *A new opto-mechanical effect in solids.* Physical Review Letters, 2001. **8701**(1): p. 015501.
17. Bar-Cohen, Y., *Electroactive polymers as artificial muscles: A review.* Journal of Spacecraft and Rockets, 2002. **39**(6): p. 822-827.
18. Kupfer, J. and Finkelmann, H., *Nematic Liquid Single-Crystal Elastomers.* Makromolekulare Chemie-Rapid Communications, 1991. **12**(12): p. 717-726.
19. Madden, J.D.W., Vandesteeg, N.A., Anquetil, P.A., Madden, P.G.A., Takshi, A., Pytel, R.Z., Lafontaine, S.R., Wieringa, P.A. and Hunter, I.W., *Artificial muscle technology: Physical principles and naval prospects.* IEEE Journal of Oceanic Engineering, 2004. **29**(3): p. 706-728.
20. Wermter, H. and Finkelmann, H., *Liquid crystalline elastomers as artificial muscles.* e-Polymers, 2001(no.13): p. 1-13.

21. Mol, G.N., Harris, K.D., Bastiaansen, C.W.M. and Broer, D.J., *Thermo-mechanical responses of liquid-crystal networks with a splayed molecular organization.* Advanced Functional Materials, 2005. **15**(7): p. 1155-1159.
22. Harris, K.D., Bastiaansen, C.W.M., Lub, J. and Broer, D.J., *Self-assembled polymer films for controlled agent-driven motion.* Nano Letters, 2005. **5**(9): p. 1857-1860.
23. Yu, Y.L., Nakano, M. and Ikeda, T., *Directed bending of a polymer film by light - Miniaturizing a simple photomechanical system could expand its range of applications.* Nature, 2003. **425**(6954): p. 145-145.
24. Harris, K.D., Cuypers, R., Scheibe, P., van Oosten, C.L., Bastiaansen, C.W.M., Lub, J. and Broer, D.J., *Large amplitude light-induced motion in high elastic modulus polymer actuators.* Journal of Materials Chemistry, 2005. **15**(47): p. 5043-5048.
25. Tajbakhsh, A.R. and Terentjev, E.M., *Spontaneous thermal expansion of nematic elastomers.* European Physical Journal E, 2001. **6**(2): p. 181-188.
26. Finkelmann, H., *Liquid Crystalline Elastomers*, in *The encyclopedia of materials science and technology*, K.H.J. Buschow, Editor. 2001, Elsevier: Amsterdam ; New York.
27. Odian, G.G., *Principles of Polymerization.* 3rd ed. 1991: Wiley-Interscience.
28. Komp, A., Ruhe, J. and Finkelmann, H., *A versatile preparation route for thin free-standing liquid single crystal elastomers.* Macromolecular Rapid Communications, 2005. **26**(10): p. 813-818.
29. Finkelmann, H. and Wermter, H., *LC-Elastomers and Artificial Muscles.* Abstracts of Papers of the Americal Chemical Society, 2000. **219**: p. 189-PMSE, Part 2.
30. Broer, D.J., *Creation of supramolecular thin film architectures with liquid-crystalline networks.* Molecular Crystals and Liquid Crystals Science and Technology Section a-Molecular Crystals and Liquid Crystals, 1995. **261**: p. 513-523.
31. Wang, X.F., Engel, J. and Liu, C., *Liquid crystal polymer (LCP) for MEMS: processes and applications.* Journal of Micromechanics and Microengineering, 2003. **13**(5): p. 628-633.
32. van der Zande, B.M.I., Steenbakkers, J., Lub, J., Leewis, C.M. and Broer, D.J., *Mass transport phenomena during lithographic polymerization of nematic monomers monitored with interferometry.* Journal of Applied Physics, 2005. **97**(12): p. 123519-1 - 123519-8.
33. Sousa, M.E., Broer, D.J., Bastiaansen, C.W.M., Freund, L.B. and Crawford, G.P., *Isotropic "Islands" in a Cholesteric "Sea" – Patterned Thermal Expansion for Responsive Surface Topologies.* Advanced Materials, 2006. **14**: p. 1842-1845.
34. Buguin, A., Li, M.H., Silberzan, P., Ladoux, B. and Keller, P., *Micro-actuators: When artificial muscles made of nematic liquid crystal elastomers meet soft lithography.* Journal of the American Chemical Society, 2006. **128**(4): p. 1088-1089.
35. Hikmet, R.A.M. and Broer, D.J., *Dynamic Mechanical-Properties of Anisotropic Networks Formed by Liquid-Crystalline Acrylates.* Polymer, 1991. **32**(9): p. 1627-1632.

36. McCabe, J.F. and Wassell, R.W., *Thermal-Expansion of Composites.* Journal of Materials Science-Materials in Medicine, 1995. **6**(11): p. 624-629.
37. Perera, D.Y., *Effect of thermal and hygroscopic history on physical ageing of organic coatings.* Progress in Organic Coatings, 2002. **44**(1): p. 55-62.
38. Anseth, K.S., Bowman, C.N. and Peppas, N.A., *Polymerization Kinetics and Volume Relaxation Behavior of Photopolymerized Multifunctional Monomers Producing Highly Cross-Linked Networks.* Journal of Polymer Science Part a-Polymer Chemistry, 1994. **32**(1): p. 139-147.
39. Hecht, E., *Optics.* 2002, Reading, Mass.: Addison-Wesley Pub. Co.
40. Escuti, M.J., Cairns, D.R. and Crawford, G.P., *Optical-strain characteristics of anisotropic polymer films fabricated from a liquid crystal diacrylate.* Journal of Applied Physics, 2004. **95**(5): p. 2386-2390.
41. Gandhi, J. and Anderson, J., *Experimental Measurement of Cauchy Values for delta(n) of Nematic Liquid Crystals.* SID International Symposium Digest of Technical Papers, 2002. **33**(1): p. 582-585.
42. Broer, D.J., Hikmet, R.A.M. and Challa, G., *Insitu Photopolymerization of Oriented Liquid-Crystalline Acrylates .4. Influence of a Lateral Methyl Substituent on Monomer and Oriented Polymer Network Properties of a Mesogenic Diacrylate.* Makromolekulare Chemie-Macromolecular Chemistry and Physics, 1989. **190**(12): p. 3201-3215.
43. Haller, I., Huggins, H.A., Lilienth.Hr and McGuire, T.R., *Order-Related Properties of Some Nematic Liquids.* Journal of Physical Chemistry, 1973. **77**(7): p. 950-954.
44. Elias, A.L., Harris, K.D., Bastiaansen, C.W.M., Broer, D.J. and Brett, M.J. *Polymeric Helices With Submicron Dimensions for MEMS Devices.* in *Proceedings of SPIE, Smart Sensors, Actuators, and MEMS II.* 5846: 41-55.
45. Hikmet, R.A.M., Lub, J. and Broer, D.J., *Anisotropic Networks Formed by Photopolymerization of Liquid-Crystalline Molecules.* Advanced Materials, 1991. **3**(7-8): p. 392-394.
46. Gibson, H.W., *Cholesteric Mesophases*, in *Liquid crystals : the fourth state of matter*, F.D. Saeva, Editor. 1979, M. Dekker: New York.
47. Jorez, S., Cornet, A. and Raskin, J.P., *MEMS profilometry by low coherence phase shifting interferometry: Effect of the light spectrum for high precision measurements.* Optics Communications, 2006. **263**(1): p. 6-11.
48. Degroot, P. and Deck, L., *Surface Profiling by Analysis of White-Light Interferograms in the Spatial-Frequency Domain.* Journal of Modern Optics, 1995. **42**(2): p. 389-401.
49. Saleh, B.E.A. and Teich, M.C., *Fundamentals of photonics.* 1991, New York: Wiley.
50. Wyant, J.C. and Creath, K., *Advances in Interferometric Optical Profiling.* International Journal of Machine Tools & Manufacture, 1992. **32**(1-2): p. 5-10.
51. Pfortner, A. and Schwider, J., *Red-green-blue interferometer for the metrology of discontinuous structures.* Applied Optics, 2003. **42**(4): p. 667-673.
52. den Toonder, J.M.J., *Mechanics of Solid Materials*, Eindhoven University of Technology: Eindhoven, 2000,

53. Payne, J.A., Francis, L.F. and McCormick, A.V., *The effects of processing variables on stress development in ultraviolet-cured coatings.* Journal of Applied Polymer Science, 1997. **66**(7): p. 1267-1277.
54. Francis, L.F., McCormick, A.V., Vaessen, D.M. and Payne, J.A., *Development and measurement of stress in polymer coatings.* Journal of Materials Science, 2002. **37**(22): p. 4897-4911.
55. Khang, D.Y., Jiang, H.Q., Huang, Y. and Rogers, J.A., *A stretchable form of single-crystal silicon for high-performance electronics on rubber substrates.* Science, 2006. **311**(5758): p. 208-212.
56. Gad-el-Hak, M., *The MEMS handbook.* The Mechanical engineering handbook series. 2002, Boca Raton, FL: CRC Press.

7 Micro-Patterning Liquid Crystalline Polymers Using Templating-Based Processes

7.1 Introduction

In Chapter 6, the material properties of liquid crystalline polymers were investigated, with an emphasis on evaluating the suitability of these materials for use in micro-actuator devices. An overview of microfabrication techniques which have previously been used to pattern these unique materials was also given. In this chapter, three new techniques for micro-patterning liquid crystalline polymers will be presented. These techniques are based on the GLAD templating processes discussed in Chapters 3 and 4 of this thesis. The first method which will be described here is double-templating, which (as mentioned in Section 4.5) can be used to make liquid crystalline polymer helices. The alignment of the LC monomers in the helices can either be dictated by the surface of the photoresist pores, or controlled by an externally applied electric field. Limited actuation of these structures will be presented. In the second technique, a single-templating process is used to make thin films of liquid crystalline polymer perforated with helical pores. However, these films exhibit surprisingly low responsivity when heated, for reasons which will be explained using theoretical calculations. Because of this low responsivity, an additional technique was developed. This third technique is a modified single-templating process which can be used to make a composite structure consisting of a perforated thin film which, in some areas, is reinforced with 'nanorebar': i.e., GLAD structures. This composite layer is mounted on top of a thick polymer under-layer. Structures made using this process have been shown to undergo large deformations, and the fabrication and characterization of these structures will be presented in detail for samples fabricated from both liquid crystalline and isotropic monomers.

Throughout this chapter the material which will be patterned is the thermally responsive liquid crystalline polymer poly(M1:M2, 88:12) described in Chapter 6. In all mixtures these two components (M1 and M2) are combined in a ratio of 88:12. Most mixtures also contain initiator (Irgacure 184 or Irgacure 369), added in a quantity of 1% to 2% of the weight of the M1/M2 mixture. In some cases, the chiral dopant (BASF LC756) is

employed to achieve a chiral director profile in the film when this alignment is deemed to be advantageous. This component is added in a quantity of 5% of the weight of the M1/M2 mixture.

7.2 GLAD Templating: Liquid Crystalline Polymer Helices

7.2.1 Fabrication

Liquid crystalline polymer helices can be made using the double-templating process described in Chapter 4 to structure the liquid crystalline monomer mixture (M1:M2, 88:12, 1% initiator) described in Chapter 6. The monomers discussed in Chapter 6 were chosen for investigation based on the fact that they are compatible with photoresist templates, and do not dissolve this material (unlike many of the other monomers which were screened). Only a slight variation in the fabrication process described in Chapter 4 is required to produce liquid crystalline polymer helices. While in Chapter 4 isotropic polymers were filled into the template and polymerized at room temperature, here the monomer mixture must be heated into the desired phase before polymerization. Typically samples were prepared by heating the monomer mixture into the isotropic phase (63 °C) and spreading it onto the intermediate template. The sample itself was heated to the nematic phase of the mixture (55 °C) during polymerization. An example of liquid crystalline polymer helices produced using this process is shown in Figure 7.1:

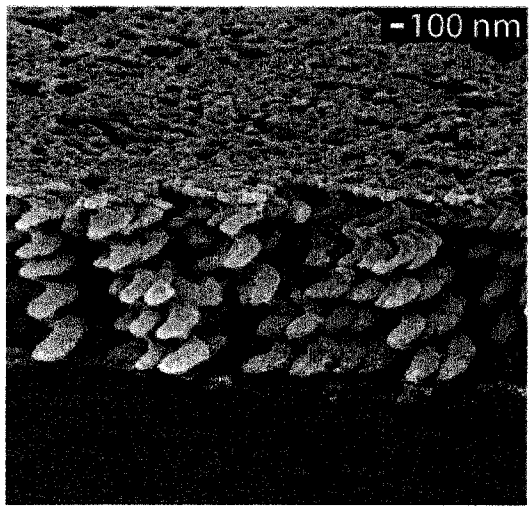

Figure 7.1: Poly(M1:M2, 88:12) polymer helices. Recall that the substrate beneath the helices is also comprised of liquid crystalline polymer.

The alignment of the liquid crystals within the helices is difficult to predict. Based on the NMR study of Chapter 5 of LCs in a GLAD template film, it is possible to hypothesize that the LCs follow the chiral twist of the pores at a constant rise angle. However, this prediction assumes that the LCs in a helical pore follow the same alignment as LCs aligned by a helix, which is not necessarily true. In order to ensure that the alignment of the LCs within the helices was known, it was decided to polymerize the sample in an electric field, which would result in alignment parallel to the long axes of the helices, as shown in Figure 7.2:

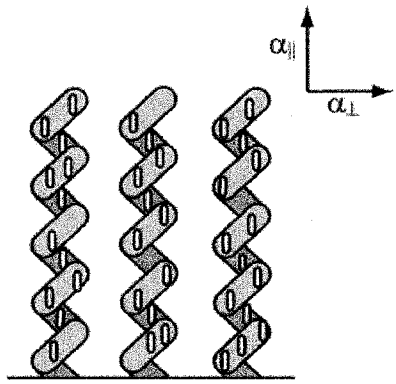

Figure 7.2: LC alignment in liquid crystalline polymer helices. Alignment perpendicular to the substrate should result in a large (negative) thermal expansion coefficient in this direction, causing the helices to contract when actuated.

When aligning the liquid crystalline monomers in an electric field, the direction of alignment is determined by the dielectric anisotropy of the molecules. If the dielectric anisotropy is negative, then the liquid crystals will tend to align will their long axes perpendicular to the field. The liquid crystals used here have a net positive dielectric anisotropy, which causes the molecules to align with their long axes oriented in the direction of the electric field.

The fabrication process to produce these helices is in essence the same as described in Section 4.4, but will be reviewed here to highlight the few changes required. The intermediate template used in this process was still a photoresist perforated thin film, only this film was fabricated on a conducting substrate in order to apply the electric field to align the liquid crystals. Here, doped silicon wafers were used. To fill the template, the

LC mixture was heated into the lower range of the isotropic phase (63 °C). The mixture was then applied to the intermediate template, also in the isotropic phase. A plate of glass coated with indium tin oxide (ITO) was placed on top of the LC mixture to act as the counter electrode for the electric field. This plate also acted as a substrate for the liquid crystalline polymer helices, although there was a thick (~15 μm) layer separating the helices from the ITO. At this point in the process, a pair of small clips was often used to force the plates of the electrodes as close together as possible to minimize the thickness of this layer. A voltage of 100 V – 150 V at a frequency of 1000 Hz was applied across the sample to align the liquid crystals. The use of an AC field was required to prevent electrochemical reactions – such as the injection of charge carriers into the LC layer – from occurring at the electrodes [1]. The sample was then cooled to the nematic phase (55 °C), and the monomer mixture was polymerized in UV light (using the home-built lamp described in Chapter 4). After removing the electric field and UV light source, the sample was heated to 100 °C to encourage additional polymerization, and then cooled. The composite layer (consisting of the photoresist intermediate template and liquid crystalline polymer) could be delaminated preferentially from the original silicon substrate by immersing the sample in liquid nitrogen, or simply by prying the cell apart with a razor. The photoresist intermediate template could then be dissolved in solvent, leaving liquid crystalline polymer helices comprised of aligned liquid crystalline units. The key points of this fabrication process are summarized in Figure 7.3.

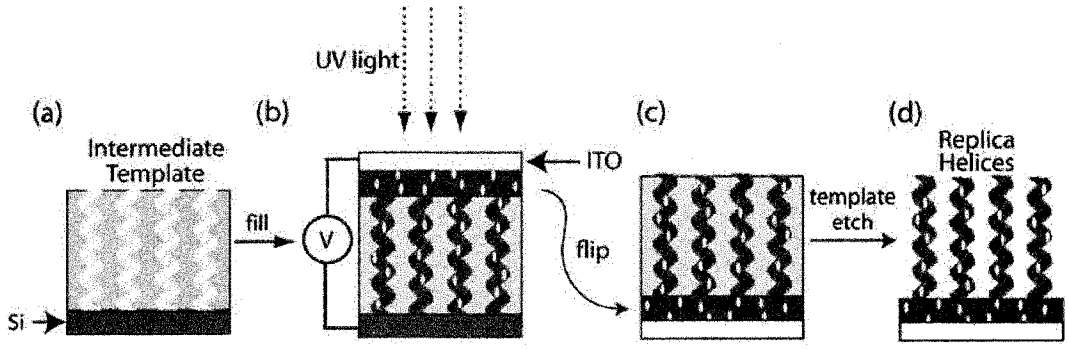

Figure 7.3: Fabrication of electrically-aligned liquid crystalline polymer helices. The intermediate template is fabricated on a substrate of doped silicon (a). This template is filled at a temperature within the isotropic region of the monomer mixture and a transparent, conducting electrode is placed on top of the mixture. An electric field is applied across the sample. The sample is cooled to the nematic phase and the electric field causes the liquid crystals to align parallel to the field lines. The sample is polymerized in UV light (b). The composite polymer layer is removed from the substrate by immersing the sample in liquid nitrogen, or by prying the cell open with a razor blade (c). The intermediate template is then dissolved in solvent (d).

The alignment of the liquid crystals within a sample can be verified by observing the optical characteristics of the sample between crossed polarizers. A well-aligned homeotropic sample appears dark between crossed polarizers when viewed directly along the axis perpendicular to the plane of the sample itself, but begins transmitting light when tilted off-axis. This optical behavior was observed for the majority of our samples, and the liquid crystalline units within the sample were therefore concluded to be aligned in a direction perpendicular to the substrate.

One of the hardest steps to control in the fabrication process was the delamination of the composite liquid crystalline polymer-photoresist layer from the silicon substrate. This step only worked if the polymer adhered more strongly to the ITO than the photoresist adhered to the silicon substrate. To encourage adhesion between the ITO plate and the polymer, the ITO could be surface treated in an O_2 plasma before placing it on top of the monomer mixture. This surface treatment changed the surface chemistry of the ITO plate, creating more OH groups and therefore making it more hydrophilic, as shown in Figure 7.4:

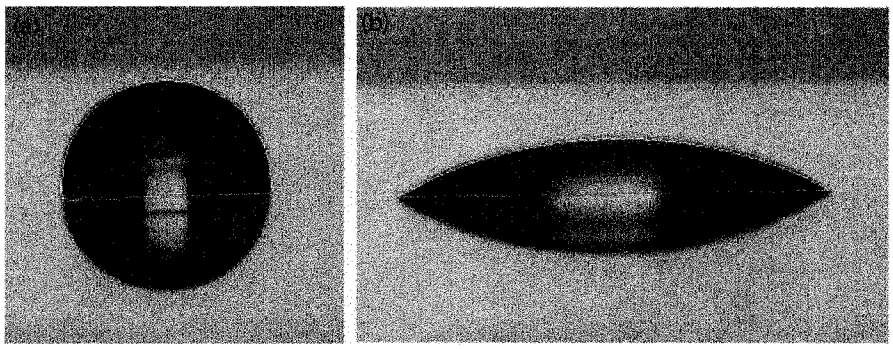

Figure 7.4: Contact angle of water on ITO. Before O_2 plasma treatment, the contact angle of water on glass is 96.6°. After the plasma treatment the contact angle is reduced to 28.0°.

Before the plasma treatment the contact angle of water on ITO is quite high (96.6°). After treatment the contact angle is reduced to 28.0°. This treatment has also been observed by eye to improve the wetting of the liquid crystalline monomer on ITO and glass. Treating the ITO with the O_2 plasma also improved the adhesion between the ITO and the polymer mixture.

7.2.2 Actuation

Measuring the thermomechanical behavior of the helices was not trivial. As described above, it was expected that the helices in which the LCs were aligned homeotropic with respect to the substrate would contract when heated. However, this behavior was not easily measured due to the small dimensions of the helices themselves. A number of characterization methods were considered, including:

1) Observing the reflection band of the helices during heating using a spectrophotometer. The peak reflected wavelength should shift as the pitch of the helices changes. Unfortunately the helices were not sufficiently uniform to measure the reflection band, and this method could not be used.
2) Using the optical profilometer to observe the change in height of the helices as a function of temperature. This scheme could not be successfully implemented for a number of reasons. The tops of the helices are themselves too small to image clearly using the profilometer, but sufficiently large to scatter the light incident upon them, thus making accurate measurements difficult to obtain. In addition, any change in thickness of the overall film would result from a combination of the

changing thickness of the helices and the changing thickness of the thick layer of aligned liquid crystalline polymer between the helices and the substrate. Isolating the behavior of the helices would, therefore, be difficult. The contribution from the substrate layer would also prevent characterization of the helices using mechanical techniques (such as monitoring the position of an AFM tip as a function of temperature).

3) Imaging the helices in the SEM during heating. This approach was implemented, and is described below.

Imaging of the helices in the SEM during heating was achieved using a heating stage. The samples were covered in a thin (~5 nm to 10 nm) layer of gold, and adhered to a copper substrate holder using copper conductive tape. A thermocouple wire was inserted into the back of the sample holder to provide feedback as to the sample temperature during measurement. Samples were scanned in the direction perpendicular to the expected direction of deformation to prevent drift of the sample from affecting the thickness measurement. The results of one such study are shown in Figure 7.5:

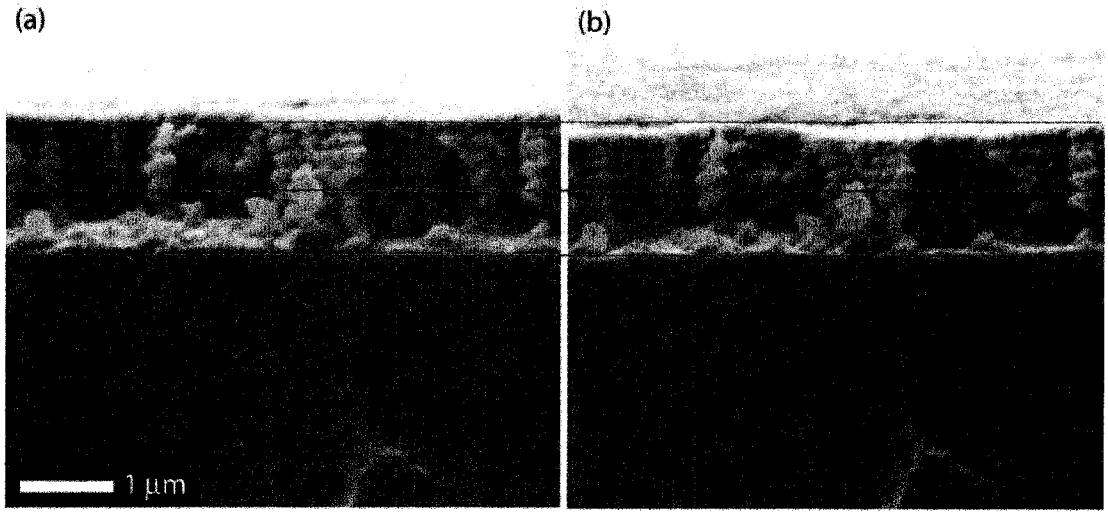

Figure 7.5 Actuation of liquid crystalline polymer helices. Liquid crystalline polymer helices were imaged using scanning electron microscopy at 25 °C (a) and 80 °C (b). Some guidelines are included to allow the comparison of the distance between features of interest.

In these SEM images the thickness of the helical layer does appear to contract by a small amount, however this amount is difficult to quantify due to the uncertainty in the measurements. Although the images are ostensibly all taken at a magnification of 5000x, if any of the images are less than perfectly focused the nominal magnification (and the corresponding thickness measurement) will not be accurate. In addition, shifting, delamination, and bulk movement of the substrate during heating could distort the appearance of the sample in the images. The images shown here represent the best possible data that was attained using this technique.

Characterization was also attempted for samples which were not aligned in an electric field. In this case it might be expected from the NMR results of Chapter 5 that the LCs would be aligned parallel the helical arms, at a constant rise angle. Actuation of these structures also proved difficult to quantify, due to the small dimensions involved.

7.3 Fabrication of liquid crystalline polymer perforated thin films from templates deposited by glancing angle deposition

7.3.1 Fabrication

Liquid crystalline polymer perforated thin films (LCP-PTFs) can be made using the single-templating process described in Section 3.1. A master film with the desired features is deposited by glancing angle deposition. A mixture of LC monomers is then spin-coated into the film from a solution of dichloromethane, PGMEA (propylene glycol methyl ether acetate), or toluene. Note that for each film the viscosity of the solution must be optimized. When filling the film, it is desirable to fill the porous GLAD structures completely, while leaving only a very thin layer of excess material on top of these structures. In general, the solids content of the solution (percentage of liquid crystalline monomers and initiator vs. solvent in the total mixture) required to perfectly fill the GLAD film varies with the thickness of the film itself. A typical mixture used to fill a 4 μm tall GLAD film contained 48% monomer mixture and 52% solvent, and was spin-coated at 5000 rpm. After spin-coating, samples were baked at a low temperature to drive off any residual solvents, flushed with nitrogen, and polymerized in UV light at a

temperature within the nematic phase. The etch-back step was best achieved using reactive ion etching (RIE).

RIE is a plasma etching process in which the sample to be etched is placed on one of the electrodes that powers the plasma. During etching, radicals in the plasma bombard the surface of the sample. The radicals and the target material undergo reactions which create gaseous products, thereby removing material from the surface of the sample. Etching can occur via 2 different mechanisms: either the surface atoms and radicals can react to form gaseous products directly, or the radicals can react with atoms at the surface itself, forming compounds which can be knocked free by high-energy ions from the plasma which collide with the sample.

For the work described in this thesis, polymers were etched using the Micro-etch RIE. Samples were etched using a gas mixture of O_2 and CF_4, at a pressure of 100 mTorr to 107 mTorr, and an RF power of 210 W (66%). The etch time was dependent on the amount of material to be removed.

After RIE, samples were immersed in buffered oxide etch to remove the GLAD template film, leaving a perforated thin film of liquid crystalline polymer, as shown in Figure 7.6:

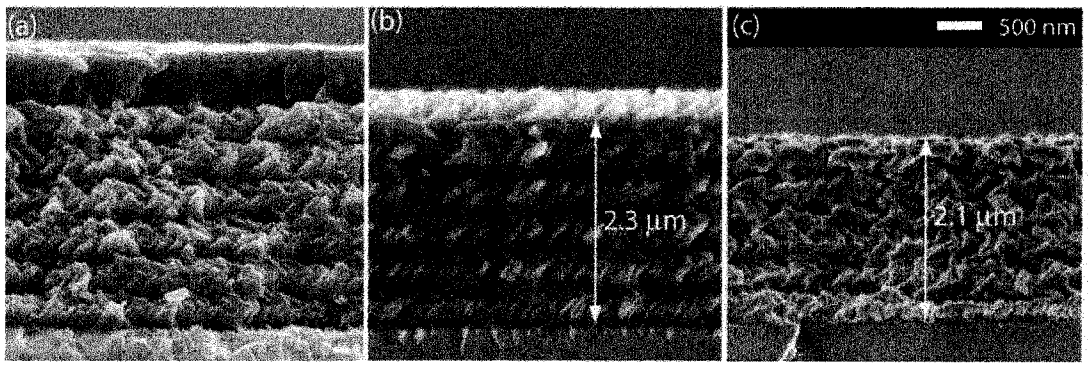

Figure 7.6: Liquid crystalline polymer perforated thin film. The film is shown just after filling and polymerization, and is overfilled by nearly 500 nm (a). This excess layer is removed by reactive ion etching (b). The SiO_2 helices can then be removed using buffered oxide etch (c). Although the images were all taken at the same magnification the final film (c) appears slightly thinner than the others.

Note the change in appearance of the film between image (b) and image (c) in Figure 7.6. The pores themselves change slightly in appearance: whereas the pores in the photoresist perforated thin films presented in Chapter 3 looked like exact negatives of the positive GLAD structures, here the pores appear less well-defined. This may be a result of the cleave: the liquid crystalline polymer used in this process has a low glass transition temperature (22 °C to 25 °C), which means that at room temperature this material is somewhat malleable. The material may therefore have undergone some plastic deformation before cleaving during the sample preparation for the SEM. Nonetheless, the 5 turns of the helix remain visible. Although the images were all taken at the same magnification, the film appears slightly thinner after the removal of the template GLAD film. The overall height of the film is reduced by a small amount (200nm, which is 10% of the overall film thickness). There are two probable reasons for this reduction in height. The first is that the sample itself was etched back slightly further at the spot imaged in 7.6(c) than in 7.6(b). The second cause is that the film itself has contracted somewhat after the helices were removed, due to polymerization shrinkage. Polymerization shrinkage is a common effect in UV-polymerized acrylates as well as many other materials. During polymerization, the monomer molecules move more closely together as they become covalently bonded into the network [2]. It has been observed that multifunctional acrylates can shrink by 10% to 30% (by volume) upon polymerization [3]. Polymerization shrinkage can lead to extensive stress in multi-functional acrylate thin films which are polymerized on a rigid substrate, since interaction with the substrate prevents the contraction of the film in two dimensions. This leads to tensile stress in the plane of the film [3]. The stress (σ) which develops in a thin film coating during polymerization is shown in Equation 7.1 [3]:

$$\sigma = \frac{E_c}{1-\nu_c}\varepsilon(t) \qquad [7.1]$$

Where E_c is the elastic modulus of the coating, ν_c is the Poisson's ratio, and $\varepsilon(t)$ is the difference in strain between the state at time t and the stress free state. If relaxation is permitted to take place (for example by delaminating the film from the substrate), then $\varepsilon(t)$, and therefore σ, will be low. Inside of the GLAD film, the polymer is prevented from shrinking by the reinforcement provided by the helical structures. As the film wants

to contract but cannot, this generates a stress in the composite film. Once the GLAD template is removed, this stress is relieved by the slight collapsing of the film. The effect of polymerization shrinkage can be seen by examining the figures and noting that each layer of the film is slightly thinner after the template removal. Overall it can be estimated that 50% of the change in thickness is due to polymerization shrinkage and 50% is due to non-uniformities in the etch-back process. Each of these factors is therefore responsible for a change of approximately 5% change in the overall thickness.

To precisely gauge the extent to which the film contracted due to polymerization shrinkage when the GLAD template was removed, a sample was filled, polymerized and etched-back as per usual. Before removing the GLAD template in BOE, part of the film was lithographically masked with photoresist. This area was therefore protected during the etch-removal of the GLAD film. This ensured that all of the contraction seen in the perforated area as compared with the non-perforated area would be due to the polymerization shrinkage, as opposed to non-uniform etching. The results are shown in Figure 7.7:

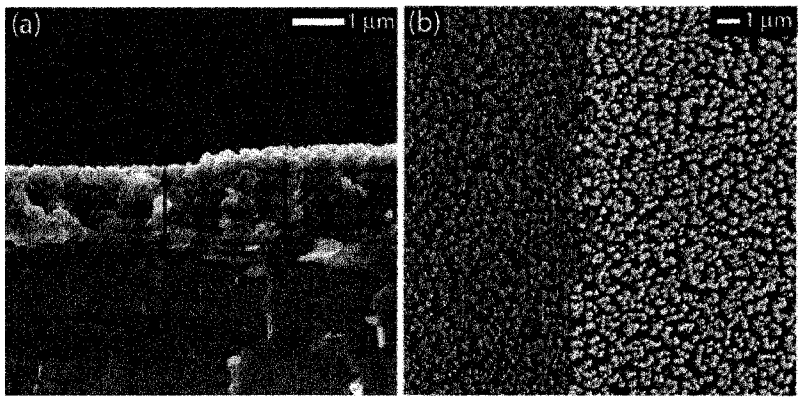

Figure 7.7: Lithographically-patterned perforated thin film. The film is shown from the side (a) and top (b). This sample is anchored to a silicon substrate.

Figure 7.7 allows the change in thickness as a function of polymerization shrinkage of the sample to be gauged without having to take into account the non-uniformity in the etch-back process. In the nanorebar reinforced part of the sample, the polymer layer is 1.83 µm tall, whereas the perforated film layer is only 1.71 µm tall. The sample has contracted by 0.12 µm, which corresponds to a shrinkage of 6.5%.

7.3.2 Actuation

Actuation of perforated thin films was extremely difficult to measure. The films themselves are quite thin (2 μm to 3 μm), which makes strains of a few percent difficult to distinguish from the noise. In addition, the surfaces of the films are quite rough, which makes measurement by interferometry difficult due to scattering.

The change in surface profile as a function of temperature of a liquid crystalline polymer perforated thin film is shown in Figure 7.8. This data was collected using the Fogale ZoomSurf 3D profilometer. In Figure 7.8(a) the surface profile of the film is shown during heating, measured against a bare area of substrate from which the film was removed with a razor blade. As the sample itself is only 3.2 μm thick, it is very difficult to discern any strain above the uncertainty in the measurement. Figure 7.8(b) shows the change in step height of the sample as a function of temperature. This change in thickness was calculated by averaging the data collected for the lower step, the upper step, and subtracting the difference. The uncertainty in each measurement was used to generate the error bars shown. Clearly the change in thickness is less than the scatter in the measurements, and no solid conclusions about the change in thickness of the film as a function of temperature can be made.

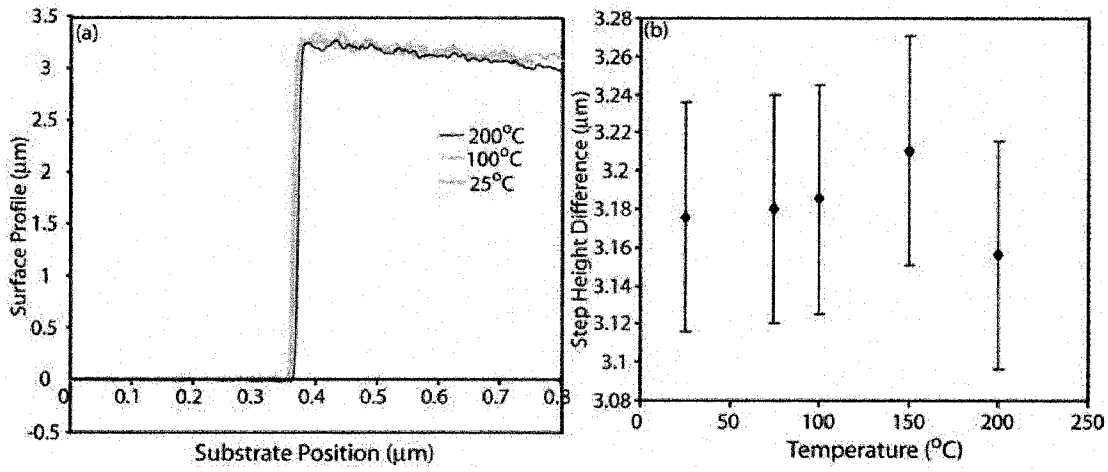

Figure 7.8: Actuation of a liquid crystalline polymer perforated thin film. The actual surface profile is shown relative to a bare area of substrate (a). The surface profile changes only slightly on heating, and the roughness of the surface makes it difficult to measure this change accurately. The change in step height difference as a function of temperature is also shown (b), but it is not possible to discern the true strain in the sample beyond the uncertainty in the measurement.

The low responsivity of these films was surprising, especially given that the surface anchored thin films of the same material characterized in Chapter 6 were able to undergo deformations of 2% to 11% upon heating, depending on the LC alignment. It was actually expected that the liquid crystalline polymer perforated thin films would undergo even larger deformations, since the results of Chapter 3 indicated that perforated thin films have lower moduli than bulk films of the same material.

The most likely explanation for the reduced responsivity of this material is the composition of the material itself. It was initially assumed that once the template film was removed, the resulting perforated thin film would be free to expand and contract when heated and cooled. However, the process used to remove the GLAD template cannot effectively etch all of the structures that comprise the master film. As described in Chapter 2, when a film is deposited by glancing angle deposition, competitive growth among the structures being deposited leads some columns to become extinct. These columns are shorter than the overall thickness of the film, as illustrated in Figure 7.9 (a) and Figure 7.9 (b).

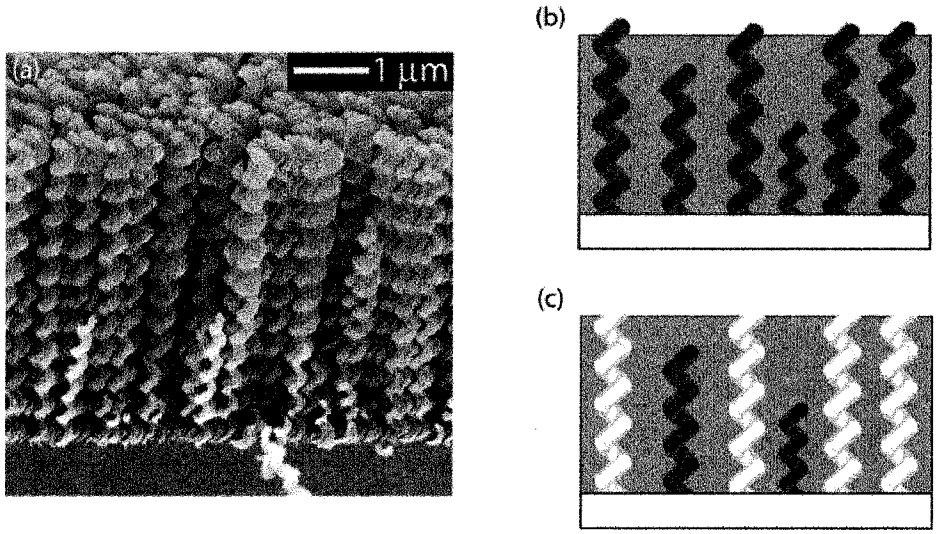

Figure 7.9: Etch-back of perforated thin films. In a GLAD film some columns become extinct during the deposition process, and are therefore shorter in height than the film itself. After filling and etch-back, these extinct columns are completely surrounded by the matrix material (b), and therefore are not accessible to the wet etchant used to remove the template film. After etch-removal of the template film, these shorter columns are preserved in the matrix material (c).

When the filled structure is etched back and the master film is etch removed, shorter structures are protected from the wet etchant by the material that surrounds them, as shown in Figure 7.9 (c). These structures are therefore preserved in the final perforated thin film and likely act as 'rebar', preventing the material from contracting and expanding freely.

7.3.3 Theoretical Calculations

To verify that the limited responsivity of the material was caused by unetched GLAD, a mathematical model was developed to compare the expected deformation of the composite material with that of a perfectly-etched structure.

If every GLAD helix could be etch-removed from the polymer matrix, then, ignoring the spring-like characteristics of the pores, the modulus of the resulting perfectly-etched film could be approximated using effective medium theory, as shown in Equation 7.2:

$$E_{eff} = \rho_p E_p + (1-\rho_p)E_v \qquad [7.2]$$

Where ρ_p is the fractional density of the polymer, and $(1-\rho_p)$ is the fractional density of the voids. Since the voids themselves are essentially air, $E_v = 0$ and the second term of the equation is equal to 0. For an SiO_2 helical film deposited at 85°, $\rho_p \sim 0.7$, based on the fact that the density of the SiO_2 has been measured to be approximately $0.3\rho_{bulk}$ [4]. At room temperature the mean elastic modulus of poly(M1:M2, 88:12) can be estimated by Equation 7.3:

$$E_p = \sqrt{\frac{2E_{\perp}^2 + E_{\parallel}^2}{3}} \qquad [7.3]$$

Where $E_{\perp}$ (22 MPa) and $E_{\parallel}$ (125 MPa) are the elastic moduli measured in the directions parallel and perpendicular to the direction of molecular alignment in a sample with uniaxial alignment. The average value of E_p can be calculated to be 74 MPa. The effective modulus of a perfectly-etched polymer PTF can therefore be determined using Equation 7.2, as shown in Equation 7.4:

$$E_{eff} = \rho_p E_p = 0.7 \times 74\ MPa = 52\ MPa \qquad [7.4]$$

If the GLAD film is imperfectly etched, as is thought to occur when the film is etched from the top, then the composite film is comprised of three different materials: the polymer, the air voids, and the unetched SiO_2 GLAD structures. Ignoring the spring-like qualities of the pores, the effective modulus of the film can be approximated using Equation 7.5:

$$E_{eff} = \rho_p E_p + \rho_r E_r + \rho_v E_v \qquad [7.5]$$

Where E_p is the modulus of the polymer, ρ_p is again the fractional density of the polymer, ρ_r is the fractional density of the GLAD rebar structures, E_r is the modulus of the GLAD rebar, and ρ_v and E_v are the fractional density and the modulus of the voids. As the voids are made up only of air, $E_v = 0$. However, this term will be kept to develop the most general solution possible.

The sum of the partial fractional densities of the film (ρ_p, ρ_r, ρ_v) is 1, as shown in Equation 7.6:

$$1 = \rho_p + \rho_r + \rho_v \qquad [7.6]$$

As the density of a GLAD film remains essentially constant with thickness [4], the value of ρ_p is invariant. However, the value of ρ_r and ρ_v change as a function of film thickness. Equations that describe these two variables can be developed based on the geometric characteristics of a GLAD film itself. As was described in Chapter 2, as a GLAD film is deposited, the number of columnar structures decreases with increasing thickness due to competition effects [5]. As one structure shadows another, the dominated structure is deprived of incoming flux, and becomes extinct. As the density of the film remains relatively constant throughout the film [6], the persisting columns must therefore increase in diameter. It has been shown that the average column width (w) at a particular height within the film can be modeled as a function of column height (h) using a power law, as expressed in Equation 7.7 [7, 8]:

$$w(h) = mh^{\beta} \qquad [7.7]$$

In this equation β is an experimentally determined constant, and m is a constant of proportionality. For an SiO_2 film deposited at 87°, the constant in the exponential term has been determined to be $\beta = 0.82$ [7]. As this value has not been measured for a deposition angle of 85°, this is the value that will be used here, although the effect of varying this parameter will also be investigated. Note that the relationship described in Equation 7.7 applies equally to the SiO_2 GLAD structures and the voids, since the voids are just the pores that remain when the GLAD structures are etch-removed. The values of β and m are the same for both cases.

The fractional density of voids (ρ_v) and SiO_2 nanorebar (ρ_r) at a particular height (h) within a film can be expressed in terms of column width (w). Consider slicing the film at height h in a direction parallel to the substrate, and examining the composition of this layer over an arbitrary area A, which contains N_v voids. This concept is illustrated schematically in Figure 7.10:

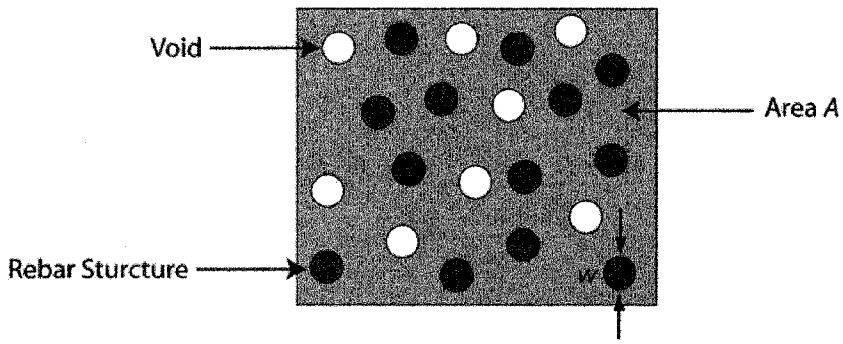

Figure 7.10: Top view of a cross-sectional slice of a composite film. The fractional density of the voids can be determined by multiplying the number of voids by the average area of each void, and dividing by the total area A.

The fractional density of voids (ρ_v) can be determined by multiplying area occupied by a void (a_v) by the number of voids, and dividing by the area A. The area of a void can be determined from its width, which was expressed as a function of height in Equation 7.7. The fractional density of the voids at height h is given as a function of h in Equation 7.8:

$$\rho_v(h) = \frac{N_v(h) \times a_v(h)}{A} = \frac{N_v(h)}{A} \pi \left(\frac{w}{2}\right)^2 = \frac{N_v(h)\pi}{4A} m^2 h^{2\beta} \qquad [7.8]$$

Boundary conditions can be applied to determine the value of the unknown quantity $N_v(h)m^2/A$. For a PTF which has been etched from the top, all of the SiO_2 rebar structures are removed from the top layer of the film corresponding to thickness $h = h_f$. The boundary conditions shown in Equations 7.9 and 7.10 can therefore be deduced:

$$\rho_r(h_f) = 0 \qquad [7.9]$$

$$\rho_v(h_f) = 1 - \rho_p \qquad [7.10]$$

The number of voids at the top of the film $N_v(h_f)$ can be determined by substituting Equation 7.10 into Equation 7.9, as shown in Equation 7.11:

$$N_v(h_f) = \frac{4A}{\pi} \frac{(1-\rho_p)}{m^2 h_f^{2\beta}} = N_v \qquad [7.11]$$

The number of voids or pores is constant throughout the film thickness, since any pore within the film must have been etched from the top, and any column which is etch-removed must have nucleated at the bottom of the film thickness (i.e. at the substrate). New voids cannot appear midway through the film thickness, and likewise existing voids cannot terminate. Therefore N_v is a constant, although the density of the voids does change as a function of film thickness, since the columns broaden as the thickness increases. The density of the voids can be determined as a function of film height (h) by substituting Equation 7.11 into Equation 7.8, as shown in Equation 7.12:

$$\rho_v(h) = (1-\rho_p)\left(\frac{h}{h_f}\right)^{2\beta} \qquad [7.12]$$

The fractional density of the rebar material can now be determined by combining Equations 7.12 and 7.6, as shown in Equation 7.13:

$$\rho_r(h) = (1-\rho_p)\left[1-\left(\frac{h}{h_f}\right)^{2\beta}\right] \qquad [7.13]$$

The fractional density of the rebar and of the voids are plotted in Figure 7.11 (a) and (b) respectively, for $\rho_p = 0.7$, and a film thickness $h_f = 5$ μm. These values are plotted for a variety of values of β (as indicated inset on each graph). In all cases, the rebar fraction decreases from 0.3 to 0 throughout the film thickness, while the void fraction increases from 0 to 0.3.

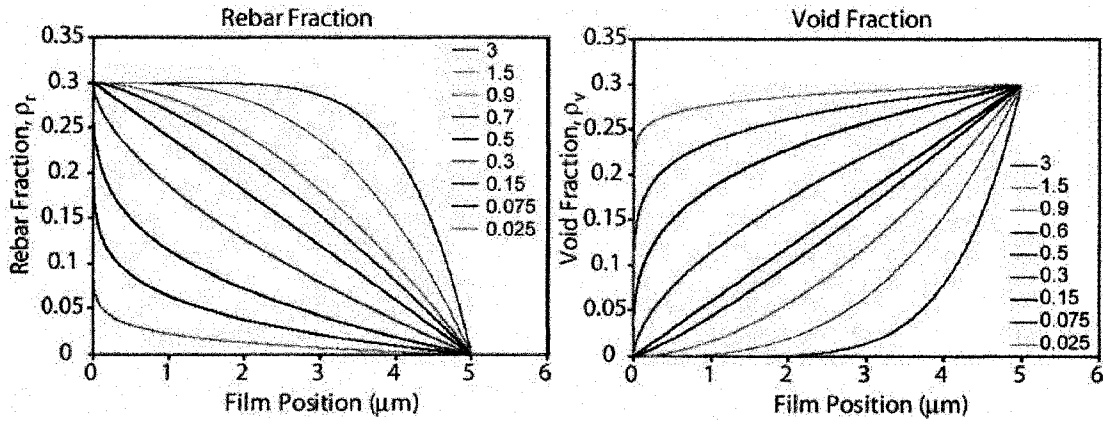

Figure 7.11: Fractional densities as a function of film position (h). The fractional density of rebar in the film decreases from 0.3 at the surface of the substrate to 0 at the surface of the film. The fractional density of the voids increases from 0 at the surface of the substrate to 0.3 at the surface of the film. Both functions are plotted for a variety of values of β, as indicated in the legend of each plot.

These graphs show that if the value of β employed throughout these calculations (0.82) is too high, then the fraction of voids throughout the film will be under-estimated. The modulus (and responsivity of the material) will therefore likely be over-estimated. If the value of β is too low, then the number of voids will be over-estimated and the modulus will be under-estimated.

Before the effective modulus of a slice of film at height h can be evaluated using Equation 7.5, the elastic modulus of the nanorebar (E_r) must be determined. Simply using the bulk modulus of SiO_2 (72 GPa [9]) is not sufficient, since a previous study has shown that SiO GLAD helices are approximately 1000 times more compliant than bulk SiO, due to their spring-like nature [10]. The modulus of the helical springs can be estimated from their geometry, using Equations 7.14 and 7.15 [10, 11]:

$$k = \frac{E_{bulk} D^4}{2(1+\nu)64 r_h^{\ 3} N}\left[1 - \frac{3}{64}\frac{D^2}{r_h^{\ 2}} + \frac{(3+\nu)}{2(1+\nu)}\tan^2\theta_r\right]^{-1} \quad [7.14]$$

$$E = \frac{kh_f}{A} \quad [7.15]$$

Where E_{bulk} is the modulus of the bulk material, N is the number of turns in the film, D is the cross-sectional diameter of the helix, ν is Poisson's ratio of the bulk material, θ_r is the rise angle of the helix, and r_h is the helical radius. This set of equations is likely to underestimate the modulus of the nanorebar, since Equation 7.14 describes the case of a helix surrounded by air, not by another material. Nonetheless, it is felt to be an acceptable approximation since the modulus of the polymer matrix is so much lower than the modulus of the SiO_2 structures. The parameters used to evaluate Equations 7.14 and 7.15 are summarized in Table 7.1:

Parameter	Value
E_{bulk}	74 GPa
D	55 nm
ν	0.16 [9]
θ_r	39°
r_h	75 nm
A	$\pi(55\text{ nm}/2)^2$
N	5

Table 7.1: Geometric parameters used to determine the modulus of nanorebar.

Using these parameters, the modulus of the rebar is determined to be 974 MPa. Returning to Equation 7.5, Equations 7.12 and 7.13 can be used to generate an expression for the local modulus of a slice of film at height h ($E_{loc}(h)$), as shown in Equation 7.16:

$$E_{loc}(h) = \rho_p E_p + (1-\rho_p)\left[1 - \left(\frac{h}{h_f}\right)^{2\beta}\right]E_r + (1-\rho_p)\left(\frac{h}{h_f}\right)^{2\beta} E_v \quad [7.16]$$

The material constants used to determine $E_{loc}(h)$ are summarized in Table 7.2:

Parameter	Value
ρ_p	0.3
E_p	74 MPa
E_v	0
E_r	974 MPa
h_f	2 μm
β	0.82

Table 7.2 Top-etched perforated thin film material parameters. These are the parameters which are employed in Equation 7.16 to determine the local modulus of an imperfectly-etched PTF.

Most of these parameters have been explained throughout this section, with the exception of the final film thickness, h_f, which was chosen the reflect the thickness of the film shown in Figure 7.7. The effective modulus of the imperfectly-etched film can be plotted as a function of film position (along the height of the film) from Equation 7.16, as shown in Figure 7.12:

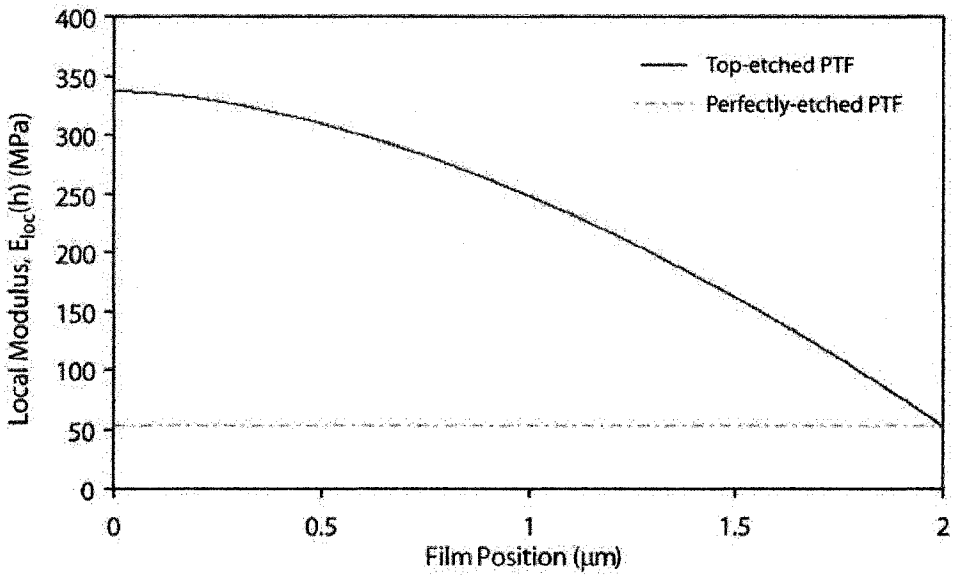

Figure 7.12 Local modulus of a perfectly-etched and imperfectly-etched PTF. The height dependent local modulus of both a perfectly-etched PTF and an imperfectly-etched PTF is plotted as a function of film thickness. While the modulus of the perfectly-etched film is constant throughout the sample, the modulus of the imperfectly-etched film varies as a function of film thickness.

To determine the effective modulus of the imperfectly-etched film, the local modulus must be integrated over the entire thickness of the film. Analogous to the case of resistors in parallel, the effective modulus is not additive, but rather adds as reciprocals.

Consider applying a uniform stress to a stack of n slices. Each slice has the same cross-sectional area, the same thickness (dh), and a different modulus (E_n). When a stress σ is applied to the stack, each slice deforms by an amount du_n. The total strain in the section is found by dividing the change in length (du_n) by the differential thickness (dh), and is related to the stress using Hooke's law, as shown in Equation 7.17:

$$\sigma = E_n \varepsilon_n = E_n \frac{du_n}{dh} \qquad [7.17]$$

The effective modulus of the total film (E_{eff}) is proportional to the total strain ε_{eff}, as shown in Equation 7.18:

$$\sigma = E_{eff} \varepsilon_{eff} = E_{eff} \frac{du}{dh} \qquad [7.18]$$

In this equation, du is the total change in length of the film, which can be expressed as a sum of all of the incremental changes in length (du_n) as illustrated in Equations 7.19:

$$du = du_1 + du_2 + du_3 + ...du_n \qquad [7.19]$$

Combining Equations 7.17 – 7.19 results in Equation 7.20:

$$\frac{\sigma}{E_{eff}} dh = \frac{\sigma}{E_1} dh + \frac{\sigma}{E_2} dh + \frac{\sigma}{E_3} dh + ... \frac{\sigma}{E_n} dh \qquad [7.20]$$

Simplifying this equation by canceling the stress in each term, and integrating both sides over the thickness of the film (h_f) yields Equation 7.21:

$$\frac{1}{E_{eff}} = \frac{1}{h_f} \int_0^{h_f} \frac{1}{E_{loc}(h)} dh = \frac{1}{h_f} \int_0^{h_f} \frac{dh}{\rho_p E_p + (1-\rho_p)\left[1-\left(\frac{h}{h_f}\right)^{2\beta}\right] E_r + (1-\rho_p)\left(\frac{h}{h_f}\right)^{2\beta} E_v} \qquad [7.21]$$

Equation 7.21 is difficult to solve analytically due to the exponentials in the denominator, and was instead evaluated numerically using Excel. The effective modulus of the

imperfectly-etched PTF was determined to be 185 MPa. This is nearly 4 times as large as the value found for a perfectly-etched PTF (52 MPa).

When a stress σ – such as that caused by polymerization shrinkage or thermal expansion – is applied to the imperfectly-etched film, it undergoes a corresponding strain ε, where $\sigma = E\varepsilon$. The ratio between the strain generated in a fully-etched PTF (ε_{full}) in response to an applied stress and the strain generated in an imperfectly-etched PTF ($\varepsilon_{partial}$) in response to an equal applied stress is therefore given by Equation 7.22:

$$\frac{\varepsilon_{full}}{\varepsilon_{partial}} = \frac{E_{partial}}{E_{full}} = \frac{185\ MPa}{52\ MPa} = 3.6 \qquad [7.22]$$

An imperfectly-etched PTF is therefore theoretically predicted to undergo a strain which is 3.6 times smaller than the strain determined for the perfectly-etched film. This means that the GLAD present in the imperfectly-etched film impedes the responsivity of the film itself, and that finding a way to completely remove the GLAD template would enable much larger actuations to be achieved.

A few approximations have been made throughout these calculations. A value for β was selected from the literature for a slightly different deposition angle than the one employed here, the implications of which were briefly touched upon. The modulus of the SiO_2 rebar was calculated by treating each GLAD helix as a uniform spring with constant cross-sectional area and helical radius, which ignores the broadening of these structures. In addition, the equation used to determine the spring constant of a helical structure assumed a helix in air, whereas in this case the helix is encased by a soft polymer. This could lead to an underestimation of the modulus. In Chapter 3 it was found that the modulus of a perforated thin film could be tuned by varying the rise angle of the helical pores, due to the spring-like behavior of the pores themselves. This geometric effect was not taken into account here. Therefore the calculations described in this section are not intended to perfectly predict the behavior of perfectly and imperfectly-etched PTFs, but rather to give an idea of the differences between these two materials. Based on these

results it is concluded that the SiO_2 GLAD which is reinforcing the film impedes the full actuation of the polymer layer.

7.4 Bilayer composite films selectively-reinforced with nanorebar

In the previous section, it was hypothesized that a much more compliant liquid crystalline polymer perforated thin film could be made if the GLAD template film could be completely removed from the master film. One way to do so would be to etch the GLAD film from the bottom of the composite layer, as illustrated in Figure 7.13:

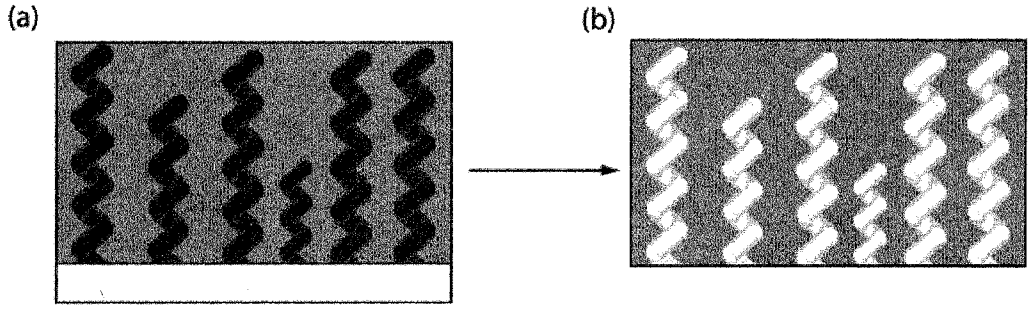

Figure 7.13: Etch-removal of the master template from the bottom. Once the master template is filled with liquid crystalline polymer (a), the template can be completely removed by separating the sample from the substrate and etching the GLAD structures from the bottom of the film (b).

As can be seen in Figure 7.13, the master film can only be etched from the bottom if the substrate is removed. In order to be able to handle these thin layers, an excess cap is formed on top of the GLAD film during the fabrication process. This layer adds structural support to the sample, and acts as a sort of substrate, as shown in Figure 7.14:

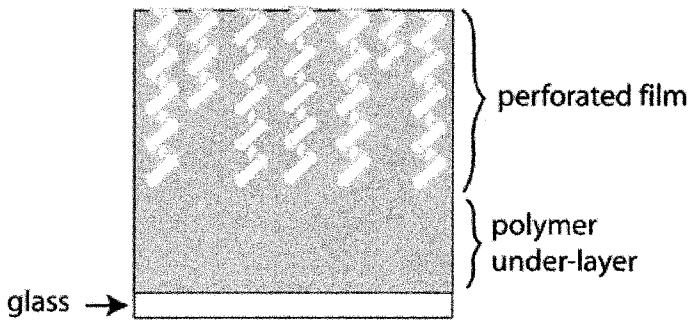

Figure 7.14: Schematic diagram of the bilayer structure. A thick polymer under-layer provides structural support to the perforated film, and anchors it to a substrate. Note that the sample has been flipped over with respect to its original configuration.

To measure the actuation of the perforated film layer using the optical profilometer, the expansion or contraction of this layer must be isolated from the expansion or contraction of the polymer under-layer. This can be achieved by selectively preserving some of the GLAD structures in the top layer, as illustrated in Figure 7.15:

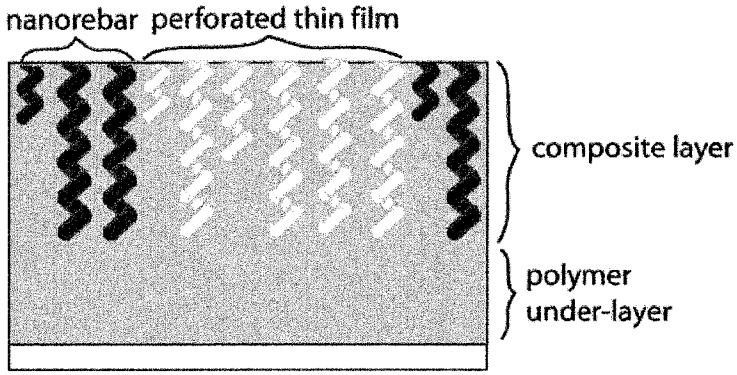

Figure 7.15: A selectively-reinforced bilayer composite film. If the GLAD template is only selectively removed, the remaining GLAD acts as nanorebar, providing structural reinforcement to the perforated thin film layer. This reinforcement provides stationary points of reference for interferometry measurements.

This selective reinforcement acts as a sort of 'nanorebar', providing structural reinforcement by preventing the polymer around it from expanding or contracting during measurement. The reinforced areas act as points of reference, allowing the expansion or contraction of the perforated thin film to be measured with respect to a stationary surface.

In Section 7.4.1, the fabrication process used to make selectively-reinforced bilayer composite structures will be presented. In Section 7.4.2, the actuation of samples with homeotropic and cholesteric alignment will be described, along with the actuation of samples fabricated using isotropic polymer.

7.4.1 Fabrication

Bilayer composite films which are selectively-reinforced with nanorebar can be fabricated using a modified single-templating process. In the first step of the process, a GLAD film with the desired structure is deposited onto a substrate which has been spin-coated with a layer of photoresist. This layer of resist acts as a sacrificial material later on in the process. A drop of liquid crystalline monomer mixture (such as poly(M1 88%,M2

12%) is heated into the isotropic phase and applied to the GLAD template film. A piece of glass is placed on top of this material. Typically this glass is cleaned using an oxygen plasma to increase its hydrophilicity, which encourages good bonding with the polymer. If the bottom and top substrates are conducting, then an electric field can be applied across the sample to align the liquid crystals (if desired). Once the sample is cooled to the nematic phase the monomer mixture is polymerized using UV light (either the mask aligner or Philips Solarium described in Chapter 4). After polymerization the sample may be heated to overcome vitrification effects, as per usual. The sample can then be immersed in liquid nitrogen, which causes the bottom substrate to delaminate from the photoresist layer due to the thermal stress induced by rapid cooling. Alternatively, the cell can be pried open with a razor blade, sometimes after soaking the sample for a few minutes in ethanol. The photoresist on the bottom of the sample is then rinsed off using a solvent such as ethanol. The sample is flipped over, and the top layer of polymer is removed by etching in the RIE for 16 s to 20 s. The nanorebar can then be patterned using standard lithographic procedures:

(1) a layer of photoresist (HPR 504) is deposited by spin coating.

(2) The solvent is removed from the photoresist by soft-baking in the oven for 30 minutes at 110 °C.

(3) The sample is cooled, and exposed to UV light for 4 s using a mask aligner and mask. The standard mask used in this process consists of 100 μm lines with a pitch of 500 μm. This exposure changes the solubility of the resist in a basic solution of developer.

(4) The sample is immersed in developer for 25 s with light agitation, and then rinsed in water.

The pattern from the mask is effectively transferred to the layer of photoresist on top of the sample. This resist acts as a mask itself during the selective etching of the GLAD template film. To remove the GLAD film in selected areas, the masked sample is immersed in buffered oxide etch for 5 minutes, and then rinsed in water. The photoresist mask can be stripped by rinsing the sample with acetone and IPA. This process is illustrated in Figure 7.16:

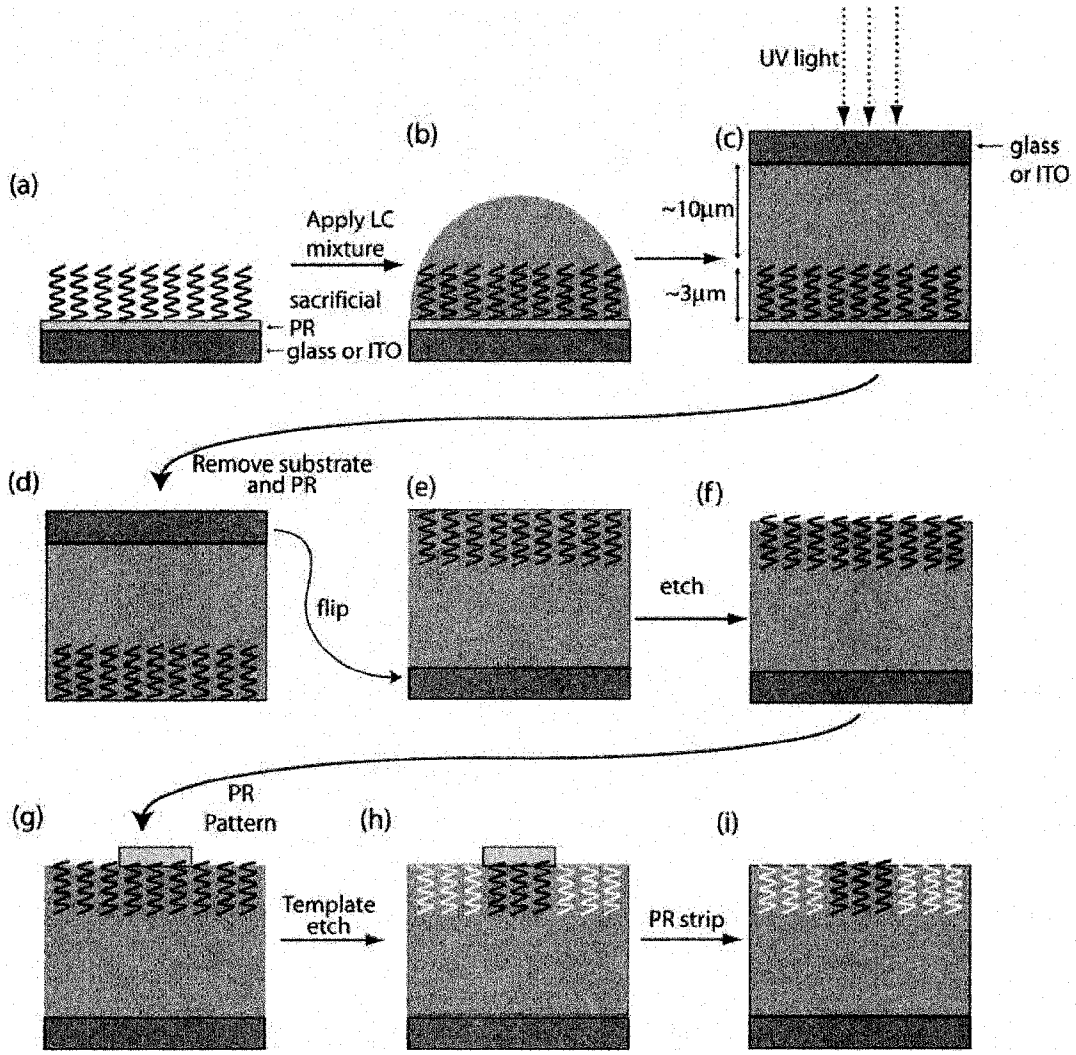

Figure 7.16: Fabrication of selectively-reinforced bilayer composite films. A GLAD film is deposited on a substrate (glass or ITO) that has been coated with a sacrificial layer of photoresist (a). A drop of liquid crystalline monomer mixture (in the liquid crystalline phase) is placed on top of the film (b). A piece of glass (or ITO) is placed on top of the monomer mixture, causing an even layer to form. If desired, an electric field can be applied across the sample at this point, provided that both substrates are conducting. The mixture is polymerized in UV light (c). After heat treatment, the sample is removed from the original substrate by immersion in liquid nitrogen. Stress at the photoresist-substrate interface causes the film to delaminate (d). Excess photoresist on the sample is rinsed off in ethanol. The sample is flipped over (e), and etched back using reactive ion etching (f). Photoresist is spin-coated onto the sample, soft-baked, exposed, and developed, leaving a photoresist mask (g). The template film can then be removed by etching in buffered oxide etch (h). The photoresist mask can then be removed by rinsing the sample in ethanol (i), leaving a selectively nanorebar reinforced composite structure.

While this process has many steps, the steps themselves are quite reliable and repeatable as compared with some of the other techniques described in this thesis. For example, in this process filling is easily achieved by placing a drop of monomer mixture on the substrate and placing a piece of glass on top of the mixture. This technique is far more convenient and reliable than spin-coating, which is used in the standard single-templating process. To fill a film by spin-coating, the correct spin speed and solvent concentration must be determined in order to ensure that the helical structures are completely filled, but that a large capping layer of excess material does not form on top of the structures. The etch-back procedure described here is also simpler for selectively-reinforced bilayer composite samples than for samples made using the single-templating process. In the normal single-templating process, it is easy for the thickness of the excess layer of matrix material to vary, which makes it hard to know the correct etch time. In the nanorebar fabrication process, the helices are perfectly filled every time. This is due to the fact that etching takes place from the bottom of the sample, which was perfectly bounded by the substrate during filling, preventing any under- or over-filling from occurring. The etch-back time therefore remains quite constant for all samples. The main complication of the process used to make selectively-reinforced bilayer composite films is that sometimes the sample does not delaminate correctly in liquid nitrogen, and the composite layer sticks to the wrong substrate, or remains partially on each substrate.

SEM images of some selectively-reinforced bilayer composite films are shown in Figure 7.17:

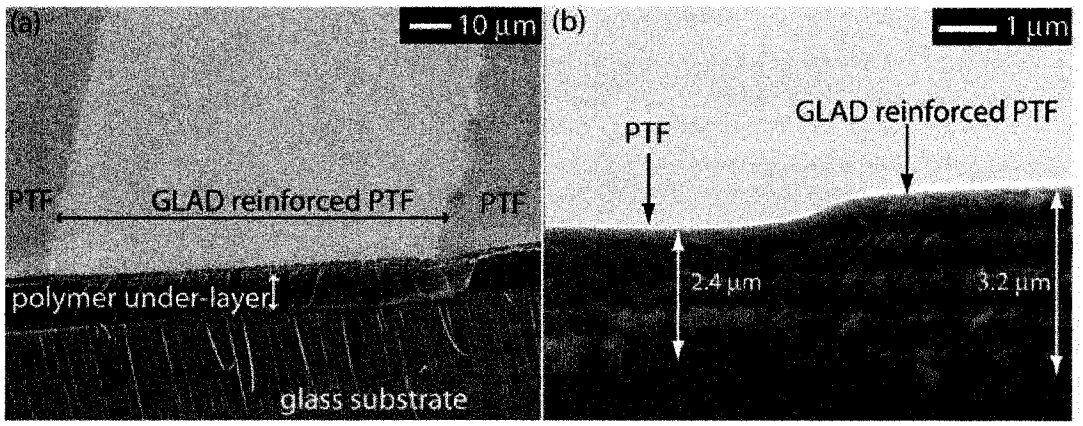

Figure 7.17: SEM images of selectively-reinforced bilayer composite films. A 100 μm stripe of GLAD reinforced perforated thin has been patterned in between regions of perforated film, as shown at an oblique angle (a). The perforated thin film (PTF) area, GLAD reinforced area, polymer under-layer, and glass substrate are all visible in this picture. A similar structure is shown from the side (b). The perforated thin film has contracted significantly as compared with the reinforced area. The liquid crystalline moieties in this particular film were aligned homeotropic to the substrate using an electric field.

As can be seen from Figure 7.17, the sample undergoes a considerable reduction in thickness when the template film is removed, resulting in a large step height difference between the reinforced and perforated film areas at room temperature. As in Section 7.3, this feature is due to polymerization shrinkage. During polymerization of a multi-functional acrylate, monomers achieve closer packing as they join the network, leading to an overall reduction in volume of the thin film itself [2]. The amount of shrinkage which occurs depends on a plethora of factors, including polymerization temperature, irradiation intensity, type of monomer employed, etc. [12]. For acrylates, volume changes of 10% to 30% (by volume) have been observed [3, 12]. For the bilayer composite samples described here, the polymer is initially prevented from shrinking by the interaction between the GLAD film and the polymer itself. This creates a large stress in the sample. It is known that stress can develop in a section of the sample which is prevented from contracting, either by a substrate, by another section of material which contracts by a different amount, or by a defect [13]. When the GLAD template is removed, the polymer is free to contract in the direction of the film thickness, thereby relieving the stress which has accumulated. As will be shown in Section 7.4.2, when the sample is

subsequently heated, the perforated film region expands. The thickness of the perforated thin film can again approach the thickness of the reinforced area. The nanorebar reinforced area is not as free to expand due to the presence of the nanorebar. When the sample is then cooled the perforated film area contracts, increasing the step height.

Note that while in Section 7.3 the perforated thin film fabricated from the same material by direct templating shrunk by only 6.5% of the total film thickness when the GLAD template was removed, here the bilayer composite film undergoes a much larger contraction (as was shown seen in Figure 7.17). The thickness of the perforated thin film area is 800 nm less than the thickness of the reinforced area. This corresponds to a change of approximately 25% of the total thickness of the GLAD template. The total strain of the perforated thin in the composite layer is 3.9 times as large as the strain in the film which was etched from the top, which agrees very well with the value predicted by the calculations performed in the previous section (3.6). Note that for the selectively-reinforced samples, the shrinkage may be slightly overestimated from the SEM images in Figure 7.17, as it is difficult to judge how far the GLAD film was etched back by RIE before the structures were removed.

7.4.2 Actuation

Just as it has been shown that bilayer composite films are able to undergo a larger shrinkage than a regular, top-etched perforated thin film due to its increased compliance, these films are also expected to undergo much large deformations upon heating. Actuation of selectively-reinforced nanorebar samples is demonstrated in this section using an optical profilometer (Zygo or Fogale Zoom-Surf 3D) and a homebuilt resistive heating stage.

7.4.2.1 Selectively-Reinforced Homeotropic Films

To achieve a uniform alignment of the liquid crystalline moieties, ITO substrates were employed and a voltage (50 V to 100 V, 1 kHz) was applied to align all of the LCs throughout the sample homeotropic to the substrate. A 3-d surface map of a homeotropic sample generated using the optical profilometer is shown in Figure 7.18:

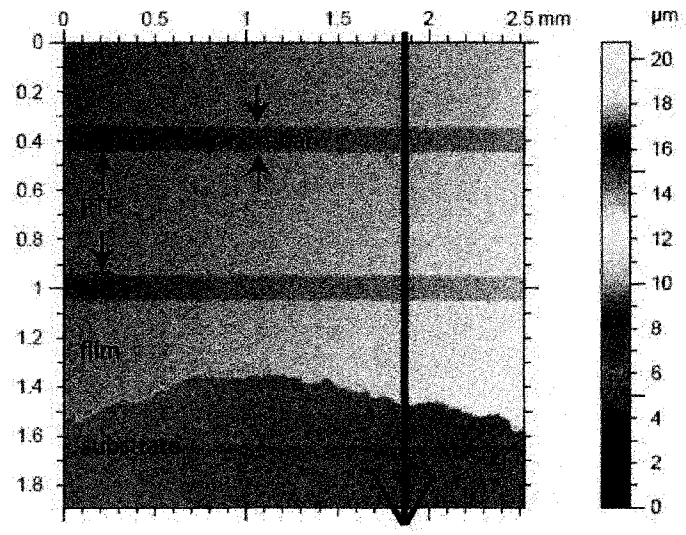

Figure 7.18: Bird's eye view of a homeotropic, selectively-reinforced sample. This surface profile was collected at room temperature using an optical profilometer. The blue area of the image is the substrate, which has been exposed to allow the surface profile to be measured relative to a flat, constant reference plane. The red arrow indicates the line along which the profile in Figure 7.18 is generated.

The profile of the surface along the red line from Figure 7.18 is shown as a function of temperature in Figure 7.19:

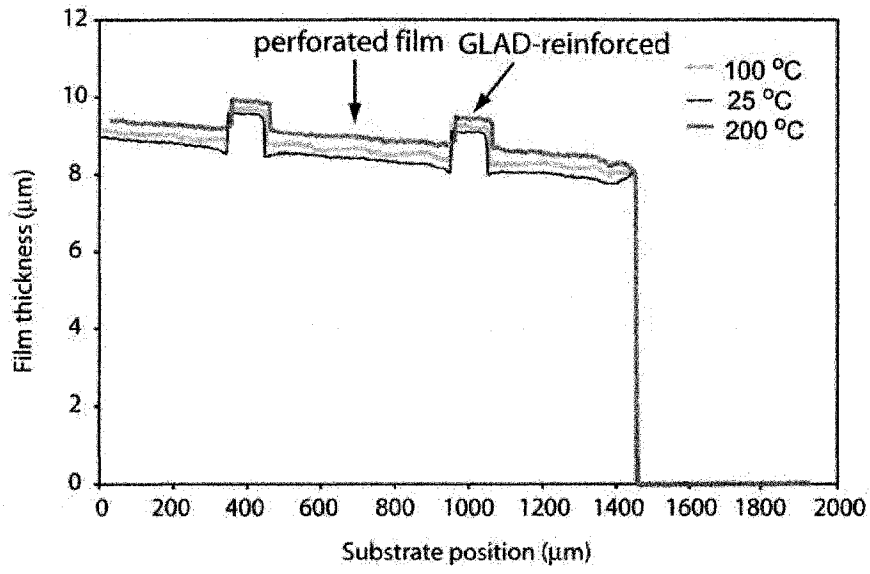

Figure 7.19: Surface profile of homeotropic, selectively-reinforced sample. In this figure the film profile is shown relative to the substrate at three different temperatures.

As the sample is heated, two changes take place: the overall thickness of the sample increases, and the step height difference between the perforated film and the GLAD-reinforced areas decreases. Both of these changes will be discussed in this section, beginning with the film thickness. The increase in thickness shown in Figure 7.19 is expected given the results of Chapter 6. Here the film thickness (as measured from the substrate to the top of the reinforced area closest to the cut) changes from 9.07 ± 0.06 μm to 9.42 ± 0.04μm. These values can be expressed as a percentage of the total film thickness as 3.9% ± 0.8%. This value is slightly higher than observed for homeotropic films in Chapter 6 (2%), which may be due to small differences in the alignment of the liquid crystals within the film.

The change in the step height difference between the perforated film and GLAD-reinforced areas will now be discussed. To simplify comparison, the surface profiles at various temperatures are shown in Figure 7.20, aligned such that the labeled GLAD-reinforced areas are level.

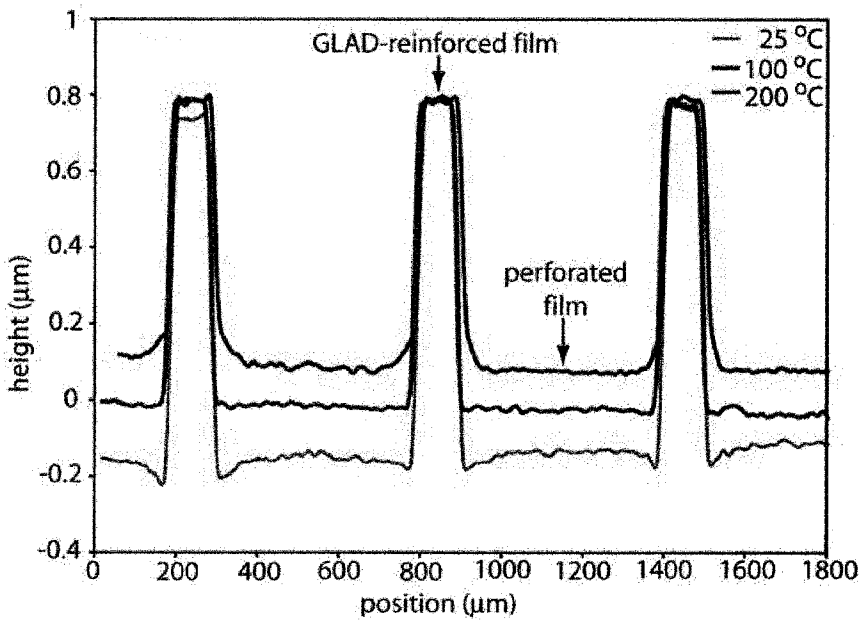

Figure 7.20: Actuation of a homeotropic, selectively-reinforced sample. In this figure, the profiles are aligned such that the top of the GLAD-reinforced areas are level. When the sample is heated to 200 °C the step height difference between the reinforced and perforated areas is reduced from 920 nm to 710 nm. This corresponds to a change in step height of 210 nm (23%).

Figure 7.20 shows that at room temperature the film studied here has a 920 ± 20 nm step height at room temperature. This indicates that a considerable amount of stress was relieved when the GLAD reinforcement was removed (again, a small part of this difference may be due to the etch-back step). When the sample is heated to 200 °C, the step height difference is reduced to 710 ± 20 nm. This corresponds to an effective change in height of 23% ± 3%. This effect was found to be reversible when the sample was cooled. Note that the change in step height difference between patterned and un-patterned areas (23% ± 3%) changes significantly more than the thickness of the polymer under-layer (3.9% ± 0.9%), which means that there is an additional mechanism driving the change in profile in the patterned area other than thermal expansion. This mechanism is based on the relief of stress created during polymerization shrinkage.

7.4.2.2 Selectively-Reinforced Cholesteric Films

A selectively-reinforced bilayer composite film was fabricated from a mixture of poly(M1:M2, 88:12) containing 5% BASF LC 756 chiral dopant. The sample was heated into the cholesteric phase before polymerization, and after polymerization exhibited a red reflection band. This red reflection band is indicative of the alignment in the thick polymer under-layer, however the alignment within the GLAD layer is not clear, since it would be influenced by both the effect of the GLAD film and the chiral dopant. After fabrication, the surface profile of the sample was monitored using an optical profilometer as it was heated. The results are shown in Figure 7.21:

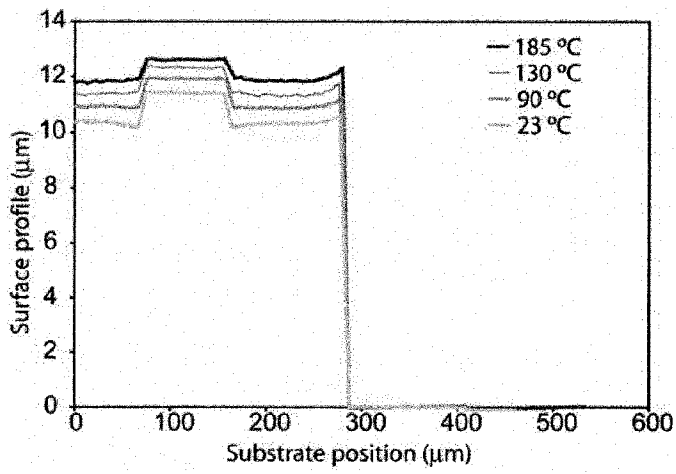

Figure 7.21: Actuation of a cholesteric, selectively-reinforced sample. The surface profile is shown as a function of temperature.

The room temperature step height between the nanorebar-reinforced and perforated film areas was 1130 ± 20 nm. Upon heating to 185 °C this step height difference was reduced to 850 ± 40 nm. This corresponds to a change of 25% ± 4%. The thermomechanical behavior of this sample is very similar to that of the homeotropic sample, suggesting that this behavior is determined more by the film composition than by the alignment of the liquid crystalline moieties.

7.4.2.3 Selectively-Reinforced Isotropic Polymer Films

Given that large actuations could be achieved using liquid crystalline polymers regardless of the alignment, it was decided to investigate the possibility of fabricating and actuating nanorebar reinforced composite films using an isotropic (non-liquid crystalline) polymer. Additional samples were therefore fabricated using the isotropic polymer triethylene glycol diacrylate (TEGDA, Polysciences Inc.), which is shown in Figure 7.22:

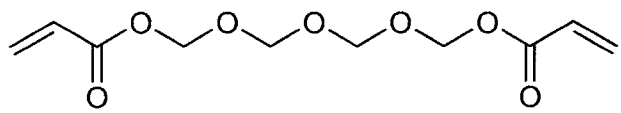

Figure 7.22: TEGDA monomer

This monomer is a diacrylate, having a double bond at each end, and can be polymerized when combined with Irgacure 184 initiator and illuminated in UV light. Isotropic samples were prepared using the same technique described above, only the filling and polymerization of the liquid monomer were performed at room temperature (rather than at an elevated temperature). An SEM image of the resulting structures is shown in Figure 7.23 along with a microscope picture depicting two of the nanorebar-reinforced regions:

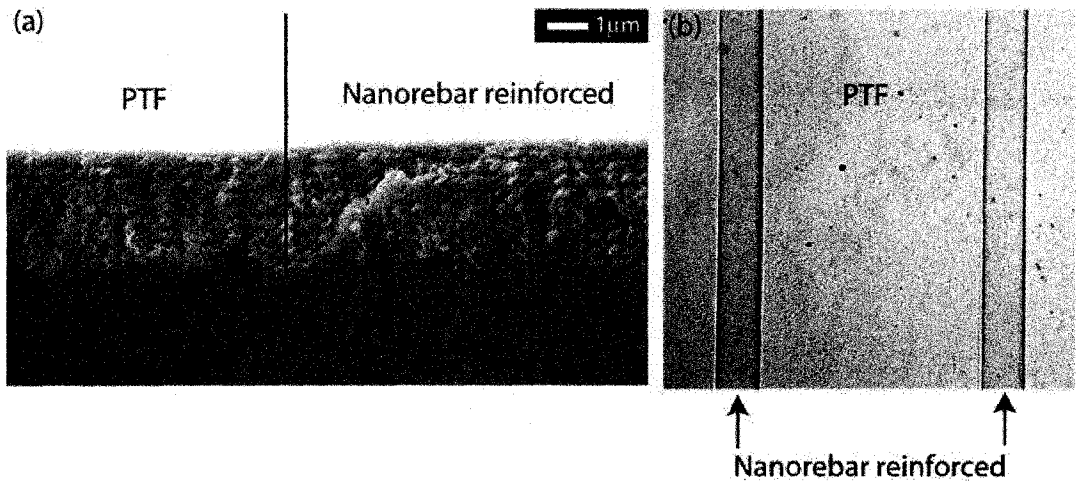

Figure 7.23: A selectively-reinforced TEGDA sample. SEM imaging shows that for this sample the height difference between the perforated and reinforced areas is approximately 400 nm, or 13% of the film thickness (a). The sample was also imaged using optical microscopy, and the thinner strips of nanorebar reinforced areas which separate the larger areas of perforated thin film are clearly visible (b).

Like the liquid crystalline polymer samples, this film contracts when the GLAD film itself is removed. The change in thickness is smaller than for the liquid crystalline polymer samples, approximately 330 nm for a film 3200 nm thick (corresponding to a change in thickness of ~10%). Selectively-reinforced composite TEGDA structures are also able to undergo large deformations when heated, as illustrated in Figure 7.24.

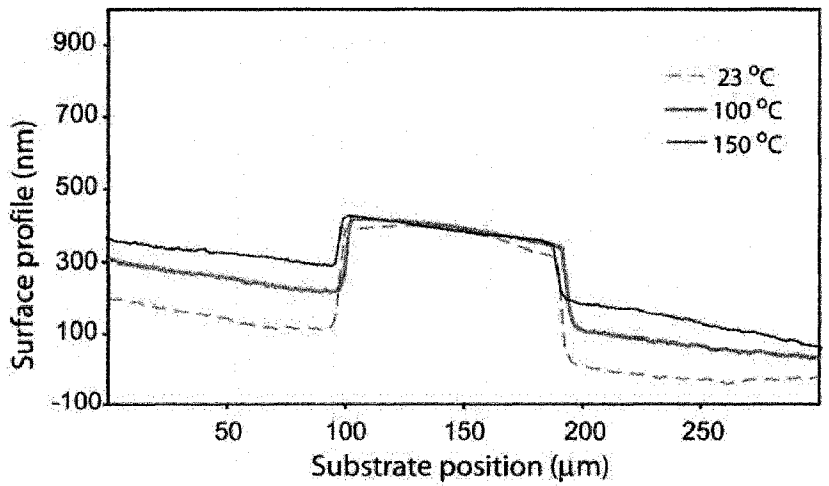

Figure 7.24: Actuation of a selectively-reinforced TEGDA sample. The relative step height difference between the reinforced and perforated areas changes significantly as the sample is heated to 150 °C.

At room temperature, the step height difference was determined to be 330 ± 10 nm, and when the sample was heated to 150 °C the step height difference decreased to 150 ± 10nm, corresponding to a total change in thickness of 45% ± 1%.

7.4.3 Summary

Thermally responsive surface relief structures can be made using an extended single-templating technique, which ensures that the master film is more completely removed than in the standard single-templating process used to make perforated thin films. Removal of the template film causes the perforated thin film to contract considerably, due to stress generated during polymerization. This creates a step height difference between perforated areas and areas which are reinforced with GLAD nanorebar. The step height difference of these regions decreases significantly when the samples are heated. This actuation was demonstrated for structures made using liquid crystalline polymers with a variety of alignments, and also with an isotropic polymer.

7.5 Conclusion

Three techniques for micro-patterning liquid crystalline polymers were presented in this chapter. Each of these techniques incorporates templating from a master film deposited by glancing angle deposition to achieve complex, high-aspect ratio microstructures in the final film.

The first technique presented was a double-templating process that could be used to make helical liquid crystalline polymer structures with submicron dimensions. An external electric field could be incorporated into the fabrication process to achieve homeotropic alignment of the liquid crystalline monomers with respect to the substrate. Preliminary results of actuation of these structures were presented, although the very small feature sizes makes characterization difficult.

The second technique presented was a single-templating process that could be used to make a solid liquid crystalline polymer film perforated with helical pores. This process could potentially also be extended to other types GLAD structures (i.e., slanted posts, square spirals, etc.). These films were shown to expand by only a small amount when

heated. Theoretical calculations were used to show that the actuation of the sample is impeded by GLAD structures which are preserved in the matrix during fabrication.

The third technique was also a single-templating process, in which the master film was etch-removed from the bottom rather than the top, ensuring a more complete removal of the master film. This technique could be used to make composite bilayer structures, which are comprised of a polymer under-layer and a perforated thin film top layer. Standard photolithography was used to pattern the top layer of the sample, which consists of alternating regions of perforated thin film and perforated thin film reinforced with helical GLAD structures. The step height difference between these two regions is significantly reduced upon heating, and changes in step height difference of nearly 50% have been observed for samples heated to 150 °C. Potential applications for composite bilayer structures include making self-sealed micro-pumping systems, tactile displays, and controllable surfaces for aerodynamic applications.

7.6 References

1. de Gennes, P.-G., *The physics of liquid crystals*. 2nd ed. The International Series of Monographs on Physics. 1993, Oxford Eng.: Clarendon Press.
2. Stansbury, J.W., Trujillo-Lemon, M., Lu, H., Ding, X.Z., Lin, Y. and Ge, J.H., *Conversion-dependent shrinkage stress and strain in dental resins and composites*. Dental Materials, 2005. **21**(1): p. 56-67.
3. Francis, L.F., McCormick, A.V., Vaessen, D.M. and Payne, J.A., *Development and measurement of stress in polymer coatings*. Journal of Materials Science, 2002. **37**(22): p. 4897-4911.
4. Gospodyn, J. and Sit, J.C., *Characterization of dielectric columnar thin films by variable angle Mueller matrix and spectroscopic ellipsometry*. Optical Materials, 2006. **29**: p. 318-325.
5. Malac, M. and Egerton, R.F., *Observations of the microscopic growth mechanism of pillars and helices formed by glancing-angle thin-film deposition*. Journal of Vacuum Science & Technology A, 2001. **19**(1): p. 158-166.
6. Gospodyn, J., Brett, M.J. and Sit, J.C. *Characterization by variable angle spectroscopic ellipsometry of dielectric columnar thin films produced by glancing angle deposition*. in *Engineered Porosity for Microphotonics and Plasmonics*. Mater. Res. Soc. Proc. 797: W5.19.1-6.
7. Vick, D., Smy, T. and Brett, M.J., *Growth behavior of evaporated porous thin films*. Journal of Materials Research, 2002. **17**(11): p. 2904-2911.
8. Karabacak, T., Singh, J.P., Zhao, Y.P., Wang, G.C. and Lu, T.M., *Scaling during shadowing growth of isolated nanocolumns*. Physical Review B, 2003. **68**(12).

9. Shackelford, J.F. and Alexander, W., *CRC materials science and engineering handbook*. 3rd ed. 2001, Boca Raton: CRC Press.
10. Seto, M.W., Dick, B. and Brett, M.J., *Microsprings and microcantilevers: studies of mechanical response.* Journal of Micromechanics and Microengineering, 2001. **11**(5): p. 582-588.
11. Young, W.C., Budynas, R.G., Roark, R.J. and Knovel (Firm), *Roark's formulas for stress and strain*. 7th ed. 2002, New York: McGraw-Hill, pp 398.
12. Anseth, K.S., Bowman, C.N. and Peppas, N.A., *Polymerization Kinetics and Volume Relaxation Behavior of Photopolymerized Multifunctional Monomers Producing Highly Cross-Linked Networks.* Journal of Polymer Science Part a-Polymer Chemistry, 1994. **32**(1): p. 139-147.
13. Lei, H., Francis, L.F., Gerberich, W.W. and Scriven, L.E., *Stress development in drying coatings after solidification.* Aiche Journal, 2002. **48**(3): p. 437-451.

8 Micro-Patterning of Liquid Crystalline Polymers: Photopatterning and Micro-Transfer Printing

8.1 Introduction

In Chapter 7, three techniques for micro-patterning liquid crystalline polymers based on templating from GLAD films were presented. In this chapter, three techniques which do not involve templating from GLAD films will be developed and explored. The main advantage of these processes is their simplicity, which may make them easier to incorporate with existing MEMS fabrication processes. The first two processes presented are called multi-phase and single-phase photo-patterning, and can be used to pattern liquid crystalline polymer thin films to make planar structures that undergo large deformations out of the plane of the substrate when heated. The final technique investigated is a form of stamping called micro-transfer printing. Micro-transfer printing is the simplest of the techniques presented, and therefore probably has the greatest potential for integration into commercial applications. The fabrication and actuation of structures using each of these techniques will be discussed. The material investigated throughout this chapter will be poly(M1 88%, M2 12%) as described in Chapter 6. The chiral dopant LC756 (BASF) will also be incorporated into the mixtures wherever possible to maximize the deformations which can be achieved. Micro-transfer printing will also be demonstrated using a humidity responsive polymer. In every case, the fabrication processes presented in this chapter involve simple techniques and technologies, which is important when considering bringing LCP actuator technology to eventual commercial use. Some of the results presented in this chapter have been published in the Journal of Materials Chemistry [1], while other results have been submitted to Molecular Crystals and Liquid Crystals [2].

8.2 Photopatterning

Photopatterning is a reliable method of pattern transfer that is extensively used in microfabrication. Typically, thin films are patterned by coating the film with a layer of photoresist, selectively exposing the photoresist through a mask, developing the resist to wash away exposed areas, and then using the photoresist itself as a chemically-resistant barrier during the etching of the thin film. In a simplified version of this process,

photopatterning can be used to directly pattern photo-sensitive materials. For example, Schadt et. al have demonstrated that photo-polymerizable layers could be irradiated through a mask with polarized light to make patterned alignment layers for liquid crystals. Complex patterns can be generated using successive exposures through different masks with light of different polarizations [3].

As described in Chapter 6, van der Zande *et al.* showed that liquid crystalline monomer mixtures containing UV initiators could be irradiated through a mask to form patterned samples. By exposing selected parts of the sample through a mask in the nematic phase, heating the sample to the isotropic phase, and flood exposing the remaining monomers, physically continuous but optically patterned films for transflective displays were produced [4]. A major focus of the study presented by van der Zande was to investigate diffusion effects which occurred during polymerization. Van der Zande found that the films produced were not uniformly flat, but rather exhibited a corrugated surface profile. This profile resulted from a number of factors, including the diffusion of monomers from unexposed to exposed regions, differences in surface tension between nematic and isotropic regions, and polymerization shrinkage effects. The exact profile was dependent on the material composition, polymerization conditions, and feature size. Sousa *et al.* also investigated the use of photopatterning, this time to make liquid crystalline polymer thin films with patterned cholesteric and isotropic regions for micro-actuator devices [5]. Their work focused on systems comprised of diacrylate liquid crystalline monomers, which formed a highly crosslinked network. This material was patterned with alternating lines of cholesteric and isotropic material, where each line was 100 μm wide. As in the work of van der Zande a step height difference was seen between the two regions at room temperature: the cholesteric region was initially 175 nm higher than the isotropic region. Upon heating to 175 °C, the difference between these two regions rose to 275 nm, and reverted to the original height difference upon returning to room temperature. This change in height corresponds to <1% of the overall film thickness.

In this section, we present a variation on the work described above: photopatterning is used to create isotropic and cholesteric regions using a mixture of M1 (88%), M2 (12%),

and chiral dopant. Because this mixture contains considerably less crosslinker than in the work of Sousa *et al.*, much larger deformations should be achievable. This fabrication method will be referred to as multi-phase patterning, since the films produced have regions which were polymerized in two phases (cholesteric and isotropic). Single-phase patterning will also be presented, in which a sample is polymerized in the cholesteric phase and the remaining material is rinsed off, leaving patterned lines anchored on the substrate. Actuation of both types of structures will be presented.

8.2.1 Fabrication

The single-phase and multi-phase photopatterning methods are illustrated in Figure 8.1 on the next page. Both techniques begin by filling a cell with a mixture of liquid crystalline monomers (M1/M2 88:12 blend, 93%), UV initiator (2%), and chiral dopant (5%). An alignment layer on the surface of the cell is employed to ensure that the liquid crystals lay parallel to the surface of the glass, such that the helical axis is aligned in the direction perpendicular to the plane of the substrate. The glass plates of the cell are adhered together with Norland Optical Adhesive, which in some cases is mixed 10 μm or 18 μm spacers. The cell is filled with the monomer mixture in the isotropic phase and then cooled to the cholesteric phase, which can be witnessed visually by watching for the appearance of a colored reflection band. A mask is placed on top of the samples prior to polymerization. A number of different masks were used during this study, including aluminum cut-outs and quartz plates patterned with thin films of chrome. The most commonly used mask consisted of 100 μm wide chrome lines separated by gaps of 400 μm on a quartz plate. Samples were typically polymerized at 55 °C to 57 °C for 40 s to 1 min using either the home-built UV lamp or Xe lamp described in Chapter 4. The Xe lamp was used together with a collimating tube (20 cm in length) to achieve a more directional light source that the home-built UV lmap. The home-built UV set-up employed a lamp with an area larger than the sample itself at a very small distance from the sample (8.5 cm), and flooded the sample with light from a larger range of angles. Multi-phase samples were then immediately heated to 100 °C to 110 °C and polymerized using the Philips Solarium lamp for 3 minutes, followed by a heat treatment to 200 °C. The top substrate could then be removed by opening the cell with a razor. Single-phase

samples were opened immediately after polymerization, and washed in acetone to remove unreacted material. These samples could then be heat treated to 200 °C to encourage completion of the polymerization reaction. Single and multi-phase photopatterning are illustrated in Figure 8.1:

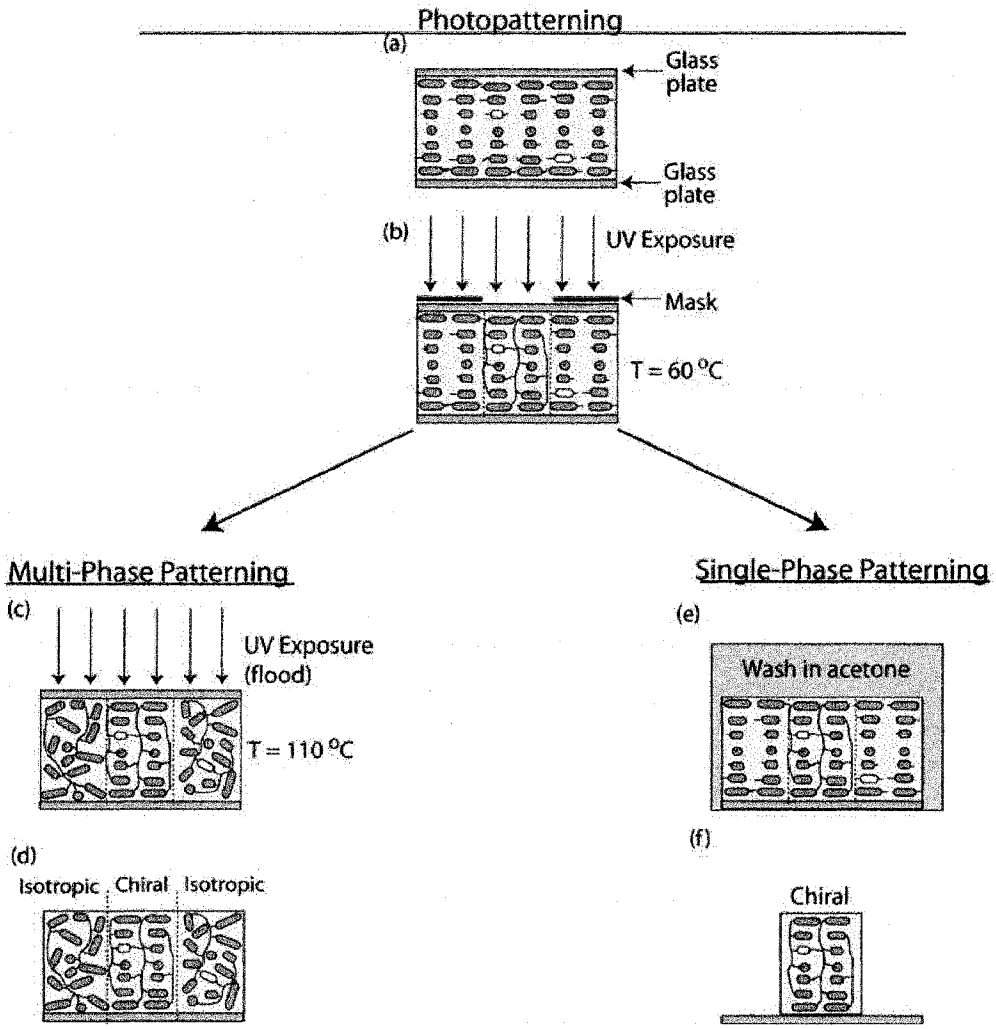

Figure 8.1: Single and multi-phase photopatterning. In both patterning methods, a cell is filled with a mixture of liquid crystalline monomers, UV initiator, and chiral dopant and heated in the desired phase (the cholesteric phase is shown here) (a). The sample is selective polymerized through a mask (b). In the case of multi-phase patterning the sample is then heated into the isotropic phase and flood exposed to polymerize any remaining unreacted material (c). The cell can then be opened, leaving a solid film with regions with unaligned and chiral-aligned liquid crystals (d). For the case of single-phase patterning, after the first (and only) UV exposure the cell is opened, and the unreacted material is washed in acetone (e), leaving patterned lines on a bare substrate (f).

Examples of multi-phase samples made using this technique are shown in Figure 8.2:

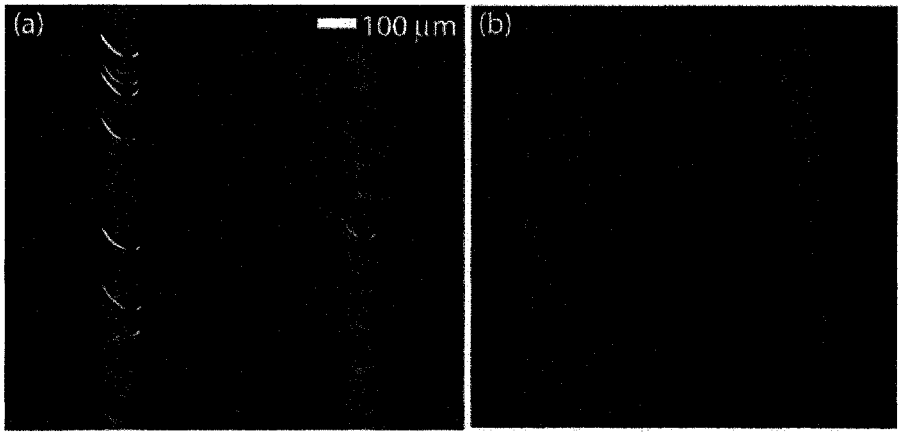

Figure 8.2: Multi-phase patterned samples. Two individual patterned lines are imaged using a 10x microscope objective (a). An entire patterned cell (having approximate dimensions of 1 in. x 1 in.) is also shown (b). Both samples are imaged between crossed polarizers, which makes the isotropic areas appear black and the cholesteric areas appear red. Since the sample is illuminated from the back, red light is being transmitted preferentially through the structures and the reflection band of the polymerized samples is actually in the green region of the spectrum.

The patterned lines shown in Figure 8.2(a) are sharp and well-defined. Some bands or streaks of color are visible throughout the cholesteric regions. These "oily streaks" are actually a type of defect that is commonly seen in cholesteric films, and occur when the chiral planes are mismatched between adjacent regions [6]. This defect is not expected to be detrimental to the thermo-mechanical behavior of the samples, as the liquid crystals within each region remain aligned parallel to the substrate, which will enable out of plane deformations upon heating.

In the fabrication processes described above, samples are produced using cells consisting of two pieces of glass separated by glue and spacer layers. This configuration was selected for a number of reasons: good uniformity in film thickness can be achieved throughout each cell, the height of the patterned structures can be controlled by varying the spacer diameters, and the high thicknesses attainable using cells makes the actuation of the structures easy to observe using interferometry. However, there are also some drawbacks to this method. The thick glass top substrate is detrimental to the lithographic process, as the light passing through it is subject to diffraction. The minimum resolution

achievable is approximately given by $15(\lambda t_{gap}/200)^{1/2}$ [7], where λ is the wavelength of light and t_{gap} is the thickness of the gap. For a top plate 1 mm thick, the minimum resolution achievable is 20 μm (assuming perfect contact between the mask and sample). Additionally, when the cells are opened, the polymerized material can adhere to either substrate, when in fact it would be preferable to select the substrate to which the material is anchored. To avoid these problems, single-cell configurations can also be used. In this case, the monomers are spin-coated from a solvent to form thin (<3 μm) layers of material on glass substrates coated with rubbed polyimide. The mask can then be placed directly on the monomer layer for the first UV exposure. Reasonably good lithographically-defined structures can be formed using this technique. Photographs of single-substrate multi-phase patterned samples are shown in Figure 8.3:

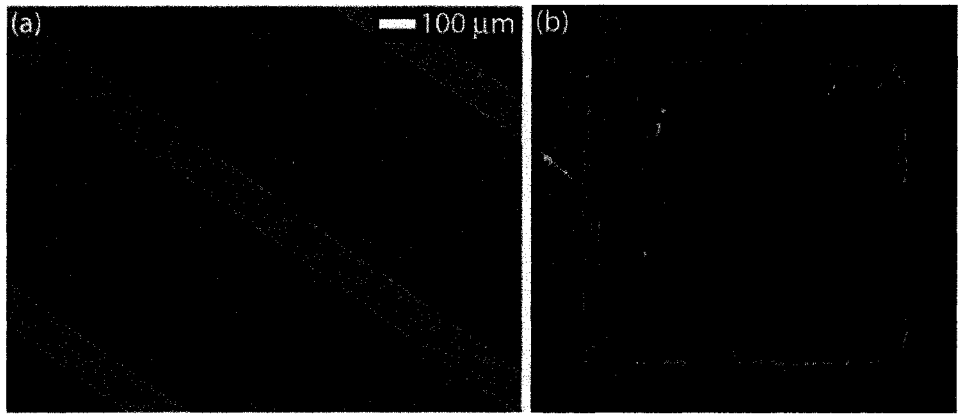

Figure 8.3: Single-substrate multi-phase photopatterned structures. This sample was polymerized from a single-substrate configuration, and photographed between crossed polarizers using a 10x microscope objective to magnify the 100 μm lines (a) and using a camera to capture an image of the entire 1 in. cell (b).

The main disadvantage of spin-coated samples is that they are quite thin, which means that the overall change in dimension of a sample as a function of temperature is smaller than for films prepared from cells. This makes the change in dimension that occurs upon actuation difficult to quantify. Therefore, in the remainder of this thesis, characterization data will be presented solely for samples fabricated from cells.

8.2.2 Actuation

Actuation of single- and multi-phase photopatterned samples was measured using the Fogale ZoomSurf 3D optical profilometer and home-built heating stage. All samples were pre-baked to 200 °C on a hotplate prior to measurement.

8.2.2.1 Actuation of Multi-Phase Photopatterned Samples

A multi-phase sample was made using a cell with a 6 μm gap (in this case the glue binding the cell contained no spacers) and a monomer mixture containing a blend of monomers M1 and M2 in an 88:12 ratio, initiator (2%) and the chiral dopant LC756 (5%). The cell was filled in the isotropic phase, and cooled to the cholesteric phase at 56 °C. The sample was then polymerized through a mask for 60 s under the Xe lamp described in Chapter 4. The chrome mask used in the preparation of this sample consisted of 400 μm lines with 100 μm gaps. After this first polymerization, the sample was moved to a hotplate at 110 °C and flood exposed using the Philips Solarium lamp. The cell was then opened, and the sample was heated to 200 °C as a heat treatment. Actuation of this multi-phase sample is shown in Figure 8.4:

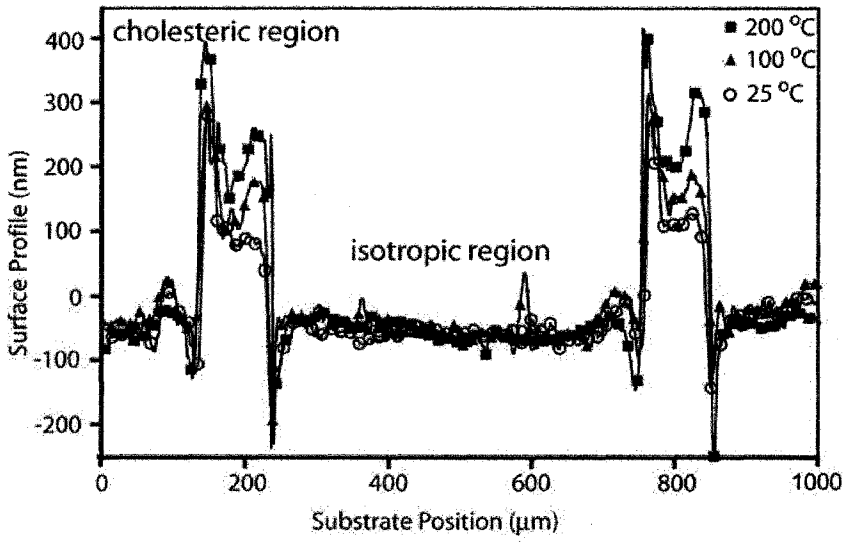

Figure 8.4: Surface profile of a multi-phase sample. The profile was mapped at 25 °C, 100 °C, and 200 °C using optical profilometry. The 100 μm wide cholesteric region protrudes above the isotropic region, even at room temperature.

The profile of the surface at room temperature shows the presence of upward pointing spikes at either end of the cholesteric regions which border on downward pointing spikes

at the edge of the isotropic regions. This profile is indicative of diffusion during polymerization [4]. As monomers are reacted into the network in the exposed region (achieving a higher packing density), other monomers diffuse into this area from the masked portions on either side. The width of the spikes is determined by the rate of diffusion. While the slope of the spikes appears quite sharp, bear in mind that the x-axis of the graph is compressed by 3 orders of magnitude relative to the y-axis.

When heated to 200 °C, both the chiral and isotropic regions are expected to expand. In Chapter 6 isotropic reference samples were found to expand by 5% when heated to 200 °C, and chiral reference samples were found to expand by 11%. Therefore the net expansion of the chiral region with respect to the isotropic region was expected to be 6% (360 nm for this 6 μm thick film). Figure 8.4 shows that the chiral region expands preferentially by only approximately 100 nm (1.6%). The reduced change in responsivity may occur due to stress at the interface between the two regions, or because diffusion of monomers into the exposed region reduces the overall order in the chiral region as compared with the reference sample. Evidence of this intermediate region between the cholesteric and isotropic areas can be seen in Figure 8.5, in which the sample is oriented at 45° to crossed polarizers:

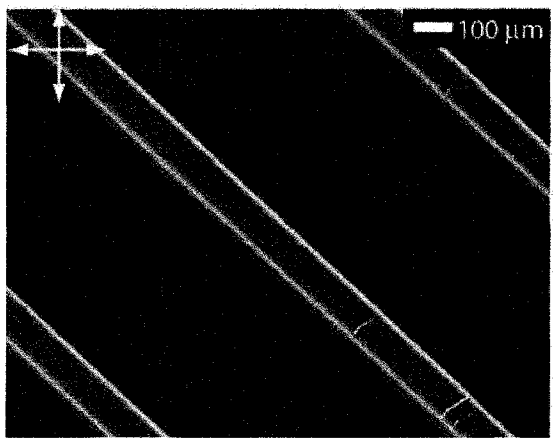

Figure 8.5: Multi-phase patterned sample. The sample was imaged oriented at 45° to crossed polarizers using an optical microscope. The interface between the isotropic and cholesteric regions (along the patterned lines) is bright white, suggesting that the liquid crystals in this region are aligned planar to the substrate.

In Figure 8.5 the region between the isotropic and cholesteric areas appears white between crossed polarizers, whereas in Figure 8.2 (a) when the sample was aligned parallel to crossed polarizers this region appeared dark. This suggests that the liquid crystals in this area are aligned planar to the substrate in a direction parallel to the lines themselves. The issue of diffusion will be discussed in more depth when presenting the results of the single phase samples.

8.2.2.2 Actuation of Single-Phase Photopatterned Samples

The actuation of single-phase patterned samples was also observed using white-light interferometry. Here the actuation of two different samples is presented: Sample (A), which consists of 250 μm wide lines 16.6 μm tall at room temperature, and Sample (B) which consists of 100 μm wide lines 3.8 μm tall at room temperature.

Sample A was fabricated using a cell with a thick gap (by including 18 μm spacers in the glue). The sample was illuminated through an aluminum cut-out mask of rectangles of various sizes. UV light from a Xe lamp was used to polymerize the sample for 41 s at a temperature of 58 °C. The intensity of the lamp at the sample was calculated to be approximately 1 mW/cm^2. After exposure, the cell was cooled for 15 s, opened, and rinsed in ethanol for 30 s. The surface profile of this sample as a function of temperature is shown in Figure 8.6.

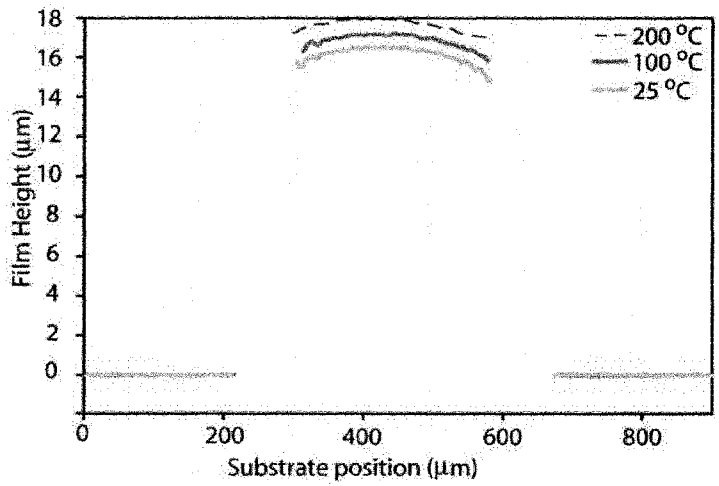

Figure 8.6: Actuation of a single-phase patterned structure. The sample was measured on cooling from 200 °C to 25 °C.

The surface profile of the patterned area is slightly curved. Although the curvature appears significant as shown, it is actually somewhat magnified by the scale of the graph. Note that the x-axis is greatly compressed with respect to the y-axis, and if the actual dimensions of the sample are taken into account the grade of the curvature is less than 1°. This slope is likely caused by a diffusion of the monomers during the polymerization process.

The data in Figure 8.6 was measured as the sample was cooled from 200 °C to 25 °C. At 200 °C the peak thickness of the film was determined to be 18.0 ± 0.1 μm, whereas 25 °C the peak thickness of the film was 16.6 ± 0.1 μm. This corresponds to a total change in thickness of 8.4% ± 0.8% (expressed as a percentage of the thickness of the film at room temperature). The total change in thickness was somewhat lower than expected, given that in Chapter 6 it was determined that a solid cholesteric thin film anchored on a substrate expands by 11% when heated from 25 °C to 200 °C. This reduced responsivity may also be due to diffusion of the monomers from unexposed to exposed areas during polymerization. The new material arriving would reduce the overall alignment of the sample, and therefore also reduce the anisotropic expansion of the material. Evidence for this theory can be seen in Figure 8.7, which shows the change in thickness of unpatterned isotropic and cholesteric reference samples as a function of temperature overlaid with the change in thickness of the single-phase patterned sample.

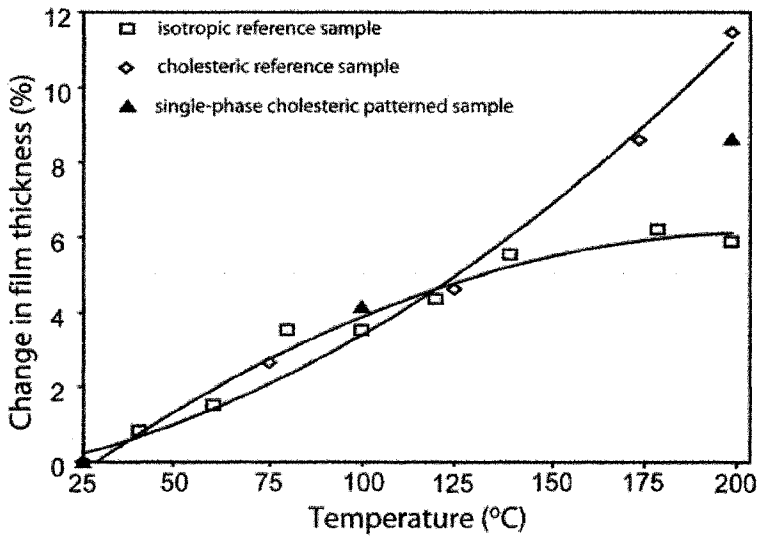

Figure 8.7: Actuation comparison of patterned and unpatterned samples. The change in thickness as a function of temperature of a single-phase patterned sample, isotropic reference sample, and cholesteric reference sample is shown. The change in thickness of the patterned sample falls midway between the change in thickness of the cholesteric and isotropic reference samples. The solid lines are included as a guide to the eye.

At 100 °C, all three samples have expanded by nearly equal amounts. At 200 °C, the cholesteric sample has increased in thickness the most, the isotropic sample the least, and the patterned sample is intermediate. While 8.4% ± 0.8% is below the cholesteric reference sample described in Chapter 6, it remains much higher than current state-of-the-art micro-actuator materials such as silicon.

Sample (B) was prepared using a similar method, only using a cell with a much smaller gap (as no spacers were included in the glue of the cell). The actuation of sample (B) is shown in Figure 8.8.

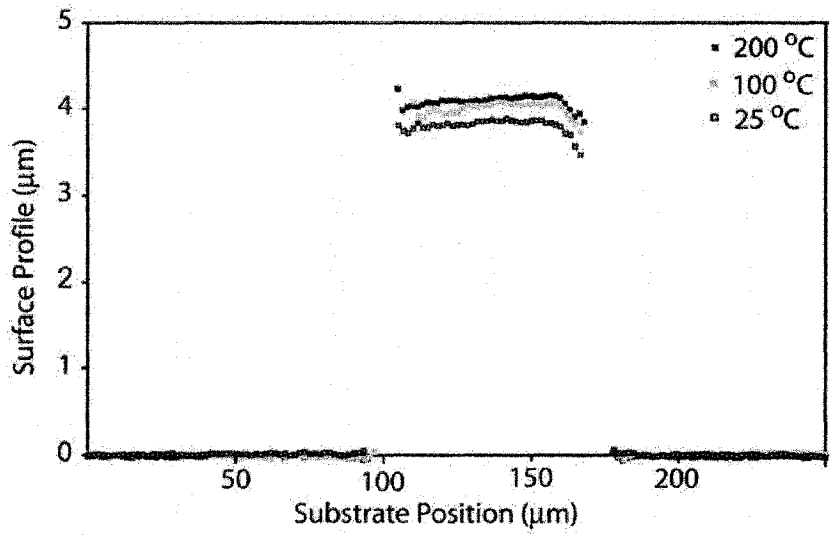

Figure 8.8: Surface profile of single-phase patterned sample. The surface profile of sample (B) was mapped at 25 °C, 100 °C, and 200 °C using the optical profilometer. The surface of this sample is somewhat rougher than shown in Figure 8.5. The initial and final thicknesses of the sample at 25 °C and 200 °C are 3.82 ± 0.05 μm and 4.11 ± 0.05 μm, which corresponds to a change in thickness of 7.4% ± 1.6%.

The initial thickness of the film at 25 °C was determined to be 3.82 ± 0.05 μm by averaging the thickness of the sample over the central 50 μm section of the relief structure. The thickness after heating to 200 °C was determined to be 4.11 ± 0.05 μm. Overall the change in thickness of the sample when it is heated from 25 °C to 200 °C is 7.4% ± 1.6%, which is within the uncertainty of Sample (A), but suffers from a large uncertainty due to the small thickness overall.

8.3 Micro-Transfer Printing

8.3.1 Fabrication

The final technique which will be discussed in this thesis is micro-transfer printing, which is depicted in Figure 8.9.

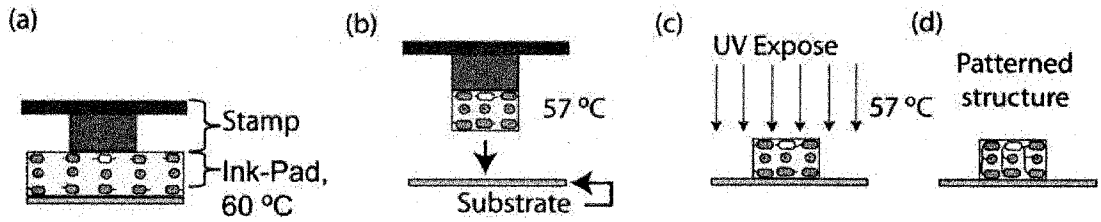

Figure 8.9: Micro-transfer printing. An 'ink-pad' is formed by heating a mixture of monomers into the cholesteric or nematic phase. A stamp is pressed into the surface of the ink-pad (a). The stamp is brought into contact with a substrate, which is also heated to the nematic/cholesteric phase of the ink. The sample is polymerized by exposing it to UV light in a nitrogen environment for 5 minutes (c), which produces an aligned, polymerized sample on a glass substrate (d).

This technique is a printing process which has many advantages that become significant for the large-scale production of liquid crystalline polymer actuators. The amount of waste material generated in this process is small – the liquid crystalline 'ink' is transferred efficiently from the inkpad to the stamp to the substrate. Compared to a process such as spin-coating, where a significant portion of the mixture is spun off of the substrate, or to a process such as single-phase patterning, where unpatterned material is washed away, this generates very little waste. In addition, the need for large amounts of environmentally unfriendly solvents is circumvented. The printing process also boasts the advantage that it could potentially be scaled up to roll-to-roll production, although temperature control at the stamps and substrates would be required.

For this thesis, preliminary investigations of the micro-transfer printing process were undertaken. Printing of liquid crystalline monomers was demonstrated using commercially-purchased rubber stamps. A mixture of M1/M2 monomers in an 88:12 ratio, chiral dopant LC756 (5%), and 184 initiator (2%) was spread onto a glass slide coated with an alignment layer of rubbed polyimide, which acted as the ink-pad. This 'ink-pad' was heated to 60 °C and the stamp was pressed into the liquid crystalline monomer mixture. The stamp was then pressed onto the final substrate: a glass slide also coated with an alignment layer of rubbed polyimide, heated to 57 °C. The patterned mixture could then be polymerized in UV light in a nitrogen environment for 5 minutes, and heat treated as desired.

An example of two printed structures is shown in Figure 8.10:

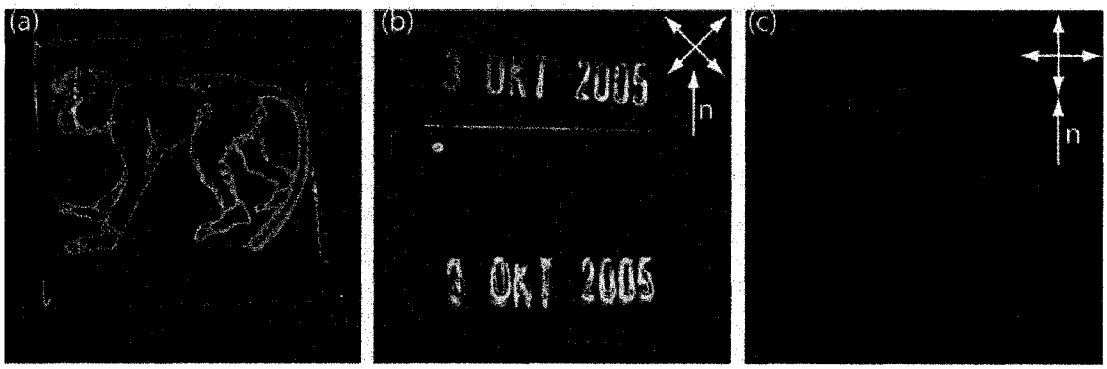

Figure 8.10: Printed structures. A poly(M1 88%, M2 12%, chiral dopant) monkey is shown photographed against a black background, and appears red due to the reflection band of the material (a). A nematic mixture of poly(M2,M3) was printed on rubbed polyimide, and exhibits nematic alignment as shown in (b) and (c). When the director (shown as a white arrow labeled n) is aligned at 45° to the transmission axes of the crossed polarizers (indicated by the white arrows), the sample appears bright (b). When the sample is rotated in the plane such that the director of the sample is aligned parallel to one of the transmission axes the sample appears dark (c). As a reference, note that each substrate measures approximately 1 in. by 1 in.

The structure depicted in Figure 8.10 (a) was polymerized from a mixture of monomers M1/M2 in an 88:12 ratio, initiator (2%) and chiral dopant (5%). The sample appears somewhat red in the figure, due to the reflection band of the chiral-aligned liquid crystalline units. This shows that reasonably good alignment was achieved.

The sample shown in Figure 8.10(b) and (c) was polymerized from a slightly different mixture of monomers, comprised of a 43:6:1 ratio of M3:M2:(184 initiator), where M3 is shown in Figure 8.11:

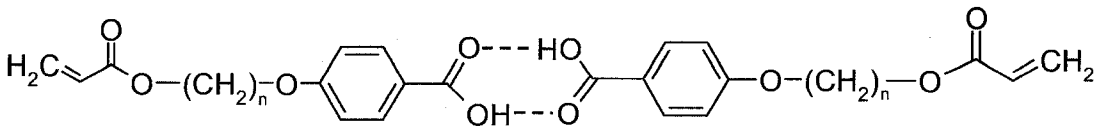

Figure 8.11: Molecule M3. This molecule is actually a supramolecular liquid crystal consisting of two individual molecules which are hydrogen bonded together (as denoted by the dashed lines). This molecule can be sensitized to humidity by exposure to an alkaline solution.

M3 is actually a supramolecular liquid crystal comprised of two smaller molecules which are connected together by hydrogen bonding between adjacent carboxylic acid groups (as indicated by the dotted lines in Figure 8.11) [8-10]. When these molecules are hydrogen bonded, the resulting supramolecule is rod-like and exhibits liquid crystallinity. Note that there is an acrylate group present on the end of each molecule (i.e.: on each end of the supramolecule), which may be polymerized to form a network. M3 may be aligned and polymerized as for M1 and M2. Once polymerized, M3 is a pH and humidity sensitive mesogen. The hydrogen bridged network is sensitive to chemical stimuli – for example, if poly(M3) is exposed to a sufficiently basic solution, hydrogen bonds in the network are broken, and the order of the polymer is reduced. In addition, the network becomes more hygroscopic, and the films begin to swell anisotropically in water. The strength of the hydrogen bonds can also be weakened on heating, leading again to a loss in order. Adding a small amount of M2 (12%) to the network ensures that on removing the stimulus the network will return to its original organization. The modulus of a uniaxial sample of poly(M3 88%, M2) at room temperature is very high: 3.8 GPa parallel to the direction of orientation and 1.5 GPa in the perpendicular direction.

The sample shown in Figure 8.10 (b) and (c) was polymerized from a mixture of M3, M2, and 184 initiator (in a ratio of 43:6:1). A thick layer of the monomer mixture was heated to the nematic phase on a rubbed-polyimide ink pad, stamped, transferred to a substrate of rubbed polyimide on glass, and polymerized for 5 minutes in UV. That reasonably good uniaxial alignment was achieved can be seen from the optical properties of the sample between crossed polarizers (as shown in Figure 8.10(b) and (c)): when the sample is oriented with the director at 45° to the direction of the transmission axes the sample appears bright, and when the nematic director is parallel to the transmission axis of one of the polarizers the sample appears dark. This sample is included in this section only to show that the technique can easily be extended to other liquid crystalline polymers.

8.3.2 Actuation

Actuation of the cholesteric poly(M1 88%, M2 12%) sample fabricated using micro-transfer printing was observed using white-light interferometry, as shown in Figure 8.12:

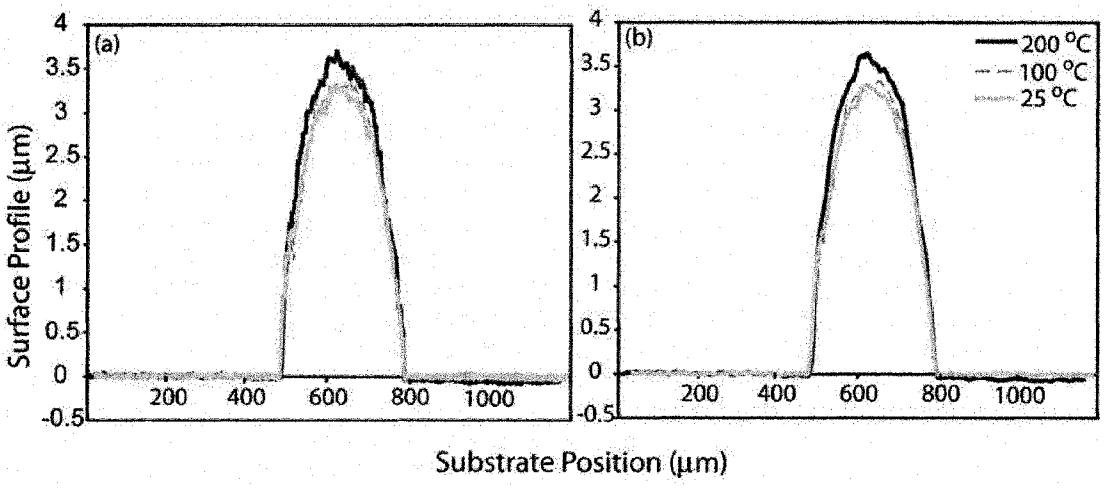

Figure 8.12: Actuation of a sample made by micro-transfer printing. The peak thickness of the sample increases by 11% ± 1% when the sample was heated from 25 °C to 200 °C. Two plots are shown, unfiltered data (a), and data which has been filtered by averaging each point with 12 neighboring points using a Gaussian weighting with a standard deviation of 2 points (b).

At room temperature, the surface profile of the sample is rounded, with the maximum height occurring at the center of the patterned area. The patterned structure is approximately 300 μm wide, as determined by the feature size of the stamp itself. In the future it may be possible to scale down this value by using PDMS stamps fabricated in the laboratory from lithographically defined silicon masters. The structured region is 3.25 ± 0.02 μm tall at room temperature, which is quite small as compared with the thickness of the best samples constructed using photopatterning (16.6 μm). This value is dependent mainly on the viscosity and surface tension of the liquid crystalline monomer mixture, and is therefore not easily increased. When the sample is heated to 200 °C the thickness increases to 3.62 ± 0.02 μm, which corresponds to an expansion of 11% ± 1%. Note that the thickness values given here were estimated from the filtered data, which was generated by averaging each point with 12 of its neighbors using a Gaussian distribution with a standard deviation of $\sigma = 2$ μm, as was described in Equation 6.3.

The overall change in thickness observed upon heating corresponds very well to the change in thickness observed for the chiral reference samples measured in Chapter 6 (11%). This suggests that the liquid crystals are very well aligned using the micro-transfer printing process and that the printing process is a feasible way of patterning these materials.

8.4 Conclusion

A variety of techniques for patterning liquid crystalline polymers on the microscale have been demonstrated. Photopatterning is a simple process in which a liquid crystalline monomer mixture in a liquid crystalline mesophase is selectively polymerized through a mask. The sample can then either be heated to the isotropic phase and flood exposed to produce multi-phase samples, or the sample can be rinsed in solvent to produce patterned single-phase structures. It was found that multi-phase samples have surface topographies at room temperature which expand reversibly when heated (1.6%, 200 °C), which was less than expected based on the behavior of the reference samples described in Chapter 6 (6%). Single-phase samples were found to undergo much larger strains, expanding by 8.4% ± 0.8% when heated to 200 °C from 25 °C. This value was slightly less than seen for chiral reference samples in Chapter 6 (11%). The reduced responsivity of both samples can be attributed to diffusion processes which occur during the polymerization process, reducing the alignment of the liquid crystalline moieties.

Micro-transfer printing was also investigated. This process produces structures similar to single-phase photopatterning. Good alignment and responsivity was achieved using this process (11% ± 1% expansion when heated to 200 °C from 25 °C). This process is well worth exploring in the future for the fabrication of devices.

Micro-transfer printing was also explored with a humidity-responsive polymer, and was found to be a feasible way of patterning this material. Overall these techniques show promise for micro-patterning liquid crystalline polymers for a variety of micro-applications.

8.5 References

1. Elias, A.L., Harris, K.D., Bastiaansen, C.W.M., Broer, D.J. and Brett, M.J., *Photopatterned liquid crystalline polymers for microactuators.* Journal of Materials Chemistry, 2006. **16**(28): p. 2903-2912.
2. Elias, A.L., Harris, K.D., Bastiaansen, C.W.M., Broer, D.J. and Brett, M.J., *Three techniques for micropatterning liquid crystalline polymers.* Submitted to Molecular Crystals and Liquid Crystals, July 31, 2006.
3. Schadt, M., Seiberle, H. and Schuster, A., *Optical patterning of multidomain liquid-crystal displays with wide viewing angles.* Nature, 1996. **381**(6579): p. 212-215.
4. van der Zande, B.M.I., Steenbakkers, J., Lub, J., Leewis, C.M. and Broer, D.J., *Mass transport phenomena during lithographic polymerization of nematic monomers monitored with interferometry.* Journal of Applied Physics, 2005. **97**(12): p. 123519-1 - 123519-8.
5. Sousa, M.E., Broer, D.J., Bastiaansen, C.W.M., Freund, L.B. and Crawford, G.P., *Isotropic "Islands" in a Cholesteric "Sea" – Patterned Thermal Expansion for Responsive Surface Topologies.* Advanced Materials, 2006. **14**: p. 1842-1845.
6. Zhang, F. and Yang, D.K., *Evolution of disclinations in cholesteric liquid crystals.* Physical Review E, 2002. **66**(4): p. 041701-1 - 041701-5.
7. Broers, A.N., *Resolution, overlay, field-size in lithography systems.* Ieee Transactions on Electron Devices, 1981. **28**: p. 1268-1278.
8. Kang, S.K. and Samulski, E.T., *Liquid crystals comprising hydrogen-bonded organic acids - I. Mixtures of non-mesogenic acids.* Liquid Crystals, 2000. **27**(3): p. 371-376.
9. Kato, T. and Frechet, J.M.J., *New Approach to Mesophase Stabilization through Hydrogen-Bonding Molecular-Interactions in Binary-Mixtures.* Journal of the American Chemical Society, 1989. **111**(22): p. 8533-8534.
10. Harris, K.D., Bastiaansen, C.W.M., Lub, J. and Broer, D.J., *Self-assembled polymer films for controlled agent-driven motion.* Nano Letters, 2005. **5**(9): p. 1857-1860.

9 Conclusion

9.1 Summary of Results

The objective of this thesis has been to develop and investigate methods to structure a variety of organic and inorganic materials on the micro- and nanoscale, and to determine how the properties of these materials change as a result.

Most of the fabrication techniques investigated in this thesis were based on templating from inorganic thin films deposited by glancing angle deposition. Glancing angle deposition (GLAD) is a physical vapor deposition process which results in the growth of independent columnar microstructures with highly-tunable architectures. These non-cylindrically symmetric, high surface area structures can be directly replicated into a number of different materials using the single-templating technique described in Chapter 3. The materials investigated include metals (nickel, gold) and polymers (polystyrene, liquid crystalline polymers). These films are called perforated thin films. New techniques for fabricating perforated thin films based on melt-processing and electroplating were presented, which greatly increased the range of materials which could be patterned with GLAD-like pores. The mechanical properties of nickel perforated thin films were investigated both experimentally and using finite element modeling. Among other results, it was found that within the model, the modulus of the templated films could be tuned from 65% to 100% of the modulus of the bulk material by varying the rise angle of the helical master film.

In Chapter 4, a double-templating technique was presented, which could be used to fabricate GLAD-like helices from different types of multi-functional acrylate polymers. This was the first demonstration of the large-area fabrication of multiple polymer helices with submicron dimensions. There is considerable interest demonstrated in the literature in making helical polymer structures, which is driven by the desire to use these structures as mechanical devices, photonic crystals, and high-surface area sensor devices.

It was shown that liquid crystalline polymers could also be shaped using both single- and double-templating processes. With an eye on making micro-actuator devices, the properties of these polymers were investigated. Liquid crystalline polymers are often referred to as a type of artificial muscle, and have been used to make numerous macroscopic actuator devices. However, the properties of these materials on the microscale had not been extensively investigated. Controlling the alignment of the liquid crystalline moieties within these materials is critical for designing and maximizing the deformations of these materials. It has been previously shown that when liquid crystals are infiltrated into films deposited by glancing angle deposition, interesting optical properties can result, owing to the alignment imparted from the GLAD template to the LCs. However, the alignment itself was not easily resolved. In Chapter 5 nuclear magnetic resonance of deuterated liquid crystals in a GLAD film was used to determine the alignment of the liquid crystals. The results indicated that the molecules align parallel to the surface of the helical structures at a constant rise angle and follow the twist of the helices, with a Gaussian distribution of a few degrees.

In Chapter 6 the mechanical, thermo-mechanical, and thermo-optical properties of liquid crystalline polymers were studied in detail. It was found that the magnitude of the mechanical deformation of thermally-responsive samples was dependent on the ratio of monoacrylate (M1) to diacrylate molecules (M2) within the sample. The optimal ratio was found to be 88:12 of M1:M2. Uniaxially aligned samples of this material were found to contract by 22% along the direction of molecular alignment when heated from 25 °C to 200 °C. Similar samples were measured over the same temperature range in the direction perpendicular to the director, and were found to expand by 19%. Optical studies in which the birefringence of the samples was monitored during heating confirmed that these deformations occurred due to a loss of order of the liquid crystalline molecules.

Anchoring liquid crystalline polymer films on glass substrates was found to significantly change the thermomechanical behavior of these materials. Finite element modeling was used to confirm that this change in behavior was due to the confinement placed on the film by the surface of the substrate. Cholesteric surface-anchored films were both

predicted, and demonstrated to undergo much larger deformations than planar or homeotropic surface anchored films, because for this configuration the stress in the plane of the substrate is minimized due to averaging of the thermal expansion coefficients. Cholesteric films were able to increase in thickness by 11% when heated to 200 °C, which was lower than for free-standing films, but still much higher than current state-of-the-art micro-actuator materials such as silicon, which is quite brittle and can only undergo strains of approximately 1% without fracturing [1-3].

In Chapter 7, three template-based fabrication processes were explored for microstructuring liquid crystalline polymers. The fabrication of liquid crystalline polymer helices with two different alignments was demonstrated using double-templating, and the thermal actuation of these structures was explored using scanning electron microscopy. Due to the small feature sizes of these helices, actuation was difficult to quantify. Single-templating was also used to pattern liquid crystalline polymers, and the responsivity of the resulting material was observed to be surprisingly low. Thermal actuation of the samples could not be distinguished from noise in the measurement. Theoretical calculations were used to show that the limited responsivity of liquid crystalline polymer perforated thin films was due to the presence of SiO_2 helices which remained embedded in the structure after the template was removed. These structures were not removed in the master-template etch because they became extinct during the deposition of the master GLAD film, and were therefore were shielded from etching by the polymer matrix due to their reduced height. A modified single-templating process was developed, in which the master film was etched from the bottom of the sample. This allowed the SiO_2 structures to be completely removed. To allow the thermomechanical behavior of the perforated film layer to be isolated from the thick layer of polymer beneath it, a lithographically patterned mask was used to protect some of the GLAD structures during the etch of the master film. The masked areas were therefore selectively reinforced with GLAD, which acted as 'nanorebar' during heating, preventing the polymer matrix around it from expanding or contracting as a function of temperature. At room temperature, large step height differences were found to exist between reinforced and non-reinforced areas, due to polymerization shrinkage. When the samples

were heated, this step height was reduced by 20% to 45% depending on the material involved (samples were fabricated using liquid crystalline and isotropic polymers). These selectively-reinforced bilayer composite structures could potentially be used in a number of applications, including micro-pumps, tactile displays, and controllable surfaces for aerodynamic applications.

In Chapter 8, some simpler processes for micro-patterning liquid crystalline polymer films were investigated, including single-phase photopatterning, multi-phase photopatterning, and micro-transfer printing. Single-phase photopatterning was used to make patterned lines of well-aligned liquid crystalline polymer anchored on a bare substrate. Multi-phase photopatterning was used to make thin films with patterned regions of aligned and isotropic liquid crystalline polymer. It was found that single-phase patterned structures made from liquid crystalline polymer with chiral-aligned molecules could expand by up to 8.4% ± 0.8% when heated from 25 °C to 200 °C. Micro-transfer printing, a simple printing process, was used to print liquid crystalline monomers. It was found that these thin structures were able to expand by 11% ± 1% when heated from 25 °C to 200 °C.

9.2 Outlook

Some promising methods for micro-patterning organic and inorganic materials have been presented. I hope that some of these processes will provide a valuable 'toolkit' for researchers working on application-specific projects. There are a plethora of projects underway within the GLAD group which will benefit from these techniques. For example:

1) It has been mentioned that perforated thin films in which the pores are shaped like square spirals are predicted to exhibit larger photonic bandgaps than direct square spirals. Colleague Mark Summers is currently working to create perforated thin film structures with square-spiral pores.
2) One of the fields of GLAD research with the most commercial potential is sensors. The high porosity of GLAD films is very useful for this application as it

can result in increased sensitivity and decreased response times over solid films. However, in the past, the range of materials from which GLAD-based sensors could be fabricated was limited to materials that could be deposited directly. Template-based fabrication techniques enable research into a whole new range of materials, which can be tailored to a specific application. For example, polyimide is a common active layer in many humidity sensors, but this material cannot be deposited directly using glancing angle deposition. However, this material could be made into a perforated thin film using techniques described in Chapter 3.

3) The optical properties of photoresist helical perforated thin films have been studied previously by former GLAD-group member Ken Harris [4]. These films were found to have interesting optical properties, selectively transmitting and reflecting circularly polarized light with opposite and like handedness with a selectivity that far exceeded the template films from which they were made. One limitation in creating optical devices from helical films deposited by glancing angle deposition has been the non-uniformity of the helices themselves. Characteristics such as pitch, helical radius, and inter-column spacing can vary significantly throughout a film, which can be detrimental to the optical properties of these films. It has recently been demonstrated that GLAD films can be deposited from the small-molecule organic material Alq_3, to create structures with excellent uniformity in all three dimensions, which maintain constant cross-sectional areas throughout the deposition (with the exception of the wetting layer deposited in the first few hundred nanometers). These films exhibit strong circular Bragg effects. For this reason there is a renewed interest in fabricating perforated thin films for optical studies, this time using Alq_3 films as the master template. If the inverse structures show excellent optical properties, they could also form the basis for optical sensing devices.

A large portion of this thesis has focused on characterizing, patterning, and actuating liquid crystalline polymer films, with the goal of incorporating these materials into microscaled devices such as actuators. The thermomechanical behavior of these materials was studied, and the effect of anchoring these materials to substrates was

presented. Many different patterning techniques were explored. However, there is still considerable work to be done in this area. Two of the simplest techniques examined were photopatterning and micro-transfer printing. The photopatterning process was greatly limited in terms of resolution by the fact that a mask aligner could not easily be incorporated into the set-up. Most samples needed to be polymerized at an elevated temperature, preferably in a nitrogen environment, which precluded the use of a mask aligner. Therefore, less collimated light sources were usually employed. To overcome this problem, Casper van Oosten at the Eindhoven University of Technology is currently building a mask aligner with temperature controller and nitrogen environment for sample polymerization. This should facilitate the fabrication of samples with much smaller feature sizes. There are other very interesting experiments that can be undertaken in this area, which include:

1) Micro-patterning liquid crystalline polymer films with splay or twisted nematic alignment of the liquid crystals. If these films could be partially released from the substrate, they would curl up on heating, allowing out of plane actuation with large strain.
2) Examining liquid crystalline monomers which respond to different stimuli, including pH, humidity, light or electricity. Electrical actuation in particular would be more useful for making usable microelectromechanical devices. Some of this work is also being taken up by Casper van Oosten.

The micro-transfer printing work presented here barely scratches the surface of the potential of this technique. The most obvious next step for this project is to reduce the dimensions of the patterned structures using PDMS stamps patterned from lithographically defined silicon masters. Again, it would be quite interesting to investigate this technique for patterning materials that respond to different stimuli. The simplicity of this process combined with the fact that it leads to the generation of very little waste material could make it a powerful fabrication process for manufacturing devices on a larger scale.

I would like to conclude that liquid crystalline polymers show great potential for incorporation into micro-actuator devices. Of course, no material can easily replace silicon. Integration is always a major issue for any new material being considered for microscaled applications. Nonetheless the benefits of using this material could push this work forward for a number of important niche applications.

9.3 References

1. Gad-el-Hak, M., *The MEMS handbook.* The Mechanical engineering handbook series. 2002, Boca Raton, FL: CRC Press.
2. Khang, D.Y., Jiang, H.Q., Huang, Y. and Rogers, J.A., *A stretchable form of single-crystal silicon for high-performance electronics on rubber substrates.* Science, 2006. **311**(5758): p. 208-212.
3. Zhu, Z.T., Menard, E., Hurley, K., Nuzzo, R.G. and Rogers, J.A., *Spin on dopants for high-performance single-crystal silicon transistors on flexible plastic substrates.* Applied Physics Letters, 2005. **86**(13).
4. Harris, K.D., Sit, J.C. and Brett, M.J., *Fabrication and optical characterization of template-constructed thin films with chiral nanostructure.* IEEE Transactions on Nanotechnology, 2002. **1**(3): p. 122-128.

Appendix 1: MATLAB Code For NMR Modeling

The following MATLAB programs were used to generate the theoretical spectra shown in Section 5.6 of this thesis. Each of these programs generates a spectrum based on an assumed alignment of liquid crystals within a GLAD film. For each assumed alignment, two different scenarios are modeled: the first is when the external magnetic field B_o is aligned parallel to the helices themselves, and the second is when the magnetic field is aligned perpendicular to the helices.

Case 1, B parallel to helical axis

```
%Case 1, where the magnetic field is aligned parallel to the helical axis, is the simplest
%case. For this scenario, all of the liquid crystals are aligned at the same angle theta1
%with respect to the B field.

syms t                          %indicates that symbolic math is required, with variable t
bulk=55000;                     %this is the splitting frequency of the bulk
theta1=49*pi/180;               %here all the LCs are aligned at 49 deg. to the Bfield

time=linspace(0,.002044, 511);          %defines the 512 points in the time domain
frq=linspace(-62500,62500,511);         %defines the 512 points in the freq. domain

delta_nu=bulk*(1.5*cos(theta1)^2-.5);   %determines the splitting for angle theta1
G=exp(j*2*pi*int(delta_nu,t));          %sets up the inverse fourier transform
g=subs(G,time);                 %substitutes variable 'time' into eqn. G

k=exp(-2500.*time);             %defines a decaying exponential in the time domain
h=g.*k;                         %multiplies the decaying exponential by the signal
d=fft(real(h));                 %this command takes the fast fourier transform of h
s=fftshift(real(d));            %required to display the solution as a function of frequency

figure
subplot(2,2,1)
xlabel=('Time (s)')
plot(time,real(h))              %plots the results in the time domain
subplot(2,2,2)
plot(frq,s)                     %plots the results in the frequency domain
xlabel=('Frequency (Hz)')
```

Case 1, B perpendicular to helical axis

```
%case 1: liquid crystal are circular in plane, with a constant rise angle
%of alphadegrees. The field is perpendicular to the helices.
```

```
clear xlabel
clear ylabel
syms t
bulk=55000;

time=linspace(0,.002044, 511);
frq=linspace(-62500,62500,511);

%r is the angle between the lcs and the field. Even when the LCs are
%'parallel' to the field in the plane, they are still at 41 degrees to the
%field. All angles are equally probable.

alpha = 41;                    %this is the min angle between the field and LCs
rmin = 1;                      %this is the min. angle WITHIN the plane
rmax = 90;                     %max angle WITHIN the plane
step = 1;

%there are LCs at every angle within the plane (r). r ranges from 0 to 90. But the angle
%(theta) between the field and the LCs ranges from 0 to 41. Here we determine theta for
%each r. At rmin, theta =41. At rmax, theta =90. Every angle in between is assigned
%linearly.

for r=rmin:step:rmax

   theta(r)=pi/180*(alpha+r*(90-alpha)/90);
   theta(r)*180/pi
   delta_nu(r)=bulk*(1.5*cos(theta(r))^2-.5);

%in the previous case there was only %one delta_nu. Now there are many.
%Each delta_nu gets its own inverse Fourier transform. These are added together in the
%time domain. This can be done because the Fourier transform is linear.

   G=exp(j*2*pi*int(delta_nu(r),t));
   gnew=subs(G,time);

 if r ==1
      gadditive = gnew;

 else
      ggadditive = gadditive + gnew;
      gadditive = ggadditive;
 end
end

%After this, the analysis proceeds as for case 1.
```

```
k=exp(-2500.*time);
h=gadditive.*k;
d=fft(real(h));
s=fftshift(real(d));

figure
subplot(2,2,1)
xlabel=('Time (s)')
plot(time,real(h))
subplot(2,2,2)
plot(frq,s)
xlabel=('Frequency (Hz)')
```

Case 2: B field parallel to helical axis

```
% this case is very similar to case 1. The LCs are aligned at a constant angle, only with a
% small Gaussian distribution. To model this system, the splitting (and inverse Fourier
% transform) is calculated for every angle from 1° to 90° in 1° steps. The inverse Fourier
% transform is then weighted by its probability, i.e. multiplied by a Gaussian. These
% weighted transforms are then added together, and the Fourier transform is taken to
% produce the overall spectrum.

syms t
bulk=55000;
mean = 49; %enter the angle in degrees measured from the field (perp. to the substrate)
sigma = 3;

time=linspace(0,.002044, 511);
frq=linspace(-62500,62500,511);

% a is all possible angles between the lcs and substrate parallel.  mean is one of
%these angles, and it is the most probable one

%theta is the angle between the lc and the field
amin = 1;
amax = 90;
step = 1;
a=49;

%phi is the angle of the lc in the plane of the substrate (azimuthal angle)
phimin = 1;
phimax = 90;
stepphi=1;

for a=amin:step:amax
%    a
```

```
   for phi = phimin:stepphi:phimax
      %phi
      theta(phi)=pi/180*(a+(90-a)/90*phi);
      th = theta(phi)*180/pi;
   delta_nu(phi)=bulk*(1.5*cos(theta(phi))^2-.5);
   G=exp(j*2*pi*int(delta_nu(phi),t));
   gnew=subs(G,time)*1./(sigma*((2*pi)^5)).*exp(-((a-mean).^2)./(2*sigma.^2));

      if a==1
         if phi==1
         gadditive = gnew;
         end
      else
      ggadditive = gadditive + gnew;
      gadditive = ggadditive;
      end
   end
end

k=exp(-2500.*time);
h=gadditive.*k;
d=fft(real(h));
s=fftshift(real(d));

figure
subplot(2,1,1)
xlabel=('Time (s)')
plot(time,real(h))
subplot(2,2,2)
plot(frq,s)
xlabel=('Frequency (Hz)')
```

Case 2: B field perpendicular to helical axis

```
% this case is very similar to case 1. The LCs are aligned at a constant angle, only with a
% small Gaussian distribution. Therefore this model is very similar to case 1, B_perpendicular,
% only for each angle computed the inverse fourier transform is weighted by the
% Gaussian probability, before they are added together to form the signal.

clear
syms t
bulk=55000;

rmin = 1;
rmax = 90;
step = 1;
```

```
mean=pi/180*41;
sigma=pi/180*3;

time=linspace(0,.002044, 511);
frq=linspace(-62500,62500,511);

for r=rmin:step:rmax

   theta(r)=r*(pi/180);
   delta_nu(r)=bulk*(1.5*cos(theta(r))^2-.5);
   G=exp(j*2*pi*int(delta_nu(r),t));
   gnew=subs(G,time)*1/(sigma*((2*pi)^.5))*exp((-((r*(pi/180))-
mean)^2)/(2*sigma^2));

      if r == 1
      gadditive = gnew;
   else
      ggadditive = gadditive + gnew;
      gadditive = ggadditive;
   end
end

   k=exp(-2500.*time);
   h=gadditive.*k;
   d=fft(real(h));

s=fftshift(real(d));

figure
subplot(2,2,1)
xlabel=('Time (s)')
plot(time,real(h))
subplot(2,2,2)
plot(frq,s)
xlabel('Frequency (Hz)')
```

Case 3: B field parallel to helical axis

```
% Case 3 is somewhat different than the others.  In this case the orientation of each LC is
% proportional to its distance from the helix, ie: it's radius.  Here r varies from 75nm to
% 200nm, where 75nm is the width of the helix, and 200nm is the distance from the
% center of a helix to the center of the cavity which surrounds it.
```

```
clear
syms t
bulk=55000;

rmin = 75;
rmax = 200;
step = 1;

   time=linspace(0,.002044, 511);
   frq=linspace(-62500,62500,511);

% the angle theta between each LC and the B field varies linearly from 49° to 0°, as a
function of position.

for r=rmin:step:rmax
   theta_dist(r)=(pi/180)*(49-(49/125).*(r-75));
   delta_nu(r)=bulk*(1.5*cos(theta_dist(r))^2-.5);
   G=exp(j*2*pi*int(delta_nu(r),t));
   gnew=subs(G,time)*r;

% each inverse Fourier transform is weighted by it's radius. This is because the number
% of LCs at each value of r is proportional to r itself. Ie: there are many more LCs at
% r=200nm than at r=75nm.

   if r ==75
      gadditive = gnew;
   else
      ggadditive = gadditive + gnew;
      gadditive = ggadditive;

   end
 end

 k=exp(-2500.*time);
h=gadditive.*k;
d=fft(real(h));
s=fftshift(real(d));

figure
subplot(2,1,1)
plot(time,real(h))
xlabel=('Time (s)')
subplot(2,2,2)
plot(frq,s)
xlabel=('Frequency (Hz)')
```

Case 3: B field perpendicular to helical axis

```
syms t
bulk=55000;
time=linspace(0,.002044, 511);
frq=linspace(-62500,62500,511);

%r is the radius
%alpha is the angle between the lc tilt out of the plane and plane of the field
%theta is the angle between the lc and the field
rmin = 75;
rmax = 200;
step = 1;

ao = 41; %ao is the out of plane angle at the surface of the helix

%phi is the angle of the lc in the plane of the substrate (azimuthal angle)
phimin = 1;
phimax = 90;
stepphi=1;

% here a linear function is established that assigns an angle for a given radius (r). This
% value varies from 41 to 90, depending on the position of the LC in the cavity.

for r=rmin:step:rmax
  alpha(r-74)= ao+(90-ao)/125*(r-75);
  for phi = phimin:stepphi:phimax
    theta(phi) = (alpha(r-74)+((90-alpha(r-74))/90)*phi)*pi/180;  %this is in radians
  delta_nu(phi)=bulk*(1.5*cos(theta(phi))^2-.5);
  G=exp(j*2*pi*int(delta_nu(phi),t));
  gnew=subs(G,time)*r;

% each inverse Fourier transform is weighted by it's radius. This is because the number
% of LCs at each value of r is proportional to r itself. Ie: there are many more LCs at
% r=200nm than at r=75nm.

    if r==75
      if phi==1
      gadditive = gnew;
      end
    else
    ggadditive = gadditive + gnew;
    gadditive = ggadditive;
    end
  end
end
```

```
k=exp(-2500.*time);
h=gadditive.*k;
d=fft(real(h));
s=fftshift(real(d));

figure
subplot(2,1,1)
xlabel=('Time (s)')
plot(time,real(h))
subplot(2,2,2)
plot(frq,s)
xlabel=('Frequency (Hz)')
```